William & Mary
CHARTERED 1693

W&M ScholarWorks

Dissertations, Theses, and Masters Projects

Theses, Dissertations, & Master Projects

2004

Dual energy scanning beam X -radiography

Randolph Frank Wojcik
College of William & Mary - Arts & Sciences

Follow this and additional works at: https://scholarworks.wm.edu/etd

Part of the Investigative Techniques Commons, Materials Science and Engineering Commons, and the Nuclear Commons

Recommended Citation

Wojcik, Randolph Frank, "Dual energy scanning beam X -radiography" (2004). *Dissertations, Theses, and Masters Projects.* Paper 1539623461.
https://dx.doi.org/doi:10.21220/s2-p883-0h78

This Dissertation is brought to you for free and open access by the Theses, Dissertations, & Master Projects at W&M ScholarWorks. It has been accepted for inclusion in Dissertations, Theses, and Masters Projects by an authorized administrator of W&M ScholarWorks. For more information, please contact scholarworks@wm.edu.

DUAL ENERGY SCANNING BEAM X-RADIOGRAPHY

A Dissertation

Presented to

The Faculty of the Department of Applied Science

The College of William and Mary in Virginia

In Partial Fulfillment

of the Requirements for the Degree of

Doctor of Philosophy

---

by

Randolph Frank Wojcik

2004

Reproduced with permission of the copyright owner. Further reproduction prohibited without permission.

APPROVAL SHEET

This dissertation is submitted in partial fulfillment of

the requirements for the degree of

Doctor of Philosophy.

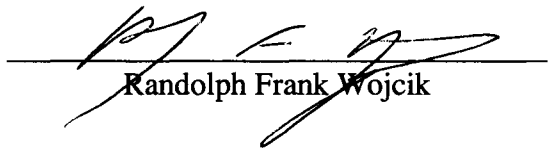

Randolph Frank Wojcik

Approved by the Committee, November 2004

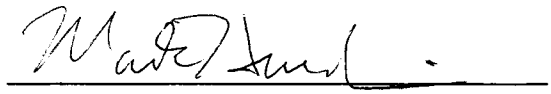

Mark Hinders, Chair

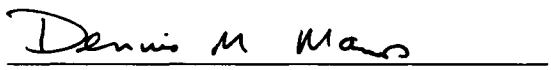

Dennis M. Manos

Robert Welsh

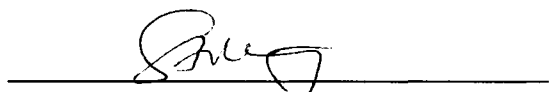

Stan Majewski
Thomas Jefferson National Accelerator Facility

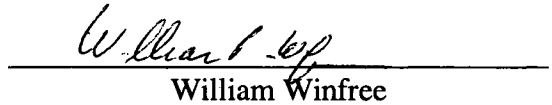

William Winfree
NASA-Langley Research Center

Reproduced with permission of the copyright owner. Further reproduction prohibited without permission.

To my lovely wife and wonderful daughter for all their patience and support.

Reproduced with permission of the copyright owner. Further reproduction prohibited without permission.

TABLE OF CONTENTS

	Page
Acknowledgements	vi
List of Tables	vii
List of Figures	viii
Abstract	xv
Introduction	2
Chapter I. Radiation and Matter	4
History	4
Production of x-rays	6
Interaction of x-rays with matter	10
Photoelectric absorption	11
Compton scattering	12
Rayleigh scattering	14
Linear Attenuation Coefficient	15
Chapter II. Conventional x-radiography	17
Chapter III. Scanning beam x-radiography	20
Laminography	23
Optimizing the Detector	24
Optimizing the scintillator	25
Optimizing the PMT assembly	29
Optimizing the preamplifier	35
X-ray flux calculation	39
Chapter IV. Dual Energy x-radiography	44
Monoenergetic sources	44
Polyenergetic sources	51
Prior work on dual energy x-radiography	55
Chapter V. Scanning beam dual energy x-radiography	61
Detector development	61
Detective quantum efficiency	68
Calibration	73
Calibration procedure	88

Reproduced with permission of the copyright owner. Further reproduction prohibited without permission.

Image Projection 91
Phantoms 105

Chapter VI. Conclusions and Future Directions 111

Appendix A. Normalization program 115

Appendix B. Example of thickness – energy transmission data 122

Appendix C. Least Squares fit program 125

Appendix D. Levenberg-Marquardt program 148

Appendix E. US Patent #5,742,660 167

References 174

Vita 180

Reproduced with permission of the copyright owner. Further reproduction prohibited without permission.

ACKNOWLEDGMENTS

Many people have helped in the completion of this work. I would like to express great appreciation to the members of my committee: Drs. Robert Welsh, Stan Majewski, Dennis Manos, Mark Hinders, and William Winfree for being so patient with me with my busy schedule. I wish to thank my thesis advisor and mentor, Dr. Stan Majewski for sharing with me his vast knowledge of particle physics detection and for the many hours he spent showing me how radiation detectors are produced and operate. He has also made it possible for me to be involved in applying nuclear physics detectors to problems in various fields including Non-destructive testing and medical imaging. I thank Dr. William Winfree for providing his time and resources including equipment, funding, and labor which made this work possible. I thank Dr. Welsh for his insightful comments and for helping to steer me through to completion of this Dissertation. I thank Ray Parker of NASA-Langley for assisting me in the imaging measurements and teaching me how the Digiray system operates as well as his many suggestions and useful discussions. I thank Dr. Richard Albert, the president of Digiray and the inventor of this scanning x-ray imaging technology, for his many helpful suggestions.

Many others have contributed their time and ideas to the development of this technology including John Granger, Daniel Perey, and Ed Scales all of NASA-Langley. I thank Keith Welch of Jefferson Lab for the loan of some radiation detectors and checking out the ScanRay Torrex II Fluoroscopic radiation cabinet.

I also thank Kathee Card, Marcy Rosa Borges, Wanda Carter, and Carol Davanay in Applied Science for all their assistance with registration and university requirements.

I gratefully acknowledge the funding assistance from the Southeastern Universities Research Association (SURA) which operates the Thomas Jefferson National Accelerator Facility for the United States Department of Energy under contract DE-AC05-84ER40150.

Reproduced with permission of the copyright owner. Further reproduction prohibited without permission.

LIST OF TABLES

Table	Page
1. Characteristic spectral lines	8
2. Interactions of gamma rays with matter	9
3. Results of Rayleigh scattering	15
4. Partial list of scintillators	26
5. Voltage readings	33
6. Transmission of 100 keV x-rays	36
7. Standard deviation of the signal for various feedback capacitors	38
8. Results of x-ray induced light output measurements	65
9. Thickness (in mm) of the calibration phantoms	74
10. RMS error in the fitting results of the thickness for Copper or Aluminum	83
11. RMS error in the fitting results of the thickness of Acrylic	83
12. Measured subtraction and measured and calculated projection angles	107

Reproduced with permission of the copyright owner. Further reproduction prohibited without permission.

LIST OF FIGURES

Figure	Page
1. Cathode ray tube	5
2. X-ray of Mrs. Roentgen's Hand	5
3. The modern day x-ray tube invented by W.D. Coolidge	6
4. Schematic Diagram of an x-ray Generator	6
5. Example of a modern rotating anode x-ray tube	7
6. The energy spectrum from an x-ray tube	9
7. Photoelectric interaction of an x-ray photon with an atom	10
8. Linear attenuation coefficients for acrylic	12
9. Linear attenuation coefficients for aluminum	12
10. Compton scattering of an x-ray photon by an electron	13
11. Angular distribution of Compton scattered photons	14
12. Conventional x-ray set-up using anti-scatter grid	17
13. Diagrams illustrating the effect of the x-ray focal spot size	18
14. Geometrical setup for Scanning beam x-radiography	20
15. Correlation of the raster scan of the x-ray beam	20
16. Diagrams illustrating the effect of the x-ray spot size	21
17. Image of cadaver's hand in a plastic surgeon's glove	22
18. Top and side view of a multi-detector laminography setup	24
19. Laminography performed on a quarter	24
20. Digiray x-ray detector block diagram	25

Reproduced with permission of the copyright owner. Further reproduction prohibited without permission.

21. Image of a lead phantom and horizontal profile cut 25

22. Images of a lead phantom using "slow" and "fast" YAP 27

23. Same object as in fig. 22 imaged using GSO 27

24. Horizontal profile cuts through the lead phantom for various crystals 27

25. Image acquired using a square scintillator 29

26. Diagram showing how the active surface area of a scintillator changes 29

27. Dynode configurations 31

28. Active voltage divider used for the Digiray PMT 32

29. Image of line pair gauge from a PMT without a scintillator 33

30. Experimental set ups to analyze streaking effect 34

31. Measurement of streaking for different scintillators in different configurations 36

32. Amplifiers used in the studies 37

33. Profile cut across the 8 line pairs per mm section of a calibration phantom 37

34. Profile cut across the 8 line pairs per mm section of a calibration phantom for the new amplifier 38

35. Proposed circuit diagram of optimized data acquisition system 39

36. Timing diagram for data acquisition 39

37. Calculated photon spectrum from Digiray's x-ray tube 40

38. Design of battery powered pre-amplifier 41

39. High speed counting system used to measure x-ray flux 41

40. Theory vs. measured x-ray production from Digiray's RGX system 43

41. Representation of material x in the basis material-thickness plane 48

42. Adding of material vectors 48

Reproduced with permission of the copyright owner. Further reproduction prohibited without permission.

43. Object made of two different materials, m and n with a total thickness of L 50

44. Reconstruction from polychromatic projection data of a water phantom 50

45. Cross section of a reconstructed water phantom 50

46. X-ray spectra obtained using 70 kV and 140 kV settings 56

47. X-ray absorption spectra for a two detector dual energy system 56

48. Dual energy fan beam scanning x-ray system 58

49. Standard chest x-ray, bone subtracted, and soft tissue subtracted images 59

50. Dual energy bone densitometry scanner 59

51. Images from a dual energy x-ray CT luggage scanner 60

52. Absorption spectra of a 5% Pb loaded plastic scintillator and YAP 62

53. Absorption and transmission spectra for 200 μm thick YAP 62

54. Configuration of the scintillators, light guide and PMTs 63

55. Absorption of 200 μm YAP verses 200 μm YAP plus 1 cm BC408 65

56. Experimental setup to measure response of samples to x-rays 65

57. Absorption spectra of the x-ray energy detectors for 100 keV x-ray voltage 66

58. Figure 56 with the low and high energy absorption peaks normalized 66

59. Absorption spectra of the x-ray energy detectors for 120 keV x-ray voltage 67

60. Figure 56 with the low and high energy absorption peaks normalized 67

61. Picture of the two-detector dual energy sensor used in these measurements 68

62. The dead time of a detector 70

63. Examples of DQEs of various integrating and counting detectors 70

64. Comparison of DQEs for integrating and counting detectors 72

65. Example of the importance of normalizing the image 75

Reproduced with permission of the copyright owner. Further reproduction prohibited without permission.

66. Example of the normalization of an image 76

67. Image of 16.14 mm of acrylic with aluminum step wedge 76

68. Profile cut across the high and low x-ray energy images 77

69. Diagram of scanning beam x-radiography setup using an anti-scatter grid 77

70. Comparison of profile cuts across a 5.38mm thick acrylic sheet 79

71. Thickness of Copper of the Copper / Thin Pl phantom with equation 5-21 84

72. Thickness of Acrylic of the Copper / Thin Pl phantom with equation 5-21 84

73. Thickness of Acrylic of the Copper / Thin Pl phantom with equation 5-18 84

74. Thickness of Aluminum of the Thin Al / Thin Pl phantom with equation 5-19 84

75. Thickness of Aluminum of the Thin Al / Thin Pl phantom with equation 5-17 85

76. Thickness of Acrylic of the Thin Al / Thin Pl phantom with equation 5-17 85

77. Thickness of Aluminum of the Thin Al / Thin Pl phantom with equation 5-17 85

78. Thickness of Acrylic of the Thin Al / Thin Pl phantom with equation 5-17 85

79. Thickness of Aluminum of the Step Al/Thick Pl phantom with equation 5-17 86

80. Thickness of Acrylic of the Step Al / Thick Pl phantom with equation 5-17 86

81. Thickness of Copper of the Copper / Thin Pl phantom with equation 5-17 86

82. Thickness of Acrylic of the Copper / Thin Pl phantom with equation 5-17 86

83. Thickness of Aluminum Thin Al / Thin Pl phantom with equation 5-17 87

84. Thickness of Acrylic of the Thin Al / Thin Pl phantom with equation 5-17 87

85. Thickness of Aluminum of the combined Thin Al / Thin Pl and the Step Al / Thick Pl phantom with equation 5-17 87

86. Thickness of Acrylic of the combined Thin Al / Thin Pl and the Step Al / Thick Pl phantom data using fitting equation 5-17 87

87. Profile cut along the copper step wedge from the low energy detector 88

Reproduced with permission of the copyright owner. Further reproduction prohibited without permission.

88. Profile cut along the Thin Al step wedge from the high energy detector 88

89. Profile cut along the Thin Al step wedge from the low energy detector image showing no Compton scattering 88

90. Profile cut along the Step Al phantom from the high energy detector image showing only minor Compton scattering effects 88

91. Comparison of a profile cuts along the copper step wedge for the Copper / Thin Pl phantom for the images obtained with fitting equation 5-21 92

92. Comparison of a profile cut along the copper step wedge for the Copper / Thin Pl phantom using fitting equation 5-17 93

93. Profile cut across the step wedge showing the results of using the worst fit, fitting equation 5-18, on the Copper / Thin Pl phantom 94

94. Copper and Acrylic projection images of the Copper/ Thin Pl phantom using equation 5-17 94

95. Comparison of profile cuts along the aluminum step wedge for the Thin Al / Thin Pl phantom of the aluminum projection obtained with equation 5-19. 95

96. Comparison of a profile cut along the thin aluminum step wedge for the Thin Al / Thin Pl phantom images obtained with fitting equation 5-17 96

97. Aluminum projection image and close up of the top steps of the Thin Al / Thin Pl phantom obtained with fitting equation 5-19 97

98. Aluminum and Acrylic projection images of the Step Al/ Thick Pl phantom using equation 5-17 97

99. Comparison of a profile cut along the aluminum step wedge for the Step Al / Thick Pl phantom for the images obtained with fitting equation 5-17 98

100. Comparison of a profile cut along the aluminum step wedge for the Step Al/ Thick Pl phantom for the images obtained with fitting equation 5-21 99

101. Comparison of a profile cut along the aluminum step wedge for the Thin Al / Thin Pl phantom for the images obtained with fitting equation 5-17 99

102. Acrylic projection images of the Thin Al/ Thin Pl phantom with equation 5-17 100

Reproduced with permission of the copyright owner. Further reproduction prohibited without permission.

103. Comparison of a profile cut along the aluminum step wedge for the Step Al / Thick Pl phantom for the images obtained with fitting equation 5-17 100

104. Acrylic projection images of the Step Al/ Thick Pl phantom using the Step Al/ Thick Pl data with equation 5-17 101

105. Acrylic subtraction images of the Thin Al / Thin Pl and Step Al/ Thick Pl phantoms using the Copper / Thin Pl data with fitting equation 5-17 101

106. Aluminum subtraction images of the Thin Al / Thin Pl and Step Al/ Thick Pl phantoms using the Copper / Thin Pl data with equation 5-17 102

107. Aluminum subtraction images of the Thin Al / Thin Pl phantom 103

108. Aluminum subtraction images of the Thin Al / Thin Pl and Step Al/ Thick Pl phantoms using the Copper / Thin Pl data with equation 5-21 104

109. Aluminum projection images of the Thin Al / Thin Pl at 3.25° and the Step Al/ Thick Pl at 5.00° with fitting equation 5-17 105

110. Low x-ray energy image of phantom one containing Acrylic and aluminum sheets as well as Teflon, Nylon, and ABS plastic cylinders 106

111. Acrylic projection of figure 109 identifies which plate is Acrylic and which plate has which holes 106

112. Aluminum projection of figure 109 107

113. ABS plastic subtraction image of figure 109 107

114. Nylon subtraction image of figure 109 108

115. Teflon subtraction image of figure 109 108

116. Images showing the aluminum plugged hole 108

117. Low x-ray energy image of a riveted aircraft phantom 109

118. Construction of the riveted aircraft phantom 109

119. Steel and aluminum subtracted images of the riveted aircraft phantom. The image shows the aluminum band is intact while the head of the rivet it cut 109

120. Photographs of the front and back of the riveted aircraft phantom 110

Reproduced with permission of the copyright owner. Further reproduction prohibited without permission.

121. Original low energy x-ray image, tungsten subtracted image, and aluminum subtracted image of tungsten foils 110

122. Photographs of the XP1700 series of multianode PMTs 113

123. Layout of 8 x 8 YAP crystal array coupled to the XP1702 113

124. Energy spectrum from a single YAP crystal directly coupled 113

125. Energy spectrum from a single YAP crystal couple through a 3 mm fiber 113

Reproduced with permission of the copyright owner. Further reproduction prohibited without permission.

ABSTRACT

Dual energy X-radiography is a method first developed in the mid-1970's by which one uses the information contained in the energy spectrum of the transmitted X-ray flux through an object. With this information one can distinguish the types of materials present in a radiograph and thus allow a computer to subtract them from the image enhancing the contrast of the remaining materials. Using this method, one can see details, which would have been hidden by overlying structures of other materials such as seen in radiographs of parts, made up of mixtures of metals and composites. There is also great interest in this technique for medical imaging of the chest where images of the organs are significantly improved by subtracting the bones. However, even with the enhanced capabilities realized with this technique, the majority of X-radiography systems only measures the bulk transmitted X-ray intensity and ignores the information contained in the energy spectrum. This is due to the added expense, time requirements, and registration problems incurred using standard radiographic methods to obtain dual energy radiographs. This dissertation describes a novel method which overcomes these problems and allows one to perform inexpensive, near real time, single shot dual energy X-radiography. The work of this thesis resulted in US patent #5,742,660.

Reproduced with permission of the copyright owner. Further reproduction prohibited without permission.

DUAL ENERGY SCANNING BEAM X-RADIOGRAPHY

Reproduced with permission of the copyright owner. Further reproduction prohibited without permission.

INTRODUCTION

Non destructive evaluation (NDE) is a descriptive term used for the examination of materials and objects in a way that allows materials to be imaged without changing or destroying their usefulness. NDE plays a crucial role in everyday life and is necessary to assure the safety and reliability of equipment. Typical examples are found in aircraft, motor vehicles, pipelines, bridges, trains, power stations, refineries and oil platforms which are all inspected using NDE. In security applications, NDE can detect explosives, nuclear materials, and weapons faster and more reliably than visual inspections. There is a large variety of imaging modalities used for NDE including optical, acoustic, eddy current, ultrasonic, and x-radiography. X-radiography is one of the key techniques to peer inside objects without having to disassemble them. This can be used to check the seals inside an airbag deployment cylinder, find cracks or corrosion inside aircraft wings, as well as find a gun in a handbag. X-radiography is simple and reliable with the majority of the advancements these days coming in the form of increased resolutions and easier and faster imaging.

This thesis describes the development and testing of a novel dual energy x-radiography imaging system based on a relatively new way to image objects with x-rays – Reverse Geometry x-radiography (RGX)™. RGX, invented about 25 years ago and described below, took many years for the inventor to bring to market due to difficulties in the development of the x-ray tube. In this system, the complexity is in the x-ray tube while the imaging detector is quite simple. This offers a new flexibility in imaging objects. The simplicity of the imaging detectors allows one to produce images from inside objects rather then all the way through them, perform motionless computed tomography, and dual energy imaging. Dual energy imaging offers the ability to identify the composition of materials in an image rather than just seeing their shapes. It also allows one to subtract all objects

Reproduced with permission of the copyright owner. Further reproduction prohibited without permission.

composed of a selected material from the image so one can focus on studying the remaining materials with better contrast. Dual energy imaging is not new, however, this novel system greatly reduces the complexity and expense of obtaining such images.

In the organization of this dissertation, the first part of Chapter I gives some history and background information needed to understand some of the techniques used and difficulties encountered in x-radiography. It also introduces the basics of the production of x-rays and how they interact with matter which is important in understanding how dual energy x-radiography works. Chapter II describes how conventional x-radiography is performed. Chapter III introduces and describes the advantages and problems associated with scanning beam x-radiography. Chapter IV lays out the theoretical foundations of dual energy x-radiography. Chapter V describes the dual energy detector development, calibration procedures and results, and results of test imaging of various phantoms. Chapter VI summarizes the results and gives suggestions for future work with this device.

Reproduced with permission of the copyright owner. Further reproduction prohibited without permission.

CHAPTER I

RADIATION AND MATTER

History

To understand the intricacies of x-radiography (and thus dual energy x-radiography) one must first understand how x-rays are produced in an x-ray tube and how they interact with matter. x-rays were first discovered by Wilhelm Conrad Roentgen while investigating cathode-ray fluorescence caused by discharging electricity through a tube filled with rarified gas as shown in figure 1. Working late one Friday night in November 1895 he noticed a strange glow emanating from a small screen lying on a nearby table. Invisible rays were causing it to fluoresce. Fascinated with this new phenomenon, he investigated it day and night, eating and sleeping in the lab. He soon discovered that this radiation could penetrate solid substances and that it had the same effect on a photographic plate as light. The first "Roentgen exposures" that were made were of metal objects locked in a wooden case and of the outline of the bones in his wife's hand (fig. 2). Because "X" is used in mathematics to indicate an unknown quantity, he called these rays "x-rays." Roentgen published his findings on December 28th, 1895 and the news spread rapidly through out the world. As early as February 8, 1896, x-rays were being used clinically in Dartmouth, Massachusetts when Edwin Brant Frost produced an image of a Colles fracture, a fracture of the lower arm bone just above the wrist, in a man named Eddie McCarthy for his brother, Dr. Gilman Dubois Frost.[1] These early cold cathode gas-discharge x-ray tubes operated in an erratic fashion and had to be checked often. Since no measuring instruments were available, this was usually done by holding one's hand close to the tube and examining the resulting image. This, unfortunately, led to the first radiation induced injuries from overexposure.

Reproduced with permission of the copyright owner. Further reproduction prohibited without permission.

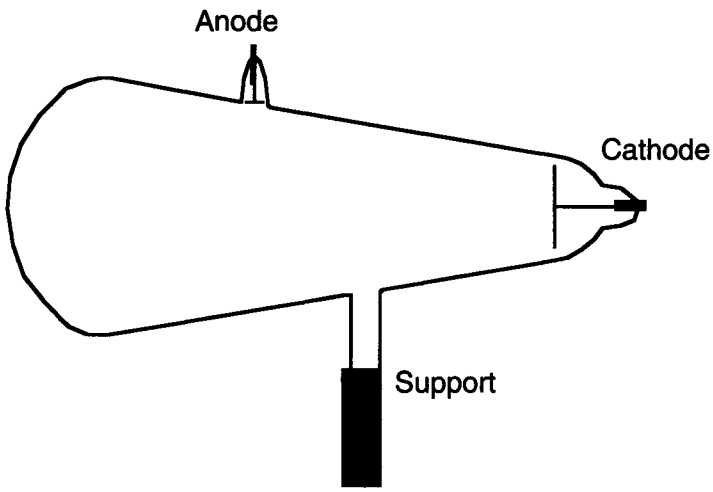

Figure 1: Cathode ray tube similar to that Roentgen used for his first experiments[2].

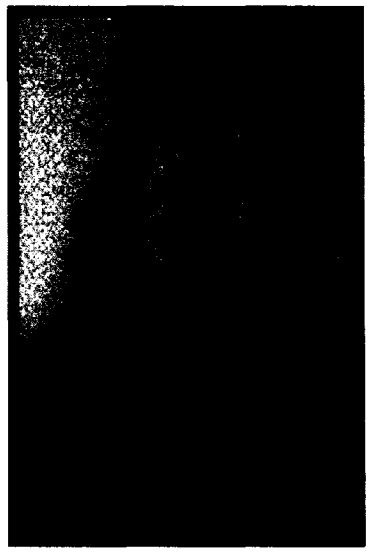

Figure 2: X-ray of Mrs. Roentgen's Hand[3].

The x-rays in these cathode ray tubes are produced when electrons, discharging from the cathode, strike the anode. To sustain the current flow some residual gas is needed. As the tube is used, some of the gas is absorbed by the walls of the tube which causes changes to the electron current of the discharge as well as requiring higher voltages to start the discharge. Since the x-ray intensity is directly proportional to the current while the penetrating power is dependent on the voltage between the plates, one can see how these changes would have a negative impact on reliable image quality.

In 1913 W. D. Coolidge invented the hot cathode x-ray tube (figs. 3, 4). In this design electrons are supplied by a hot cathode or filament in a high vacuum, usually set in an electrode shaped to provide some focusing action for the electron beam as it is directed onto the anode or target. The voltage between the anode and cathode is high enough so that all the electrons given off by the cathode are accelerated towards the anode. The electron current is controlled by varying the filament temperature while the penetrating power of the x-rays is controlled by varying the voltage between the cathode and anode. Thus, these two important parameters may be accurately and independently controlled. This design is the basis for all modern x-ray tubes.

Reproduced with permission of the copyright owner. Further reproduction prohibited without permission.

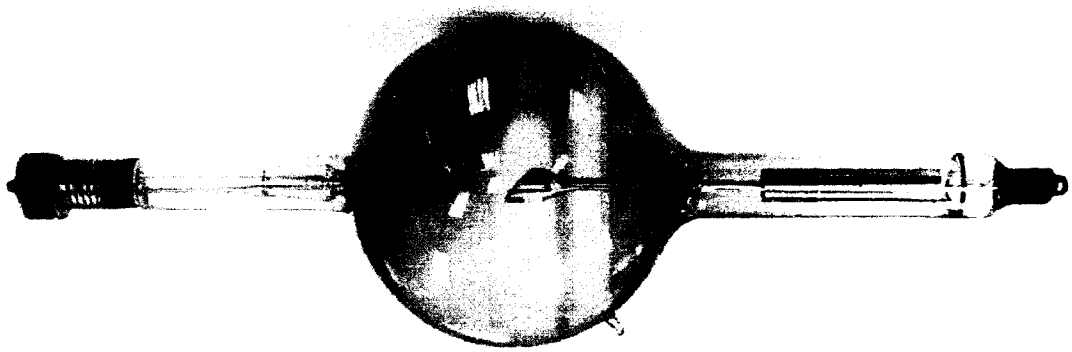

Figure 3: The modern day x-ray tube invented by W.D. Coolidge[4].

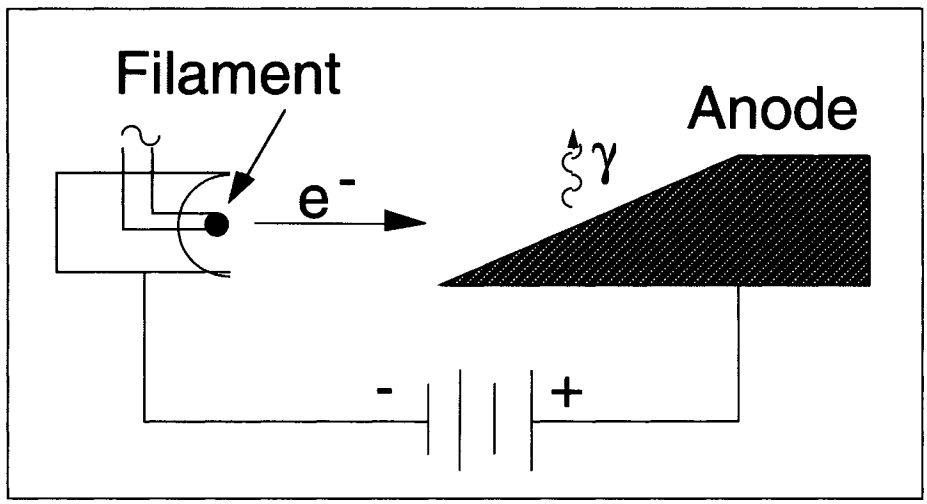

Figure 4: Schematic Diagram of an x-ray Generator. The heated filament boils off electrons, which then accelerate toward the positively charged anode.

Production of X-rays

X-ray tubes produce x-ray photons by two mechanisms: bremsstrahlung and ionization. The bremsstrahlung radiation comes from the deflection of the electrons by the electric fields of the atoms making up the anode material. For monoenergetic electrons of energy E_0 incident on a target thick compared to the electron range, the intensity (energy per photon x number of photons) of the energy distribution of the bremsstrahlung, per unit energy (E) and per incident electron, can be approximated by the linear relation[5]

Reproduced with permission of the copyright owner. Further reproduction prohibited without permission.

$$I(E) = 2kZ(E_0 - E), \qquad 0 \le E \le E_0. \tag{1-1}$$

Where E_0 is the energy of the incoming electrons in keV, Z is the atomic number of the target and $k \sim 7 \times 10^{-7}$ keV^{-1}. A plot of this equation is shown in figure 6. Integrating this over all energies gives the intensity of energy emitted as bremsstrahlung per incident electron as

$$I_{br} = kZE_0^2. \tag{1-2}$$

This can be used to find the fraction of incident electron energy converted into bremsstrahlung

$$Y(E_0) = I_{br}/ E_0 = kZE_0 \tag{1-3}$$

which is always a small fraction of the incoming energy. For 120 keV electrons hitting a tungsten anode, only 0.6% of the energy is converted into bremsstrahlung energy. The rest of the energy is converted into heat which makes heat removal an important aspect in the design of x-ray tubes. This is why x-ray tubes with a rotating anode have become quite popular (fig. 5). In this tube the anode rotates at high speed during the x-ray exposure and the beam of electrons hit the target near the outer circle of the anode. This construction permits the produced heat to be distributed over a much larger area, allowing a corresponding increase in X-ray production and reduction in exposure times.

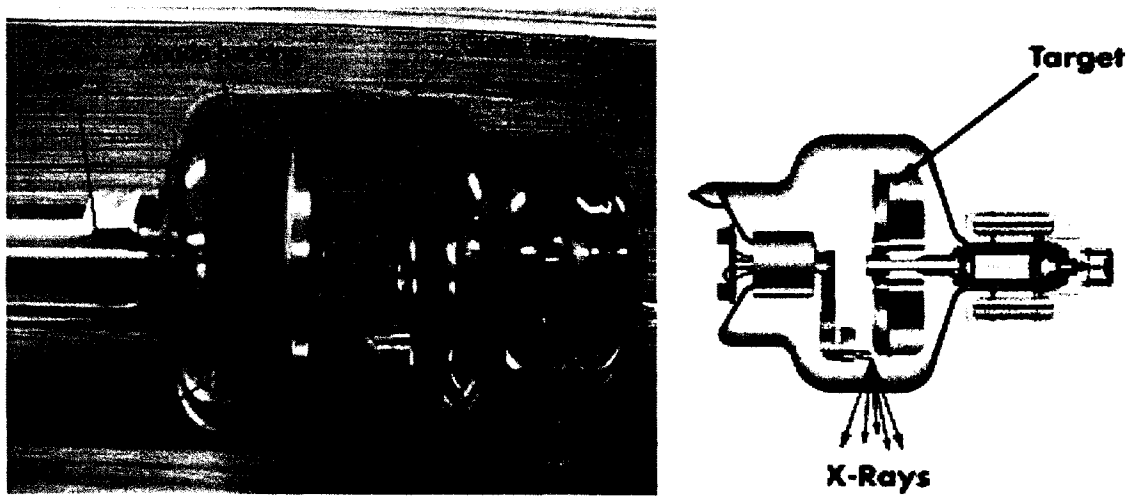

Figure 5: Example of a modern rotating anode x-ray tube.[6]

Reproduced with permission of the copyright owner. Further reproduction prohibited without permission.

X-rays are also generated by ionization, which begins when an incoming electron of enough energy "chips off" an inner shell electron from an atom of the anode. Following such an event, an outer electron drops down to fill the vacancy, emitting a photon of energy equal to the difference between the binding energies of the old and new states of this (orbital) electron. For this to happen the accelerating voltage on the electrons must be above the ionization energy of the atomic shells of the target material. Table 1 shows these values for Tungsten. For voltages, V, up to six times the critical voltage for K-shell ionization, V_k, the emission of the K_ x-rays increases approximately as $(V - Vk)^{2.7}$ These characteristic photons have energies that are, of course, well defined and dependent on the anode material. The lower energy (L-series) x-rays are usually filtered out by the housing of the x-ray tube resulting in the energy spectrum seen in figure 6. At 100 keV, the K-series x-rays make up about 5% of the of the total number of x-rays produced.

X-ray line	Emission energy (keV)	Excitation voltage (kV)
K_α	59.3182	69.525
K_β	67.2443	69.525
L_α	8.3976	10.207
L_β	9.6724	11.544

Table 1: Characteristic spectral lines from a Tungsten x-ray target.[8]

The angular distribution of bremsstralung is generally quite anisotropic and varies with the incident electron energy. Bremsstrahlung induced by low energy electrons (< 100 keV) is emitted predominately at 90° to the direction of the incident electron. The angular distribution of radiation leaving a target, however, is very difficult to compute since it depends on the target size and orientation[9]. From studying the work of others[10], one finds that about 75% of the x-rays are emitted in the forward direction while the rest are back

Reproduced with permission of the copyright owner. Further reproduction prohibited without permission.

scattered. Also there is about a 10% dip in the number of x-rays emitted directly forward of the incoming electron beam with higher intensities emitted +/- 10 to 30 degrees.

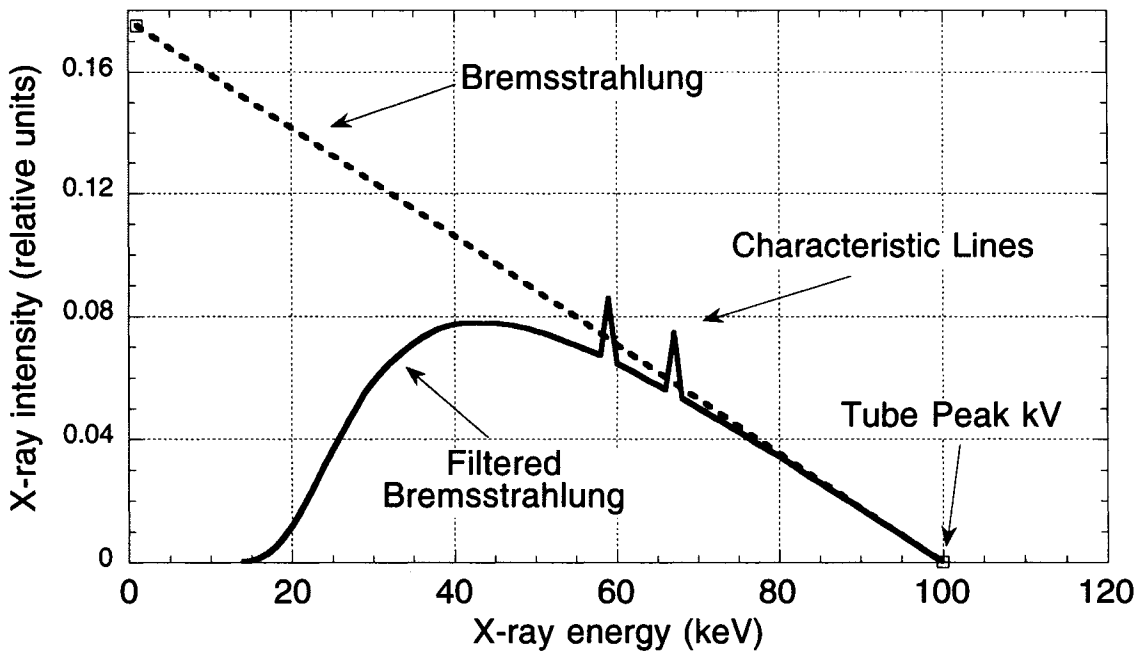

Figure 6: The energy spectrum from an x-ray tube. The solid line is the spectrum from a tube with a Tungsten anode filtered by an aluminum housing. The dashed line is the unfiltered theoretical bremsstrahlung spectrum from equation (1-1).

Kinds of interactions	Effects of interaction
1. Interaction with atomic electrons	(a) Complete absorption
2. Interaction with nucleons	(b) Elastic scattering (coherent)
3. Interaction with the electric field surrounding nuclei or electrons	(c) Inelastic scattering (incoherent)
4. Interaction with the meson field surrounding nucleons	

Table 2: Interactions of gamma rays with matter.

Reproduced with permission of the copyright owner. Further reproduction prohibited without permission.

Interaction of X-rays With Matter

There are a number of processes which can cause an x-ray to be scattered or absorbed in matter. A catalogue of the possible processes by which the electromagnetic field of the x-ray may interact with matter has been put in the systematic form shown in table 2 by Fano.[11]

There are 12 ways of combining columns 1 and 2; thus in theory there are 12 different process by which x-rays can be absorbed or scattered. Many of these processes are quite infrequent and some have not yet been observed. It turns out that in the energy domain of interest for the majority of x-radiography (10 to 200 keV), all the interactions are explainable in terms of just three of the above 12 processes. These are photoelectric absorption (1a), Compton scattering, and (1c) Rayleigh scattering (1b).

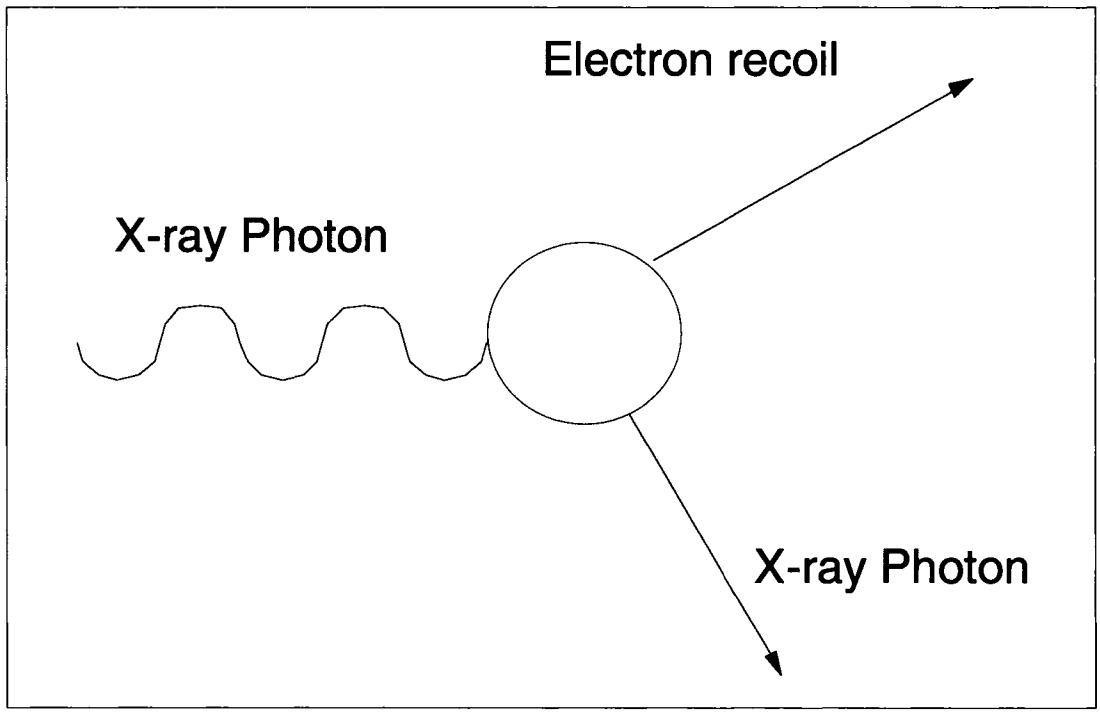

Figure 7. Photoelectric interaction of an x-ray photon with an atom.

Reproduced with permission of the copyright owner. Further reproduction prohibited without permission.

Photoelectric Absorption

At lower x-ray energies (< 50 keV) photoelectric absorption is the dominant interaction. An x-ray is absorbed by an atom of the material which then ejects a photoelectron from one of its bound shells with energy

$$E_{e^-} = h\nu - E_b. \qquad (1\text{-}4)$$

where E_b is the binding energy of the photoelectron in its original shell (fig. 7). This electron is quickly absorbed by the surrounding material.

The vacancy left by the photoelectron can be filled in a number of ways. In the simplest case, an electron from a higher energy level fills the "hole" left by the photoelectron emitting a characteristic x-ray with no directional relationship to the incoming x-ray photon. Alternatively, the energy difference may be transferred (via a virtual photon) to an outer orbital electron (Auger electron) which then escapes, leaving a doubly positive charged nucleus. The two vacancies are filled by other outer electrons, which results in more characteristic x-rays or Auger electrons. In general the lower energy x-rays are absorbed in the M and L shells, and higher energy x-rays in the K shell.

No single analytic expression is valid for the atomic cross section σ_p of photoelectric absorption per atom over all ranges of x-ray energies ($E\gamma$) and atomic number of the absorber (Z), but a rough approximation is[12]

$$\sigma_P \cong C_P \times \frac{Z^4}{E_\gamma^{\,3}} \qquad (1\text{-}5)$$

where C_P is a constant. This approximation actually works quite well for energies less than 100 keV if we ignore K-edge absorption. This shows the strong energy and atomic number dependence of the absorption probability. Thus, at lower x-ray energies, two different materials can have vastly different photoelectric attenuation while, at two different energies, the same material will also have vastly different photoelectric attenuation. Typical Linear

Reproduced with permission of the copyright owner. Further reproduction prohibited without permission.

attenuation coefficients for the three interactions are shown in figure 8 for acrylic and figure 9 for aluminum.[13]

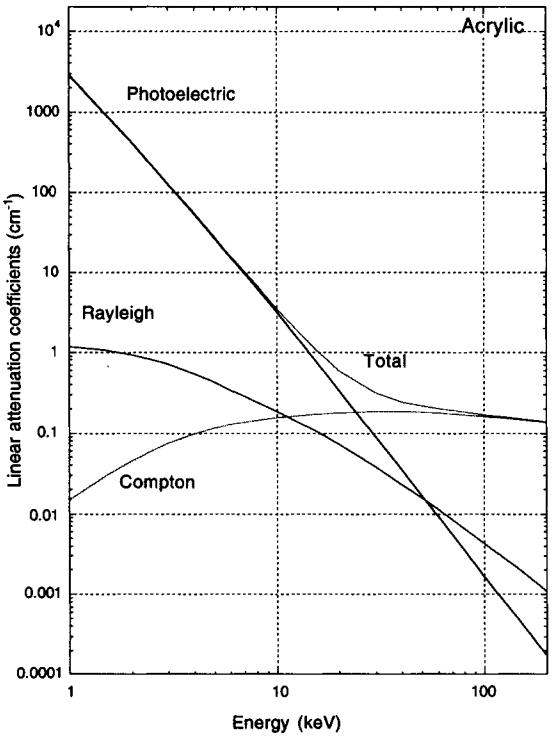

Figure 8: Linear attenuation coefficients for acrylic for Photoelectric absorption, Rayleigh scattering, and Compton scattering.

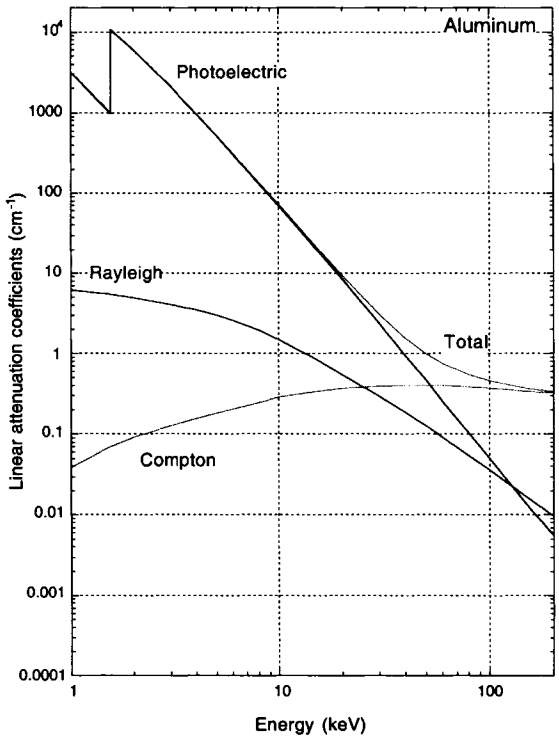

Figure 9: Linear attenuation coefficients for aluminum for Photoelectric absorption, Rayleigh scattering, and Compton scattering.

Compton Scattering

Compton or incoherent scattering dominates at the higher x-ray energies. This occurs when a photon of energy E_γ interacts with an individual electron assumed not to be bound to an atom and initially at rest. After the interaction, the photon has energy E_γ' and moves at angle ϑ_p while the electron moves with kinetic energy T at angle ϑ_e (fig. 10). Due to conservation of momentum, the energy of the scattered photon E_γ' is

Reproduced with permission of the copyright owner. Further reproduction prohibited without permission.

$$E_\gamma' = \frac{E_\gamma}{1+(E/m_e c^2)(1-\cos\vartheta_p)}. \qquad (1\text{-}6)$$

The cross section σ_C of Compton scattering per electron is given by the Klein-Nishina approximation[14]

$$\sigma_{Ce} \cong 2\pi r_e^2\left[\frac{1+\alpha}{\alpha^2}\left[\frac{2(1+\alpha)}{1+2\alpha}-\frac{1}{\alpha}\ln(1+2\alpha)\right]+\frac{1}{2\alpha}\ln(1+2\alpha)-\frac{(1+3\alpha)}{(1+2\alpha)^2}\right] \qquad (1\text{-}7)$$

where r_e is the classical electron radius (= $2.818\text{x}10^{-13}$cm) and α is Eγ(keV)/511keV. Since each atom has Z electrons we see that the total cross section increases linearly with Z and can be approximated by

$$\sigma_c \approx \sigma_{Ce} Z. \qquad (1\text{-}8)$$

One of the differential forms of equation (1-8) gives the cross-section for the energy scattered from the beam as a function of scattering angle.[15] As one would expect, due to momentum conservation, forward scattering increases at higher photon energies (fig. 11). This forward scatter is one of the major causes of image blurring in standard x-ray imaging systems. It will be shown later that the wide angle scatter seen for lower x-ray energies causes some anomalies in the image when one uses scanning beam x-radiography.

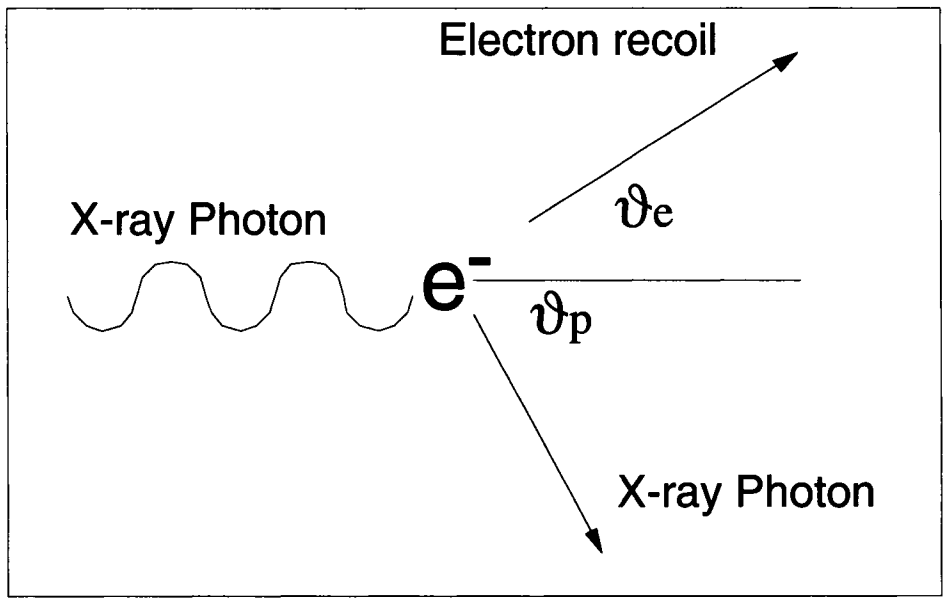

Figure 10: Compton scattering of an x-ray photon by an electron.

Reproduced with permission of the copyright owner. Further reproduction prohibited without permission.

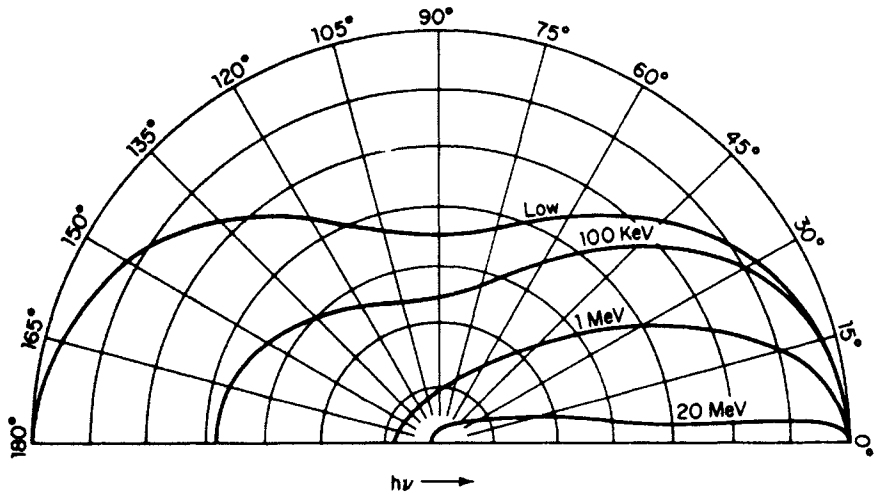

Figure 11: Angular distribution of Compton scattered photons from ref. 13.

Rayleigh Scattering

Rayleigh or coherent scattering plays a minor role in the overall attenuation of x-ray photons due to its relatively low probability of occurrence. In this case, the scattering is totally elastic and there is no atomic excitation or ionization. The recoil momentum is taken up by the atom as a whole and the cross section is approximately[16]

$$\sigma_R \cong C_R \times \frac{Z^{2.7}}{E_\gamma^{\,2}} . \qquad (1\text{-}9)$$

In this case, the constant, C_R, is such that, at 10 keV, the probability of Rayleigh scattering is about 100 times less than photoelectric absorption. For low Z objects, however, such as acrylic, Rayleigh scattering at 30 keV can account for about 10% of the interactions (fig. 8). Since, by definition, the recoil imparted to the atom must not produce atomic excitation or ionization, the energy loss of the photon is slight and the scattering angle small which appears as blurring or minor abnormalities in the image. More than three-quarters of the radiation scattered is within the cone defined by the half angle[17]

Reproduced with permission of the copyright owner. Further reproduction prohibited without permission.

$$\theta = \arcsin\left(13.24\text{keV} \times \frac{Z^{\frac{1}{3}}}{E_\gamma}\right). \qquad (1\text{-}10)$$

Some results of this equation are shown in table 3. Since the scattering angles are similar to Compton scattering, it is likely that Rayleigh scattering also contributes to some of the image anomalies seen when one uses scanning beam x-radiography, but in a much lower amount.

Material	Scattering angle θ° @ 40 keV	Scattering angle θ° @ 70 keV	Scattering angle θ° @ 100 keV
H	19	11	7.6
C	37	20	14
Al	51	26	18
Fe	79	34	23

Table 3: Results of Rayleigh scattering equation (2-10) for selected materials and energies.

Linear Attenuation Coefficient

The attenuation of x-rays though a homogeneous object is given by the well known equation

$$I = I_0 e^{-\sigma n x}, \qquad (1\text{-}11)$$

where I_0 is the incident intensity, σ is the interaction cross section per atom, x is the thickness of the object, and n is the number of atoms per unit volume

$$n = \frac{\text{Density} * \text{Avogadro's number}}{\text{Effective atomic mass}}. \qquad (1\text{-}12)$$

The quantity σn is known as the linear attenuation coefficient and is usually written as μ. Since the above interaction processes are independent of each other and are mutually exclusive,[18] equation (1-11) can be written as

Reproduced with permission of the copyright owner. Further reproduction prohibited without permission.

$$I = I_0\left(e^{-\mu_P x}e^{-\mu_C x}e^{-\mu_R x}\right), \tag{1-13}$$

where the σn's are replaced by their analogous μ's for photoelectric absorption, Compton scattering, and Rayleigh scattering. This shows the total linear attenuation for a homogeneous material can be written as

$$\mu_T = \mu_P + \mu_C + \mu_R. \tag{1-14}$$

Since the σ's are defined per atom of a material and the cross sections are unaffected by chemical or mechanical combination of the atoms, the linear attenuation coefficient for a compound, mixture, or alloy may be obtained from a sum of the contributions from each of the M elements.[19]

$$\mu_T = \sum_{i=1}^{M}\mu_{Pi} + \mu_{Ci} + \mu_{Ri} = \sum_{i=1}^{M}\mu_{Pi} + \sum_{i=1}^{M}\mu_{Ci} + \sum_{i=1}^{M}\mu_{Ri} = \mu_{PT} + \mu_{CT} + \mu_{RT} \tag{1-15}$$

Here μ_{PT} is the total photoelectric absorption linear attenuation coefficient for the material and similar for μ_{CT} and μ_{RT}.

Reproduced with permission of the copyright owner. Further reproduction prohibited without permission.

CHAPTER II

CONVENTIONAL X-RADIOGRAPHY

With standard x-radiography, one measures the bulk x-ray transmission through an object to produce a two dimensional x-ray shadow graph. The set-up used to achieve this consists of a point source x-ray tube, the object to be imaged, and a detector such as film or CCD (fig. 12).

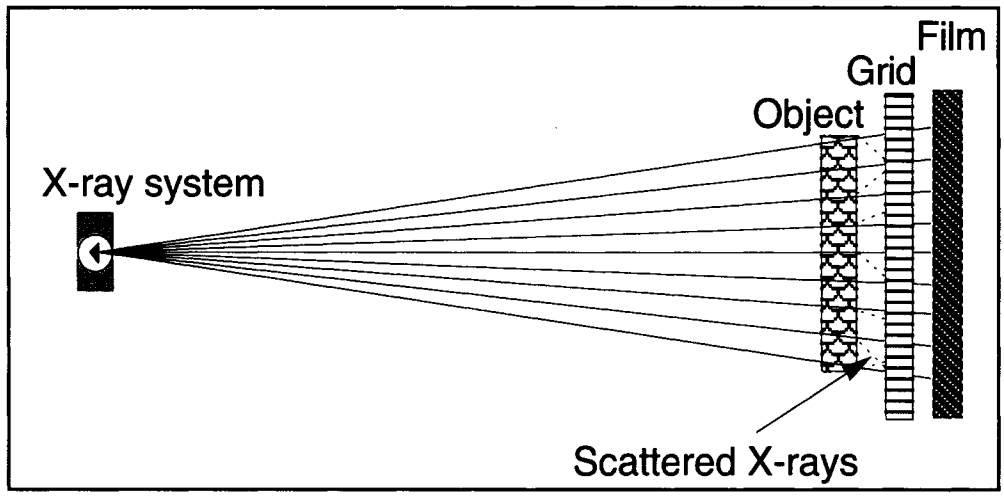

Figure 12: Conventional x-ray set-up using anti-scatter grid.

The x-ray tube produces x-rays by using a microfocused beam of electrons striking a target such as tungsten or molybdenum to produce the bremsstrahlung x-radiation spectrum which is given off over a wide angle. The sharpness of the image is mainly dependent on how well one focuses the electron beam as seen in figure 13. Since the focal spot is of some finite size, images are always surrounded by a penumbra where the film receives radiation from a part but not the whole of the focal spot. Basic geometry gives the apparent object length L'_i as

$$L'_i = L_o M + \frac{L_o h}{f - h}, \qquad (2\text{-}1)$$

Reproduced with permission of the copyright owner. Further reproduction prohibited without permission.

where f is the source to detector distance, h is the object to detector distance, L_o is the length of the object and L_s is the length of the source and M = f/(f-h) is the magnification obtained from a point source.

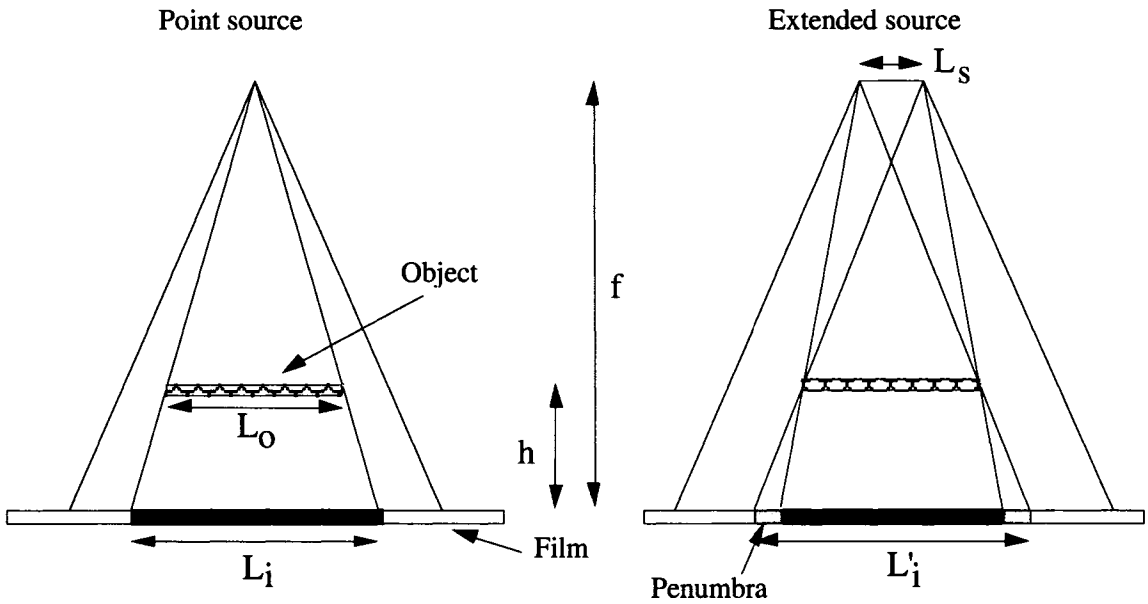

Figure 13: Diagrams illustrating the effect of the x-ray focal spot size on the sharpness of the image.

Most systems today focus the electron beam to about 25 μm and, for high resolution work, spot sizes of 1 μm are available. Of course, the smaller the spot size, the larger the localized heat load on the target. The x-rays are then collimated towards the object where they are either absorbed, scattered, or transmitted. In some cases an antiscatter grid is also used to improve the sharpness of the image by removing some of the Compton and Rayleigh scatter. The grid is usually made from very thin parallel lead strips with aluminum (or other low Z material) interspaced at 60 to 100 strips per inch. The grid is defined by the ratio of the height of the lead strips to the distance between them. Thus with interspacers 10 times as high as they are wide, a grid is said to be 10:1 ratio, etc. Generally speaking, the higher the ratio of a grid, the more scattered radiation is absorbed. The anti-scatter grid, however, also removes about 50% of the non-interacting "useful" radiation and thus requires higher radiation intensities. The imaging media may be either film or some

Reproduced with permission of the copyright owner. Further reproduction prohibited without permission.

electronic system such as a CCD. Film is inexpensive and able to yield very high resolutions (over 15 line pairs of high-contrast metal wires per mm), however, its limited dynamic range (40:1) and required developing are large disadvantages. There have been major breakthroughs in the past 5 years towards replacing film with digital detectors, however, the cost of these new digital film systems is still significant (about $100,000 not including the x-ray source) and the resolution is not as good as film (about 10 line pairs per mm), however, it is sufficient for many uses. The advantage of digital radiography lies in the wide dynamic range available (greater than 4096:1) and the digital system's ability to manipulate data, shift contrast ranges, digitally enhance, and quickly transmit images around the world. The x-ray sensitivity of these digital systems are also much higher than film and thus lower doses can be used. However, even with an antiscatter grid, these two-dimensional detectors are still prone to detecting scattered x-rays. One can reduce detected scatter by using a line detector or a point detector and mechanically scanning the detector and collimated x-ray source over the object. This is one approach being tried for mammography.[20] The main drawback is that mechanical scanning is relatively slow compared to a one shot x-ray exposure or, alternatively, electronically scanning the x-ray beam over the object. Another drawback is the possibility of the object moving during the scan, which can cause artifacts.

Reproduced with permission of the copyright owner. Further reproduction prohibited without permission.

CHAPTER III

SCANNING BEAM X-RADIOGRAPHY

Scanning beam x-radiography, also known as Reverse Geometry X-radiography (RGX)™[21], offers many advantages compared to conventional x-radiography. With this method, the object is placed next to a raster scanning x-ray source while a small x-ray detector is placed about a meter away (fig. 14). The rastering point x-ray source is produced by scanning a focused electron beam across the back of a thin Tungsten anode plate. The target has to be thick enough to be electron opaque and produce bremsstralung x-rays, yet thin enough to allow the x-rays to escape from the target, towards the object. The remote "point" x-ray detector is usually made up of a scintillator with about a one cm^2 active area coupled to a photomultiplier tube (PMT). The detector measures the intensity of the transmitted x-ray flux while avoiding most of the scattered x-rays. Correlating the digitized signal current from the detector to the location of the x-ray spot as it rasters across the object builds up a two dimensional image.

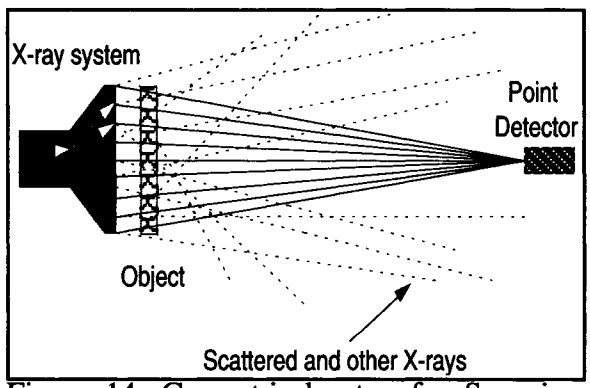

Figure 14: Geometrical setup for Scanning beam x-radiography.

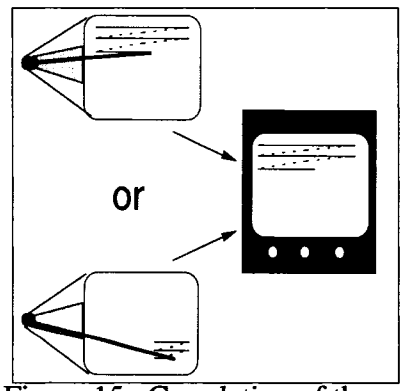

Figure 15: Correlation of the raster scan of the x-ray beam to the image on the CRT showing electronic pan and zoom.

With Digiray's RGX™ system, a 25 cm diameter area can be imaged into an image with 1024 x 1024 pixels in one second. Continually scanning the area allows near real time

Reproduced with permission of the copyright owner. Further reproduction prohibited without permission.

moving images to be acquired. By electronically shrinking the raster pattern to a smaller area, yet keeping the same 1024 x 1024 pixel readout, one obtains linear magnification of the image with no mechanical movement (fig. 15). Of course, one can also obtain linear magnification by moving the object closer to the detector. This would, however, increase the amount of detected scatter and reduce the sharpness of the image by increasing the penumbra and apparent object length by the formula (see fig. 16)

$$L'_i = L_o M + \frac{L_D h}{f - h} + 2L_s, \qquad (3\text{-}1)$$

where L_D is the width of the detector and the other variables are the same as in equation (3-1). The electron beam is focused down to 25 μm which gives a maximum resolution of 50 μm (10 line pairs per mm) when the raster pattern is zoomed to a 25 mm^2 1024 x 1024 pixel area.

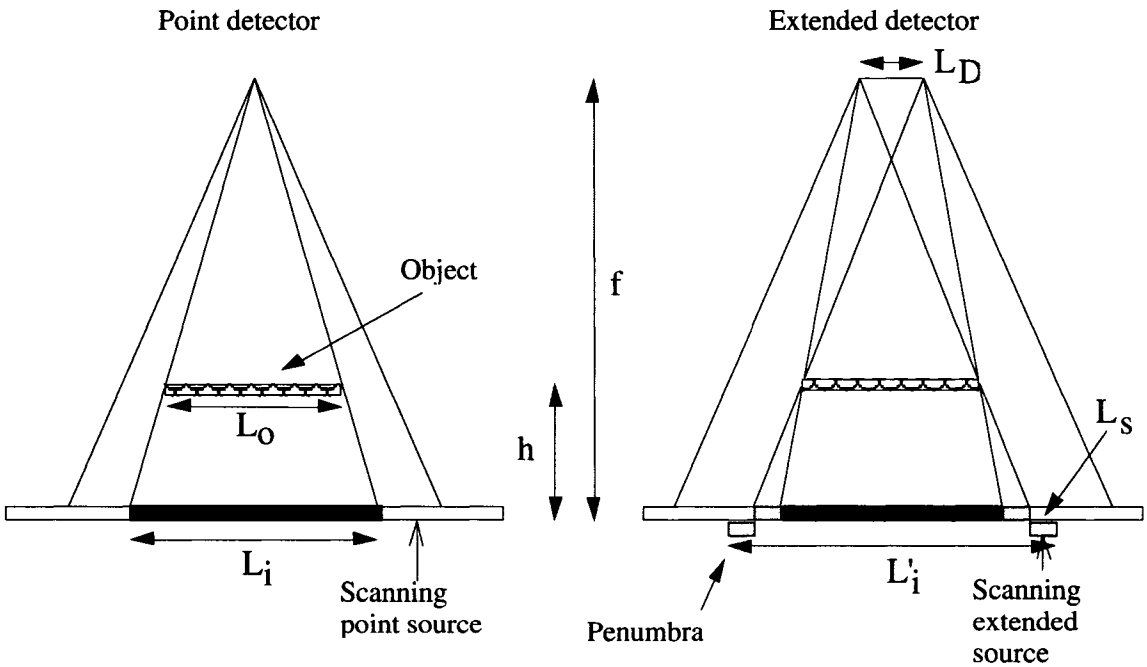

Figure 16: Diagrams illustrating the effect of the x-ray spot size and detector size on the sharpness of the image.

Reproduced with permission of the copyright owner. Further reproduction prohibited without permission.

Due to the simplicity of the detector system required, there is a major reduction in complexity as compared to current digital imaging systems. The scanning x-ray source tends to be more complex, however, the same general electron beam control techniques used in television sets are employed here. The one major drawback of this technique is that, due to the thin anode target, heat removal is much more difficult. Thus the maximum x-ray intensity one can obtain is less than one tenth that of conventional x-ray systems. The x-ray detector makes up for some of this loss due to its high sensitivity and limited scatter acceptance. One can also scan the object repeatedly and then sum and average the images to obtain better signal to noise.

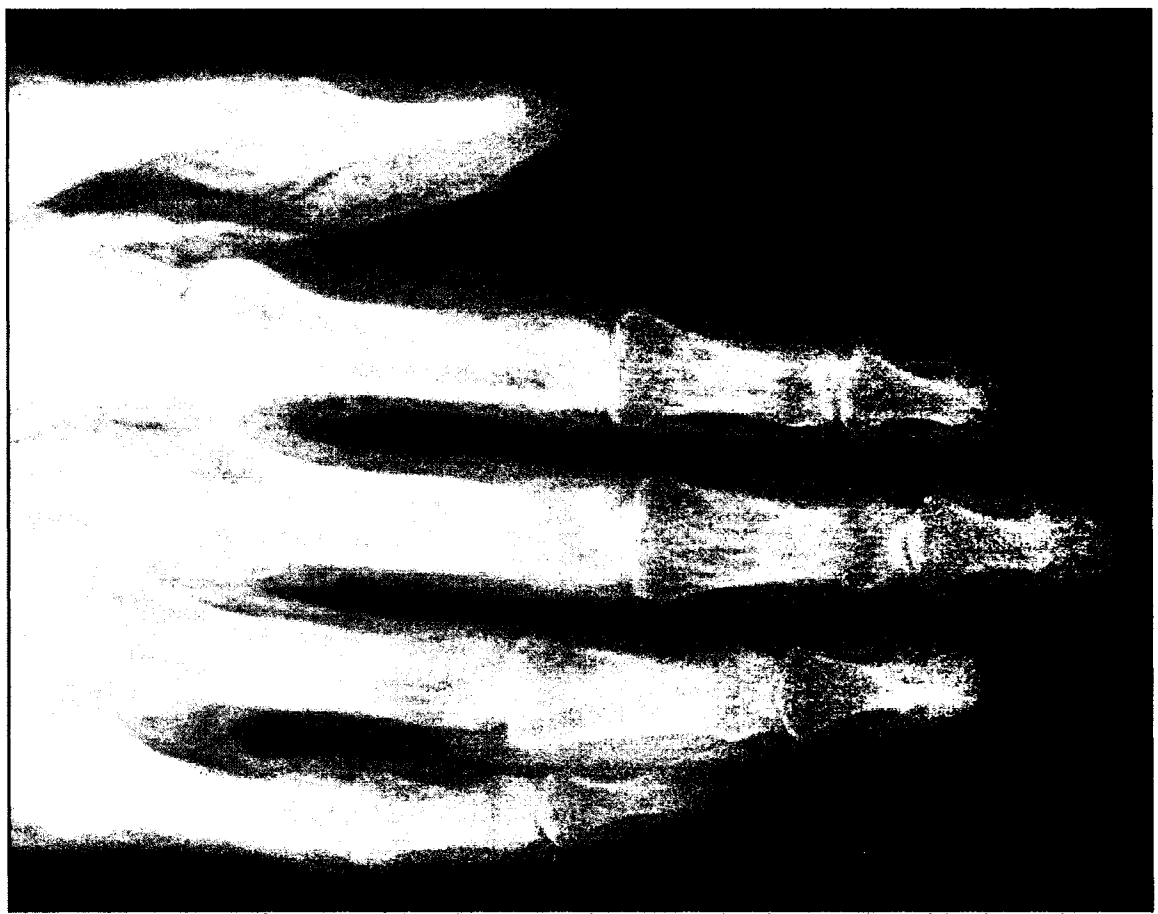

Figure 17: Image of cadaver's hand in a plastic surgeon's glove. The wide dynamic range of scanning beam x-radiography allow both the bone and the glove to be seen clearly[22].

Reproduced with permission of the copyright owner. Further reproduction prohibited without permission.

An antiscatter grid can be placed between the x-ray system and the object to reduce the dose to the object from x-rays which are not directed to the detector. This is significantly different from the use of an anti-scatter grid in a conventional system. With a scanning x-ray system, errant as well as some useful x-rays are eliminated before they interact with the object while the scattered x-rays from the object usually miss the detector. In the conventional case, useful x-rays are eliminated after passing through the object and thus higher radiation doses to the object are needed for the same image quality. For this system one would use a focusing x-ray grid where the strips are slightly inclined so that they point towards the detector. This greatly lowers the dose rate while only slightly affecting image quality. A fluoroscopy unit manufactured by Cardiac Mariners[23] uses this technique to produce a system that allows for a 10 times reduction in patient dose compared to standard fluoroscopy systems. Since the images are digital, scanning beam x-radiography has all the advantages of a convention digital system including a very large dynamic range (fig. 17).

Laminography

With standard simple x-ray irradiation there is no possibility to get information about the depth of the imaged structures. In 1932 de Plantes[24] performed the first experiments to image an object layer by layer with a technique called laminography. In order to obtain laminographic images using a standard x-ray system must either move the x-ray source or the object and get views from many different angles. Since the x-rays of a scanning beam system are given off over a wide angle, one can look at an object from many different angles at the same time using multiple detectors surrounding the object without any motion. The reconstruction of these images gives one a limited 3-D image (fig. 18). Figure 19 shows the standard x-ray image and the reconstructed top and bottom slices of a quarter.[25]

Reproduced with permission of the copyright owner. Further reproduction prohibited without permission.

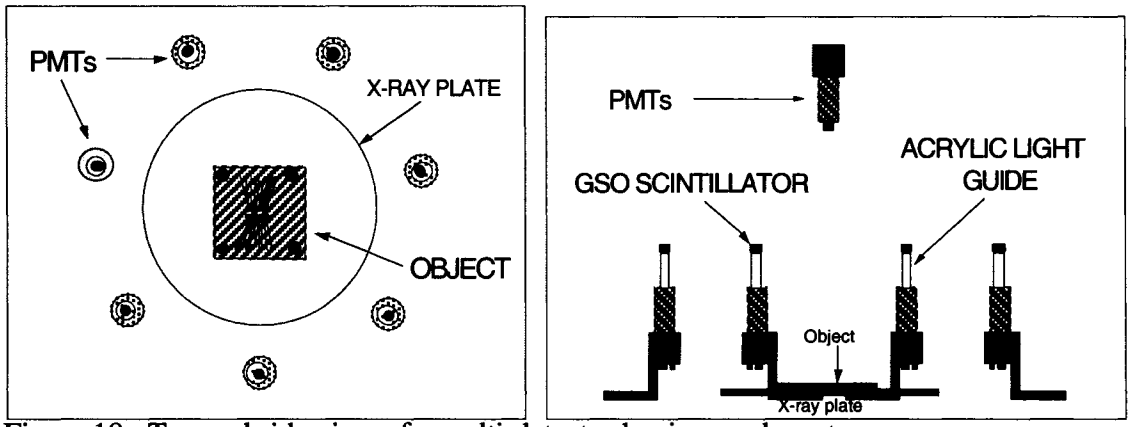

Figure 18: Top and side view of a multi-detector laminography setup.

Figure 19: Laminography performed on a quarter by the NASA-Langley NDE group. The left image is a standard x-radiograph while the right two images show the reconstructed isolated top and bottom views.

Optimizing the Standard Detector

The x-ray detector supplied with the Digiray RGX system consists of a 1 inch diameter CsI(Na) or NaI(Tl) scintillator coupled to a 1.25" diameter Hamamatsu R268 photomultiplier tube (PMT)[26] powered by a standard resistive voltage divider (fig. 20) housed in an aluminum holder. The signal is then preamplified by a common amplifier circuit before being sent to a sampling ADC. Unfortunately this simple detector produces many image artifacts.

Reproduced with permission of the copyright owner. Further reproduction prohibited without permission.

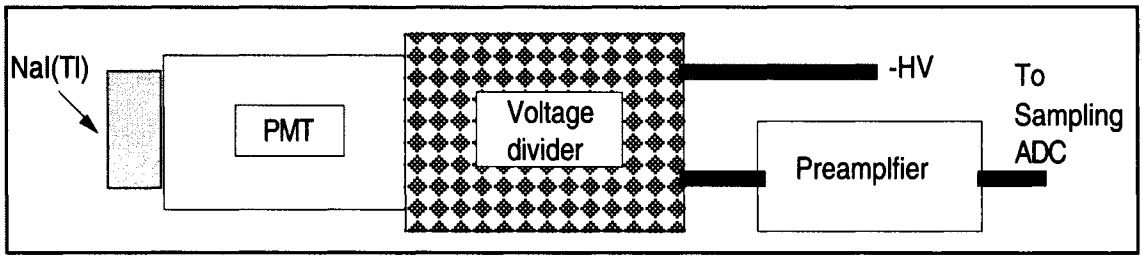

Figure 20: Digiray x-ray detector block diagram.

Optimizing the scintillator

Due to the relatively slow light decay from NaI(Tl) and especially CsI(Na) (see table 4) the leading edge of objects, as the x-ray beam scans across the object, appears to be rounded. The scintillator is still giving off light created before the beam reached the object. In order to optimize the scintillator, a test phantom composed of a 3 mm thick piece of lead 2 inches square with 1 cm hole in the center was used. Scanning was performed at the fastest allowed rate of 1 second per image which translates to 1 μs per position of the x-ray beam at 100 keV and .1 mA. Figure 21 shows the image using CsI(Na) along with a profile cut horizontally through the center. Here we see the rounded front edge as the light from the scintillator slowly decays as well as a rounded back edge as the scintillator light "charges up" again. Looking closely at the figure, one sees evidence of a very long decay which comes from the PMT and voltage divider discussed later.

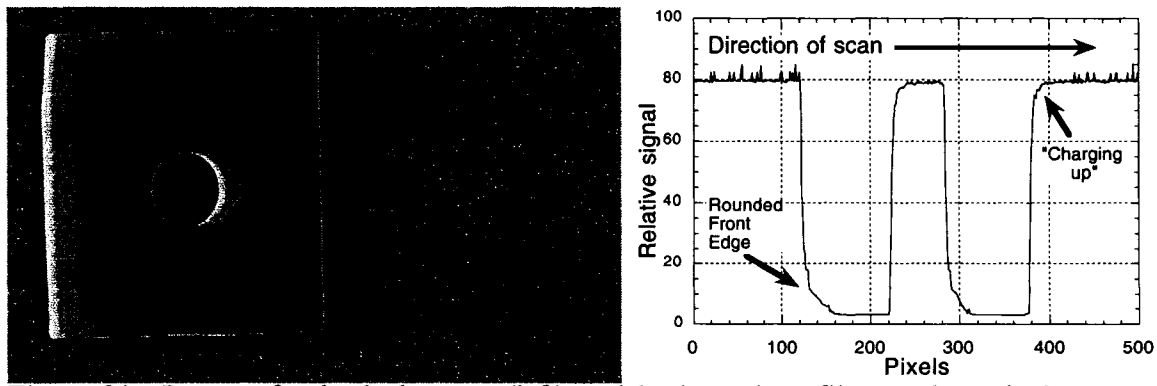

Figure 21: Image of a lead phantom (left) and horizontal profile cut through the center (right) shows artifacts due to a non-optimized detector.

Reproduced with permission of the copyright owner. Further reproduction prohibited without permission.

MATERIAL	LIGHT YIELD % of NaI(Tl)	DECAY TIME (ns)	EMISSION @ λ (nm)	DENSITY (g/cm^3)	HYGRO-SCOPIC
NaI(Tl)	100	230	415	3.67	Yes
CsI(Na)	150-190	650	420	4.57	Yes
GSO: $Gd_2(SiO_4)O$:Ce	20	30-60	440	6.71	No
YAP: $YAlO_3$:Ce	40	25	370	5.37	No
LSO: $Lu_2(SiO_4)O$:Ce	75	40	420	7.4	No
BC452 (5% lead loaded plastic)	15	2.1	424	1.08	No

Table 4: Partial list of scintillators used in these studies.

To fix this problem, the first modification performed was to replace the scintillator with a much faster one – one that has a much faster decay time of the light. From table 4, we see there are a few such scintillators, however, and that each has advantages and disadvantages. The best scintillator is Lutetium oxyorthosilicate (LSO) as it has the highest light output, good speed, and high stopping power. Unfortunately, LSO is expensive and somewhat difficult to obtain owing to patent protection and competition from the need for it in medical imaging. Yttrium-aluminum perovskite (YAP) is fast, reasonably bright, and easy to obtain, however, it suffers from poor stopping power and the quality in terms of decay time can vary greatly from different suppliers. Figure 22 shows images of our lead phantom using two different YAP samples connected via a liquid core light guide to a completely shielded PMT (the reason for this configuration will be discussed below). The YAP sample on the left from figure 22 shows a significant rounded front edge as well as a long "charging up" of the scintillator to the right of the phantom. The YAP sample on the right from Scionix[27] does not show these abnormalities. Horizontal profile cuts of these images are shown in figure 24. It is believed these differences come from different amounts of Ce dopant used.[28]

Reproduced with permission of the copyright owner. Further reproduction prohibited without permission.

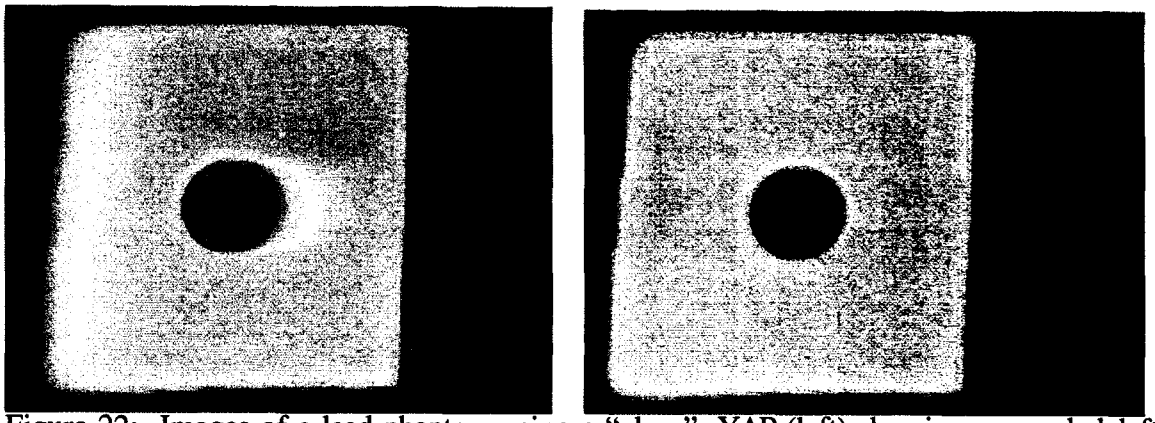

Figure 22: Images of a lead phantom using a "slow" YAP (left) showing a rounded left edge and "charging up" right edge of the phantom and a "fast" YAP (right) which does not show these problems.

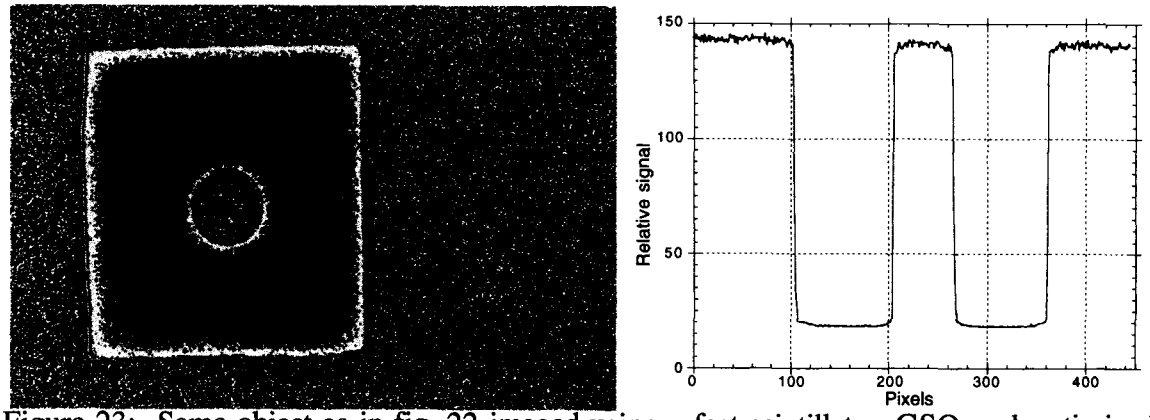

Figure 23: Same object as in fig. 22 imaged using a fast scintillator, GSO and optimized voltage divider (left) and horizontal profile cut through the center (right).

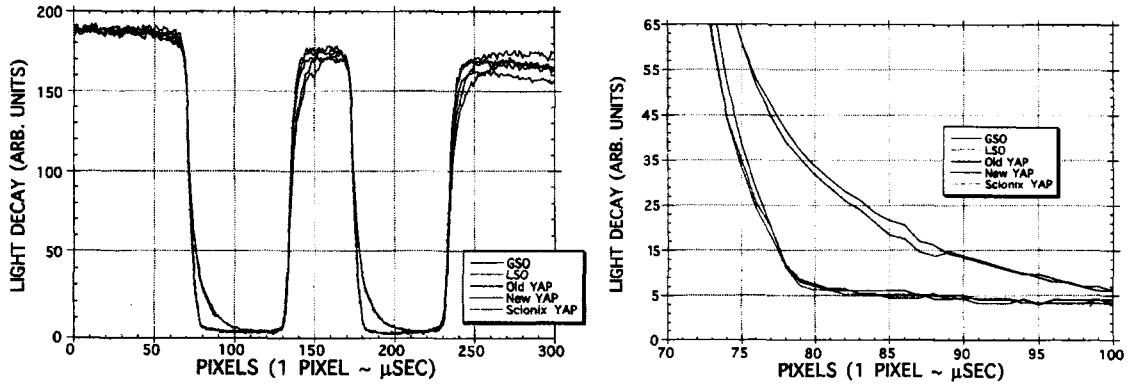

Figure 24: Horizontal profile cuts through the lead phantom for various crystals.

Gadolinium oxyorthosilicate (GSO) has good stopping power, is fast, and reasonably easy to obtain, however, the price is higher than YAP, the light output is relatively

Reproduced with permission of the copyright owner. Further reproduction prohibited without permission.

low, and it also suffers from quality problems due to the Ce content. BC452 is extremely fast, inexpensive, and easy to machine or cast to one's requirement, however, it has very low light output and stopping power. The main use for BC452 is in cases where ease of fabrication is important or if one built a scanning x-ray system which runs much faster than Digiray's. Figure 23 shows the result of using GSO along with an optimized PMT voltage divider used in the same situation as the CsI(Na) detector described above. Figure 24 shows horizontal profile cuts through the lead phantom for various crystals under these same conditions. The new and old YAP are from Scionix, the GSO is from Hitachi[29], and the LSO is from Chuck Melcher of Schlumbeger-Doll Research.[30]

In performing these studies, it was found that the shape of these high density high stopping power scintillators can affect the image if they are not properly shielded. When a cylindrical shaped scintillator was used, it appeared that there was a higher intensity of x-rays around the edge of the scanning plate than the center, producing a sort of donut shape in the x-ray intensity. When a cubed shaped scintillator was used, higher x-ray intensities were measured when the x-ray source was seen by one of the 4 corners of the crystal image causing an X shape in the image (fig. 25). The lighter areas in figure 25 correspond to lower measured intensity and are perpendicular to the side faces of the crystal. It was found that, since most of the x-rays are stopped in the first mm of the crystal, the surface area of the crystal intercepting the x-rays is extremely important. As shown in figure 26, this apparent surface area changes according to which location on the scanning plate the x-ray is striking. There are two solutions to this. One is to place a lead (or other shielding material) aperture in front of the scintillator. The second solution is to wrap the edges of the scintillator in lead foil. In either case, we limit the acceptance so that x-rays only enter the front face of the scintillator thus keeping the apparent surface area constant.

Reproduced with permission of the copyright owner. Further reproduction prohibited without permission.

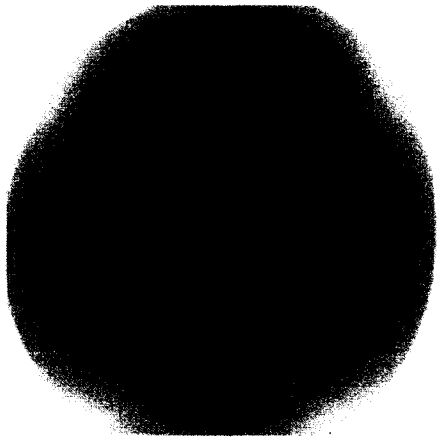

Figure 25: Image acquired using a square scintillator showing a cross pattern in the measured x-ray intensity.

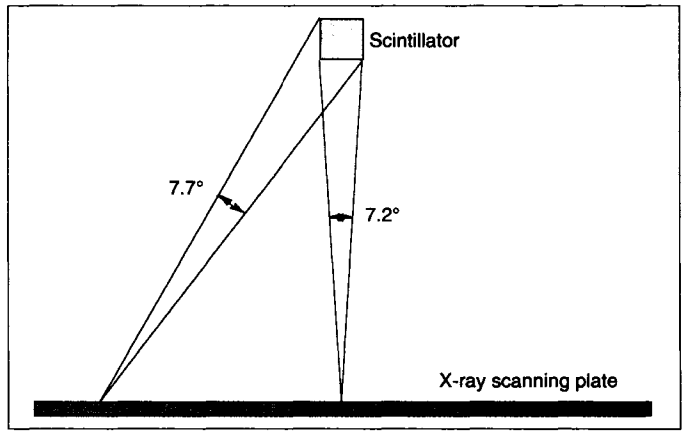

Figure 26: Diagram showing how the apparent active surface area of an unshielded scintillator changes according to where the x-rays are coming from.

Optimizing the PMT assembly

Another problem found was a streaking effect to the right of the object. This was found to result from three causes – gain instabilities caused by running the PMT at very high currents, the PMT voltage divider design, and fluorescence in the glass of the PMT from the x-rays. Originally the PMT was being operated at an anode current of over 300 μA whereas the maximum rating of the PMT was only 100 μA. One effect of this high current load is to shorten the life of the PMT, however, it was also found that the PMT would shift between a high gain and a low gain mode when the last dynode became flooded with electrons. When the x-ray flux reaching the detector was low, the PMT appeared to have a higher gain than when the x-ray flux was high. This effect would sometimes manifest itself in the image as an apparently higher x-ray flux recorded when the beam went from a lead object to air and the PMT thus exhibited its higher gain mode. The PMT would then switch to a lower gain after about 3 or 4 μs. Simply lowering the PMT high voltage from 1200V to 700V relieved this problem, however, the preamplifier then had to be modified as explained below.

Reproduced with permission of the copyright owner. Further reproduction prohibited without permission.

It was also found that few available PMTs could handle such heavily varying currents. Since there are many different designs of PMT internal structures, a preliminary study was made by Carl Zorn[31] to try to determine factors affecting stability and linearity. It was found that box and foil dynodes (fig. 27)[32] are more stable than the other structures and that CsSb metal used for the dynodes also helps. At this time only three PMTs (the Hamamatsu R268, the Electron Tubes 9125B[33] both of which use box dynodes, and the multianode Photonis XP4702 which uses foil dynodes[34]) have been found to give a linear response throughout the extremes of the incoming signals seen here.

The standard resistive PMT voltage divider used by Digiray was unable to compensate for widely changing current loads when the x-ray was attenuated by a thick object compared to no object at all. The problem lies in the constant resistance of the resistors in the voltage divider. As more current is drawn from the resistors by a larger signal, the voltage to the PMT changes following Ohms Law. This causes the voltage distribution supplied to the dynodes of the PMT to vary according to the load which affects the linearity of the measured x-ray intensity vs. PMT signal curve. To solve this problem an active FET-transistor-powered voltage divider developed for nuclear physics experiments at Jefferson Lab was used (fig. 28). The FETs change their resistance according to current demands to keep the voltage to the PMT constant in a manner similar to Zener diodes. The advantage of FETs over Zener diodes is that FETs keep the voltage ratio constant for any supplied high voltage while Zener diodes only keep the voltage drops constant and thus must be designed for a particular applied high voltage. A Zener diode was used between the cathode (K) and first dynode (DY1) to keep the collection voltage constant. This allows for the best collection of the photoelectrons from the cathode for any applied high voltage. Another feature added with this design was an increasing taper of voltage differences on the last few stages (see table 5). Under high current loads, this helps to reduce the space charge effect and improve linearity.[35]

Reproduced with permission of the copyright owner. Further reproduction prohibited without permission.

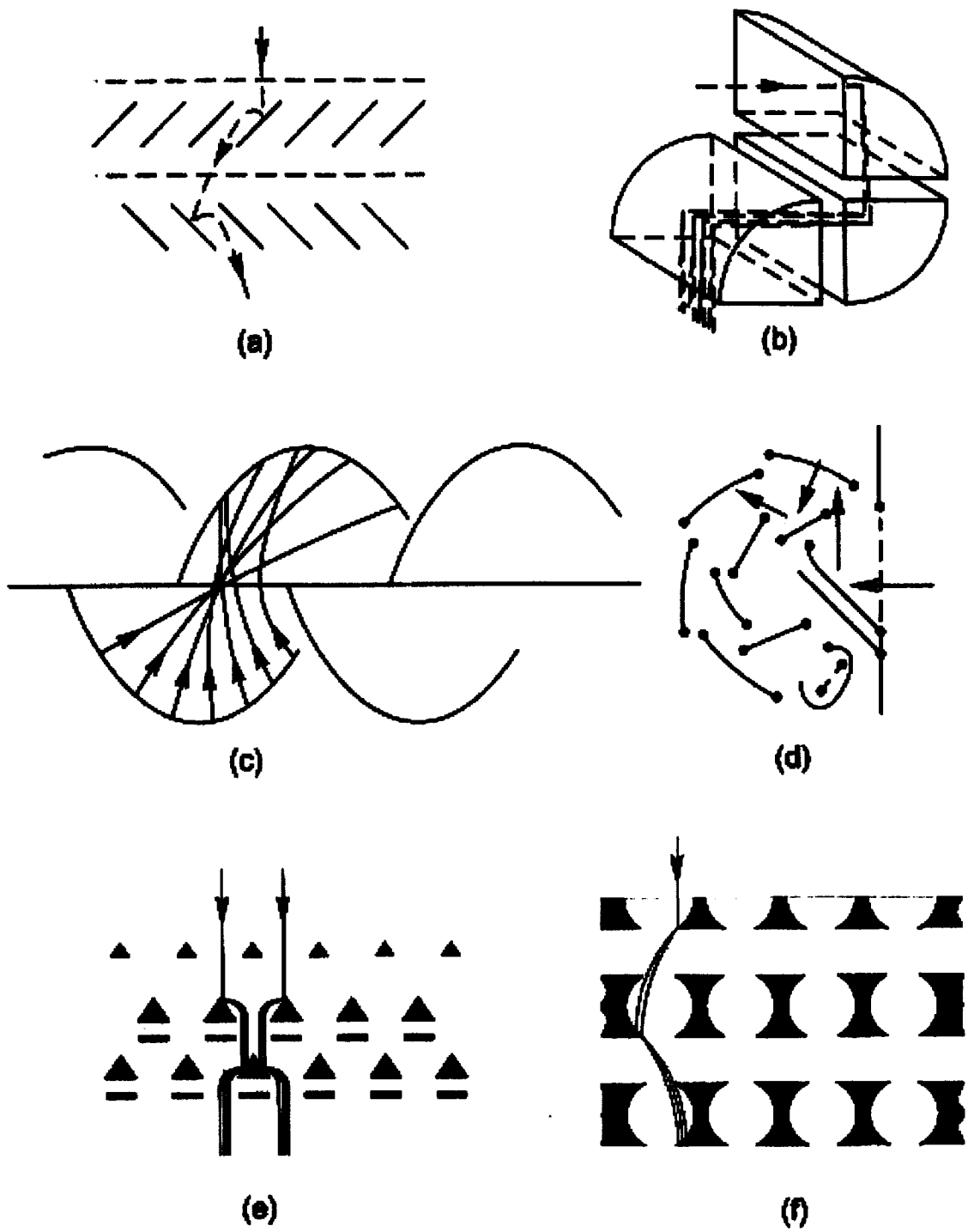

Figure 27: Dynode configurations:(a) Venetian blind, (b) box, (c) linear focusing, (d) circular cage, (e) mesh, and (f) foil.

Reproduced with permission of the copyright owner. Further reproduction prohibited without permission.

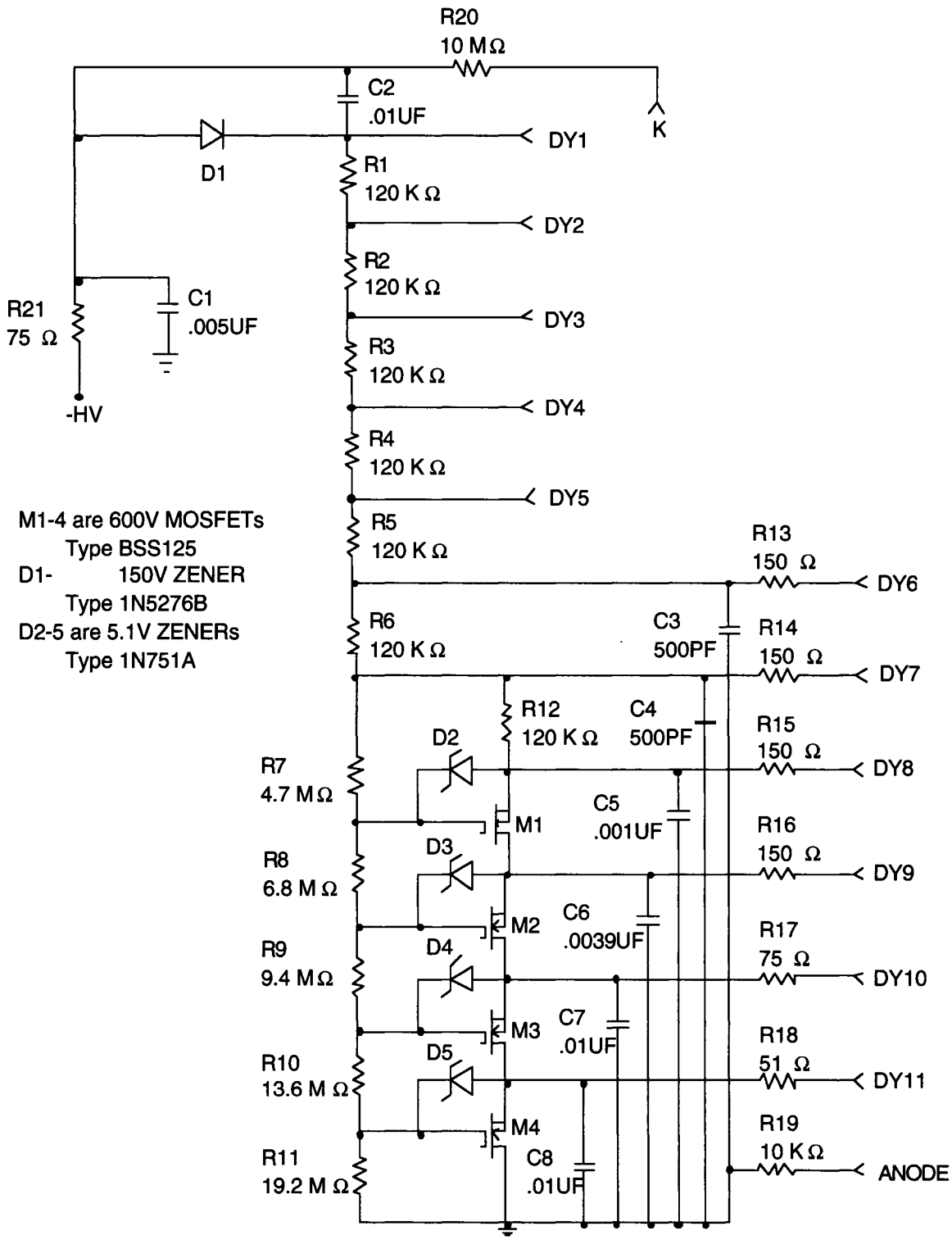

Figure 28: Active voltage divider used for the Digiray PMT.

Reproduced with permission of the copyright owner. Further reproduction prohibited without permission.

Pin	K	D1	D2	D3	D4	D5	D6	D7	D8	D9	D10	D11	A
Voltage	696	554	522	490	457	426	394	362	329	285	222	130	0
Ratio			1	1	1	1	1	1	1	1.4	2.0	2.9	4.1

Table 5: Voltage readings for the voltage divider shown in figure 28.

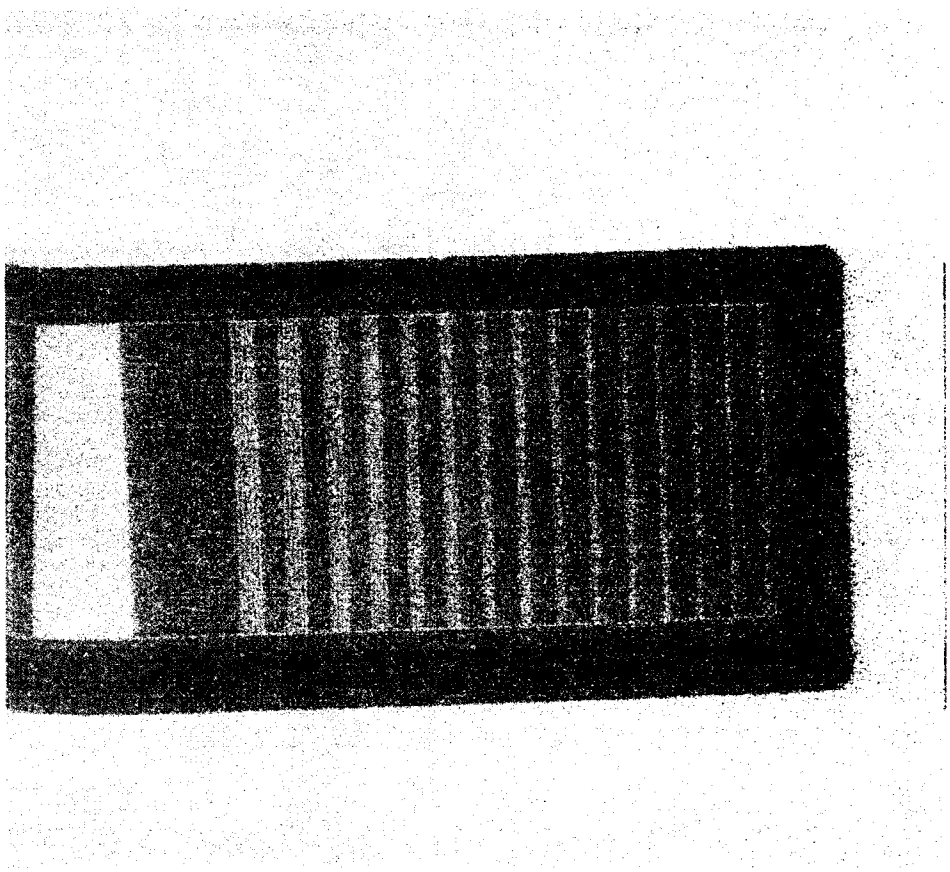

Figure 29: Image of line pair gauge from a PMT without a scintillator.

After all these modifications, there still remained a streaking effect with a decay time of up to a millisecond. This was attributed to the x-rays causing fluorescence in the glass of the PMT. Figure 29 shows the image of a calibration phantom taken with without any scintillator on a completely unshielded Hamamatsu R268 PMT. This image was quite weak and the high voltage applied (1400V) to the PMT was near the maximum rating (1500 V). When a 4.5 mm diameter lead aperture was placed on the face of the 28 mm diameter PMT, the image disappeared owing to the greatly reduced signal level. The maximum measured

Reproduced with permission of the copyright owner. Further reproduction prohibited without permission.

current coming from the PMT without shielding was 28 μA while, with the aperture, it was 0.6 μA which matches the ratio of the unshielded areas of the face of the PMT.

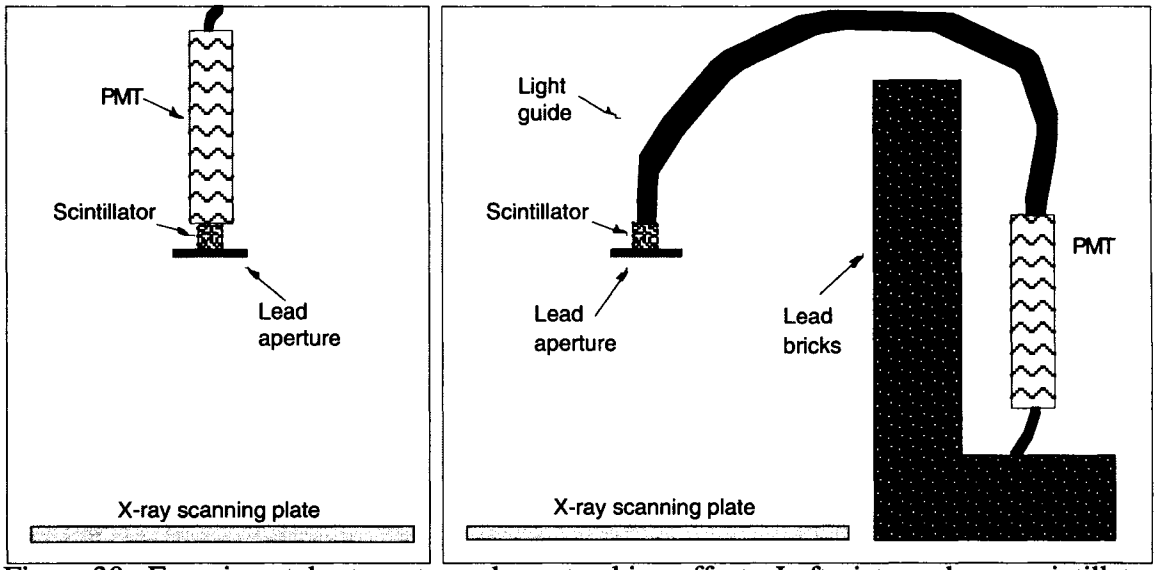

Figure 30: Experimental set ups to analyze streaking effect. Left picture shows scintillator directly coupled to PMT while the right picture shows the scintillator connected via a liquid core light guide.

In order to isolate the various causes for the streaking effect in the image, a comparison was performed between coupling the scintillator directly to the PMT with a lead aperture and coupling through a Jefferson Lab liquid core light guide to a heavily shielded PMT (fig. 30). The x-ray machine was set for 100 keV at 1 mA current for all the tests. Four scintillators were compared – LSO, GSO, YAP from Scionix, and an experimental YAP sample produced locally at Norfolk University. All scintillators were 1 cm^3 cubes except the GSO which was 8 x 8 x 10 mm, placed so that the 8 x 8 mm side faced the incoming x-rays. The scintillators were in various stages of polish with the LSO rough cut and not polished at all. All were wrapped on 5 sides with Teflon tape. The high voltage to the PMT was set to equalize the signal levels from each of the scintillators so that the maximum output current from the PMT was 50 μA. The scintillator was shielded with a 3 mm thick lead aperture with an 8 mm hole. The phantom was a 3 mm thick lead square with a hole in it. Images of the phantom were obtained by averaging 20 one second scans of the

Reproduced with permission of the copyright owner. Further reproduction prohibited without permission.

object. The amount of streaking was quantified by measuring the average value in two 10 x 10 pixel areas about one cm to the right of the object just above and just below the lower edge of the phantom and calculating the percent difference. Figure 31 shows the results for LSO, GSO, and Scionix YAP directly coupled to the PMT and the experimental YAP with and without the light guide. The differences seen between LSO, GSO and Scionix YAP when they were coupled directly to the PMT have two causes. One is the ratio of light outputs and the second is the stopping power of the scintillators. The x-ray transmission of the scintillators and 3 mm lead is seen in table 6. It is easy to see that the best case is to have a bright and high stopping power scintillator if one wishes to couple the scintillator directly to the PMT. A lower brightness scintillator has to compete with the light from the PMT glass as is the case for GSO, while a scintillator with lower stopping power will let more x-rays reach the PMT glass for a given thickness as is the case for YAP. The difference in the amount of streaking between the Scionix YAP and the experimental YAP was exactly the amount measured when the experimental YAP was coupled to the PMT through a light guide. It is also important to note that the type of light guide one uses makes a difference. The Jefferson Lab light guide was made using acrylic end plugs and silicon oil filling. By comparison, when coupling with a Lumatec[36] liquid core light guide with quartz end plugs and a calcium chloride liquid filling the image showed streaking. A measurement with the light guides alone coupled to the shielded PMT biased at -1200 V showed the Lumatec light guide produced 0.54 μA while the Jefferson Lab light guide produced only 0.031 μA maximum current. Light produced in the quartz end plugs from the x-rays is the likely source of this extra signal.

Optimizing the preamplifier

Another optimization made was to adjust the gain and shaping time of the preamplifier (fig. 32). The operational amplifiers (op amps) were changed from Digiray's

Reproduced with permission of the copyright owner. Further reproduction prohibited without permission.

proprietary op amp to the readily available LM6361 from National Semiconductor. This 50 MHz bandwidth op amp is quite stable and easy to use. Since the signal from the PMT is 3 times lower than before owing to the reduced high voltage, the gain in the amplifier was increased by a factor of 3 by increasing the feedback resistor on the first op amp. Also, since the scintillator is now much faster, it has much less self-integration. This causes the signal to vary faster making the image look more granulated when used with a sampling ADC as used in the Digiray system. By adjusting the integration of the amplifier via the feedback capacitor on the second amplifier, one can control and optimize the signal to noise versus the resolution. Figure 33 shows the results of imaging a line pair gauge with the new preamplifier with various feedback capacitors. In this measurement the x-ray intensity was 100 keV at .15 mA and the x-ray beam was zoomed in by a factor of 5 with a scanning speed of 2 seconds per image. Each image was made up of 50 scans averaged together.

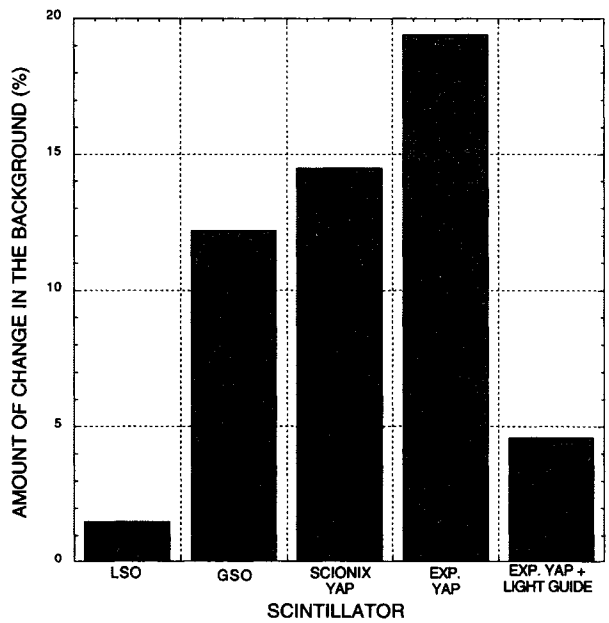

Fig. 31: Measurement of streaking for different scintillators in different configurations

Material	% Transmission
1 cm LSO	4.5 x 10E-6
1 cm GSO	3.3 x 10E-4
1 cm YAP	7.76
3mm Lead	2.2 x 10E-4

Table 6: Transmission of 100 keV x-rays for various materials.

Reproduced with permission of the copyright owner. Further reproduction prohibited without permission.

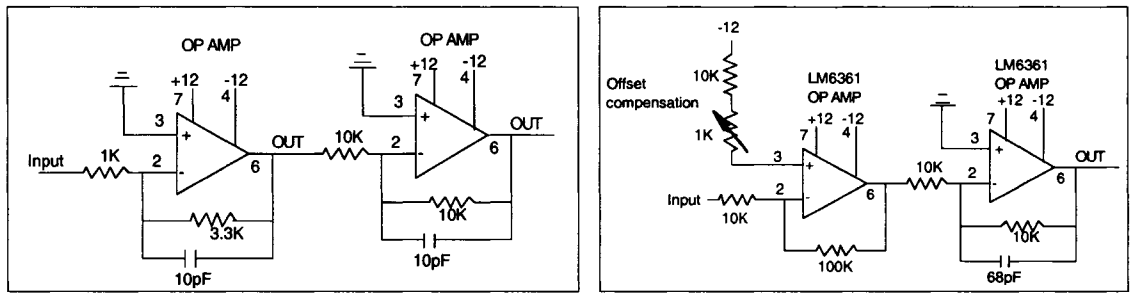

Figure 32: Amplifiers used in the studies. Left is the circuit diagram of the original amplifier and right is the optimized version for use with faster scintillators.

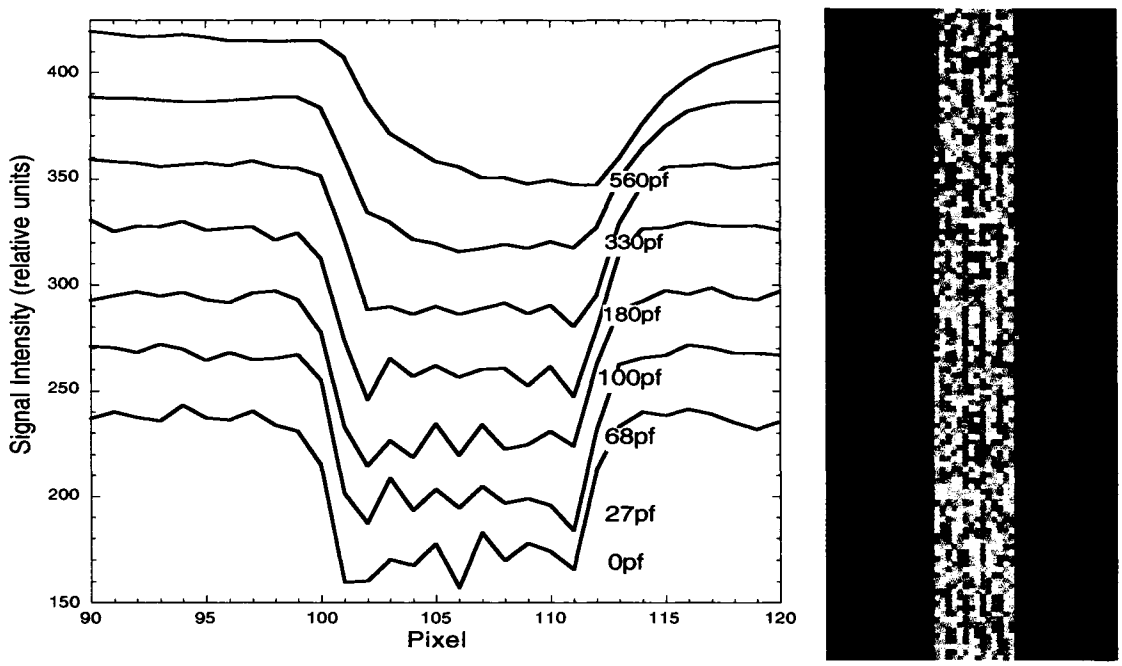

Figure 33: The plot on the left shows a profile cut across the 8 line pairs per mm section of a calibration phantom shown on the right summed 10 pixels vertically where we see 4 lines separated by .125 mm.

The plot shows a profile cut across the 8 line pairs per mm section summed 10 pixels vertically where we see 4 lines separated by .125 mm. The lines are most clearly seen when a 68 pF feedback capacitor is used. With lower values of capacitance the noise makes it harder to see the lines, while with higher values of capacitance, the lines get washed out. Figure 34 shows a comparison with the standard Digiray amplifier which has a slightly lower shaping time and thus more noise for the same 8 line pairs per mm section of the

Reproduced with permission of the copyright owner. Further reproduction prohibited without permission.

calibration phantom. Table 7 shows the standard deviation of the signal for various feedback capacitors in a 100 x 100 pixel area of the background. Measurements were also made at a scanning speed of 4 seconds per image, however, no improvement was seen in either the spatial resolution or image noise. This was the slowest scanning speed permitted by the software for this magnification factor.

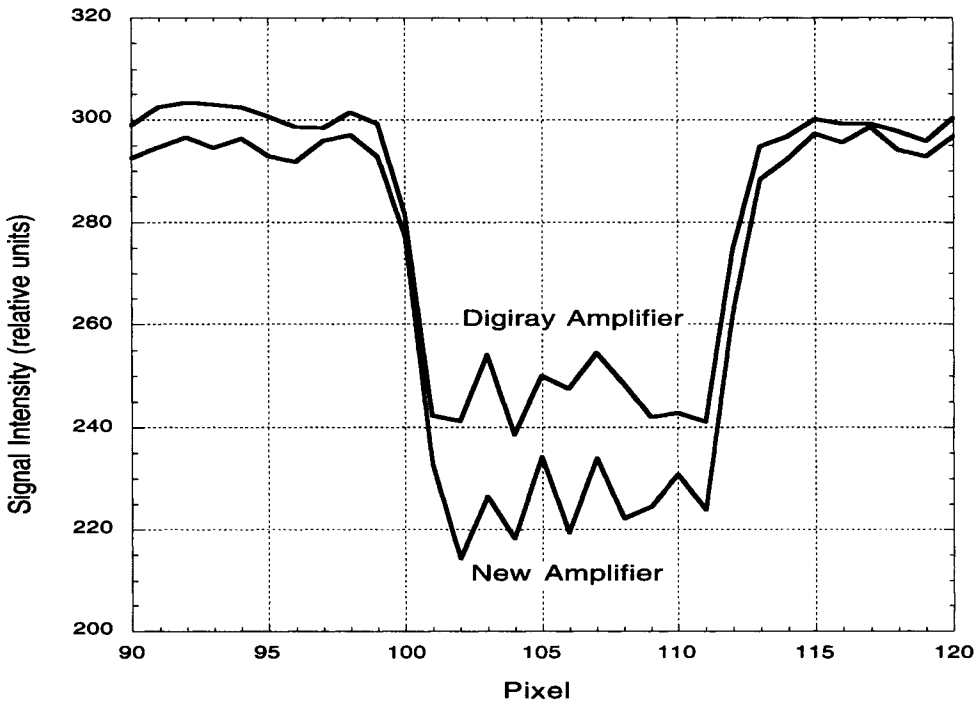

Figure 34: Profile cut across the 8 line pairs per mm section of a calibration phantom for the new amplifier with a 68 pF feedback capacitor and Digiray's amplifier.

Feedback Capacitor (pF)	Mean Value	Standard Deviation	Minimum Value	Maximum Value
0	93.86	12.87	51	151
27	90.40	11.66	52	137
68	85.18	10.25	46	129
100	84.77	9.64	50	124
180	82.02	8.48	47	114
330	79.88	7.22	54	107
560	76.18	6.15	53	101
Digiray	83.57	13.90	33	134

Table 7: Standard deviation of the signal for various feedback capacitors in a 100 x 100 pixel area of the background.

Reproduced with permission of the copyright owner. Further reproduction prohibited without permission.

The optimal data acquisition system for this type of integrating readout would be an integrating amplifier with a reset shown in figure 35 with the timing diagram shown in figure 36. In this proposed circuit, the signal from the PMT is amplified by a fast preamplifier (U1) with no integration. It is fed to an integrating op amp with a hold and reset (U2). As seen in the timing diagram, the amplifier would integrate the signal from all the x-rays for a period of time and then hold the signal while the ADC samples it. After sampling the capacitor on the integrating op amp would be cleared with the reset pulse, the x-ray beam would step to the next position, and the process would start again. This should allow one to obtain the best possible image quality, however, in order to test such a circuit, we would have to make modifications to the control logic of the system which was not feasible at this time. This circuit would allow the highest amount of signal capture while providing the lowest amount of cross-talk between positions of the x-ray beam.

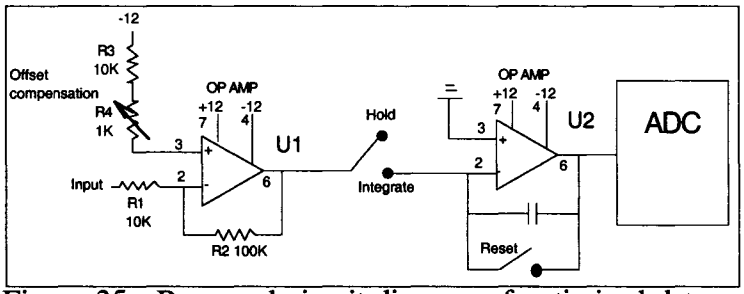

Figure 35: Proposed circuit diagram of optimized data acquisition system for the Digiray system.

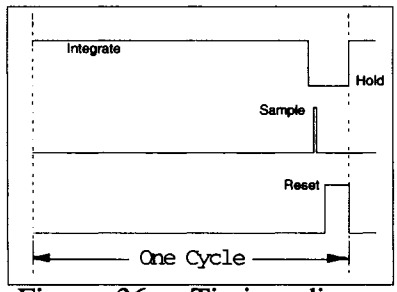

Figure 36: Timing diagram for data acquisition.

X-ray flux calculation

In order to image at a reasonable rate with scanning beam x-radiography, one needs significant x-ray flux to reduce the statistical fluctuations. To get an estimate of the x-ray flux at our detector one can start by assuming the x-ray source is isotropic and that there is no absorption or losses. In equation (1-1), bremsstrahlung intensity per electron hitting the target is defined as the energy per photon multiplied by the number of photons produced.

Reproduced with permission of the copyright owner. Further reproduction prohibited without permission.

Thus, dividing equation (1-1) by the energy and multiplying by the number of electrons hitting the target we get the number of x-ray photons produced per unit energy (E) as

$$N_{xrays}(E) = \frac{2kZ(E_0 - E)}{E} * \frac{i}{e^-}, \qquad (3\text{-}2)$$

where i is the current in amperes, e^- is the electronic charge (1.602×10^{-19}C), E_0 is the energy of the electrons, k ~ 7×10^{-7} keV^{-1} and Z is the atomic number of the target (74 for tungsten). For the Digiray system operating at 120 keV and 0.5 mA about 1.7×10^{14} x-rays greater than 1 keV are produced per second. The vast majority of these x-rays are below 20 keV and are filtered out by the 1/8" thick aluminum housing (fig. 37). This leaves about 2 $\times 10^{13}$ photons per second transmitted by the housing, however, most of those are not directed towards the x-ray detector.

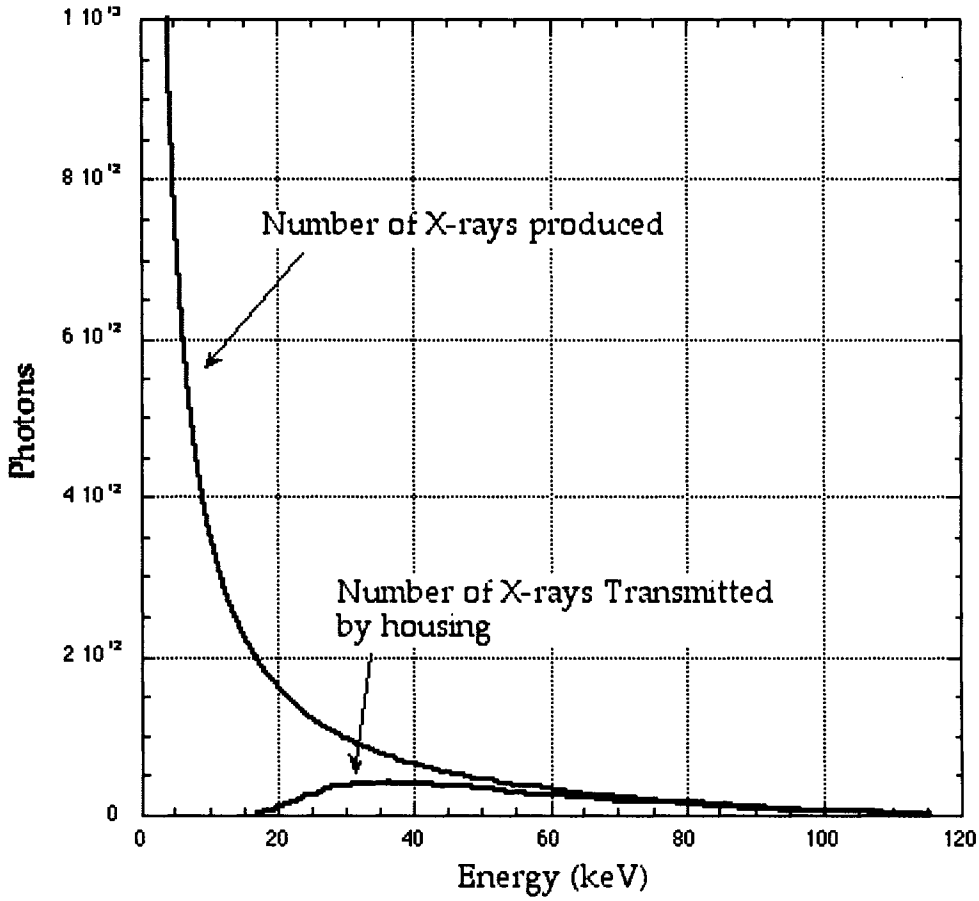

Figure 37: The calculated photon spectrum from Digiray's x-ray tube running at 120 keV .5 mA.

Reproduced with permission of the copyright owner. Further reproduction prohibited without permission.

Making the assumptions stated above, the average number of x-rays reaching a 1 cm x 1 cm x 1 cm detector placed 1 m away, including characteristic x-rays, is approximately 223 x 10^6 photons per second. Assuming standard Gaussian counting statistics, a 2 second image acquisition where each pixel acquires for 2 μs, gives a standard deviation of 21 photons per pixel or 4.74% as a best case estimate. For a 2 second acquisition using a GSO scintillator, it was found that the signal, an indirect measure of the number of photons, had a standard deviation of 10.5%, in reasonable agreement with our calculation. The deviation is certain to be higher than theory for two reasons. The first is that we did not take electronic noise into account and it is known that the particular system these measurements were made with has significant electronic noise caused by the x-ray power supply. The second reason we would expect lower signal to noise is the way the signal is acquired using a shaping amplifier. The signal is only sampled once every 2 μs and thus signals which arrived early in the time period have suffered some decay and are not registered the same as later arriving signals.

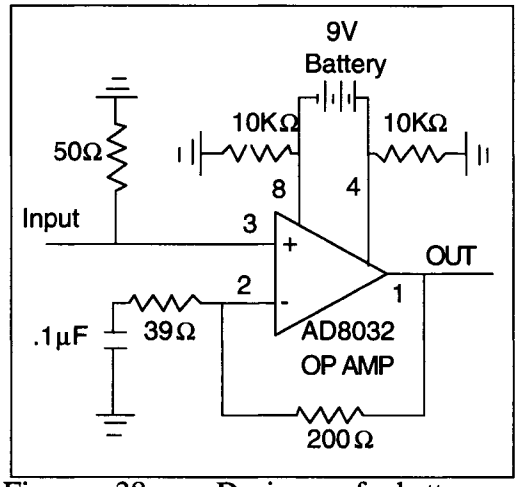

Figure 38: Design of battery powered pre-amplifier.

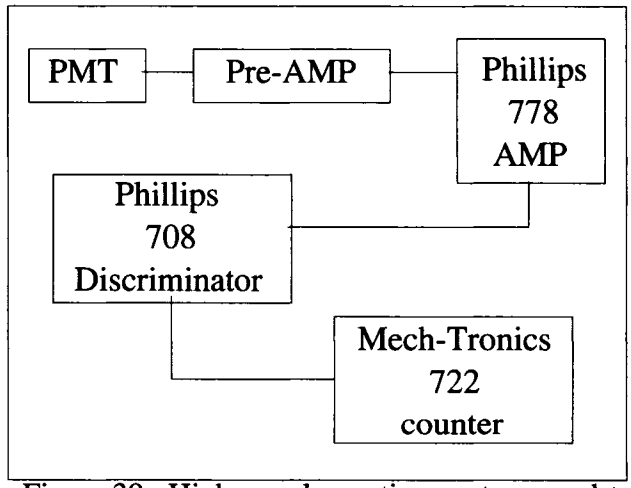

Figure 39: High speed counting system used to measure x-ray flux.

A more direct measurement of the number of photons was made by counting the pulses coming from a PMT with fast electronics. A 1 cm x 1 cm x 1 cm YAP crystal was

Reproduced with permission of the copyright owner. Further reproduction prohibited without permission.

coupled to a Hamamatsu R268 PMT with the PMT base design in figure 28. A 2.4 mm lead aperture was placed in front of the crystal and lead was wrapped around the sides of the PMT. This assembly was positioned 1.64 m above the x-ray scanning plate. Due to excessive electronic noise coming from the x-ray high voltage power supply, a high speed, low current, battery powered pre-amplifier was designed to amplify the signal coming from the PMT (fig. 38). The gain on this 80 MHz amplifier had to be kept low (~ x5) so that the signal width did not increase owing to the lower bandwidth/gain. This amplified signal was then sent to post amplifier, fast discriminator, and a NIM counter as shown in figure 39. The full width at half maximum of the signal was 100 ns or less and the lowest x-ray energy seen gave a signal of about 12 – 14 mV. The threshold of the discriminator was set to 10 mV and the output width was set to10 ns. This is an updating discriminator which, if a second pulse crosses the threshold while the output is triggered, the output is extended giving a wider output width. This would be called a paralyzable system, however, because the signal is much wider than the discriminator output, it acts like a nonparalyzable system until the signals overlap to the point where signal level does not go below the discriminator threshold. The x-ray energy was set to 100 keV. The current had to be kept low enough not to cause counting losses resulting from the ~100 ns dead time discussed later. The counting time was set for 60 seconds and three measurements were made at each current setting. It was found that there was an offset between the x-ray current given by the x-ray control computer and the amount actually produced. An offset value of 0.039 mA was found by linear extrapolation of the number of x-ray counts to zero. The minimum computer setting which produced x-rays was .05 mA. The theoretical number of x-rays are compared with the measured values in figure 40. The reduction in the number of measured counts at the higher currents result from counting losses from pulse pile-up which was verified with a digital oscilloscope.

Reproduced with permission of the copyright owner. Further reproduction prohibited without permission.

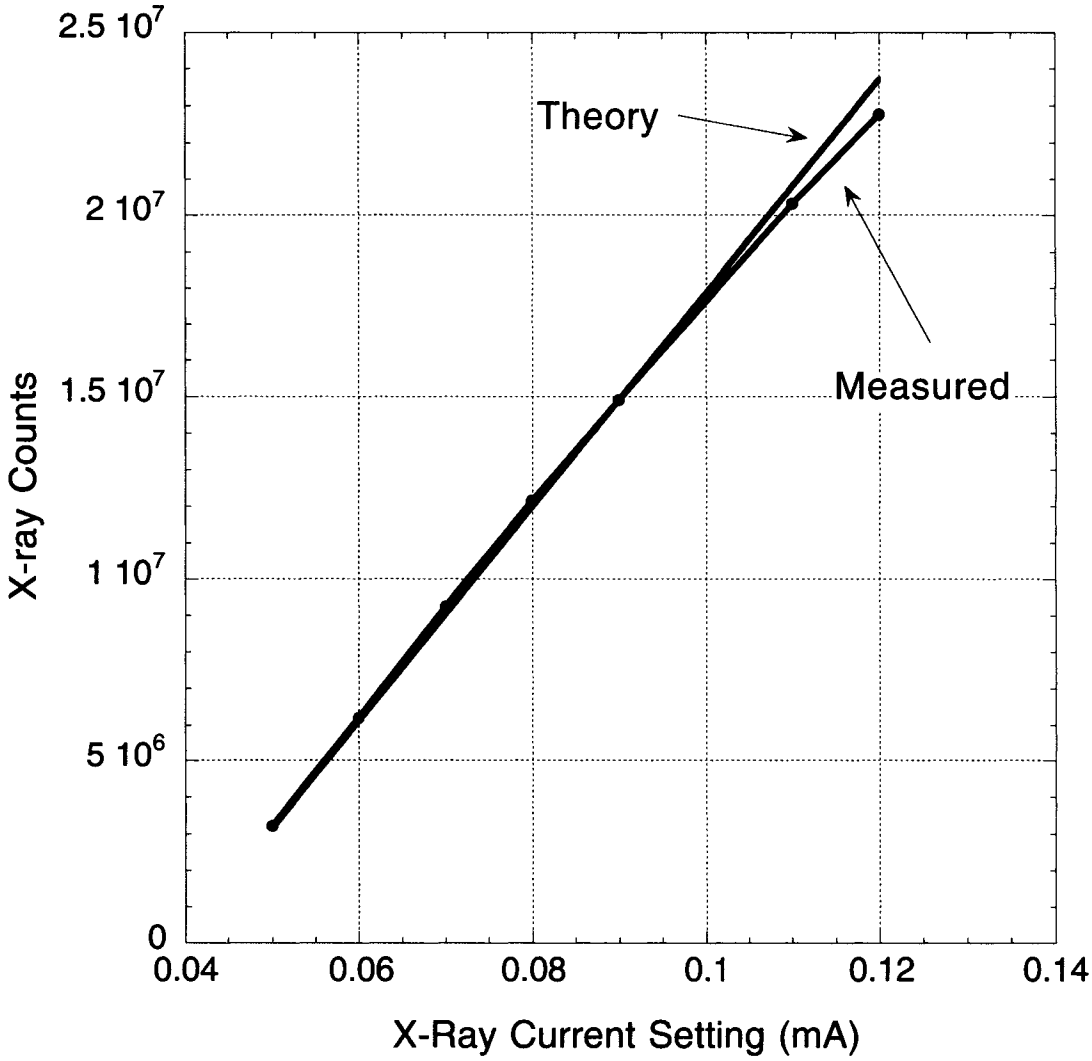

Figure 40: Theory vs. measured x-ray production from Digiray's RGX system.

Reproduced with permission of the copyright owner. Further reproduction prohibited without permission.

CHAPTER IV

DUAL ENERGY X-RADIOGRAPHY

Monoenergetic sources

Since standard x-radiography only produces a two dimensional x-ray shadow graph of an object, one cannot differentiate a thick low-stopping-power object from a thin high stopping power object. Complicated structures of one material may overlay and obscure structures of other materials. Dual energy imaging is a well known technique in medical imaging[37] which mitigates these problems by using information contained in the energy spectrum of the transmitted x-rays. As seen in Chapter I, x-rays up to about 200 keV interact with matter mainly though photoelectric absorption and Compton scattering. Rayleigh scattering is a small percentage of the total scattering and has approximately the same mathematical form as photoelectric absorption and so, in measurements, it is assumed to be mixed in with photoelectric absorption. The photoelectric absorption dominates at lower energies and is mainly dependent on the Z of the material (Z^4 from equation (1-5)) whereas Compton scattering dominates at higher energies and is mainly dependent on the electron density of the material (nZ from equations (1-8) and (1-11)). Thus, if we measure low and high energy x-ray attenuation images, we will be able to relate the results to the Z verses density of the material. This will allow a computer to identify and remove a selected material from the image thereby reducing the complexity and increasing the contrast of the remaining image.

For the simple case of monoenergetic x-ray spectra, the mathematics can be worked out as follows. If we combine equations (1-5), (1-8), (1-11), and (1-14) and ignore Rayleigh scattering we find the total linear attenuation is

$$\mu_T = C_P n \frac{Z^4}{E_\gamma^{\,3}} + \sigma_{Ce} nZ \qquad (4\text{-}1)$$

Reproduced with permission of the copyright owner. Further reproduction prohibited without permission.

which can be separated into energy dependent and material dependent parts

$$\mu_T = a_p f_p(E) + a_c f_c(E) \tag{4-2}$$

where the material dependent parts are $a_p = nZ^4$ and $a_c = nZ$ and the energy dependent parts are $f_p(E) = C_p/E_\gamma^3$ and $f_c(E) = \sigma_{Ce}$. Taking the log of equation (1-11) for two different known monoenergetic x-ray energies (h and l) for a material of known thickness T, gives

$$M_h = [a_p f_{ph} + a_c f_{ch}]T \tag{4-3}$$

$$M_l = [a_p f_{pl} + a_c f_{cl}]T$$

where $M_h = \ln(I_{0h}/I_h)$ for the original h x-ray energy intensity I_{0h} and the transmitted x-ray intensity I_h and similarly for M_l. This can be solved uniquely to identify the a_p and a_c of the material. Except for K-edge imaging, a_p and a_c completely characterize the material in x-ray imaging in our energy range. Thus measurements at more than two energies can add no new information since the equation for the third energy would be a linear combination of the first two.

Now we consider the case where we have two known materials (1 and 2) of unknown thickness (T_1 and T_2). We assume the a_p and a_c of each material are known. Then we have

$$M_h = [a_{p1} f_{ph} + a_{c1} f_{ch}]T_1 + [a_{p2} f_{ph} + a_{c2} f_{ch}]T_2 \tag{4-4}$$

$$M_l = [a_{p1} f_{pl} + a_{c1} f_{cl}]T_1 + [a_{p2} f_{pl} + a_{c2} f_{cl}]T_2$$

which can be solved uniquely to obtain the thickness of each material. Due to the linear dependence of images taken at different x-ray energies, one is only able to obtain two linearly independent equations per position in the image and thus can only determine the thickness of two overlying materials in a standard two-dimensional x-radiograph. When there are more than two overlying materials, their relative thicknesses can not be determined. This limitation, however, is actually a strength when it comes to obtaining the images. It

Reproduced with permission of the copyright owner. Further reproduction prohibited without permission.

means that the complete energy dependent information can be extracted from two simple image measurements.

Since every material is characterized purely by its a_p and a_c value we can mathematically interpret a_p and a_c as the basis of a two-dimensional space which contains all possible materials, written as

$$R^2 = \left\{ \begin{pmatrix} 1 \\ 0 \end{pmatrix}, \begin{pmatrix} 0 \\ 1 \end{pmatrix} \right\} \tag{4-5}$$

where R^2 stands for the two-dimensional space. Vector multiplication of any arbitrary $\mathbf{r}_x <- R^2$, (a_{cx}, a_{px}), by the first vector in R^2 projects out the a_{cx} term while the second vector projects out the a_p term. The linear attenuation coefficient (eq. 4-2) can then be written in matrix notation as

$$\mu_x = \mathbf{f} \cdot \mathbf{r}_x \text{ where } \mathbf{f} = \begin{pmatrix} f_c(E) \\ f_p(E) \end{pmatrix} \tag{4-6}$$

The rules of linear algebra state that a basis set is not unique. Any set of linearly independent combinations of one basis set is also a basis set. Thus we can change our basis from R^2 space to U^2 space where

$$U^2 = \left\{ \begin{pmatrix} a_{c1} \\ a_{p1} \end{pmatrix}, \begin{pmatrix} a_{c2} \\ a_{p2} \end{pmatrix} \right\}. \tag{4-7}$$

These new basis vectors represent two materials, 1 and 2. The standard transformation functions to change from one basis to another are

$$\mathbf{r} = S\,\mathbf{u} \qquad \text{and} \qquad \mathbf{u} = S^{-1}\,\mathbf{r} \tag{4-8}$$

where $\mathbf{r}$ and $\mathbf{u}$ are vectors in R^2 and U^2 space respectively and S is the transformation matrix given in this case by

$$S = \begin{pmatrix} a_{c1} & a_{c2} \\ a_{p1} & a_{p2} \end{pmatrix} \qquad \text{and} \qquad S^{-1} = \frac{1}{a_{c1}a_{p2} - a_{p1}a_{c2}} \begin{pmatrix} a_{p2} & -a_{c2} \\ -a_{p1} & a_{c1} \end{pmatrix}. \tag{4-9}$$

Thus, for an arbitrary material, x, we get

Reproduced with permission of the copyright owner. Further reproduction prohibited without permission.

$$\mathbf{u}_x = \frac{1}{a_{c1}a_{p2} - a_{p1}a_{c2}}\begin{pmatrix} a_{p2}a_{cx} - a_{c2}a_{px} \\ a_{c1}a_{px} - a_{p1}a_{cx} \end{pmatrix} = \frac{1}{n_1n_2Z_1Z_2(Z_2^3 - Z_1^3)}\begin{pmatrix} n_2n_xZ_2Z_x(Z_2^3 - Z_x^3) \\ n_1n_xZ_1Z_x(Z_x^3 - Z_1^3) \end{pmatrix}. \quad (4\text{-}10)$$

where we substituted in for the a_p's and a_c's. Thus the linear attenuation for any material can be written as

$$\mu_x = \mathbf{f}\,\mathbf{S}\,\mathbf{u}_x = (\mu_1, \mu_2)\,\mathbf{u}_x = a_\alpha\mu_1 + a_\beta\mu_2 \quad (4\text{-}11)$$

where

$$a_\alpha = \frac{n_xZ_x(Z_2^3 - Z_x^3)}{n_1Z_1(Z_2^3 - Z_1^3)} \quad \text{and} \quad a_\beta = \frac{n_xZ_x(Z_x^3 - Z_1^3)}{n_2Z_2(Z_2^3 - Z_1^3)} \quad (4\text{-}12)$$

This shows that the linear attenuation coefficient can be represented as a linear combination of the linear attenuation of two basis materials with a_α and a_β being the characteristic constants of the material, x. It is convenient to define

$$B_1 = a_\alpha T_x \qquad \text{and} \qquad B_2 = a_\beta T_x \quad (4\text{-}13)$$

where T_x is the thickness of material, x. We can then write the log attenuation (M) as

$$M = \mu_x T_x = B_1\mu_1 + B_2\mu_2. \quad (4\text{-}14)$$

Using (B_1, B_2) as the characteristic constants defining a material-thickness space we obtain the graph shown in figure 41. The angle θ of the vector from the origin to the material location in this space depends only on the effective Z of the material, x, and basis materials.

$$\theta = \tan^{-1}\left(\frac{B_2}{B_1}\right) = \frac{n_1Z_1(Z_x^3 - Z_1^3)}{n_2Z_2(Z_2^3 - Z_x^3)} \quad (4\text{-}15)$$

The length of this vector is proportional to the sample thickness. We call θ the characteristic angle of the material. This identity is not unique when there are overlapping materials in the image since the material vectors will add commutatively to form a final material vector. This means the final vector can be arrived at by the combination of a variety of materials and material thicknesses (fig. 42). Also, it is important to remember that it is the effective Z and A of the material which determines radiation absorption and scattering. These are obtained by the formulas

Reproduced with permission of the copyright owner. Further reproduction prohibited without permission.

$$Z_{eff} = \frac{\sum_i f_i Z_i^2}{\sum_i f_i Z_i} \qquad A_{eff} = \frac{\sum_i f_i A_i^2}{\sum_i f_i A_i} \tag{4-16}$$

where f_i is the fraction by weight of the i^{th} element in the material.

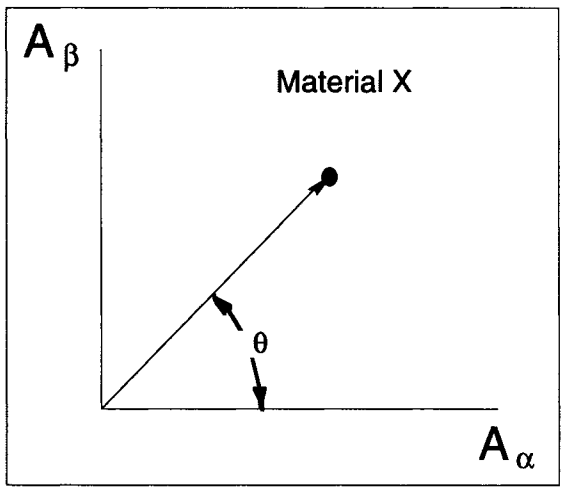

Figure 41: Representation of material x in the basis material-thickness (B_1,B_2) plane. θ defines the Z_{eff} of the material while the length of the vector gives its thickness.

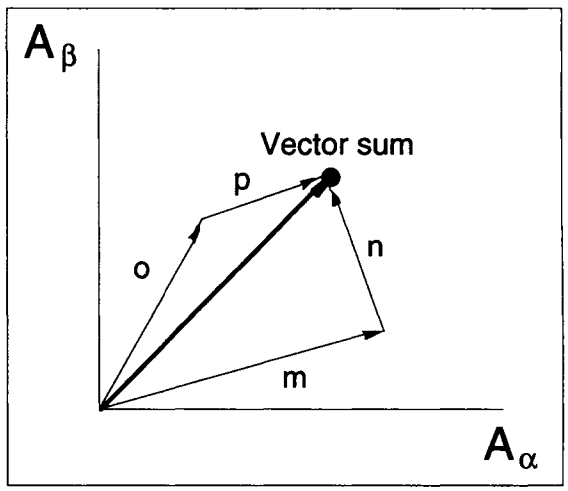

Figure 42: Material vectors add, thus the combination of materials m and n can not be distinguished from materials o and p.

If we compare equations (4-4) and (4-14) we see that B_1 and B_2 are also equivalent to the thicknesses of the basis materials which would be needed to match the attenuation of material, x ($B_1 = T_1$ and $B_2 = T_2$). It is this key point which allows us to subtract materials from the image. In order to do this, we first calibrate our two-energy system using equation (4-3) to get the a_p and a_c of our two basis materials. We then use equation (4-4) to find T_1 and T_2 for every pixel in our object of interest and produce two images, separately displaying T_1 and T_2 for every pixel. This gives us two basis images of the object, one displaying the B_1 component at every pixel and the other displaying the B_2 component at every pixel, we can then combine them into a resulting image by the equation

$$C = B_1\cos\Phi + B_2\sin\Phi \tag{4-17}$$

for any Φ we chose. If we chose Φ equal to 0 then any object made of second basis material would be removed from the final image, C. Notice that by combining the images

Reproduced with permission of the copyright owner. Further reproduction prohibited without permission.

with an angle perpendicular to the characteristic angle of an object, the length of the object becomes zero and thus it disappears. By varying Φ until an object disappears from the image, one can obtain the characteristic angle of the material since Φ is then perpendicular to the characteristic angle of the object.

When a material is subtracted from the image, a vacancy is left. Edges of this vacancy may possibly interfere with the analysis of other materials. There is a way to cause one material to look like another material, thereby removing the contrast between the two materials. The contrast of these two materials to a third material can then be enhanced. To see how this is done, we consider an object of total thickness L made up of two materials (fig. 43). The basis coordinates along the object are

$$(B_1, B_2) = \{a_{\alpha n}(L - X) + a_{\alpha m}X,\ a_{\beta n}(L - X) + a_{\beta m}X\} \qquad (4\text{-}18)$$

for materials n and m where X is the thickness of the m material. Since this is a linear equation in X, B_1 and B_2, it will fall on a straight line. Using the standard formula for a straight line, we arrive at the characteristic angle of the X parameter:

$$\theta = \tan^{-1}\left(\frac{B_2}{B_1}\right) = \frac{a_{\beta n} - a_{\beta m}}{a_{\alpha n} - a_{\alpha m}}. \qquad (4\text{-}19)$$

Note that this is not a characteristic angle of either of the materials individually. Also note that this angle does not depend on the thickness, X, Only the length of this vector is dependent on X. Using the lesson learned in the last paragraph, if we combine the basis images with an angle perpendicular to this mixed characteristic angle, the image will no longer be dependent on X and the contrast between the two materials will vanish. We can see that, if the n material was air, this is just the subtraction technique we used before. Now we see that, if we assume we live in any n material atmosphere, we can apply the same techniques to cause the contrast between the two materials to disappear and the object to vanish from view.

Reproduced with permission of the copyright owner. Further reproduction prohibited without permission.

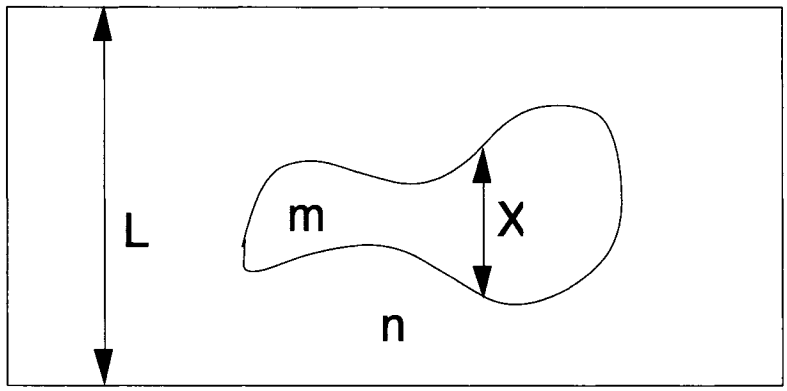

Figure 43: Object made of two different materials, m and n with a total thickness of L.

There is yet one more trick which can be employed using the added information gained from dual energy imaging. One can reconstruct the image at any selected monoenergetic x-ray energy chosen. This is true even if one is using a polyenergetic x-ray source. This can come in quite handy in computed tomographic (CT) imaging where "Beam Hardening" can cause artifacts in the image. Beam Hardening is a term that means that the lower energy x-rays are absorbed more than higher energy x-rays. Such CT reconstruction artifacts are shown in figures 44 and 45 where a CT scan of a skull filled with water is simulated for both polychromatic and monochromatic x-rays.[38]

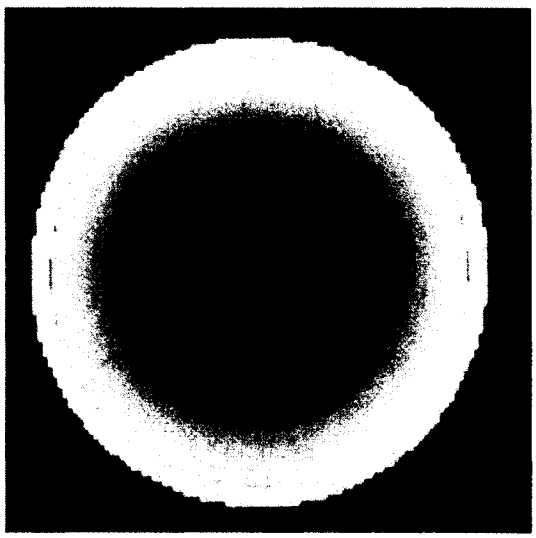

Figure 44: Reconstruction from polychromatic projection data of a water phantom inside a skull.

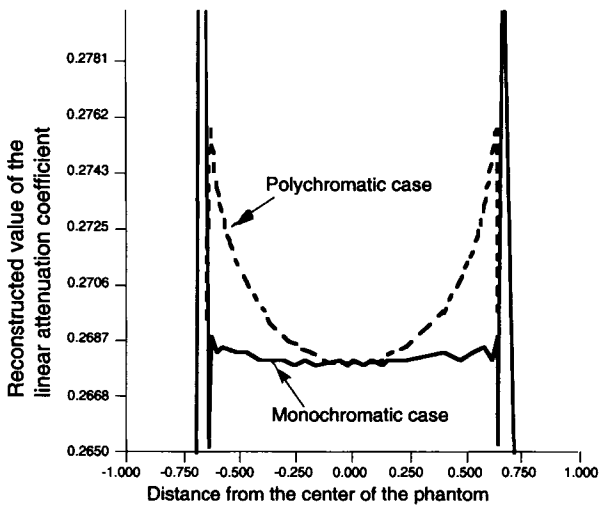

Figure 45: Cross section of a reconstructed water phantom inside a skull using polychromatic and monochromatic x-rays.

Reproduced with permission of the copyright owner. Further reproduction prohibited without permission.

To see how this is done we look at equation (4-2). If we knew all the a_p's and a_c's for each pixel in an image we could chose to evaluate $f_p(E)$ and $f_c(E)$ at any desired display energy E_d since $f_p(E)$ and $f_c(E)$ are known functions of the energy. This gives us the linear attenuation for each point as

$$\mu_T = a_p f_p(E_d) + a_c f_c(E_d). \tag{4-20}$$

By equation (4-14), we also found we can replace equation (4-20) with

$$M = B_1 \mu_1(E_d) + B_2 \mu_2(E_d) \tag{4-21}$$

using our two basis materials. Thus to obtain an image at any display energy, we just multiply the B_1 image by the linear attenuation coefficient of that material at energy E_d and add it to the B_2 image multiplied by its appropriate linear attenuation coefficient evaluated at E_d. Thus we arrive at apparent mono-energetic x-radiography.

Before going on to polyenergetic x-ray sources, we put equation (4-4) with (4-14) into a directly usable form for monoenergetic dual energy imaging. Inverting this equation to find B_1 and B_2 we get

$$B_1 = k_1 M_h + k_2 M_l \tag{4-22}$$

$$B_2 = k_3 M_h + k_4 M_l$$

where k_1,k_2, k_3, and k_4 are constants made up of a_{p1}, a_{p2}, a_{c1}, a_{c2}, f_{ph}, f_{ch}, f_{pl}, and f_{cl}. This equation is applied to each pixel in the high energy and low energy images to obtain B_1 and B_2 images. Implicit in this equation is the requirement that the high and low energy images be taken from exactly the same angle with no movement of the object.

Polyenergetic sources

As seen earlier, the typical x-ray source is polyenergetic which makes dual energy imaging more complex. However, it is still reasonably straight forward. The key problem to solve is estimating B1 and B2, the thicknesses of the basis components, from x-ray

Reproduced with permission of the copyright owner. Further reproduction prohibited without permission.

transmission measurements of a set of objects at two energies. The most straight forward way to do this is to just add higher order fitting terms to equation (4-22)[39]

$$B_1 = k_1M_h + k_2M_l + k_3M_h^2 + k_4M_l^2 + k_5M_hM_l \qquad (4\text{-}23)$$

$$B_2 = k_6M_h + k_7M_l + k_8M_h^2 + k_9M_l^2 + k_{10}M_hM_l.$$

The coefficients k_1–k_{10} are found during a calibration procedure where various thicknesses of the basis components are imaged to obtain about 100 (B_1,B_2) combinations. These equations can then be solved by the method of least squares based on singular value decomposition[40] to obtain the k_1–k_{10} coefficients. This method was found to be quite robust, fast to compute, and easy to implement. Another method is using a lookup table which is used to convert high and low energy transmissions to the (B_1,B_2) thicknesses. This, however, requires a very large amount of data to construct a table of sufficient resolution. It also does not allow for extrapolation outside the Z of the basis materials. What is purported to be the most accurate method to obtain (B_1,B_2) uses conic surface equations in three dimensions.[41]

To see how a conic surface comes about, we start from the first order or planar surface in three dimensions (B_1,B_2,M) which describes the monoenergetic case. Here, the planar surface equation form of equation (4-14) is

$$c_1B_1 + c_2B_2 - c_3M + c_4 = 0. \qquad (4\text{-}24)$$

To obtain equation (4-14), the constant c_1 would be μ_1, c_2 would be μ_2, c_3 would be 1, and c_4 would be 0. Another way to look at this equation is that it contains the 4 combinations of $B_1^pB_2^qM^r$ with the total degree (p+q+r) less than or equal to 1. We now assume that, owing to the polyenergetic nature of the x-ray source, this plane is warped slightly and smoothly into a second order surface. The most generic second order surface equation would contain 10 terms in $B_1^pB_2^qM^r$ of total degree (p+q+r) less than or equal to 2. This can be written as

$$C - DM - EM^2 = 0 \qquad (4\text{-}25)$$

where

Reproduced with permission of the copyright owner. Further reproduction prohibited without permission.

$$C = c_0 + c_1B_1 + c_2B_2 + c_3B_1^2 + c_4B_1B_2 + {}_5B_2^2 \quad (4\text{-}26a)$$

$$D = d_0 + d_1B_1 + d_2B_2 \quad (4\text{-}26b)$$

$$E = e_0. \quad (4\text{-}26c)$$

We are allowed one normalization by dividing through by any number we choose, thus we can set $d_0 = 1$. This leaves 9 independent variables to be determined.

We can use the standard quadratic formula to solve M in equation (4-25)

$$M = \frac{-D \pm \sqrt{D^2 + 4EC}}{2E} \quad (4\text{-}27)$$

where we see that, in the mono-energetic limit of D -> 1 and E -> 0, we must chose the positive root for (4-26) to remain finite. This equation describes a smooth, ripple-free, monotonic surface. It also exhibits the correct asymptotic behavior at large and small values of B_1 and B_2. For large B_1 and B_2 we can keep only the B_1^2, B_1B_2, and B_2^2 terms under the radical which allows us to simplify (4-26) to

$$M = n_1B_2 + n_2B_2 \quad (4\text{-}27)$$

where n_1 and n_2 are constants. Setting ($n_1 = \mu_1(E_{max})$ and $n_2 = \mu_2(E_{max})$) with $\mu_1(E_{max})$ being the linear attenuation coefficient of material 1 at the maximum x-ray energy and similar for $\mu_2(E_{max})$, we arrive at the standard linear attenuation formula one would expect due to beam hardening leaving only the highest energy x-rays. At small values of B_1 and B_2 a Taylor series expansion of (4-26) can be made around $(B_1,B_2) = (0,0)$ which brings us back to equation (4-22). These properties allow M to be extrapolated beyond the calibration region with relatively little error. Since E is generally small, we can, with a sight additional error, make the approximation E = 0 in which case equation (4-24) becomes

$$M = \frac{C}{D} \quad (4\text{-}28)$$

which greatly simplifies the calculation. To obtain a higher degree of accuracy, one can add a perturbation to the coefficients:

Reproduced with permission of the copyright owner. Further reproduction prohibited without permission.

$$C' = C + c_6B_1^3 + c_7B_1^2B_2 + c_8B_1B_2^2 + c_9B_2^3 \quad (4\text{-}29a)$$

$$D' = D + d_3B_1 + d_4B_2 \quad (4\text{-}29b)$$

$$E' = E + e_1B_1 + e_2B_2. \quad (4\text{-}29c)$$

This turns equation (4-24) into a third order surface, but without any cubic term in M. Thus, equations (4-26) and (4-27) still hold. Thus, the complete set of dual energy reconstruction equations are:

$$M_h = \frac{\sqrt{D_h^2 + 4E_hC_h} - D_h}{2E_h} \quad (4\text{-}30a)$$

$$M_l = \frac{\sqrt{D_l^2 + 4E_lC_l} - D_l}{2E_l} \quad (4\text{-}30b)$$

$$C_h = c_{0h} + c_{1h}B_1 + c_{2h}B_2 + c_{3h}B_1^2 + c_{4h}B_1B_2 + c_{5h}B_2^2 \quad (4\text{-}30c)$$

$$D_h = 1 + d_{1h}B_1 + d_{2h}B_2 \quad (4\text{-}30d)$$

$$E_h = e_{0h}. \quad (4\text{-}30e)$$

$$C_l = c_{0l} + c_{1l}B_1 + c_{2l}B_2 + c_{3l}B_1^2 + c_{4l}B_1B_2 + c_{5l}B_2^2 \quad (4\text{-}30f)$$

$$D_l = 1 + d_{1l}B_1 + d_{2l}B_2 \quad (4\text{-}30g)$$

$$E_l = e_{0l} \quad (4\text{-}30h)$$

for high (h) and low (l) x-ray energies. And the inverted equations are:

$$B_1 = \frac{\sqrt{G_\alpha^2 + 4H_\alpha F_\alpha} - G_\alpha}{2H_\alpha} \quad (4\text{-}31a)$$

$$B_2 = \frac{\sqrt{G_\beta^2 + 4H_\beta F_\beta} - G_\beta}{2H_\beta} \quad (4\text{-}31b)$$

$$F_\alpha = f_{0\alpha} + f_{1\alpha}M_l + f_{2\alpha}M_h + f_{3\alpha}M_l^2 + f_{4\alpha}M_lM_h + f_{5\alpha}M_h^2 \quad (4\text{-}31c)$$

$$G_\alpha = 1 + g_{1\alpha}M_l + g_{2\alpha}M_h \quad (4\text{-}31d)$$

$$H_\alpha = h_{0\alpha} \quad (4\text{-}31e)$$

$$F_\beta = f_{0\beta} + f_{1\beta}M_l + f_{2\beta}M_h + f_{3\beta}M_l^2 + f_{4\beta}M_lM_h + f_{5\beta}M_h^2 \quad (4\text{-}31f)$$

$$G_\beta = 1 + g_{1\beta}M_l + g_{2\beta}M_h \quad (4\text{-}31g)$$

Reproduced with permission of the copyright owner. Further reproduction prohibited without permission.

$$H_\beta = h_{0\beta}. \qquad (4\text{-}31h)$$

for basis materials α and β.

Prior Work on Dual Energy X-radiography

Dual energy x-radiography was originally developed by Alvarez and Macovski at Stanford University in 1976.[42] Since then many papers have been written on the subject. Except for bone densitometry and luggage inspection, however, it has remained more of a curiosity than a useful technique. The main obstacle to widespread use is the added complication and expense of the imaging system. Dual energy imaging is usually achieved either by acquiring two separate images using different x-ray tube voltages[43] or by using a dual detector sandwich with the front detector stopping the low energy x-rays while the back detector absorbs the remaining x-rays. The main determining factor of how well one can differentiate between materials using a dual energy imaging system is how well separated the two energy measurements are. With this in mind, the first method tends to produce slightly better images especially when a filter is placed in the x-ray path to attenuate the low energy x-rays when the high energy image is acquired. Figure 46 shows the resulting spectra when two x-ray energy settings are used with the high energy spectrum filtered by .3 mm of uranium. The disadvantage of this technique is that one must take two images thus doubling the imaging time, equipment load, and dose. This method is also quite sensitive to any movement between image acquisitions, x-ray tube stability, and, since the majority of x-ray systems in use today are still film based, misregistration of the images which need to be scanned into a computer in order to process the energy information. With the introduction of digital x-ray systems, this last difficulty is slowly disappearing.[44]

The second dual energy imaging method uses a two-detector approach. A front detector measures the lower energy x-rays and the back detector measures the x-rays which penetrate the first detector. An example of the absorption spectra from such a dual detector

Reproduced with permission of the copyright owner. Further reproduction prohibited without permission.

is shown in figure 47.[45] The front detector is CaF_2 coupled to a PMT and behind that is placed an NaI crystal coupled to a second PMT. It should be noted that better separation of the peak absorption energies could have been obtained by placing a filter between the detectors to further attenuate the low energy x-rays before reaching the NaI detector. This detector was used in the CT system which uses a relatively small number of low resolution detectors. If one wishes to use such a detector design for standard 2-D planer imaging, the difficulties increase significantly. The simplest method to produce a planer dual detector imager is to use a sandwich of film cassettes or imaging plates with an absorber between the cassettes to enhance the energy separation.[46] This also then requires the images to be scanned into a computer and properly registered before use can be made of the energy information. This additional step and expense greatly reduces the attractiveness of this technique. Trying to use digital detectors in place of the imaging plates is not possible due to the readout electronics mounted on the back of the detectors which would appear in the high energy image.

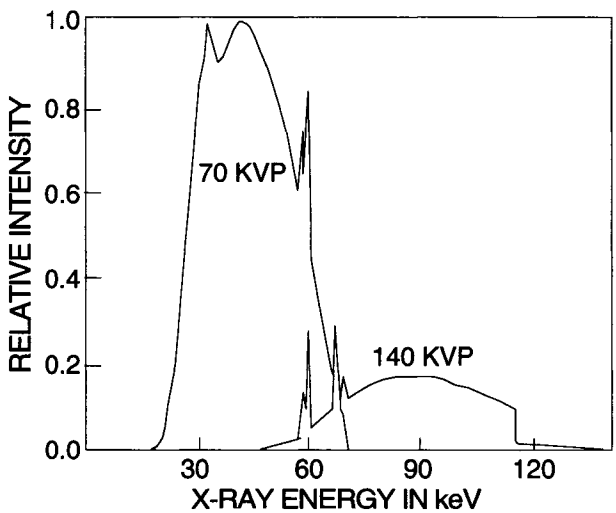

Figure 46: X-ray spectra obtained using 70 kV and 140 kV settings on the x-ray machine. The high energy x-ray setting is filtered by 0.3 mm of uranium.

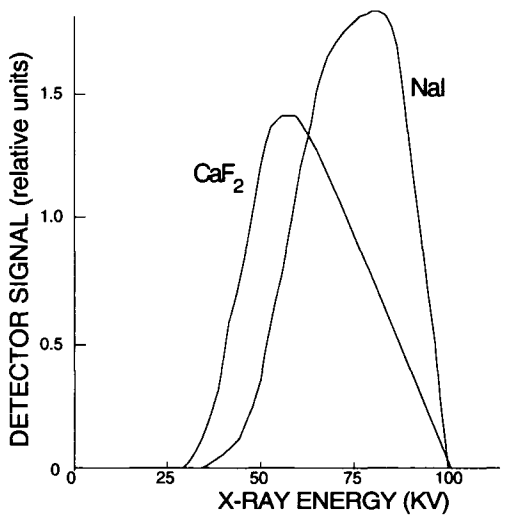

Figure 47: X-ray absorption spectra for a two detector dual energy system.

Reproduced with permission of the copyright owner. Further reproduction prohibited without permission.

Another way to obtain "single shot" dual energy x-ray images is to use a dual linear array of energy sensitive detectors with a fan beam x-ray source which is then scanned over the object to produce direct digital images such as that shown in figure 48.[47,48] Unfortunately, due to resolution requirements, one needs about 2000 channels (1000 high energy + 1000 low energy) of 200 μm wide pixels to cover a 20 cm wide area. Such highly integrated detectors tend to have poor stopping power for the higher energy x-rays. There is, however, one version of this type of detector which could make this a more attractive technique.[49] It uses a silicon strip detector in an edge-on orientation. The readout is segmented along the length of the strip to give one depth of interaction and thus energy information. It is currently under development for dual energy digital mammography by Mamea, a company in Stockholm, Sweden and will be discussed below. Another disadvantage to this method is the scanning time. Since the image is produced by mechanically scanning the detector/x-ray beam over the object, it usually takes a couple of minutes to obtain an image. Scanning beam x-radiography overcomes this by electronically scanning the beam and leaving the detector fixed to produce images in a few seconds or less.

The results achieved with dual energy imaging, even with these problematic detectors, show this technique can be quite useful. In medical physics, the quality of chest x-radiography can be enhanced to provide better detection of lesions by reducing the clutter in the image resulting from the bones (fig. 49).[50] Dual energy x-radiography has also become the gold standard in bone densitometry tests used to evaluate osteoporosis (fig. 50).[51] Its ability to accurately eliminate the soft-tissue absorption allows one to measure bone mineral density anywhere in the body. Dual energy x-radiography is even starting to play a role in luggage inspection by helping one to actually identify substances instead of merely seeing shadows (fig. 51).[52]

Reproduced with permission of the copyright owner. Further reproduction prohibited without permission.

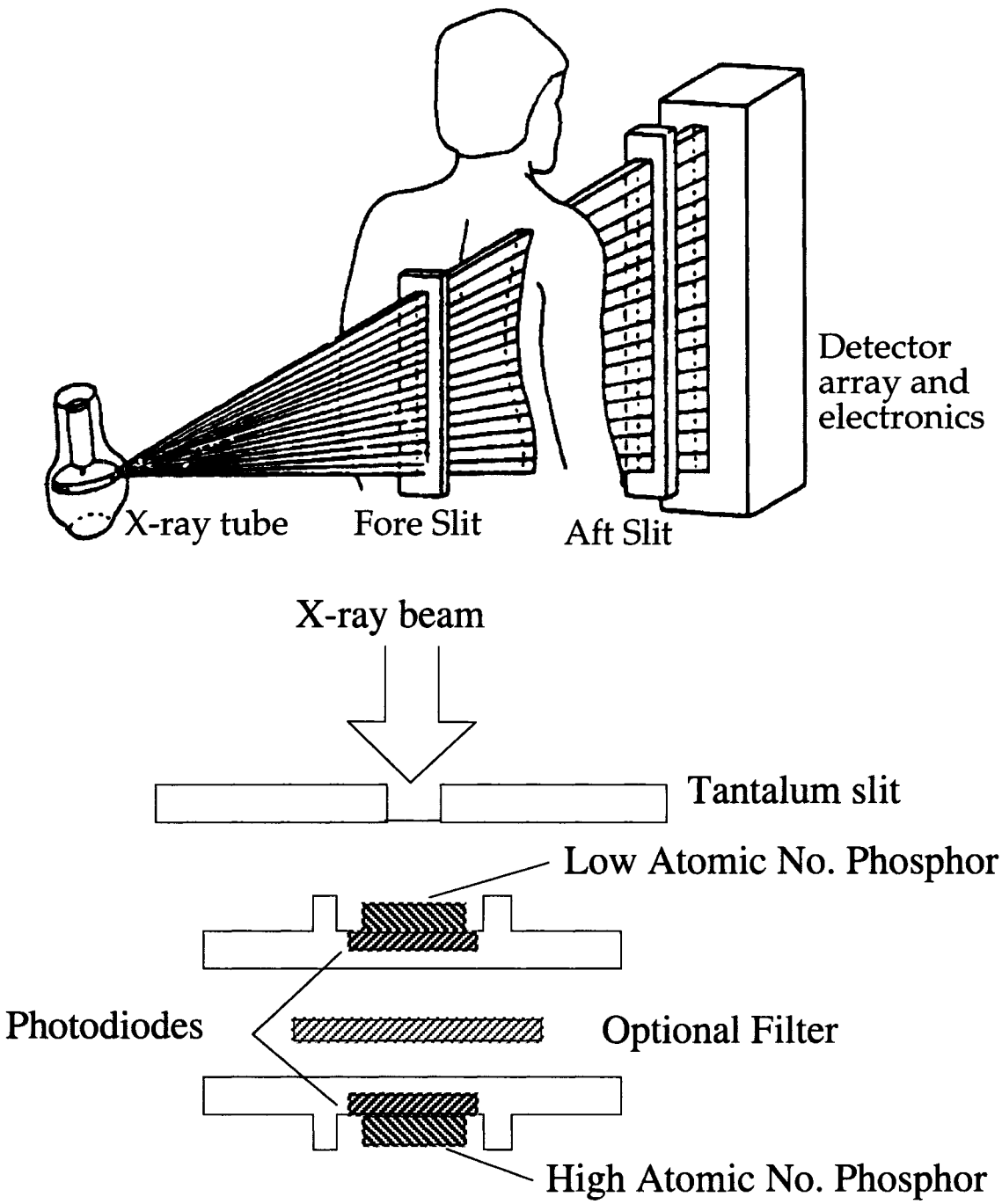

Figure 48: Dual energy fan beam scanning x-ray system. The detector array is made up of a sandwich of two linear arrays to obtain the low energy (front detector) and high energy (back detector) images.

Reproduced with permission of the copyright owner. Further reproduction prohibited without permission.

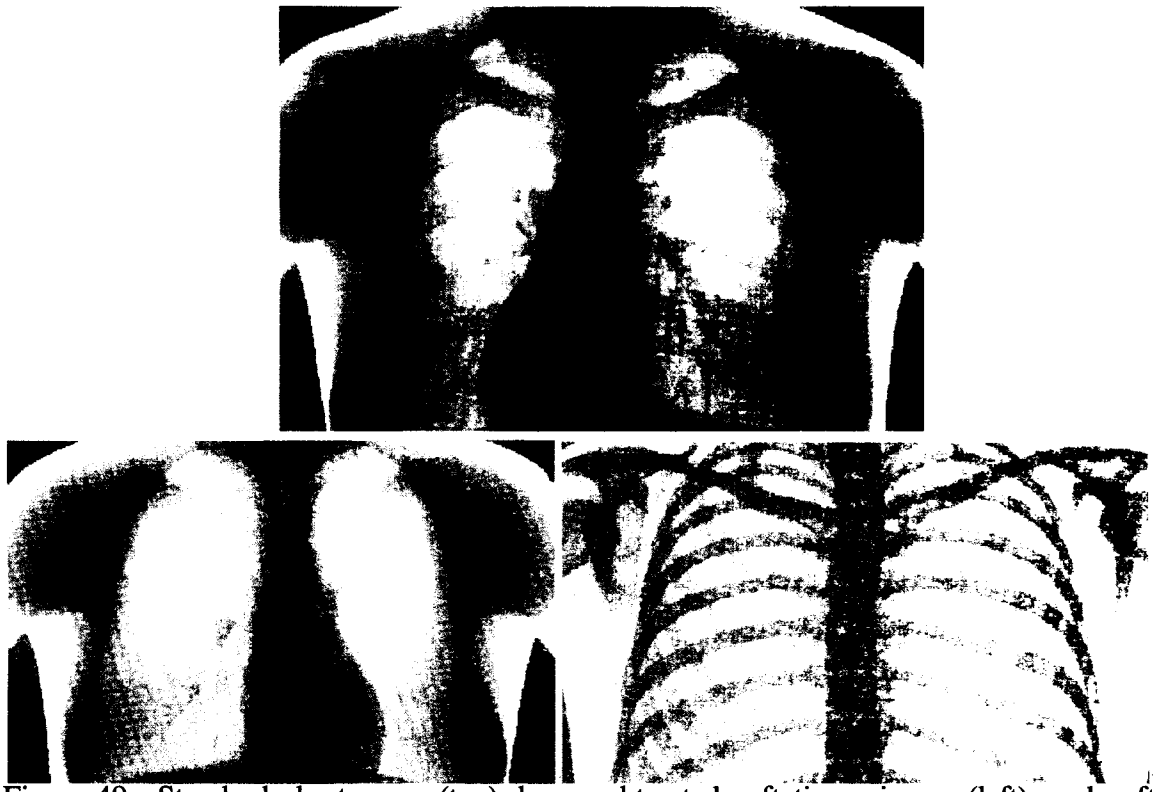

Figure 49: Standard chest x-ray (top), bone subtracted soft tissue image (left), and soft tissue subtracted bone image (right) from ref. 50.

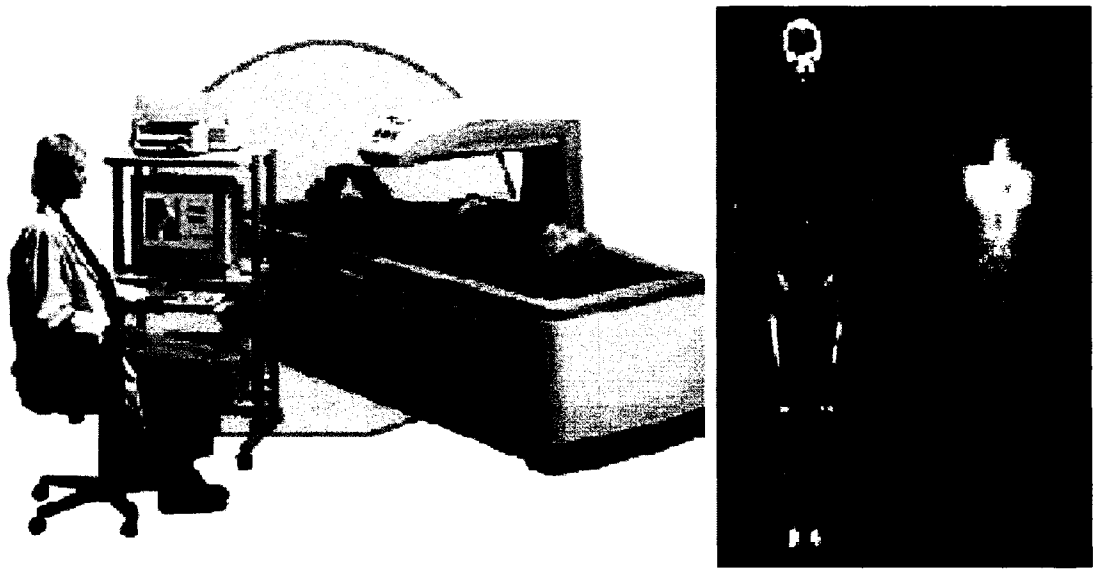

Figure 50: Dual energy bone densitometry scanner using a linear x-ray detector array (left). Results of scan (right) can show just the bones and their densities as well as fat / lean assessment from ref. 51.

Reproduced with permission of the copyright owner. Further reproduction prohibited without permission.

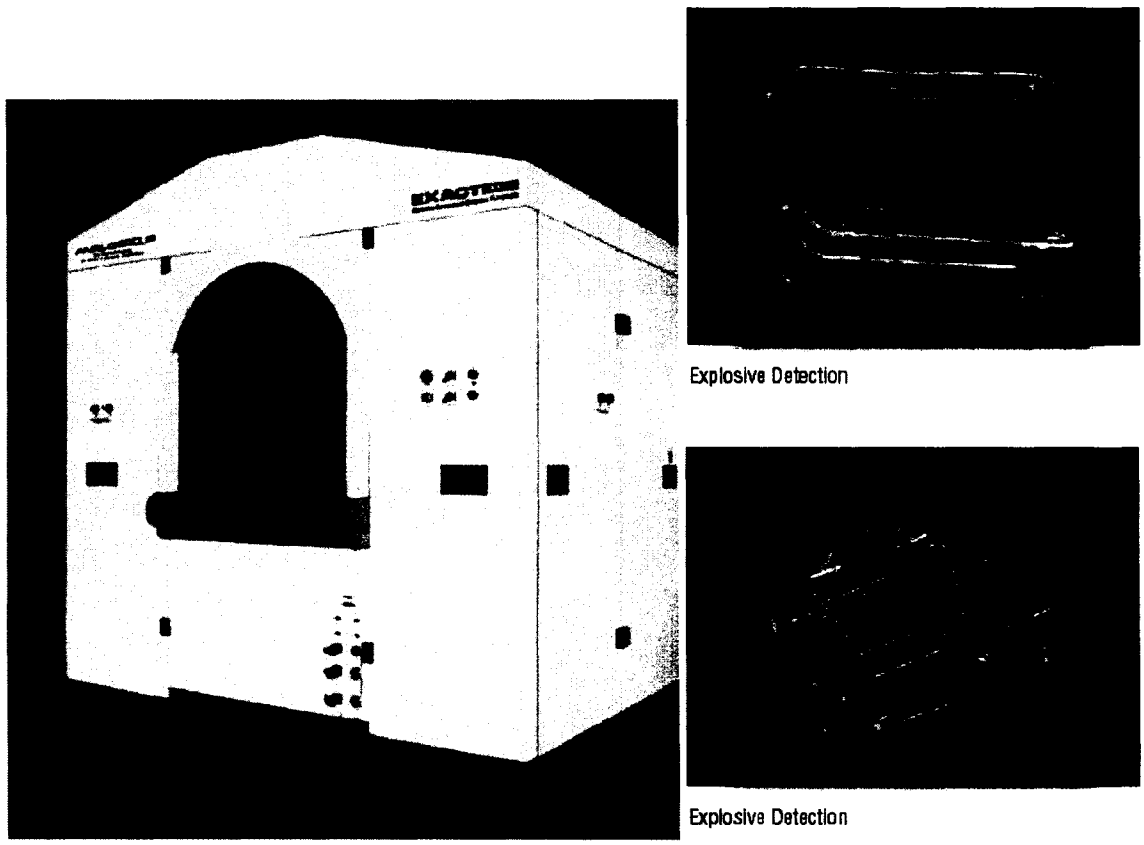

Figure 51: Images from a dual energy x-ray CT luggage scanning system being marketed by Analogic. Using dual energy, one can identify the substances in the luggage (from ref. 52).

Reproduced with permission of the copyright owner. Further reproduction prohibited without permission.

CHAPTER V

DUAL ENERGY SCANNING BEAM X-RADIOGRAPHY

Detector Development

Since only a single low resolution detector is needed to produce high resolution imaging from scanning beam x-radiography, detector development is relatively inexpensive compared to the prior art systems described in the previous chapter. The least expensive and most straight forward detector to use for this system is a dual detector using a scintillator with low x-ray stopping power in front of a high stopping power scintillator. To develop this detector the following steps were taken

1. Selection and optimization of the scintillator/absorber elements.
2. Selection of the PMTs.
3. Optimization of PMT voltage supply circuit.
4. Mechanical design / assembly.

As discussed in Chapter III, the selection of the scintillator is very important, however, one has limited choices. As seen in table 4, the scintillators which have the highest light yields yet are faster than NaI(Tl) are YAP and LSO. YAP has both a lower density and lower effective Z (39 vs. 66 for LSO) which makes it ideal for stopping the lower energy x-rays. The other low density scintillator shown on table 4, BC452 – a polyvinyltoluene (PVT, C_9H_{10}) based 5% lead loaded plastic scintillator turns out to be less appropriate than YAP due to the high Z of Pb. Figure 52 shows the absorption spectra for 200 μm YAP and 7 mm BC452 assuming a 100 keV peak x-ray source. The k-edge of the lead is seen at 88 keV thus it has significantly higher absorption of the higher energy x-rays.

Reproduced with permission of the copyright owner. Further reproduction prohibited without permission.

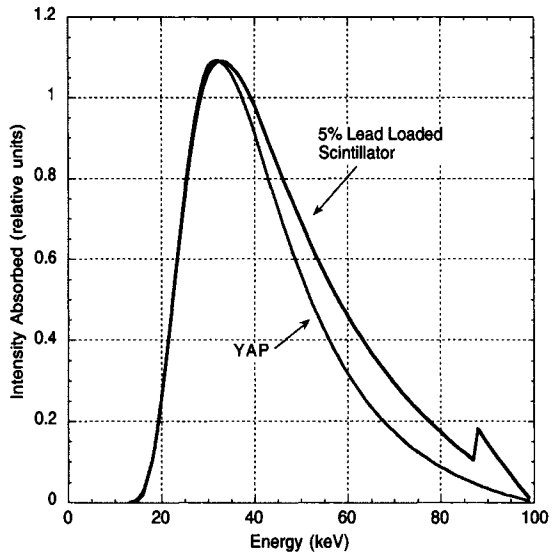

Figure 52: Absorption spectra of a 5% Pb loaded plastic scintillator and YAP.

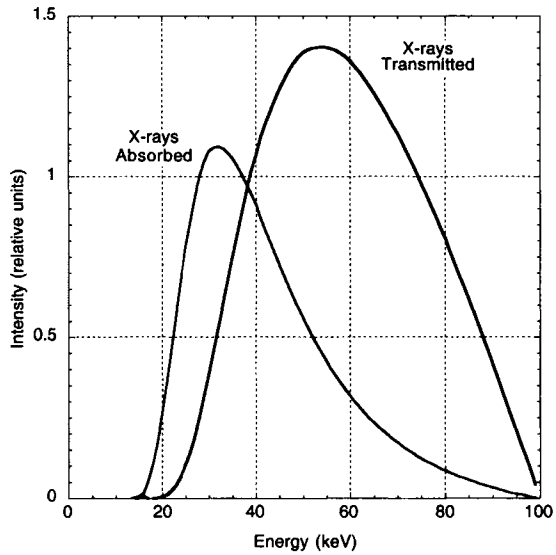

Figure 53: Absorption and transmission spectra for 200 μm thick YAP.

Having selected YAP as our lower energy scintillator, one next needs to decide how thick to make it. The thickness of the YAP controls the fraction of lower energy x-rays absorbed. Since it is a crystal of a relatively high density, it must be quite thin to allow the majority of high energy x-rays to be transmitted. Various thicknesses were simulated and it was found that 200 μm was optimal from a stopping power vs. mechanical stability point of view. Figure 53 shows the simulated absorption and transmission spectra of 200 μm YAP.

Due to its very high stopping power, high speed, and high light output, LSO is an obvious choice for the high x-ray energy detector. LSO is difficult to obtain as it was only invented in the last ten years, it is patented, and there is a high demand for it for use in medical imaging detectors. Fortunately a few 1 cm^3 samples were able to be obtained from one of the inventors, Dr. Melcher of Schlumberger-Doll Research.[53] One cm of LSO stops 99.96% of 150 keV x-rays. A second choice for the high energy scintillator is GSO. It is readily available from Hitachi Chemicals, however, some batches can exhibit an afterglow or a slow decay of the of the light output of 600 ns which causes abnormalities in the images

Reproduced with permission of the copyright owner. Further reproduction prohibited without permission.

as seen when NaI(Tl) was used. The exact cause of this problem is not known but appears to have some relationship to the Ce concentration.

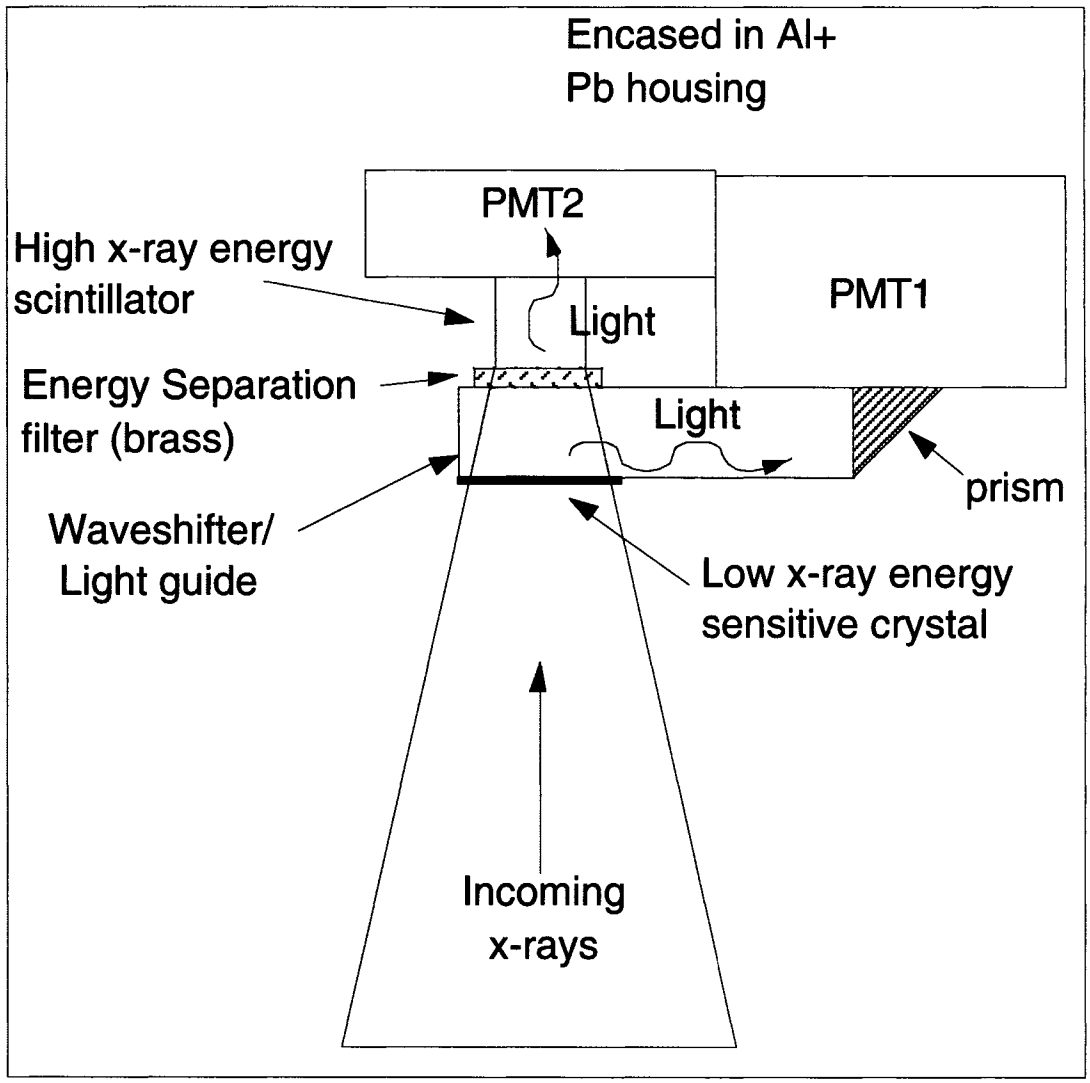

Figure 54: Mechanical configuration of the scintillators, light guide and PMTs for the dual detector dual energy system.

After the scintillators have been selected, one needs to determine how to get the light from the very thin YAP scintillator to its PMT. From previous work [54] a waveshifting or scintillator light guide appeared to be the most efficient solution. The mechanical configuration is shown in figure 54. The waveshifter absorbs the light from the YAP and emits it isotropically so that some of it can be captured by the light guide and transported to

Reproduced with permission of the copyright owner. Further reproduction prohibited without permission.

the PMT. The peak wavelength emission from YAP ranges between 347 nm to 380 nm, according to several references.[55,56,57,58] This falls in the absorption range of PVT based plastic scintillators and waveshifters from Bicron.[59] The scintillator, BC408, has an absorption peak of 345 nm and an emission peak of 420 nm while the waveshifter, BC484, has an absorption peak of 375 and an emission peak of 430. Either of these would work well as a waveshifter, however, the scintillator will also convert some of the x-rays to light. Unfortunately, according to simulations, a 1 cm thick piece of BC408 added to YAP pushes the peak x-ray absorption higher and absorbs quite a few high energy x-rays (fig. 55). The question is whether or not the waveshifter reacts to x-rays as well. An experiment was performed using the Hamamatsu R268 PMT powered by the voltage divider shown in figure 28 with three different scintillators. The x-rays were provided by a ScanRay Torrex II Fluoroscopic inspection system running at 50 keV and 1.0 mA. The scintillators tested were:

1. 46.35 X 63.37 X 10 mm thick BC408
2. 26.18 X 50.61 X 13.25 mm thick BC484[60]
3. 24.5 round X 20 mm thick CsI(Na)

The CsI(Na) scintillator was used for comparison. The scintillators were placed so that the large flat portion was against the face of the PMT (fig. 56). The output current was obtained by connecting the signal directly from the PMT anode to a Wavetek 27XT multimeter.[61] The results are shown in table 8 along with light output information provided by Bicron and the calculated relative light output to see if, very roughly, the measurements make sense, which they appear to do. From this, we see that the BC484 has practically no conversion of x-rays to light and thus is an ideal candidate for the light guide. The small signal measured by the PMT without any scintillator is likely caused by x-ray fluorescence in the glass of the PMT. The signal for BC408 is expected to be small due to lower stopping power for the x-rays than the CsI(Na).

Reproduced with permission of the copyright owner. Further reproduction prohibited without permission.

Sample	Measured PMT current (μA)	Measured relative light output (% CsI(Na))	Relative light output (% CsI(Na))
CsI(Na)	69.4	100	100
BC408	20.1	29.0	37.6
BC484	1.8	2.6	N/A
PMT alone	.9	1.3	N/A

Table 8: Results of x-ray induced light output measurements.

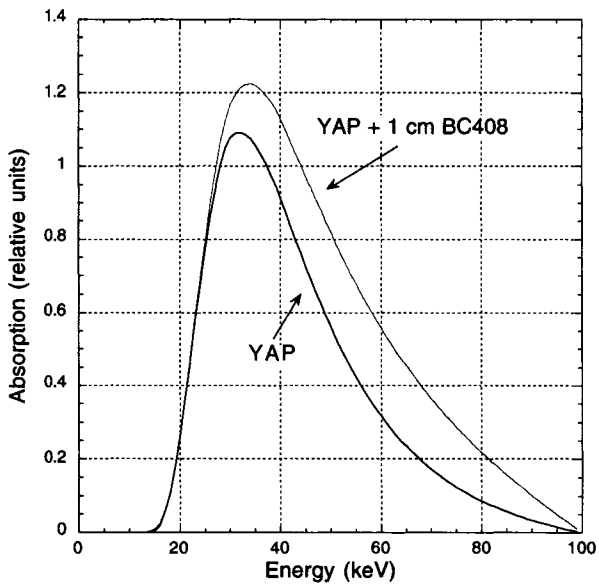

Figure 55: Absorption of 200 μm YAP verses 200 μm YAP plus 1 cm BC408.

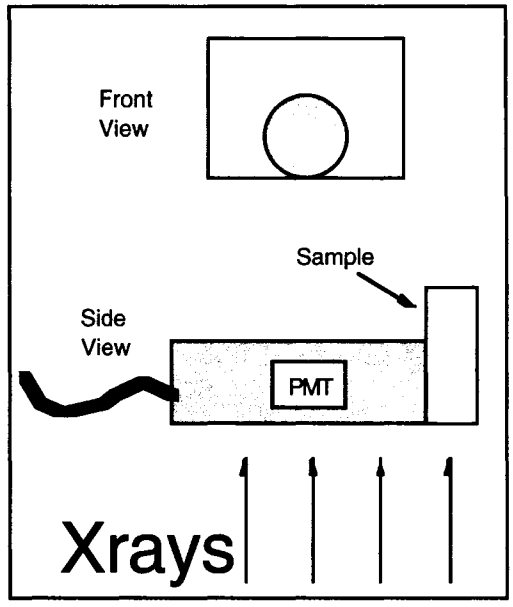

Figure 56: Experimental setup to measure response of samples to x-rays.

The YAP-waveshifter assembly is produced by coupling the YAP to the BC484 with optical grease toward one end of the waveshifter and optically gluing a prism to the other end of the waveshifter. The prism has its angled surface mirrored so even light entering at an angle which is not able to be redirected by total internal reflection is still reflected into the PMT. The entire assembly, except for the output of the prism is wrapped in white Teflon tape which has extremely good reflective properties. The prism is then coupled to the PMT with optical grease.[62] To complete the detector, the 1 ccm LSO is wrapped on 5 sides with Teflon tape. Its sides are also wrapped in lead foil, as described in chapter 4, and it is optically coupled to the second PMT with optical grease. The rest of this PMT's face is

Reproduced with permission of the copyright owner. Further reproduction prohibited without permission.

covered with 3 mm of lead shielding to prevent stray x-rays from directly interacting with the glass. To produce better energy separation a brass filter is placed between the BC484 and the LSO. Simulations performed using Photcoef showed that 0.82 mm of brass seemed to offer the best compromise between attenuating the x-ray beam too much and separating the high vs. low x-ray energy absorption peaks. The x-ray absorption for the low (YAP) and high (LSO) energy detectors are shown in figures 57 and 58 for a 100 keV x-ray voltage and in figures 59 and 60 for 120 keV x-ray voltage. The energy difference between the peaks for 100 keV is 39 keV and for 120 keV is 47 keV which, from a search of the literature, is one of the best energy separations achieved from a dual detector system and is similar to that achieved from a system switching the x-ray voltage with filtration seen above. The majority of previous systems only achieved about a 30 keV separation.

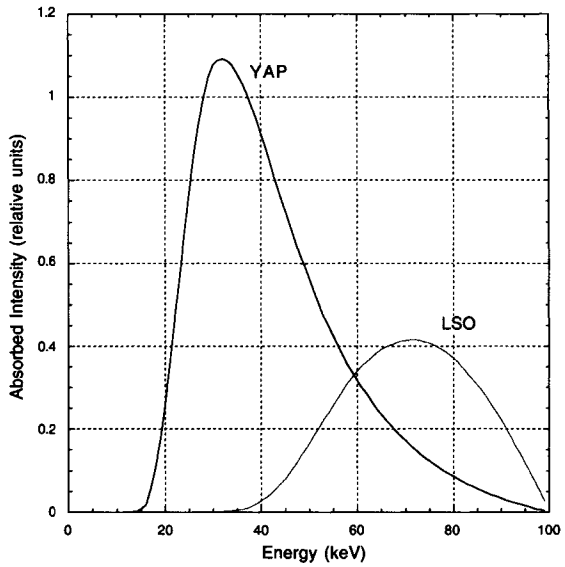

Figure 57: Absorption spectra of the low and high x-ray energy detectors for 100 keV x-ray voltage.

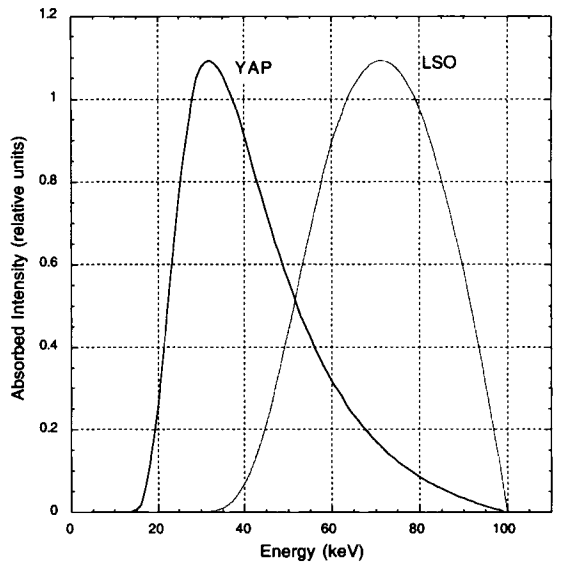

Figure 58: Same as figure 57 but with the low and high energy absorption peaks normalized.

Reproduced with permission of the copyright owner. Further reproduction prohibited without permission.

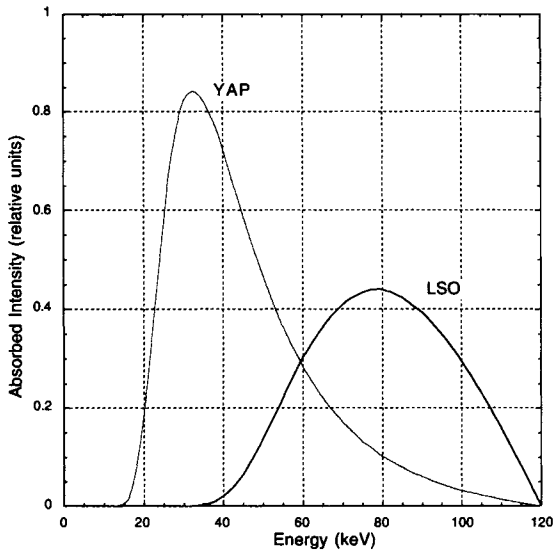

Figure 59: Absorption spectra of the low and high x-ray energy detectors for 120 keV x-ray voltage.

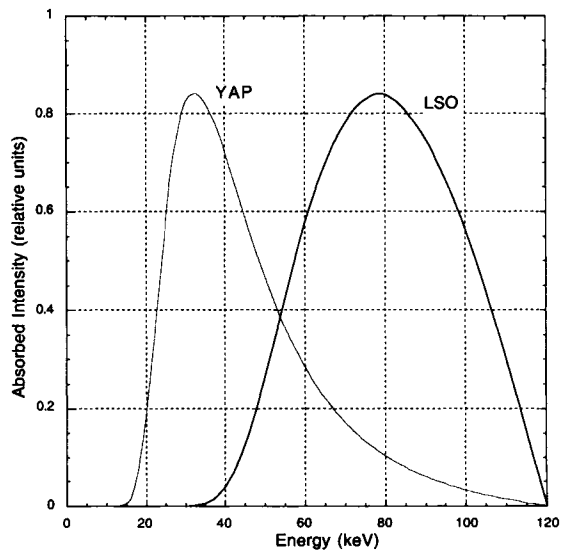

Figure 60: Same as figure 59 but with the low and high energy absorption peaks normalized.

From studies performed earlier we had identified some of the few PMTs which would work under the extreme conditions found in scanning beam x-radiography. It was found that the Electron Tubes 9125B PMT had higher gain than the Hamamatsu R268 PMT and thus it was coupled to YAP which is likely to have lower light output due to its intrinsic lower light production as well as only detecting the lower energy x-rays meaning fewer photons produced per x-ray. This particular matching of PMTs is not absolutely needed due to the overall high signal rates produced by the large number of x-rays detected. Thus we usually run the PMTs at rather low supply voltages which keeps the gain low and the anode current within acceptable limits. The FET stabilized voltage divider shown in figure 28 was used to power the PMTs

A picture of the mechanical assembly is shown in figure 61. The outer box is made of aluminum and is lined on the inside with 3 mm of lead wrapped in yellow protective tape. A square hole at the upper left end allows x-rays to enter and be absorbed by the detector assembly described above. The scintillators and light guides are held in place with red RTV sealant. The PMTs with their voltage dividers are protected inside the black plastic tubes

Reproduced with permission of the copyright owner. Further reproduction prohibited without permission.

seen in the picture and are spring loaded against their respective scintillator or light guide. The top PMT is pressed against the LSO scintillator and the bottom tube is pressed against the output from the prism. High voltage and signal cables for each detector feed through the back of the detector housing to externally mounted connectors. To insure light tightness of the housing, all holes and edges are covered with black electricians tape. For mounting purposes, a rod is screwed into one side of the housing.

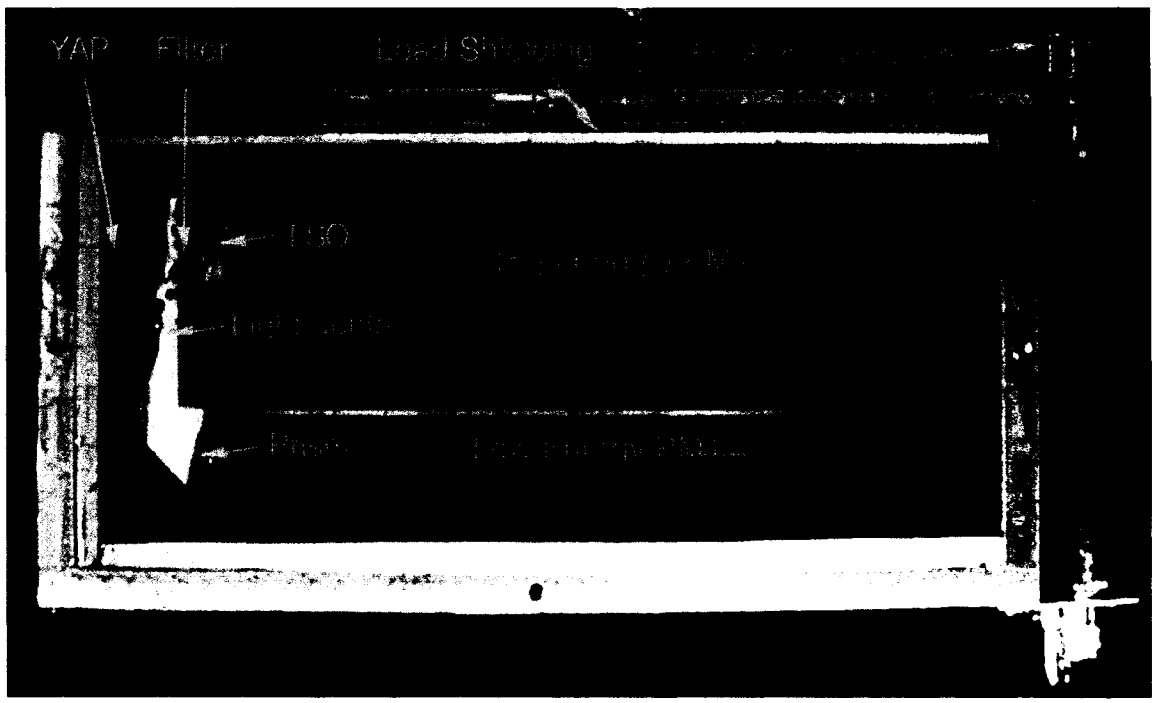

Figure 61: Picture of the two-detector dual energy sensor used in these measurements.

Detective quantum efficiency

One of the defining parameters of an imaging system is the detective quantum efficiency (DQE). The general definition of DQE is

$$\mathrm{DQE} = \frac{\text{signal recorded}}{\text{signal incident on detector}}. \qquad (5\text{-}1)$$

Reproduced with permission of the copyright owner. Further reproduction prohibited without permission.

How one applies this definition depends on the type of detector one uses. There are basically two types of detectors - integrating and single photon counting. For an integrating detector, the equation becomes

$$DQE = \frac{\left(S/N\right)^2_{out}}{\left(S/N\right)^2_{in}} \tag{5-2}$$

for signal S and noise N. For an ideal Poisson process such as the production of x-rays, the input signal to noise is just related to the number of input photons (n_{in}) as

$$\left(\frac{S}{N}\right)^2_{in} = n_{in}. \tag{5-3}$$

Similarly, the signal recorded with a detector having an efficiency of ε is

$$\left(\frac{S}{N}\right)^2_{out} = \frac{(\varepsilon n_{in})^2}{\varepsilon n_{in}}. \tag{5-4}$$

Additional noise in the system (σ_{add}) decreases the signal to noise ratio by

$$\left(\frac{S}{N}\right)^2_{out} = \frac{(\varepsilon n_{in})^2}{\varepsilon n_{in} + \sigma^2_{add}}. \tag{5-5}$$

Now, substituting equations (5-3) and (5-5) into equation (5-2) we get

$$DQE = \frac{\varepsilon^2 n_{in}}{\varepsilon n_{in} + \sigma^2_{add}}. \tag{5-6}$$

Thus, the main factors affecting the image abilities of an integrating detector are its efficiency of detecting the x-rays and the electronic noise in the system.

For a single photon counting detector there is theoretically no electronic noise to degrade the image, however, the dead time of the detector can cause counting losses (fig. 62). The type of dead time, paralyzable vs. nonparalyzable, tells one the amount of loss to expect. In both cases we assume a fixed dead time τ. For a paralyzable detector, if an event occurs during the dead time of a previous event, the dead time is extended by τ. For a nonparalyzable detector, the dead time is not extended and the detector becomes live sooner.

Reproduced with permission of the copyright owner. Further reproduction prohibited without permission.

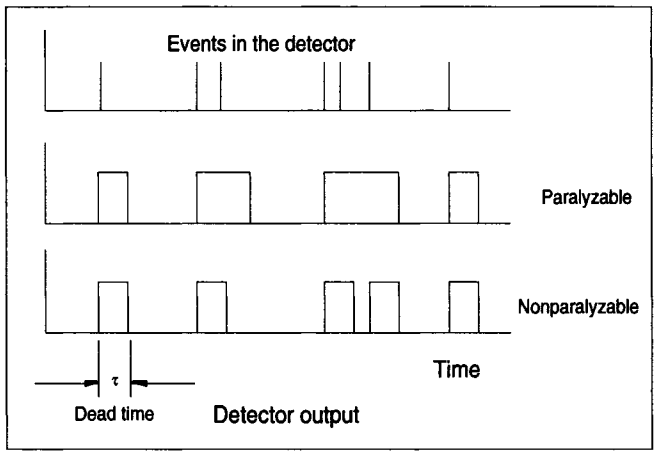

Figure 62: The dead time of a detector (τ) can cause counting losses in a single photon counting detector. The type of dead time, paralyzable vs. nonparalyzable, factors into the amount of the loss.

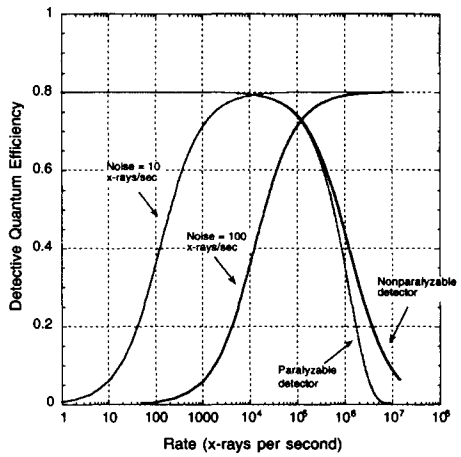

Figure 63: Examples of DQEs of various integrating and counting detectors.

The reason one might want a paralyzable detector is to make sure a previous event does not interfere with a current event as in the case of one wanting to measure pulse height of each event. To calculate the dead time losses we assume a steady state source of radiation and a long counting time so that the rates can be considered averages. For the two types of detectors we get[63]

$$m = \frac{\varepsilon n}{\varepsilon n\tau + 1} \qquad \text{Nonparalyzable detector} \qquad (5\text{-}7)$$

$$m = \varepsilon n e^{-\varepsilon n\tau}. \qquad \text{Paralyzable detector} \qquad (5\text{-}8)$$

Where n is the true count rate, m is the measured count rate, and τ is the dead time. substituting these equations into equation (5-1) we get

$$DQE = \frac{\varepsilon}{\varepsilon n\tau + 1} \qquad \text{Nonparalyzable detector} \qquad (5\text{-}9)$$

$$DQE = \varepsilon e^{-\varepsilon n\tau}. \qquad \text{Paralyzable detector} \qquad (5\text{-}10)$$

These equations do not take into account false counts where spurious noise might trigger a count or missed counts due to the signal being below the threshold of the system. To see

Reproduced with permission of the copyright owner. Further reproduction prohibited without permission.

how these equations affect the DEQ the efficiency was assumed to be 0.8, the dead time is 1 μs, and the noise was selected to be 10 photons and 100 photons per second (fig. 63). One sees that an integrating detector works best at higher x-ray exposure rates while a counting detector works best at lower rates.

In the counting measurement of x-ray flux in chapter III there was a counting loss seen at higher measurement rates. If we assume a detection efficiency of 1 and a dead time of 100 ns, the DQE according to equation (5-9) is 0.962 for an input flux of 3.9535×10^5 x-rays/s. The measured counting efficiency or DQE at this rate was 0.960. Although this DEQ is very high, it is only part of what goes into the quality of the image. The number of counts per image pixel also factors into the standard deviation one sees in the image. At this rate, one would see less than 1 count per pixel for each 2 second scan and thus it would take quite a few scans to build up an image with a low standard deviation. At the standard x-ray flux rate used during imaging, the DQE of this detector is only 0.043 (fig. 64).

In the other measurement used to estimate the x-ray flux in Chapter III, the standard deviation in an image was compared to the amount one would expect based purely on the number of x-rays theory would show hitting the detector. If we assume theory is correct and takes into account all the losses of the x-rays, then the extra amount of standard deviation would only be due to noise. The total standard deviation, σ_T, is given by

$$\sigma_T = \sqrt{\sigma_n^2 + \sigma_{add}^2} \tag{5-11}$$

where σ_n is the standard deviation due to the number of incoming x-rays and σ_{add} is the additional noise. The total standard deviation was found to be 10.5%, which, assuming 446 x-rays measured during the 2 μs dwell time for the pixel, is 47 photons. The standard deviation due to the number of x-rays is 21 which means the additional noise is equivalent to 42 photons. If we assume an efficiency of 1, the means we have a DQE of 0.20 (fig. 64). The locations of the DQEs for the different detectors on the graphs is at different rate

Reproduced with permission of the copyright owner. Further reproduction prohibited without permission.

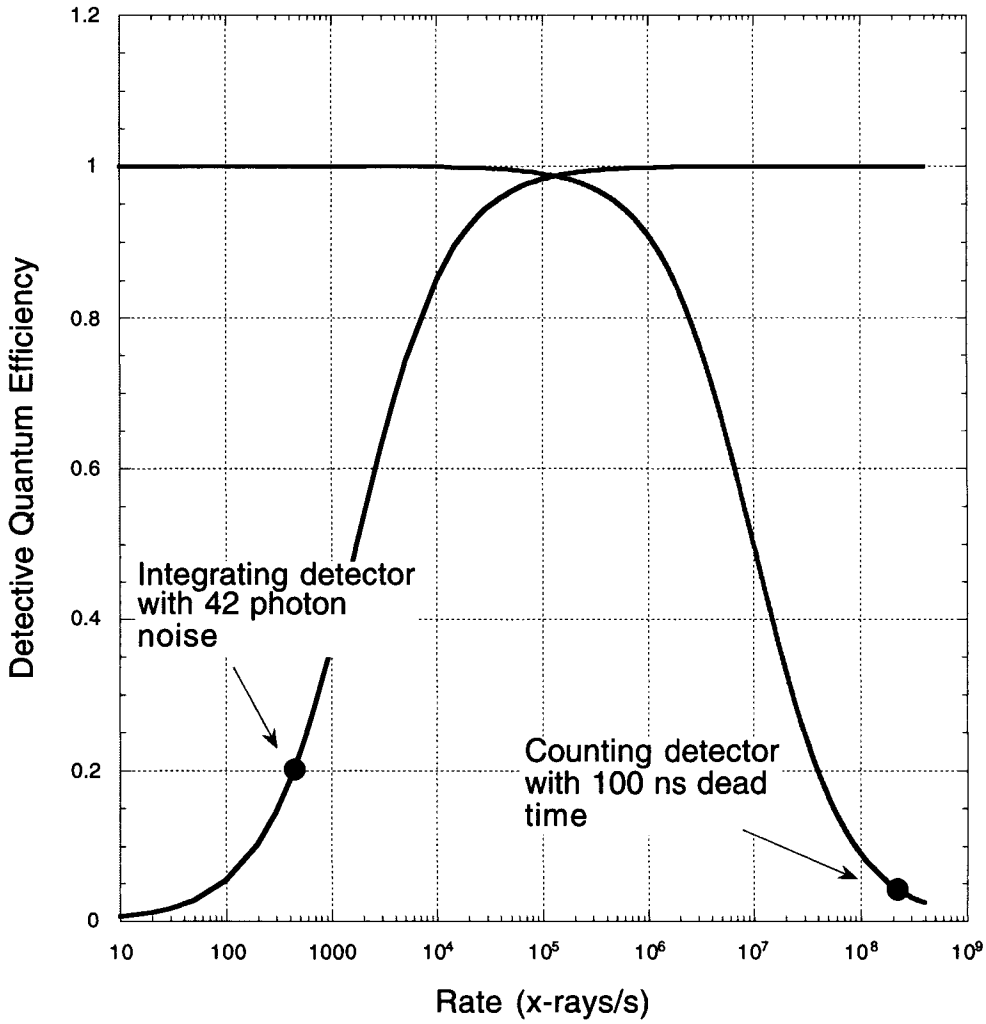

Figure 64: Comparison of DQEs for the integrating and counting detectors used in these studies.

locations because they operate very differently. The integrating detector is located at the rate of 446 because that is the number of x-rays per scan which hit the detector for that image pixel. The counting detector rate is the continuous rate since that, along with the dead time, determine how many x-rays are able to be detected. One sees that, to make improvement to the integrating detector one needs to either lower the noise or increase the number of photons delivered to the detector. To make improvements in the counting detector, one needs to increase its rate capability.

Reproduced with permission of the copyright owner. Further reproduction prohibited without permission.

Calibration

Calibration is probably one of the most difficult and most crucial parts of this technique. One must design calibration phantoms, acquire and normalize the images, and select a fitting routine which provides the best fits to the thickness of the materials. In these tests, an x-ray scattering problem was found which affects the quality of the calibration. Calibration phantoms for dual energy x-radiography usually consist of either wedges or step wedges of two different materials. For medical applications the two main materials used are acrylic (which mimics soft tissue) and aluminum (which mimics bones). For comparison to other's results, these materials were chosen to start with as well as an acrylic - copper phantom. Owing to the relatively low x-ray flux from the Digiray system, however, it is difficult to use higher Z phantoms because too few x-rays are then transmitted to the detectors.

Two different acrylic-aluminum phantoms were used, a thin version and a thick version. The thin version calibration would be most appropriate with aircraft materials which are relatively thin. The thick version calibration would be used with other industrial imaging. The thin version used 2.71 mm thick plates of acrylic and a step wedge made of 10 steps of 1.56 mm thick aluminum glued together. The thick version used 5.38 mm thick plates of acrylic and a commercial aluminum step wedge sold for testing x-ray machines which had 11 steps of approximately 3 mm each. Only the first 10 steps were used here due to the low x-ray intensity. It should be noted, however, that calibration phantoms used by others tend to be about twice as thick as these phantoms. The x-ray flux limitations from the Digiray machine tend to limit us in this respect. The acrylic – copper phantoms used 2.71 mm thick plates of acrylic with a step wedge made of 10 steps of .63 mm thick copper super glued together. Table 9 shows the thicknesses of the phantoms used.

Reproduced with permission of the copyright owner. Further reproduction prohibited without permission.

Name of phantom	Thin Al, Thin Pl		Step Al, Thick Pl		Copper, Thin Pl	
\Material Step	Acrylic	Aluminum	Acrylic	Aluminum	Acrylic	Copper
1	2.71	1.56	5.3800	4.9276	2.71	.63
2	5.42	3.12	10.760	7.9276	5.42	1.26
3	8.13	4.68	16.140	10.928	8.13	1.89
4	10.84	6.24	21.520	13.928	10.84	2.52
5	13.55	7.80	26.900	16.928	13.55	3.15
6	16.26	9.36	32.280	19.928	16.26	3.78
7	18.97	10.92	37.660	22.928	18.97	4.41
8	21.68	12.48	43.040	25.928	21.68	5.04
9	24.39	14.04	48.420	28.928	24.39	5.67
10	27.10	15.60	53.800	31.928	27.10	6.30

Table 9: Thickness (in mm) of the calibration phantoms grouped in the combinations used to perform the calibrations.

The way in which the calibration images are acquired and normalized is quite important as it will affect the quality of mathematical fit to the data and thus the ability to correctly reconstruct the images. In order to get high quality images with scanning beam x-radiography, two problems need to be solved. The first is image normalization. Since the scanning plate is flat and a small area "point" detector is used, the x-ray source to detector distance changes according to where on the scanning plate the x-rays are coming from at the moment. This is a rather large effect because of the inverse square law reduction in x-ray intensity in the cone of acceptance of the detector due to distance and not the slight extra absorption in the increased air distance. To see this effect a low energy detector was used centered 10 cm from one edge of the 25.4 cm diameter scanning plate. The distance of the detector from the scanning plate was 50 cm which, by geometry, gives one a distance of 52.3 cm from the far side of the scanning plate to the detector. Figure 65 shows the image obtained using a thick piece of lead on the plate to obtain a value for no x-rays reaching the detector. The plot in Figure 65 is a cut through the image with the "no x-ray" value subtracted from the signal. The peak value where the x-ray detector is centered is 246.52 while the value at the far edge is 225.41, which indicates an 8.5% effect. Equation (5-12) shows the inverse square law calculation in very good agreement with experiment.

Reproduced with permission of the copyright owner. Further reproduction prohibited without permission.

$$246.52 * \frac{50^2}{52.5^2} = 225.2 \qquad (5\text{-}12)$$

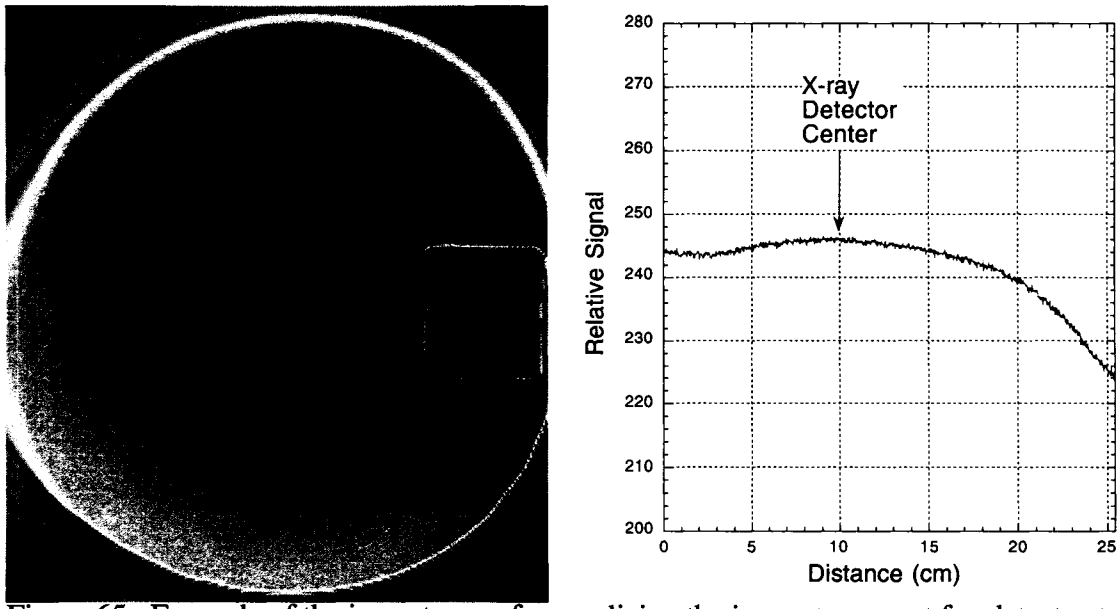

Figure 65: Example of the importance of normalizing the image to correct for detector to x-ray source distance. The image (left) is a background scan with a thick piece of lead. The plot on the right is a profile cut across the scanning plate. There is an 8.5% difference from the center of the detector to the far edge.

Another problem which must be handled by the normalization routine is that, over time, the system is not perfectly stable. Thus one needs to correct for changing offsets from the detectors and different intensities from the x-ray system. This was solved by taking a sample image and a background image in which both have an area in the image where all the x-rays are stopped by an absorber (offset) and an area where none of the x-rays are stopped (air).[64] The sample image contains the sample being imaged while the background image is the same image without the sample. The normalized image is then calculated using the formula

$$\text{Normalized Image}(x,y) = \frac{(\text{Sample}(x,y) - \text{offset1}) * (\text{air2} - \text{offset2})}{(\text{Background}(x,y) - \text{offset2}) * (\text{air1} - \text{offset1})} \qquad (5\text{-}13)$$

Thus the offset measurements correct for detector variations, the air measurements correct for x-ray intensity variations, and the background image corrects for the intensity variation

Reproduced with permission of the copyright owner. Further reproduction prohibited without permission.

caused by detector to source distance changes. Using this method, thickness variations of aluminum have been measured to within 2%. The results of this correction are shown in figure 66 for a low x-ray energy image of an aluminum step wedge where we see "Air" section flattens out considerably.

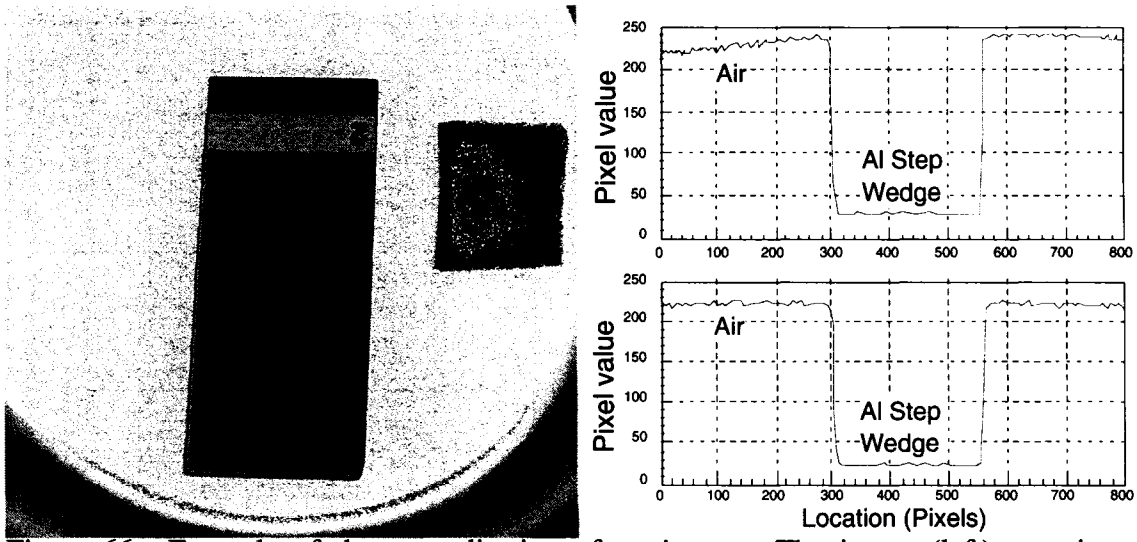

Figure 66: Example of the normalization of an image. The image (left) contains an aluminum step wedge and a thick piece of lead. The plots are a profile cut across the 7th step of the wedge before normalization (upper) and after normalization (lower).

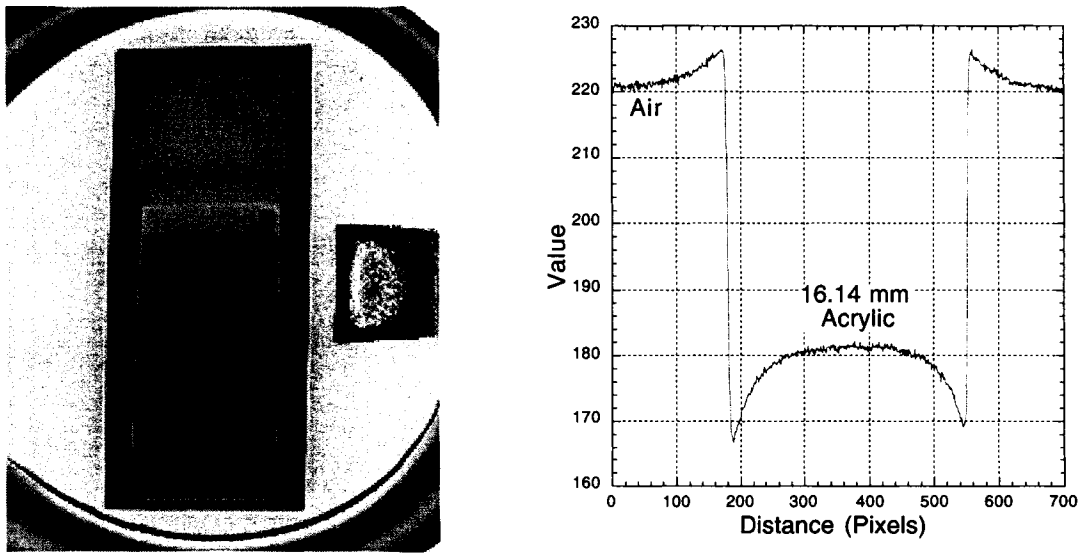

Figure 67: Image (left) of 16.14 mm of acrylic with aluminum step wedge and a profile cut (right) across the plastic showing x-ray scatter near the edges.

Reproduced with permission of the copyright owner. Further reproduction prohibited without permission.

A second problem appears to be related to scattering. Figure 67 shows the normalized low x-ray energy image of a 16.1 mm thick piece of acrylic with an aluminum step wedge sitting on it and a plot of a profile cut horizontally across the acrylic part towards the top of the image. Note the increase in the detected x-rays just before the x-ray beam reaches the acrylic in the "Air" area. Scattering from the edge of the acrylic also seems to affect the beam when it goes through the acrylic causing a loss of x-rays near the edge. Geometrical effects, i.e. x-rays travel through differing thicknesses of acrylic on their way to the detector due to detector to x-ray source differences as seen above, were ruled out as the cause as this would only amount to a 0.2% effect at 30 keV, the peak absorption of the low energy detector. We see an effect 10 times larger. Geometrical effects also would not explain why we see an increase in signal before the x-ray reaches the object.

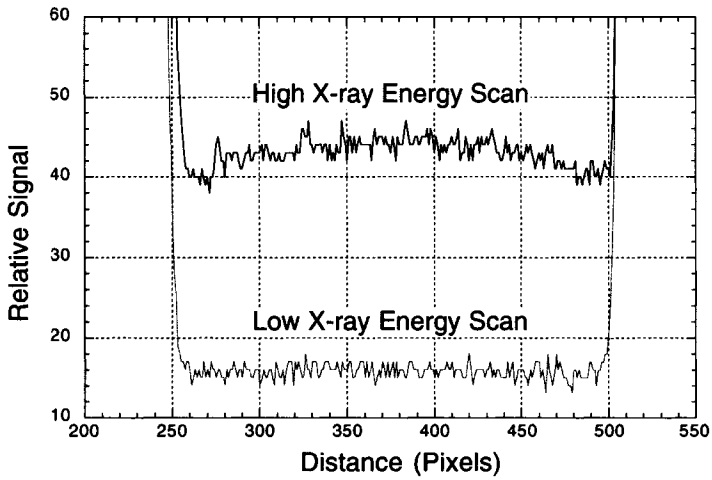

Figure 68: Profile cut across the high and low x-ray energy images of one step of the aluminum step wedge.

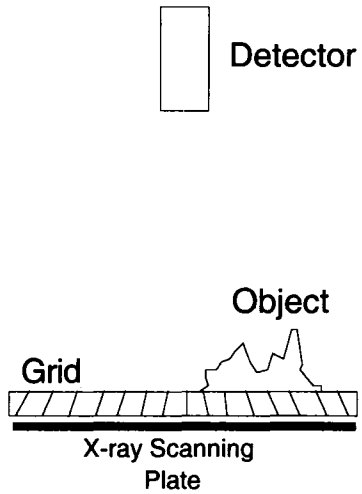

Figure 69: Diagram of scanning beam x-radiography setup using an anti-scatter grid.

A clue was found when one compares the low versus high energy x-ray images with the aluminum step wedge. If one looks at figure 66 one barely sees this effect in the lower graph. Figure 68 shows a comparison of the same scan between the high and low energy x-ray detectors. The effect is clearly visible on the high energy image but not on the low energy image. If one looks back at figures 8 and 9 one sees that, at 30 keV for acrylic,

Reproduced with permission of the copyright owner. Further reproduction prohibited without permission.

Compton scattering makes up about 60% of the attenuation while it only makes up 13% for aluminum. At 70 keV, the peak absorption energy of the high energy detector, Compton scattering makes up 67% of the attenuation for aluminum. One saw earlier that the x-rays from the Digiray system come out over wide angles (up to +/- 45°). Now, if one looks at figure 11 one sees that, at 100 keV, Compton scatter is quite significant even out to 45°. The x-rays are scattering off the objects and into the detector based on their Compton scattering component. Also, at 45°, the fraction of energy retained by the scattered photon at these energies is nearly the same as the incoming photon and thus impossible to distinguish with our detector system.

Compton scattering makes dual energy calibration more difficult. Due to these enhanced edges, one must measure the attenuation of the materials as far from the edges as possible in order to get the correct values. Also, the normalization routine can be tainted if the object is low Z and tall, which increases scatter from areas in which one measures the "Air" value. There are two solutions to this problem. The first is to make large but thin calibration phantoms to obtain a large number of thickness sample points for the fitting routine. That requires one to take many calibration images due to the limited size of the imaging area.

The second solution is to use an anti-scatter grid between the x-ray tube and the object (fig. 69). This grid only transmits those x-rays traveling towards the detectors so that wide angle x-rays that scatter off of the objects and into the detector are eliminated. Anti-scatter grids are used for medical purposes to keep scatter from the patient from reaching the film. Usually these are made of very thin lead strips with aluminum interspacers on the order of 100 strips per inch. For mammography, which uses relatively low energy x-rays (~30keV), some grids were developed with low Z fiber interspacers, however, these do not appear to be manufactured any longer. Fiber interspaced grids would be preferable in this work so that we do not attenuate our lower energy x-rays significantly. Most

Reproduced with permission of the copyright owner. Further reproduction prohibited without permission.

mammography grids today use aluminum interspacers with the lead strips angled in a focusing manner pointing towards the x-ray source. These usually have a grid ratio (the ratio of height to width of the openings between the lead strips) of 5. To see if and how well this enhances the image, a focusing grid was acquired from Soyee products.[65] This grid is aluminum interspaced 14"x17" with 85 strips per inch, a grid ratio of 6:1, and a focal distance of 34 to 44 inches. Comparisons were made between a 5.38mm thick sheet of acrylic alone, the plastic sheet sitting on top of the focusing grid, and the plastic sheet sitting on top of a sheet of aluminum of the same thickness as the focusing grid. (fig. 70). The aluminum sheet was use to see if there was any effect caused by filtering out the lower energy x-rays by the aluminum interspacers. As one can see, the focusing grid greatly improves the image.

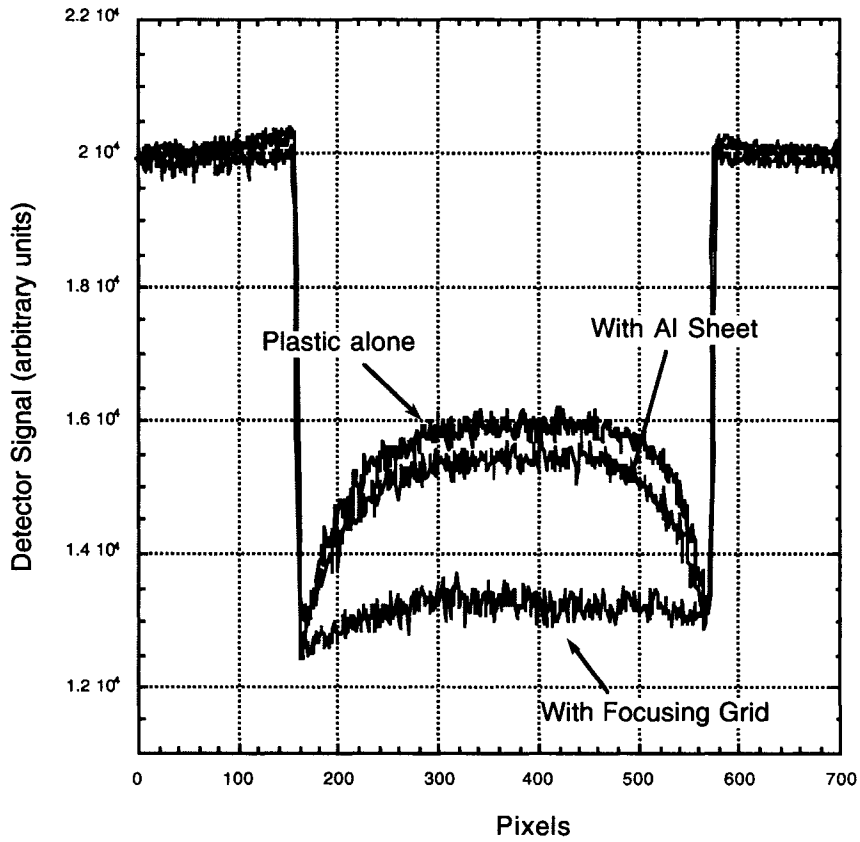

Figure 70: Comparison of profile cuts across a 5.38mm thick acrylic sheet alone, and sitting on top of an aluminum sheet, and a focusing grid with 100 keV x-rays.

Reproduced with permission of the copyright owner. Further reproduction prohibited without permission.

Once the calibration images have been acquired and normalized, the next step is to extract and fit the data. The extraction is performed by measuring the transmission values for each acrylic-aluminum or acrylic-copper combination. This is performed by measuring the pixel values in the image using a graphics program. The logarithms of these values are then used in a fitting routine to match the high and low x-ray energy transmission values to the thicknesses of the materials. The selection of the fitting routine has a great impact on how well one is able to determine the thickness of the calibration materials and thus how well one can perform substance identification. Two of the fitting routines described in Chapter IV were tried with the variety of fitting equations shown below.

Linear fit equations:

$$B_{1,2} = a_0*M_l + a_1*M_h + a_2*M_l^2 + a_3*M_l*M_h + a_4*M_h^2 + a_5*M_l^3 + a_6*M_l^2*M_h + a_7*M_l*M_h^2 + a_8*M_h^3 \quad (5\text{-}14)$$

$$B_{1,2} = a_0 + a_1*M_l + a_2*M_h + a_3*M_l^2 + a_4*M_l*M_h + a_5*M_h^2 + a_6*M_l^3 + a_7*M_l^2*M_h + a_8*M_l*M_h^2 + a_9*M_h^3 \quad (5\text{-}15)$$

$$B_{1,2} = a_0*M_l + a_1*M_h + a_2*M_l^2 + a_3*M_l*M_h + a_4*M_h^2 + a_5*M_l^3 + a_6*M_l^2*M_h + a_7*M_l*M_h^2 + a_8*M_h^3 + a_9*M_h^4 + a_{10}*M_l^3*M_h + a_{11}*M_l^2M_h^2 + a_{12}*M_l*M_h^3 + a_{13}*M_h^4 \quad (5\text{-}16)$$

$$B_{1,2} = a_0 + a_1*M_l + a_2*M_h + a_3*M_l^2 + a_4*M_l*M_h + a_5*M_h^2 + a_6*M_l^3 + a_7*M_l^2*M_h + a_8*M_l*M_h^2 + a_9*M_h^3 + a_{10}*M_h^4 + a_{11}*M_l^3*M_h + a_{12}*M_l^2M_h^2 + a_{13}*M_l*M_h^3 + a_{14}*M_h^4 \quad (5\text{-}17)$$

Conic fit equations:

$$B_{1,2} = \frac{F}{G} \quad (5\text{-}18)$$

$$B_{1,2} = \frac{\sqrt{G^2 + 4*H*F} - G}{2 * H} \quad (5\text{-}19)$$

where

Reproduced with permission of the copyright owner. Further reproduction prohibited without permission.

$$F = f_0 + f_1*M_l + f_2*M_h + f_3*M_l^2 + f_4*M_l*M_h + f_5*M_h^2 \quad (5\text{-}20a)$$

$$G = 1 + g_1*M_l + g_2*M_h \quad (5\text{-}20b)$$

$$H = h_0 \quad (5\text{-}20c)$$

Cubic fit equations:

$$B_{1,2} = \frac{F}{G} \quad (5\text{-}21)$$

$$B_{1,2} = \frac{\sqrt{G^2 + 4*H*F} - G}{2 * H} \quad (5\text{-}22)$$

where

$$F = f_0 + f_1*M_l + f_2*M_h + f_3*M_l^2 + f_4*M_l*M_h + f_5*M_h^2 + f_6*M_l^3 + f_7*M_l^2*M_h + f_8*M_l*M_h^2 + f_9*M_h^3 \quad (5\text{-}23a)$$

$$G = 1 + g_1*M_l + g_2*M_h + g_3*M_l^2 + g_4*M_l*M_h + g_5*M_h^2 \quad (5\text{-}23b)$$

$$H = h_0 + h_1*M_l + h_2*M_h \quad (5\text{-}23c)$$

As in the last chapter, B_1 and B_2 are the thicknesses of the two calibration materials and M_l and M_h are the logarithmic transmission measurements.

The linear equations were fit using a least square fitting routine based on singular value decomposition.[66] The conic and cubic equations were fit with the Levenberg-Marquardt algorithm. This iterative algorithm tends to be among the best for non-linear fitting due to its robustness and rate of convergence, however, there are many different implementations of it and some result in better fits than others. One of the better implementations is in the book by Reich.[67] The disadvantage of using this fitting routine is the requirement of supplying starting values for the fitting parameters. The generally suggested way to obtain these starting values is to minimize the linear least squares sum:

$$\sum(F - G*B_{1,2} - H*B_{1,2}) = \min \quad (5\text{-}24)$$

which can be done analytically in closed form.[41] The difficulty, however, comes when one tries then iteratively to fit using equations (5-19) and (5-22). It is quite easy for the radical

Reproduced with permission of the copyright owner. Further reproduction prohibited without permission.

to converge to an imaginary number during fitting. Even proper starting values will sometimes cause the quantity under the radical sign to become negative. It would appear that this problem tends to be dependent on the noise in the image. As a test of the algorithms, the data used by Cardinal and Fenster[41] was duplicated and nearly identical results were achieved. The data they used, however, were simulated and had very little noise. As mentioned before, our x-ray intensity is rather low and thus the images are much noisier. This hypothesis is supported by the fact that the high Z material was able to be fit with equation (5-19) when the phantoms were thin and lower Z thus allowing higher x-ray flux. The low Z material was not able to be fit with (5-19) at all. It is well known that the low Z fits are more difficult due to less contrast between the steps. Table 10 and 11 shows the RMS results for the different fitting routines using the phantoms from table 9. Two separate measurements were made with the Thin Al / Thin Pl phantom to check consistency. Also fits were made to the average measured values of the two Thin Al / Thin Pl measurements and to the combined data from the average Thin Al / Thin Pl values and Step Al / Thick Pl values. The best fitting result came from using the Copper/Thin Pl phantom with fitting equation (5-21) (figs 71 and 72), although, due to the higher attenuation of the lower energy x-rays, only the first 6 steps could be used for calibration. Figure 87 shows a profile cut along the copper step wedge from the low energy detector image. The upper steps are quite non-linear. Fitting equation (5-18) produced a very poor result with the acrylic and the results are shown in figure 73. There was only one case where equation (5-19) produced the best fit as shown in figure 74. In general, however, the linear fitting equation (5-17) produced consistently good results and, since it is a linear fit, it is fast, stable, and does not require initial fit parameters. Figures 75 through 86 show the results for all the phantoms using fitting equation (5-17). There were only minor differences between the first and second calibration measurements with the Thin Al/ Thin Pl phantom thus showing the calibrations to be reasonably consistent. The averaged Thin Al/ Thin Pl

Reproduced with permission of the copyright owner. Further reproduction prohibited without permission.

data gave average results. The combined Thin Al / Thin Pl and Step Al / Thick Pl gave the worst results which is likely due to the Compton scattering problem as described above that problem is much worse in the Thin Al/ Thin Pl case. Figure 88 shows a profile cut along the Thin Al phantom from the high energy detector image after normalization. One can see that some of the steps almost make up a saw tooth pattern which seriously affects the calibration. Figure 89 is the same profile cut from the low energy detector image showing the expected regular step pattern and figure 90 is the image from the high energy detector of the Step Al phantom. The thicker steps of the Step Al phantom greatly reduce the amount of Compton scattering. In all cases during these calibrations, the x-ray system was operated at 125 keV and 0.5 mA. The images of the phantoms were made up of the sum of 50 scans at 4 seconds per scan.

Fitting equation \ phantom	Thin Al Thin Pl	Thin Al2 Thin Pl2	Com Thin Al Com Thin Pl	Step Al Thick Pl	Copper Thin Pl	Thin+Step Al Thin+thick Pl
9 param linear (5-14)	0.37874	0.39673	0.38504	0.28530	0.03022	0.82932
10 param linear (5-15)	0.37019	0.38391	0.37453	0.27390	0.03009	0.81182
14 param linear (5-16)	0.27117	0.26948	0.26660	0.19086	0.02702	0.73730
15 param linear (5-17)	0.26919	**0.26749**	**0.26455**	**0.18935**	0.02700	0.73630
8 param A/B (5-18)	0.26496	0.28872	0.27120	0.47364	0.04366	1.34495
9 param sq rt. (5-19)	**0.26222**	0.28628	0.27107	Bad	Bad	Bad
15 param A/B (5-21)	0.41526	0.30073	0.29989	0.29890	**0.02021**	**0.69455**
18 param sq rt (5-22)	Bad	Bad	Bad	Bad	Bad	Bad

Table 10: RMS error in mm in the fitting results of the thickness of either the Copper or Aluminum in the different phantoms with different fitting equations. The bold faced numbers are the best results.

Fitting equation \ phantom	Thin Al Thin Pl	Thin Al2 Thin Pl2	Com Thin Al Com Thin Pl	Step Al Thick Pl	Copper Thin Pl	Thin+Step Al Thin+thick Pl
9 param linear (5-14)	2.06700	2.20032	2.11796	1.24061	0.93511	2.34691
10 param linear (5-15)	1.99701	2.07287	2.02148	1.19165	0.91332	2.34439
14 param linear (5-16)	1.41495	1.40371	1.38935	0.84462	0.67420	2.28083
15 param linear (5-17)	**1.41140**	**1.40321**	**1.38748**	**0.84421**	0.66832	**2.27874**
8 param A/B (5-18)	2.99812	3.05975	3.01873	1.30549	3.15107	4.68466
9 param sq rt. (5-19)	Bad	Bad	Bad	Bad	Bad	Bad
15 param A/B (5-21)	1.70334	1.42926	1.51507	1.20439	**0.61253**	2.32767
18 param sq rt (5-22)	Bad	Bad	Bad	Bad	Bad	Bad

Table 11: RMS error in mm in the fitting results of the thickness of Acrylic in the different phantoms with different fitting equations. The bold faced numbers are the best results.

Reproduced with permission of the copyright owner. Further reproduction prohibited without permission.

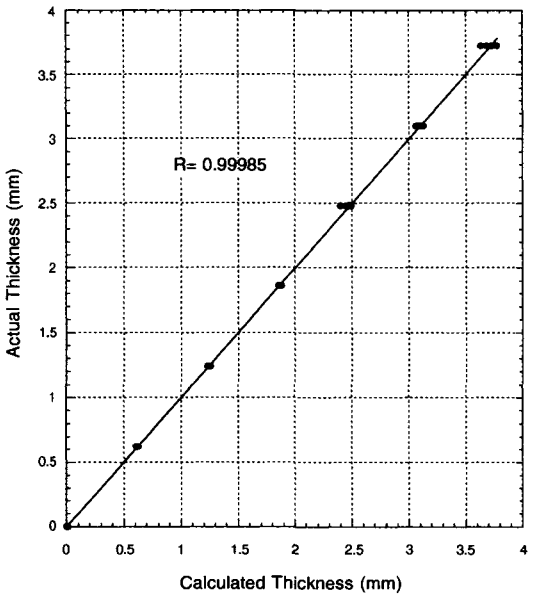

Figure 71: Calculated vs. Actual thickness of Copper based on the Copper / Thin Pl phantom using fitting equation (5-21).

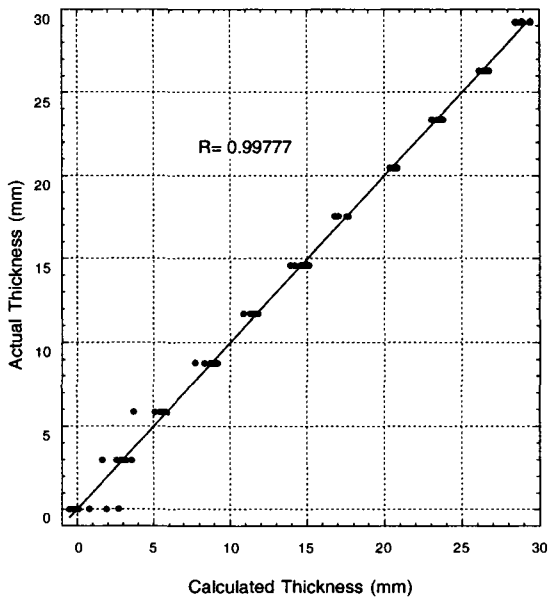

Figure 72: Calculated vs. Actual thickness of Acrylic based on the Copper / Thin Pl phantom using fitting equation (5-21).

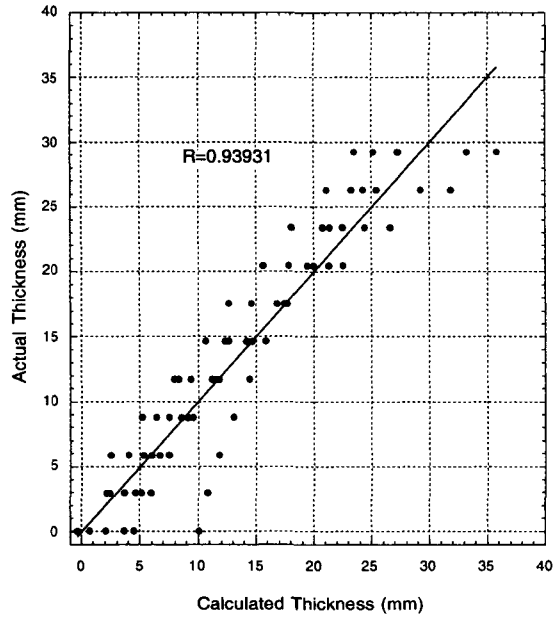

Figure 73: Calculated vs. Actual thickness of Acrylic based on the Copper / Thin Pl phantom using fitting equation (5-18) showing a very poor fit.

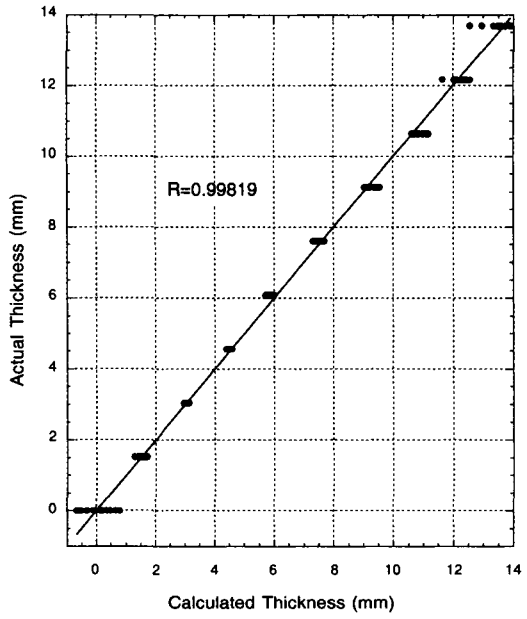

Figure 74: Calculated vs. Actual thickness of Aluminum based on the Thin Al / Thin Pl phantom using fitting equation (5-19).

Reproduced with permission of the copyright owner. Further reproduction prohibited without permission.

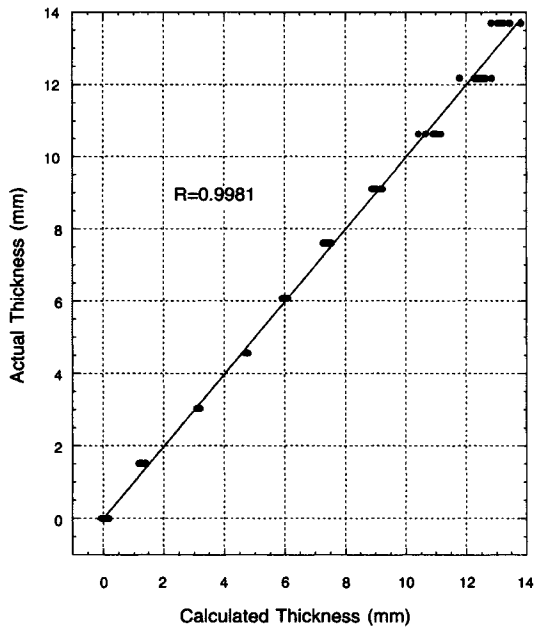

Figure 75: Calculated vs. Actual thickness of Aluminum based on the Thin Al / Thin Pl phantom using fitting equation (5-17).

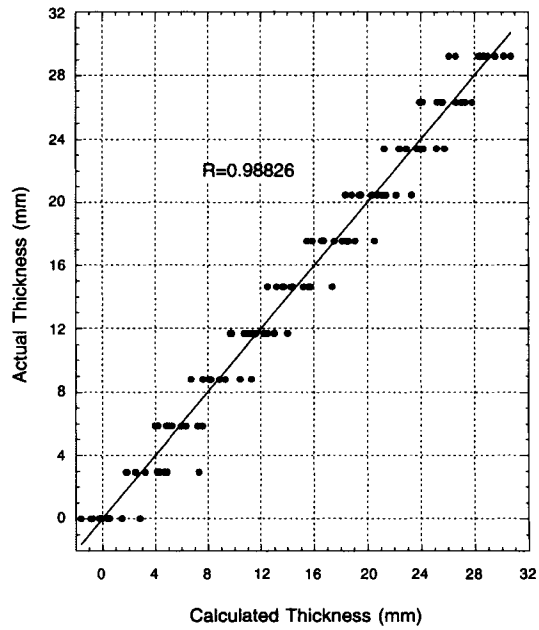

Figure 76: Calculated vs. Actual thickness of Acrylic based on the Thin Al / Thin Pl phantom using fitting equation (5-17).

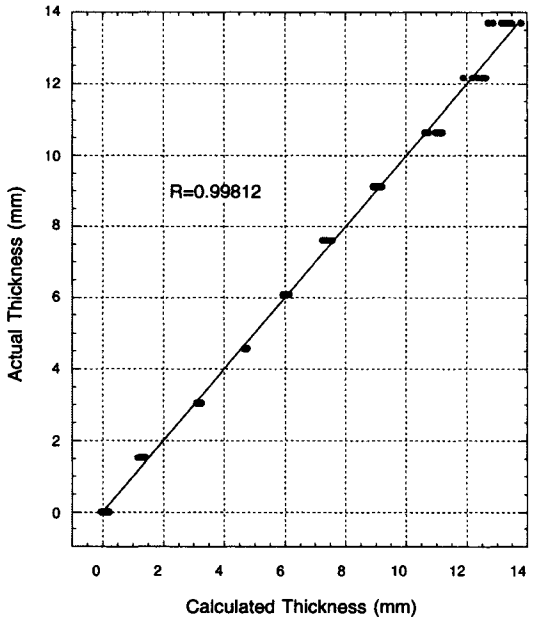

Figure 77: Calculated vs. Actual thickness of Aluminum based on the Thin Al / Thin Pl phantom using fitting equation (5-17) on a second calibration.

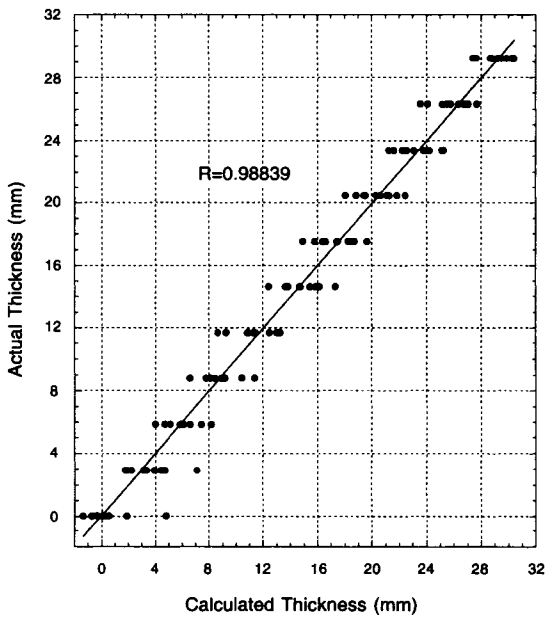

Figure 78: Calculated vs. Actual thickness of Acrylic based on the Thin Al / Thin Pl phantom using fitting equation (5-17) on a second calibration.

Reproduced with permission of the copyright owner. Further reproduction prohibited without permission.

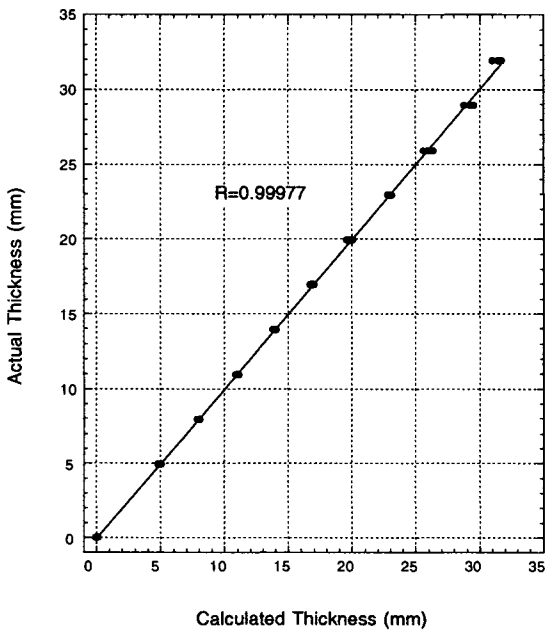

Figure 79: Calculated vs. Actual thickness of Aluminum based on the Step Al / Thick Pl phantom using fitting equation (5-17).

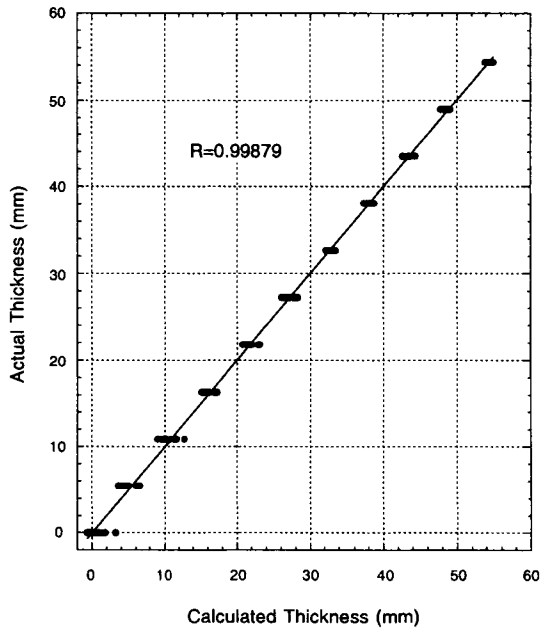

Figure 80: Calculated vs. Actual thickness of Acrylic based on the Step Al / Thick Pl phantom using fitting equation (5-17).

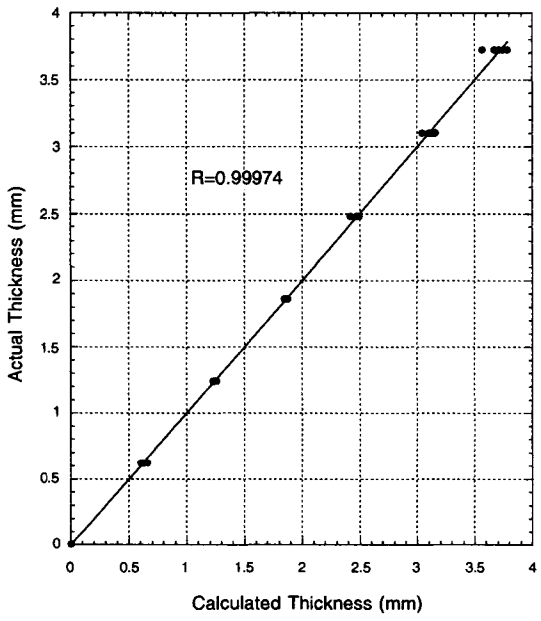

Figure 81: Calculated vs. Actual thickness of Copper based on the Copper / Thin Pl phantom using fitting equation (5-17).

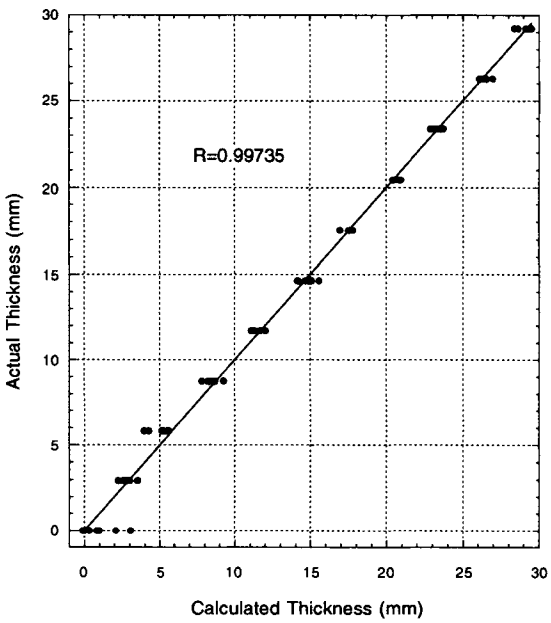

Figure 82: Calculated vs. Actual thickness of Acrylic based on the Copper / Thin Pl phantom using fitting equation (5-17).

Reproduced with permission of the copyright owner. Further reproduction prohibited without permission.

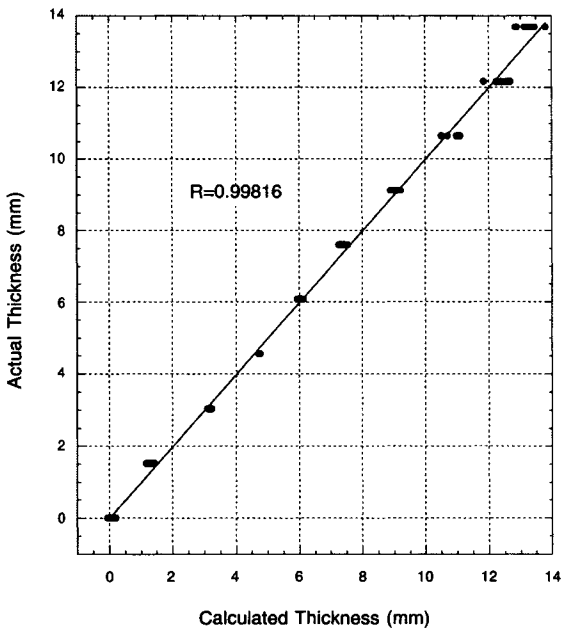

Figure 83: Calculated vs. Actual thickness of Aluminum based on the combined Thin Al / Thin Pl phantom data runs using fitting equation (5-17).

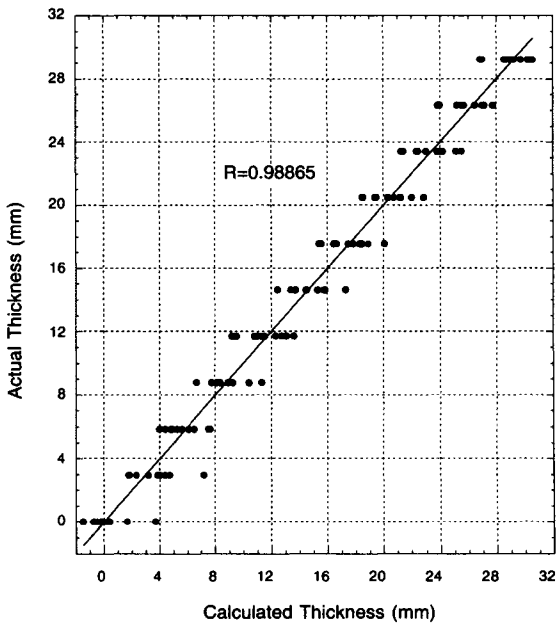

Figure 84: Calculated vs. Actual thickness of Acrylic based on the combined Thin Al / Thin Pl phantom data runs using fitting equation (5-17).

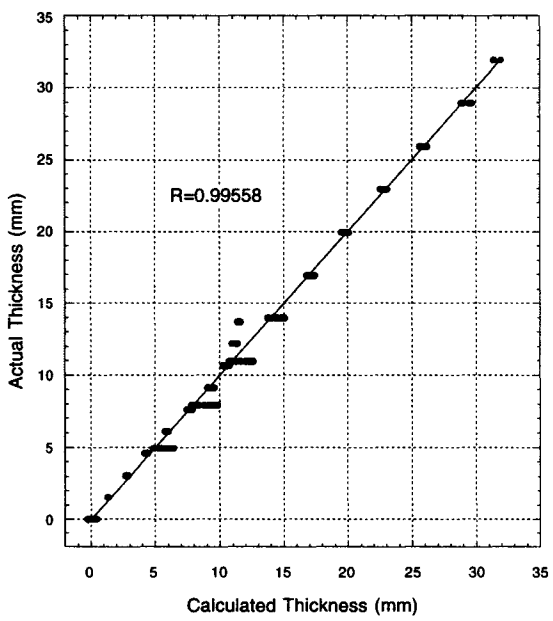

Figure 85: Calculated vs. Actual thickness of Aluminum based on the combined Thin Al / Thin Pl and the Step Al / Thick Pl phantom data using fitting equation (5-17).

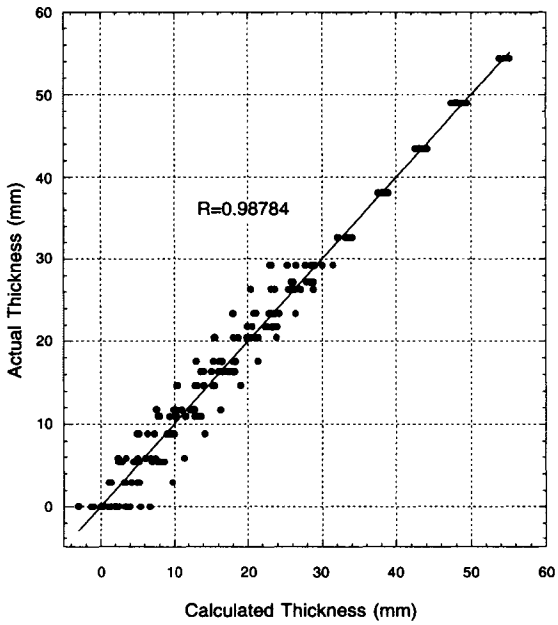

Figure 86: Calculated vs. Actual thickness of Acrylic based on the combined Thin Al / Thin Pl and the Step Al / Thick Pl phantom data using fitting equation (5-17).

Reproduced with permission of the copyright owner. Further reproduction prohibited without permission.

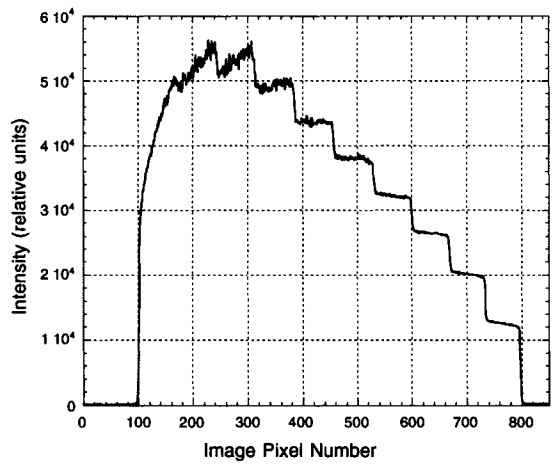

Figure 87: Profile cut along the copper step wedge from the low energy detector image showing attenuation effects on the upper steps.

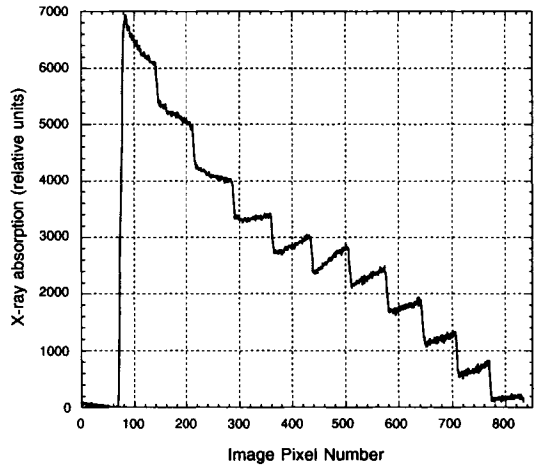

Figure 88: Profile cut along the Thin Al step wedge from the high energy detector image showing the Compton scattering problem.

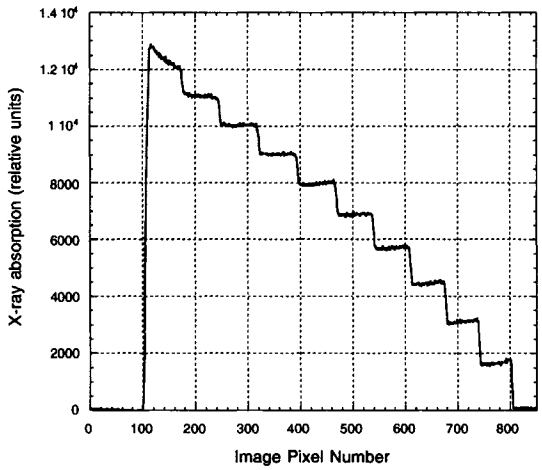

Figure 89: Profile cut along the Thin Al step wedge from the low energy detector image showing no Compton scattering.

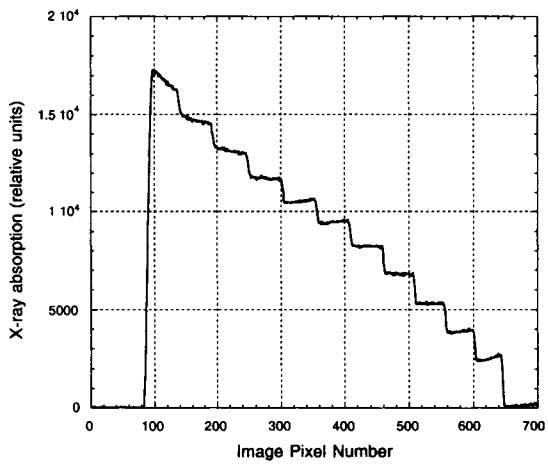

Figure 90: Profile cut along the Step Al phantom from the high energy detector image showing only minor Compton scattering effects.

Calibration procedure

We summarize here the previous sections and give a step by step calibration procedure of the Digiray x-radiography system for dual energy imaging.

1. Mount the dual energy detector 50 to 100 cm vertically from the center of the scanning plate. No objects should be on the scanning plate at this time.

Reproduced with permission of the copyright owner. Further reproduction prohibited without permission.

2. Decide if an anti-scatter grid will be used or not. If one is used, place it on the x-ray scanning plate now and mount it so that it will not move for all future scans.
3. Select the maximum x-ray energy to be used (preferably over 100 keV) on the Digiray system and run at the highest x-ray intensity it can reliably operate on. Also select the scan speed and resolution. In general the highest resolution (1024 x 1024) with its associated fastest scan time (1 to 2 seconds) was usually used. All images should be taken with these same parameters.
4. Start with a nominal high voltage of 800 V on both the PMTs and connect the signal outputs to μ–amp meters.
5. Start scanning the x-ray at the preferred scanning speed and adjust each PMT high voltage so that the peak current of the signals is about 50 μA. These voltages should be kept for all future imaging with this x-ray energy and intensity.
6. Turn off the x-ray and place a thick lead or tungsten absorber on the scanning plate to provide an imaging area where no x-rays are transmitted. A 2 inch square by 1 cm thick piece of lead was used in these studies. This should be placed near one edge to allow the maximum open area for later imaging. In order to automate the normalization procedure, this absorber should not be moved for all subsequent imaging.
7. Connect the PMT signal cables to the signal inputs of the Digiray system and start scanning the x-ray beam.
8. Adjust the computer controlled gain and offset so that the "Air" and "Absorber" regions use the entire dynamic range of the system with a small amount of head room. It is best to coarsely adjust these values in the

Reproduced with permission of the copyright owner. Further reproduction prohibited without permission.

dynamic scanning mode and then use the averaging scanning mode (with about 10 to 20 scans) to do fine tuning. Every image from that point will be acquired using the same parameters selected.

9. Determine how many scans will be needed in the averaging scanning mode to produce the desired quality of images. Usually a minimum of 20 scans should be acquired, however, 50 or more is preferred. It is also preferred that all future scanning based on this calibration be done with the same number of scans.
10. Acquire the high and low x-ray energy background images which is comprised of just the absorber sitting on the scanning plate.
11. Acquire high and low x-ray energy images of the copper or aluminum step wedge sitting on ten layers of acrylic. It is preferred to place the step wedge closer to one edge as seen in figure 65 so that values of the acrylic only transmission can be obtained. It also may be preferable to place the thick part of the step wedge towards the center of the scanning plate.
12. Remove 1 layer of acrylic while keeping the location of all the remaining objects as close to the same positions as possible. Acquire the high and low x-ray energy images of these objects.
13. Repeat step 12 until all the acrylic pieces have been removed and acquire an image the step wedge without any acrylic. One should then have 22 images (11 high and 11 low x-ray energy images) plus 2 background images.
14. Normalize the images using equation (5-13) and take the natural logarithms of the average air transmission value divided by the image pixel values. The program written here to do this is based on one provided by F.R. Parker of NASA-Langley and is found in appendix A. The resulting values were multiplied by 10000 to produce 16 bit integer pixel values.

Reproduced with permission of the copyright owner. Further reproduction prohibited without permission.

15. Use an image analysis program such as ImageJ[68] to obtain the transmission values from the images. Using this program a 30 x 80 pixel area of each combination of acrylic-metal thickness was selected. Selecting "Measure" from the "Analyze" menu gave the mean value of the pixels. The selected areas should be away from the edges and, for the step wedge, centered on the step to obtain the most accurate readings.
16. Create a data table of the high and low x-ray energy transmission values for all thickness combinations dividing back out the 10000 multiplier used in step 14. The multiplier is divided out again to reduce round off error in the calibration routine.
17. Produce a thickness – energy transmission file from this data table. A short example is shown in appendix B.
18. Run the data through the calibration routine to obtain the fitting constants. To graphically see the goodness of this fit, one can use these fitting constants to obtain the calculated values of the thicknesses of the acrylic, aluminum, or copper and plot that against the actual thicknesses.

At this point, the system is calibrated and one can used the fitting constants to project out parts of the image discussed in the next section.

Image projection

Using the fitting constants one can reconstruct the images to project out selected materials in the image. The main equation used for this is equation (4-17) where images B1 and B2 are obtained by applying the fitting equations to every pixel in the normalized high and low energy images. B1 is the Acrylic basis image and B2 is the aluminum or copper basis image. To see how well the calibrations work with the images, the B1 (Acrylic projection) and B2 (aluminum projection) images for the calibration phantom with seven

Reproduced with permission of the copyright owner. Further reproduction prohibited without permission.

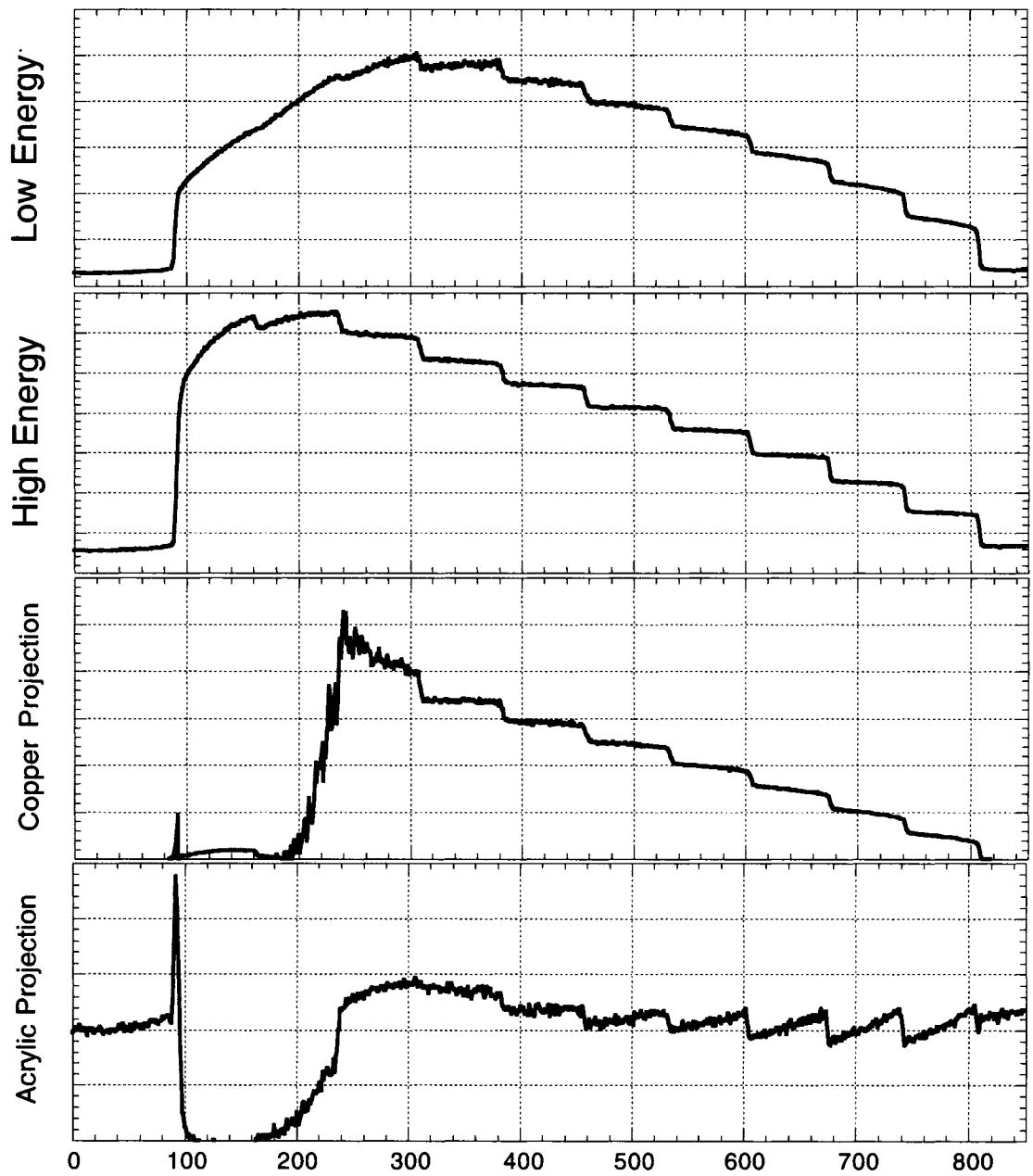

Figure 91: Comparison of a profile cuts along the copper step wedge for the Copper / Thin Pl phantom for the normalized low and high energy images and the copper and Acrylic projection images obtained with fitting equation (5-21).

layers of Acrylic were analyzed by comparing the profile cuts along the step wedges. Figure 91 shows the profile cut for the low energy, high energy, copper projected, and Acrylic projected images for the Copper / Thin Pl phantom using fitting equation (5-21).

Reproduced with permission of the copyright owner. Further reproduction prohibited without permission.

As can be seen, the problems in the low energy image greatly affect the projections on the upper steps. Edge effects, also coming from the low energy image, show up significantly in the Acrylic projected image. If the fit were perfect, the image would be a flat line. Figure 92 shows the results for this phantom using equation (5-17). The main difference between these two fitting routines is what happens at the upper steps. Fitting equation (5-21) goes negative while fitting equation (5-17) produces a high value. Figure 93 shows the result of using the worse fit, fitting equation (5-18), on this phantom for the acrylic projection. Figure 94 shows the copper and Acrylic projection images using equation (5-17).

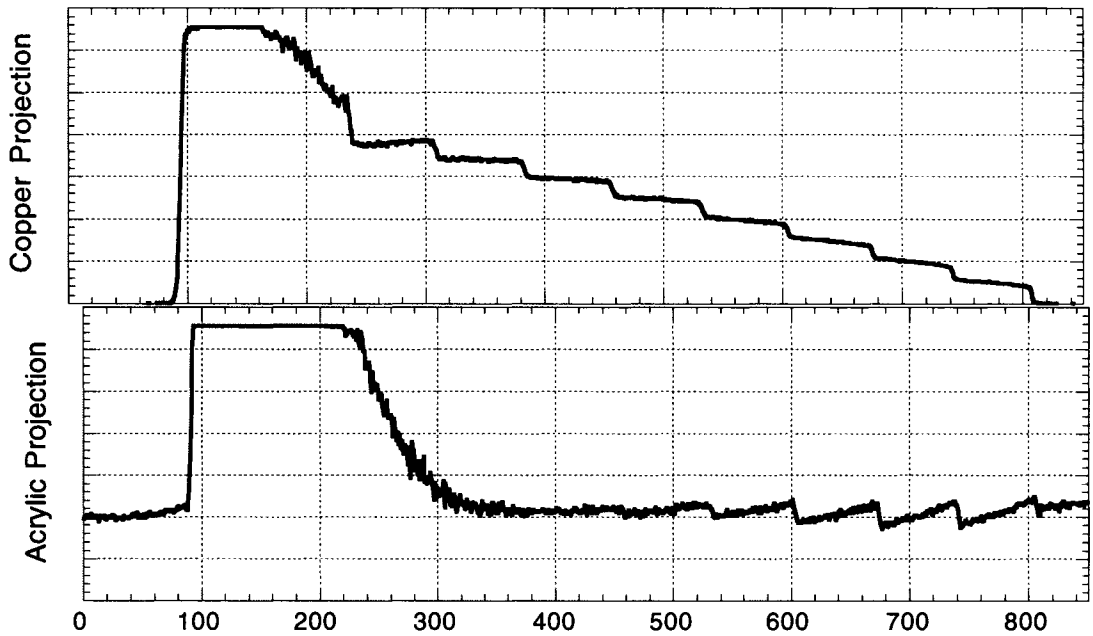

Figure 92: Comparison of a profile cut along the copper step wedge for the Copper / Thin Pl phantom using fitting equation (5-17) to obtain the copper and Acrylic projection images.

Comparison profiles of the first measurement of the Thin Al / Thin Pl phantom with seven pieces of Acrylic projected with equation (5-17) are shown in figure 96. Due to the better quality of the low energy data, the projection images are much better except at the highest step of the aluminum step wedge. The middle steps in the Acrylic projection still show some edge effects due to the Compton scattering seen in figure 88 for the high energy image of the step wedge alone. Figure 95 shows the cut across the step wedge seen in

Reproduced with permission of the copyright owner. Further reproduction prohibited without permission.

figure 97 for the aluminum projection using equation (5-19), the only time a calibration with a square root in it worked. The top image in figure 95 shows a cut along the step wedge near the center of the steps showing nonlinear behavior on the top steps. This is due to instability of the fitting equation in this area seen as black specs in the image in figure 97. The bottom image is with the profile cut near the lower edge of the step wedge which had better stability for some reason. The profile of the steps looks much better although it is quite noisy and nonlinear.

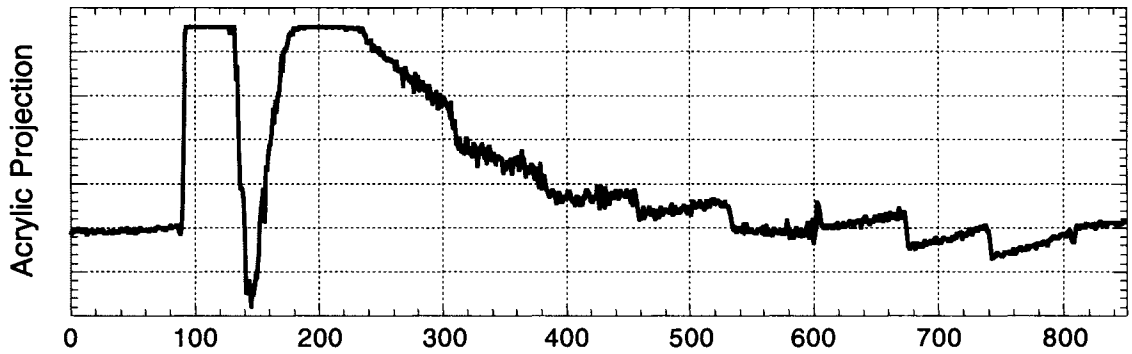

Figure 93: Profile cut across the step wedge showing the results of using the worst fit, fitting equation (5-18), on the Copper / Thin Pl phantom for the acrylic projection

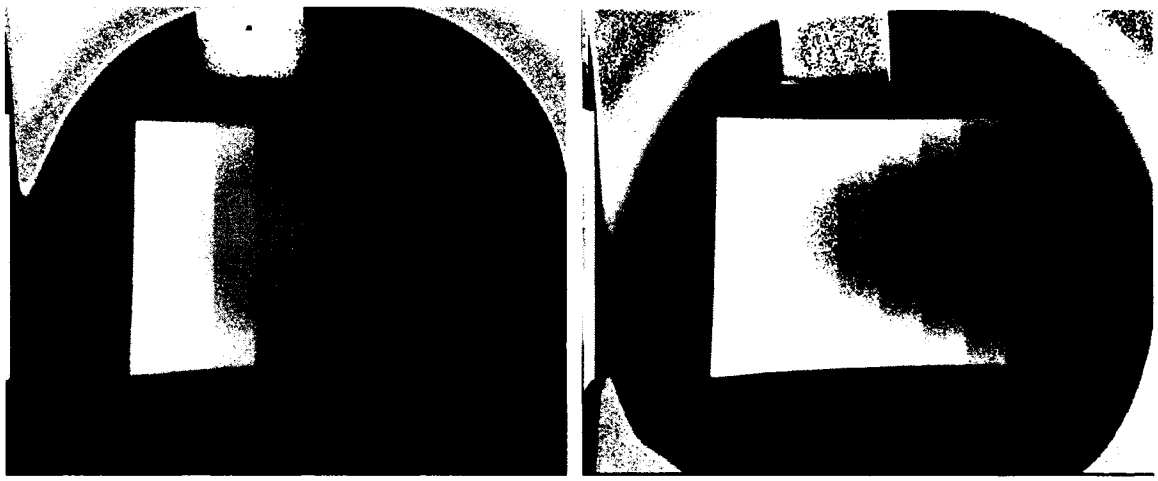

Figure 94: Copper (left) and Acrylic (right) projection images of the Copper/ Thin Pl phantom using equation (5-17).

Reproduced with permission of the copyright owner. Further reproduction prohibited without permission.

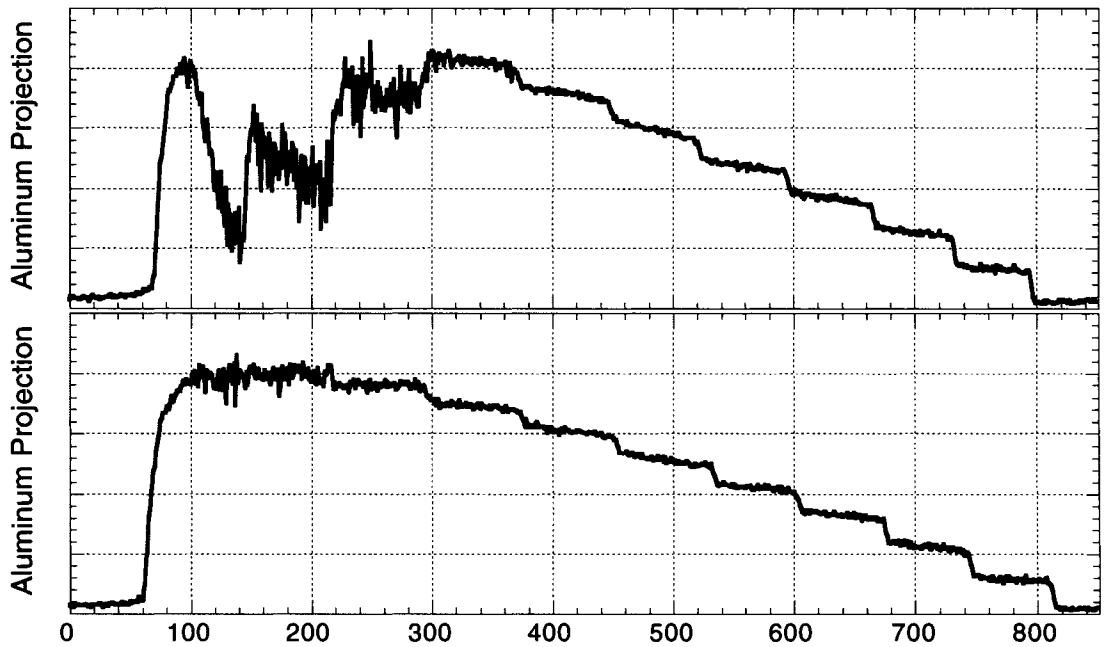

Figure 95: Comparison of profile cuts along the aluminum step wedge for the first measurement of the Thin Al / Thin Pl phantom of the aluminum projection image obtained with fitting equation (5-19). Top plot is near the center of the steps while the bottom plot is near the edge of the steps.

Comparison profiles of the Step Al / Thick Pl phantom with seven pieces of Acrylic projected with equation (5-17) are shown in figure 99. Again, the quality of the low energy image on the upper steps limits how well the aluminum and Acrylic projections works. Overall, however, the results are quite good with the Acrylic projection looking quite flat on the lower steps. The projected images are shown in figure 98 where the lead step numbers are clearly visible. For comparison, the aluminum and Acrylic projection profiles using equation (5-21) are shown in figure 100 which shows some instability on the upper steps of the aluminum projection. For most cases the stability of fitting equation (5-17) will likely be preferred by the user.

Reproduced with permission of the copyright owner. Further reproduction prohibited without permission.

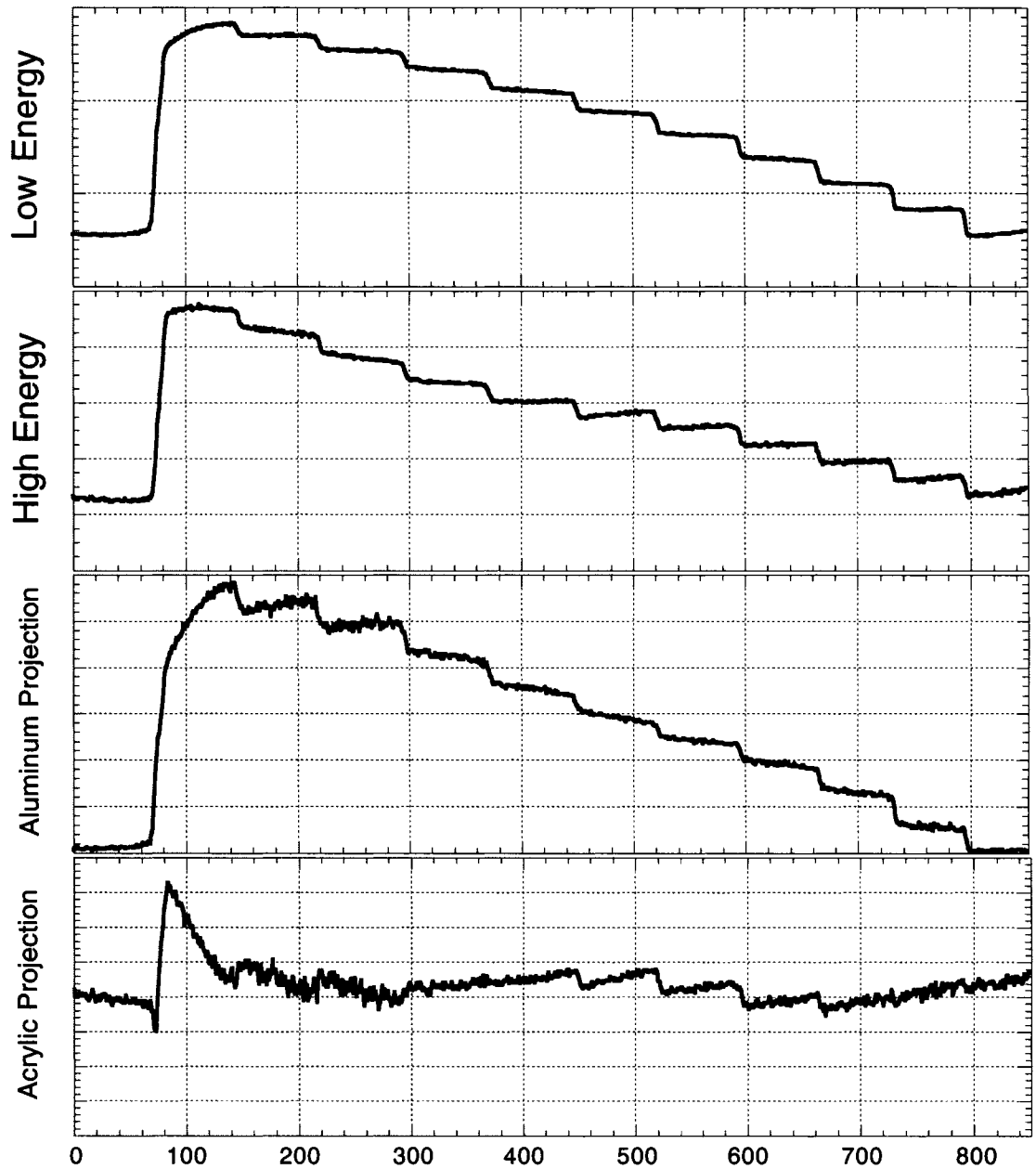

Figure 96: Comparison of a profile cut along the thin aluminum step wedge for the first measurement of the Thin Al / Thin Pl phantom for the normalized low and high energy images and the aluminum and Acrylic projection images obtained with fitting equation (5-17).

Reproduced with permission of the copyright owner. Further reproduction prohibited without permission.

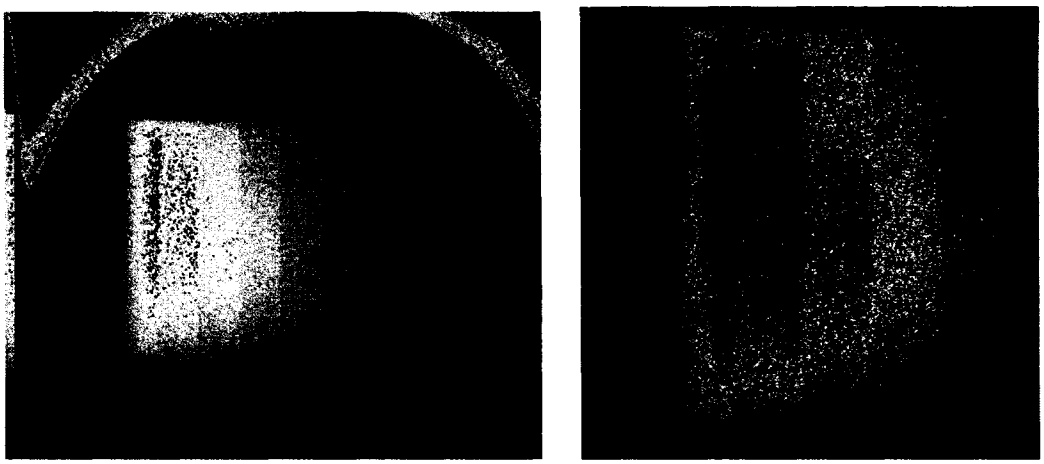

Figure 97: Aluminum projection image (left) and close up of the top steps (right) of the Thin Al / Thin Pl phantom obtained with fitting equation (5-19). The black specs on the steps have a value around zero due to instability in the fitting equation.

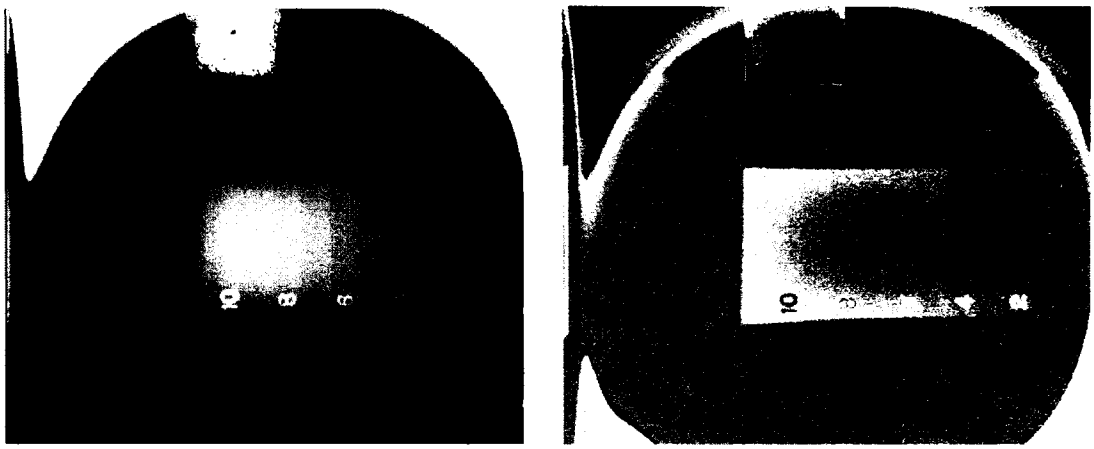

Figure 98: Aluminum (left) and Acrylic (right) projection images of the Step Al/ Thick Pl phantom using equation (5-17).

We will now consider the application of the combined Thin+Step Al / Thin+Thick Pl calibration to the two aluminum based phantoms using fitting equation (5-17). For the Thin Al / Thin Pl phantom, the profiles (fig. 101) showed a little smoother behavior compared to that seen in figure 95. The improvement in the Acrylic projection image is seen in figure 102 where the step wedge is less apparent. For the Step Al / Thick Pl phantom, the profiles (fig. 103) looked quite similar to those seen in figure 98 with a slight improvement seen in the Acrylic projection. Again an improvement in the Acrylic projection image is seen (fig. 104).

Reproduced with permission of the copyright owner. Further reproduction prohibited without permission.

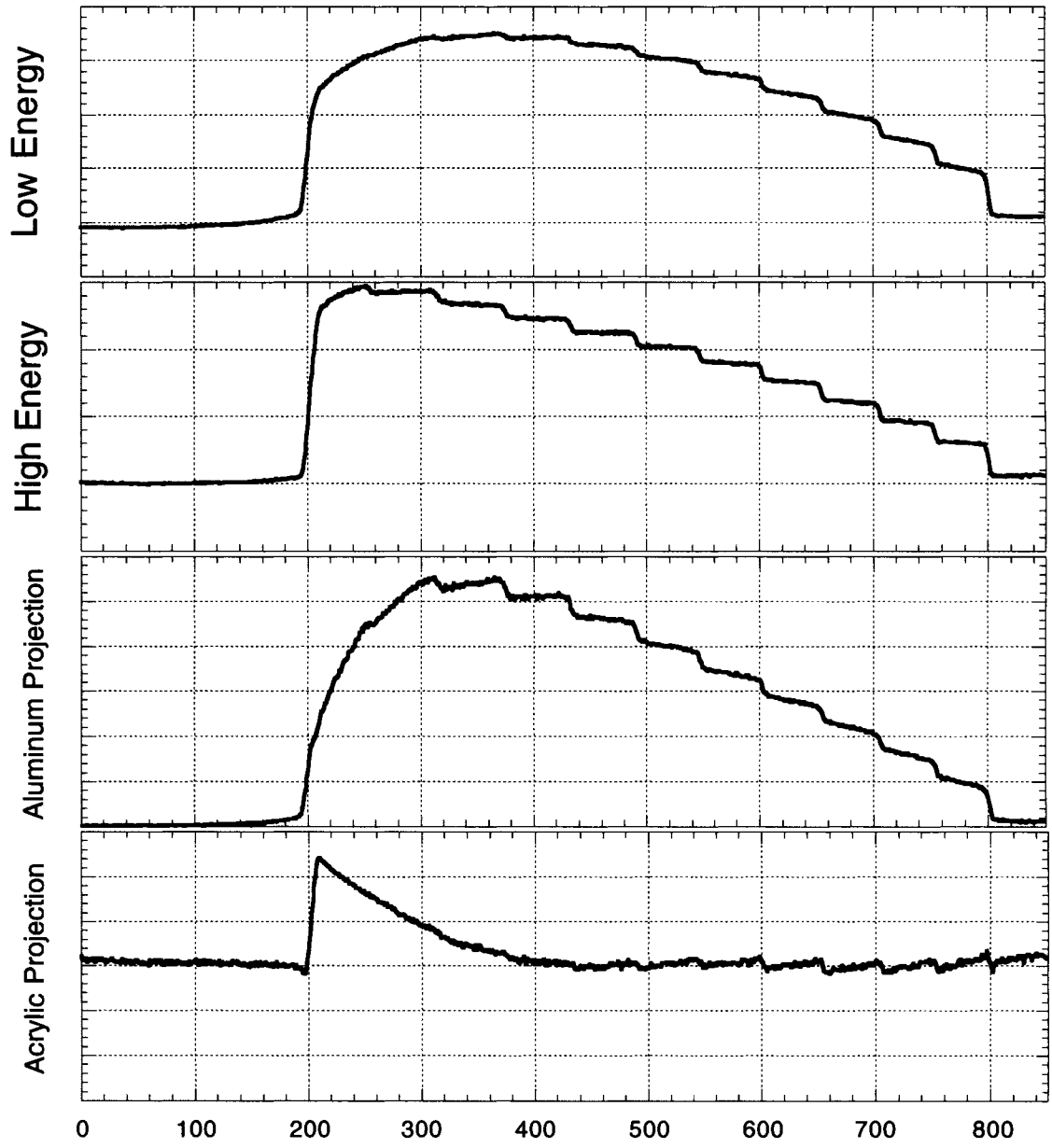

Figure 99: Comparison of a profile cut along the aluminum step wedge for the Step Al / Thick Pl phantom for the normalized low and high energy images and the aluminum and Acrylic projection images obtained with fitting equation (5-17).

Reproduced with permission of the copyright owner. Further reproduction prohibited without permission.

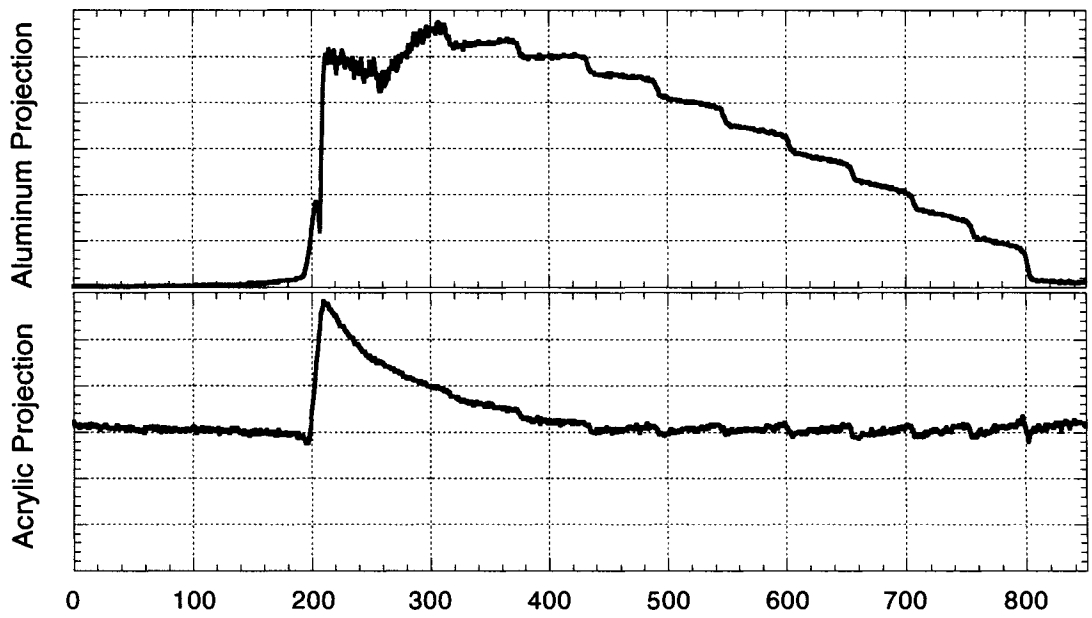

Figure 100: Comparison of a profile cut along the aluminum step wedge for the Step Al / Thick Pl phantom for the aluminum and Acrylic projection images obtained with fitting equation (5-21).

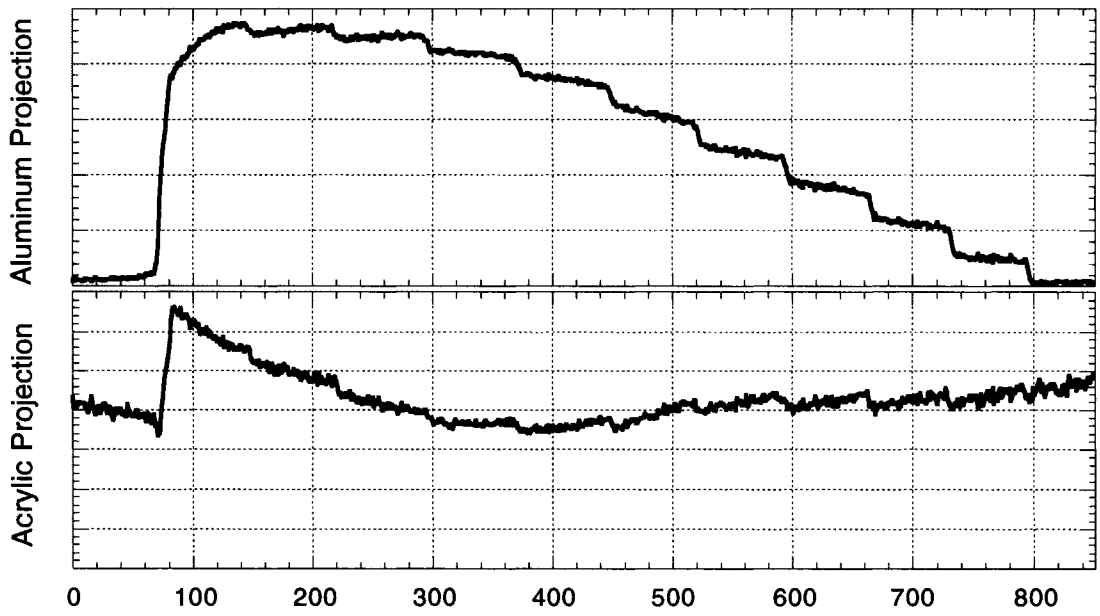

Figure 101: Comparison of a profile cut along the aluminum step wedge for the Thin Al / Thin Pl phantom for the aluminum and Acrylic projection images obtained with fitting equation (5-17) on the combined Thin+Step Al / Thin+Thick Pl calibration.

Reproduced with permission of the copyright owner. Further reproduction prohibited without permission.

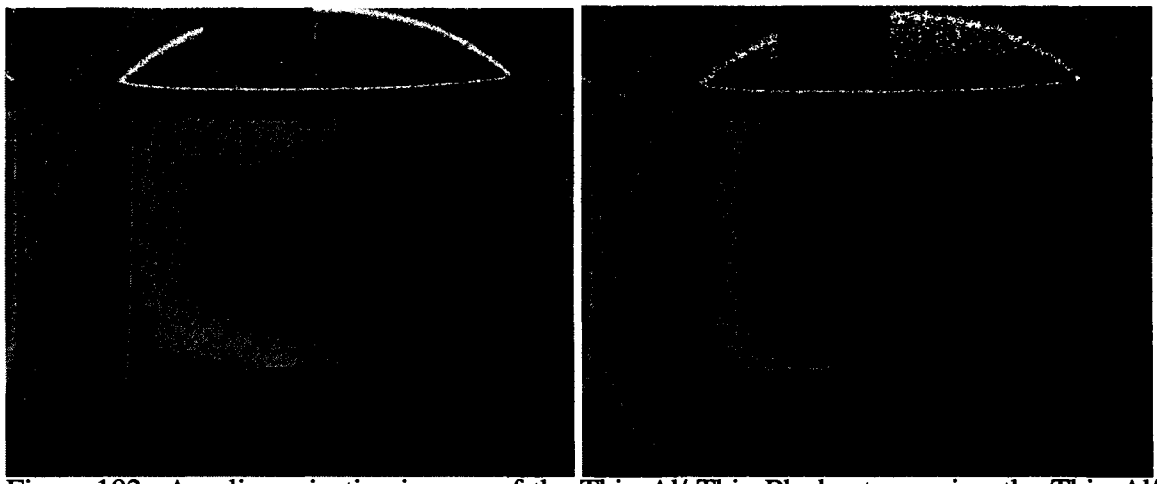

Figure 102: Acrylic projection images of the Thin Al/ Thin Pl phantom using the Thin Al/ Thin Pl data (left) and the combined Thin+Step Al / Thin+Thick Pl data (right) with equation (5-17).

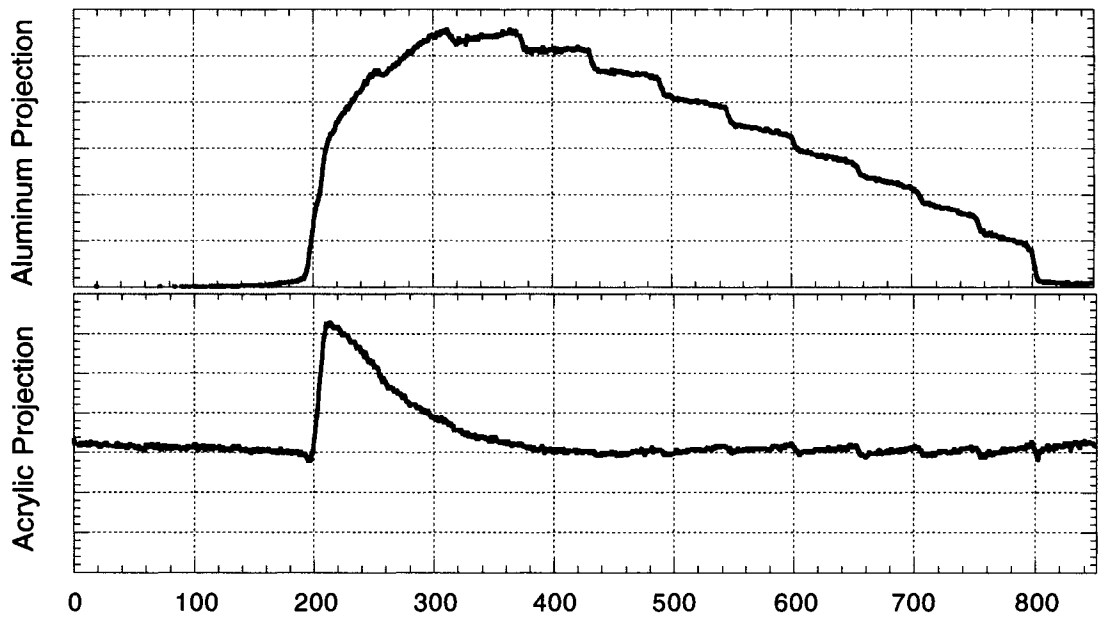

Figure 103: Comparison of a profile cut along the aluminum step wedge for the Step Al / Thick Pl phantom for the aluminum and Acrylic projection images obtained with fitting equation (5-17) on the combined Thin+Step Al / Thin+Thick Pl calibration.

To get an idea of how well one can identify, project out, and remove an unknown material, the Copper / Thin Pl calibration data obtained with fitting equation (5-17) was applied to the Thin Al / Thin Pl and Step Al / Thick Pl phantom images where the aluminum is treated as the unknown. Using 90 degrees for the angle in the combination equation (4-

Reproduced with permission of the copyright owner. Further reproduction prohibited without permission.

17), one obtains the copper projection image, also known as the Acrylic subtraction image, for the phantoms (fig. 105). In both cases there was a significant improvement in the image of the aluminum step wedge compared to the results seen in figures 95 and 98.

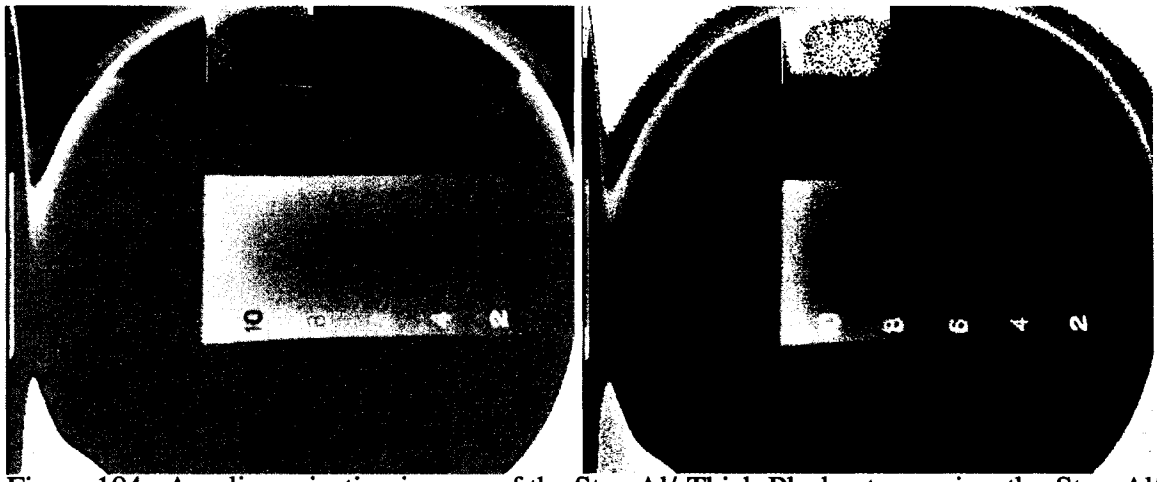

Figure 104: Acrylic projection images of the Step Al/ Thick Pl phantom using the Step Al/ Thick Pl data (left) and the combined Thin+Step Al / Thin+Thick Pl data (right) with equation (5-17).

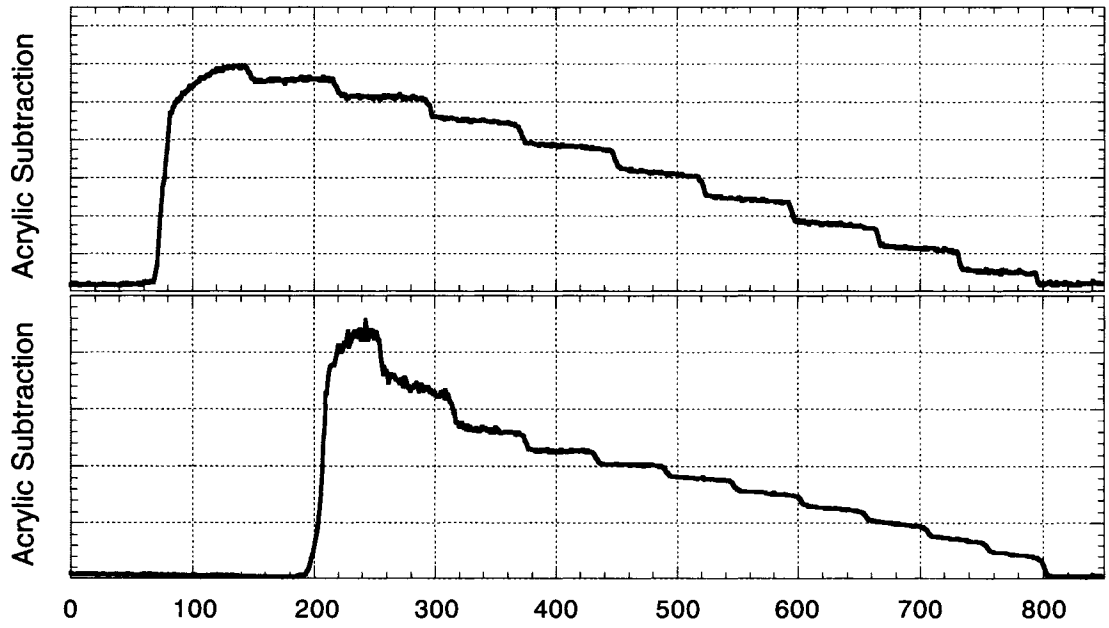

Figure 105: Acrylic subtraction images of the Thin Al / Thin Pl (top) and Step Al/ Thick Pl (bottom) phantoms using the Copper / Thin Pl data with fitting equation (5-17).

Reproduced with permission of the copyright owner. Further reproduction prohibited without permission.

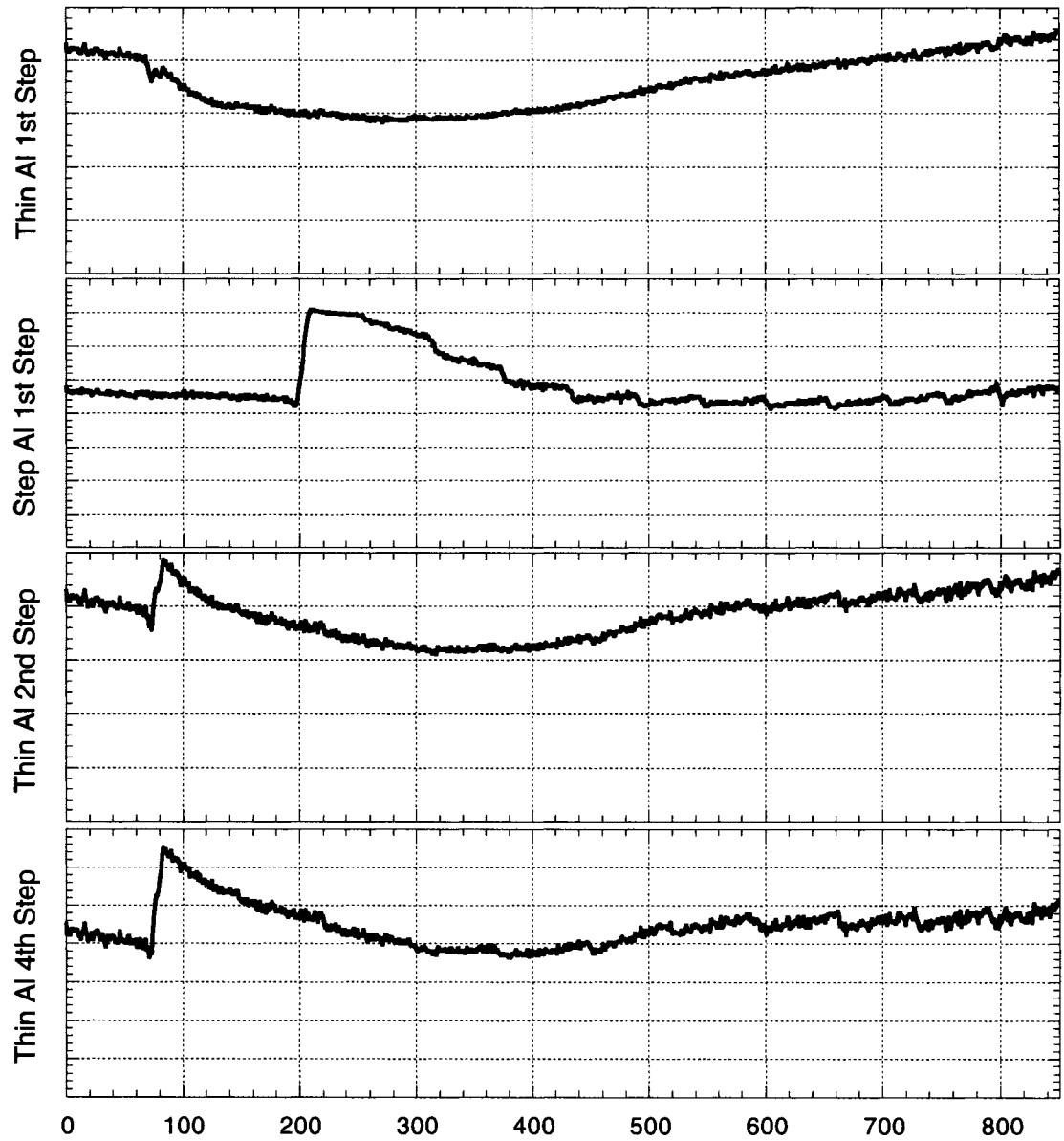

Figure 106: Aluminum subtraction images of the Thin Al / Thin Pl and Step Al/ Thick Pl (see text) phantoms using the Copper / Thin Pl data with fitting equation (5-17).

To obtain the aluminum subtraction image the angle in equation (4-17) was varied until the lower step of the step wedge ceased to contrast with the Acrylic. For the Thin Al phantom this was found to be 91.3° while for the Step Al phantom it was found to be 94.8°.

Reproduced with permission of the copyright owner. Further reproduction prohibited without permission.

The angles should be the same in both cases so there is a few degrees error between the two results. The Thin Al phantom was also reconstructed using the 2nd and 4th steps where 92.2° and 93.4° respectively were found, closer to the Step Al result. Figure 106 shows the profiles while figure 107 shows the images. Certainly the Thin Al phantom looks best using the first step with the smaller angle, however, the forth step with the larger angle is more likely correct given the quality of the original data.

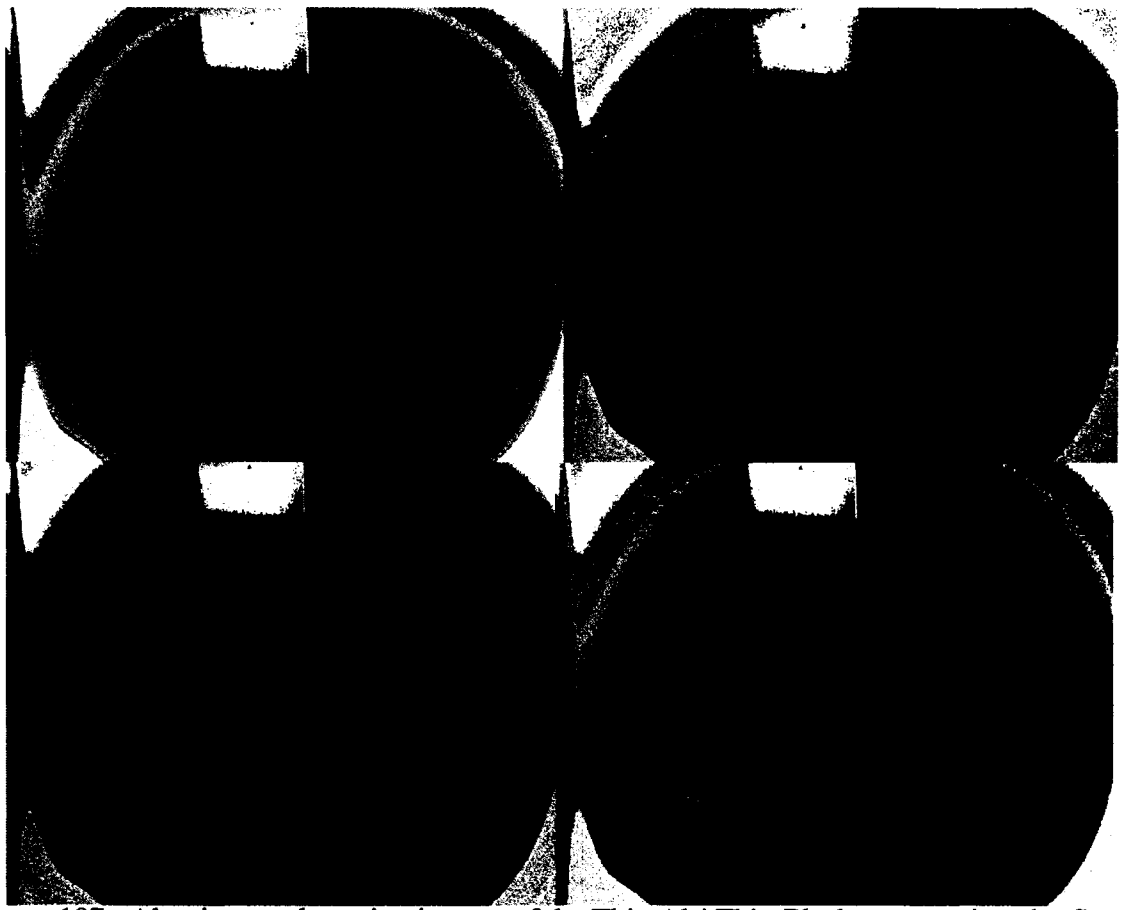

Figure 107: Aluminum subtraction images of the Thin Al / Thin Pl phantom using the first step (upper left), second step (lower left), and forth step (lower right) and the Step Al/ Thick Pl phantoms (upper right) using the Copper / Thin Pl data with fitting equation (5-17).

Reproduced with permission of the copyright owner. Further reproduction prohibited without permission.

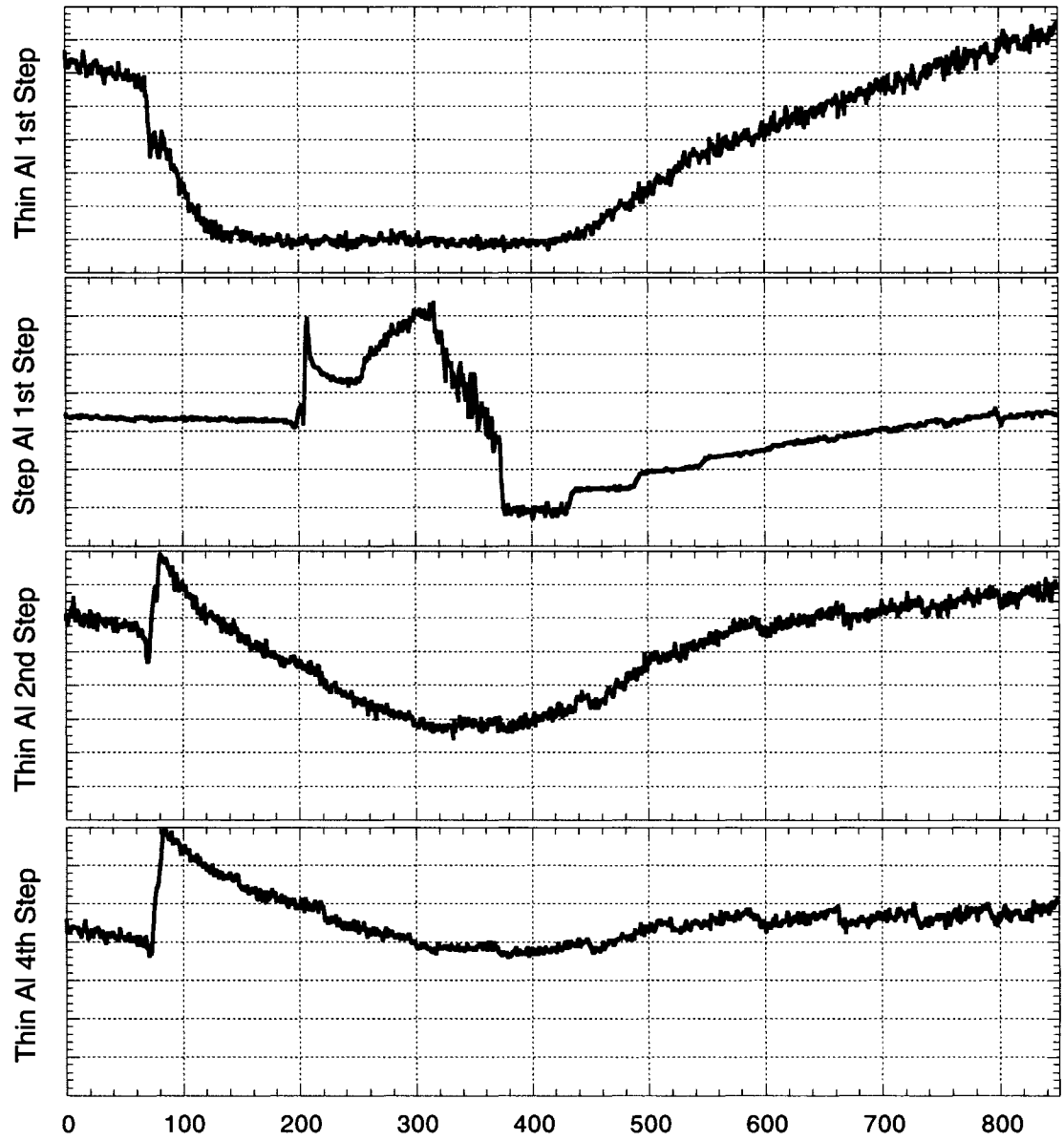

Figure 108: Aluminum subtraction images of the Thin Al / Thin Pl and Step Al/ Thick Pl (see text) phantoms using the Copper / Thin Pl data with fitting equation (5-21).

The same routine was carried out using the Copper / Thin Pl calibration data obtained with fitting equation (5-21). For the Step Al phantom, the disappearance angle for the first step was found to be 92.9°, however, the result was much less stable. For the Thin Al phantom the results were 91.0°, 91.9°, and 93.5° for the first, second, and forth steps respectively (fig. 108). The results with fitting equation (5-17) for the Step Al phantom

Reproduced with permission of the copyright owner. Further reproduction prohibited without permission.

suggests a characteristic angle of 4.8° for aluminum. An analysis to find the largest difference between the height of the first step of the Step Al phantom verses the background Acrylic for different angles found 5.0° to project out the aluminum the most which should equal the characteristic angle. For the Thin Al phantom the results were 1.3°, 2.4°, and 3.3° for the first, second, and forth steps respectively. The step wedge profiles of projections made using 5.0° for the Step Al phantom and 3.3° for the Thin Al phantom are shown in figure 109, however, they do not look as good as those using 0°.

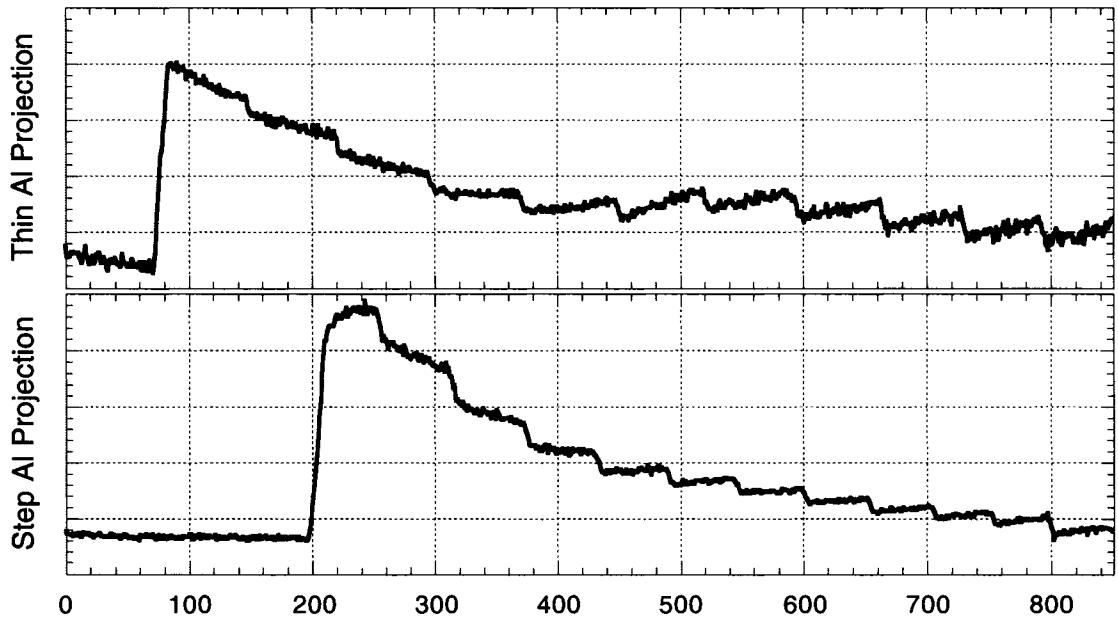

Figure 109: Aluminum projection images of the Thin Al / Thin Pl at 3.25° (top) and the Step Al/ Thick Pl at 5.00° (bottom) phantoms using the Copper / Thin Pl data with fitting equation (5-17).

Phantoms

To show the usefulness of the dual energy x-radiography technique in practice, a series of phantom images were acquired and analyzed. These images were taken with all the

Reproduced with permission of the copyright owner. Further reproduction prohibited without permission.

same parameters as the calibration images. Figure 110 shows the original low x-ray energy image of phantom one containing both Acrylic and aluminum plates as well as Teflon, Nylon, and ABS plastic cylinders. The plates have many holes with lots of cracks but one can not tell if the holes and cracks are in the aluminum or Acrylic plate. One also can not tell which plate is aluminum and which plate is acrylic. Using the Step Al / Thick Pl calibration with equation (5-17) an Acrylic projection is made at 0° which shows that the acrylic plate is the square one. It also shows that the majority of the holes and all the cracks must be in the aluminum plate since they have disappeared from the image (fig. 111). The plastic plate is seen to have a small array of holes of differing depths near the center. Figure 112 shows the aluminum projection image which highlights the cracks. An aluminum plug in the middle right hole in the plastic plate is identified by comparing the Acrylic projection where it disappears and the aluminum projection where it is quite clearly seen.

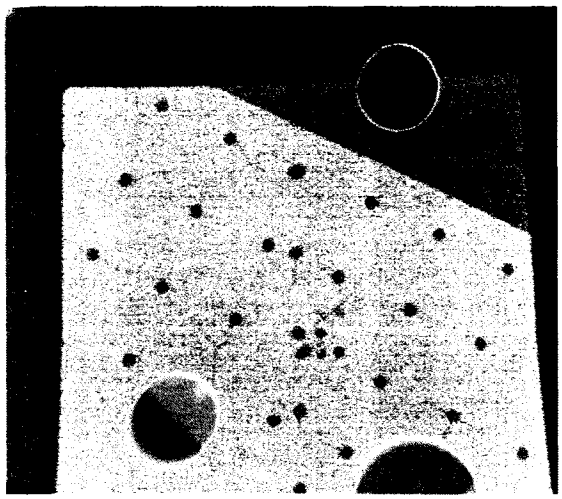

Figure 110: Low x-ray energy image of phantom one containing Acrylic and aluminum sheets as well as Teflon, Nylon, and ABS plastic cylinders.

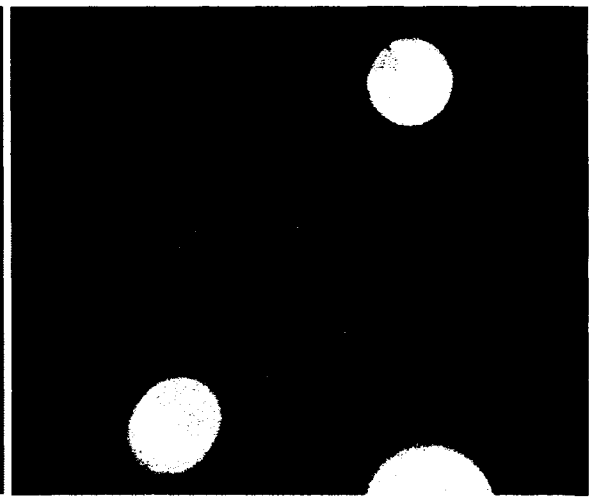

Figure 111: Acrylic projection (0 degrees) of figure 110 identifies which plate is Acrylic and which plate has which holes.

Reproduced with permission of the copyright owner. Further reproduction prohibited without permission.

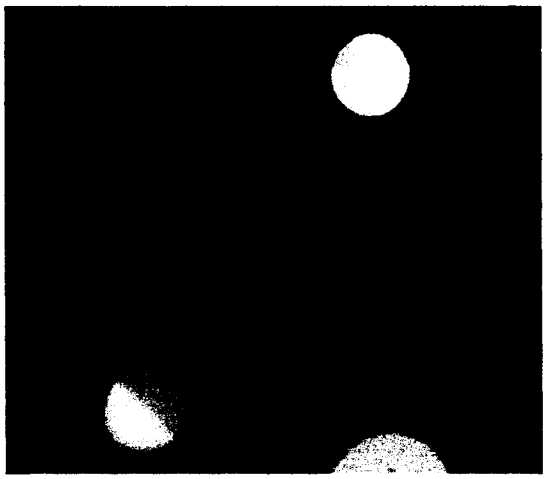

Figure 112: Aluminum projection (90 degrees) of figure 110 which highlights the cracks in the aluminum.

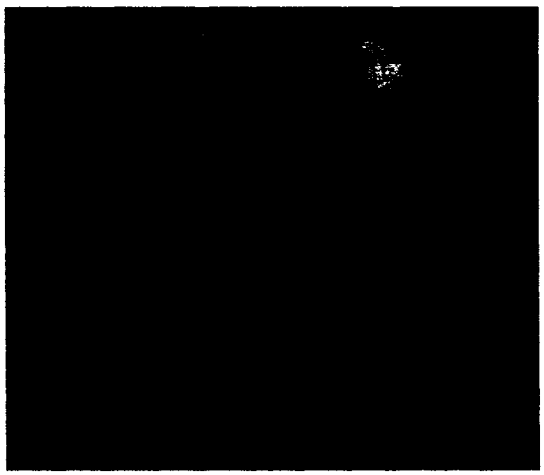

Figure 113: ABS plastic subtraction image (97.0 degrees) makes the lower right cylinder nearly disappear.

To gain more information about the other materials in the image, the high and low x-ray images were combined with different angles until each of the plastic cylinders disappeared (figs 113-115). This combination angle is then called the subtraction angle of that material. The projection angle is then 90° from that. To verify the projection angle, combinations of the high and low x-ray energy images were made at different angles until the contrast of each plastic cylinder was the greatest. Table 12 shows the projection and subtraction angles found for the materials which shows good agreement between the calculated and measured values.

Material	Subtraction angle (measured)	Projection angle (calculated from subtraction angle)	Projection angle (measured)
Acrylic	90.00	0.00	0.00
ABS	97.00	7.00	7.00
Nylon	97.72	7.72	7.72
Teflon (TFE)	102.95	12.95	12.94
Aluminum	0.00	90.00	90.00

Table 12: Measured subtraction and measured and calculated projection angles for the different materials in phantom 1.

Reproduced with permission of the copyright owner. Further reproduction prohibited without permission.

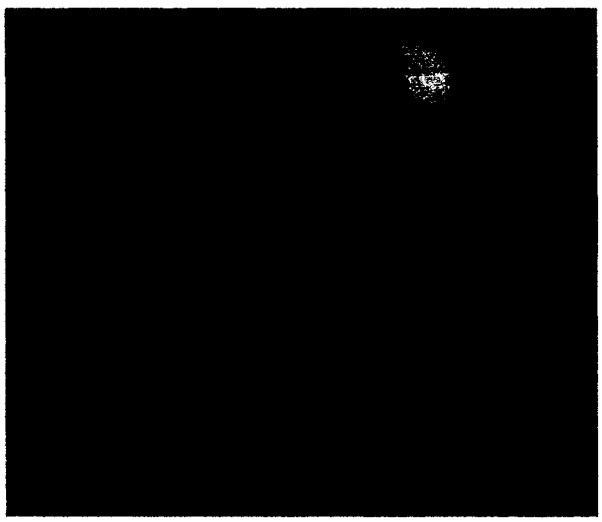

Figure 114: Nylon subtraction image (97.7°) makes the lower left cylinder nearly disappear.

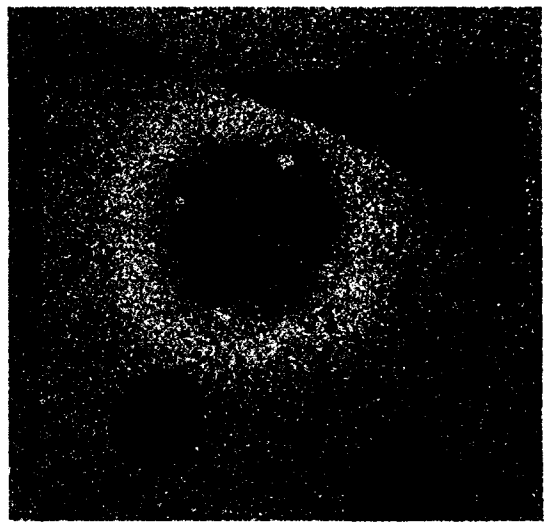

Figure 115: Teflon subtraction image (103.0°) makes the upper right cylinder nearly disappear.

As mentioned earlier one can also make one material appear to be another. Thus, if one material was filling a void in another material and one just wanted the contrast between the two materials to vanish, there is an angle for this. This was tested with the aluminum filling the small hole in the acrylic. Figure 116 shows a close-up view of the holes in the center of the acrylic plate from the original low x-ray energy image and the images reconstructed at 0°, 90° and 79.9° from left to right respectively. The small bits in the image are tungsten. One can see that by eliminating the aluminum - acrylic contrast in the right-most image, the shape of the tungsten bit is easier to discern.

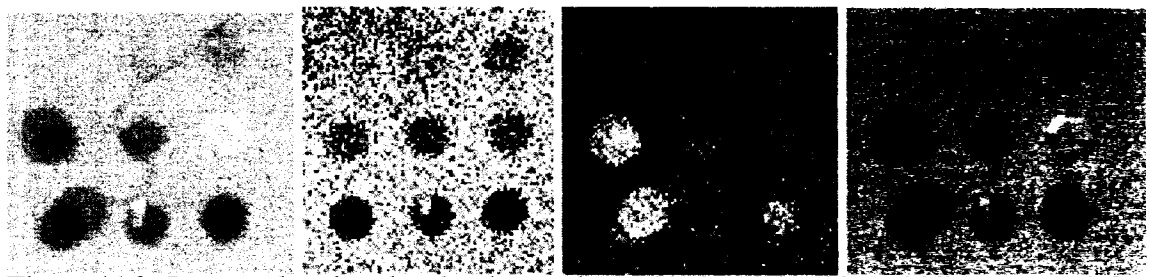

Figure 116: Images showing the aluminum plugged hole (right side, middle). From left to right are the original low energy x-ray image, and 0°, 90° and 79.94° reconstructed images. The right most image is the aluminum – acrylic look-alike angle allowing better contrast of the tungsten bit.

Reproduced with permission of the copyright owner. Further reproduction prohibited without permission.

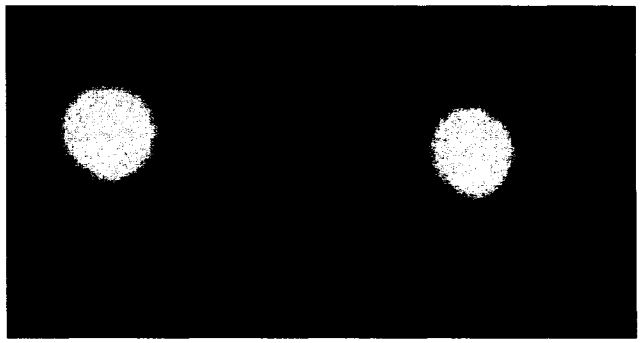

Figure 117: Low x-ray energy image of a riveted aircraft phantom.

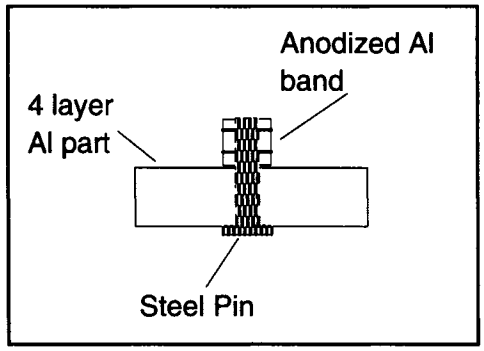

Figure 118: Construction of the riveted aircraft phantom.

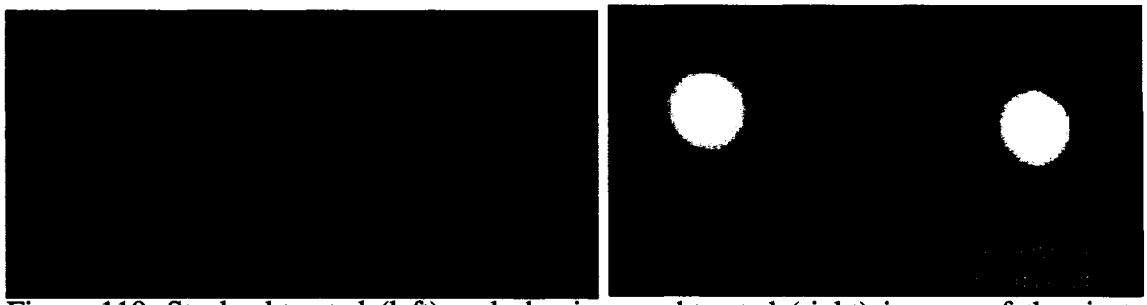

Figure 119: Steel subtracted (left) and aluminum subtracted (right) images of the riveted aircraft phantom. The left image shows the aluminum band is intact while the right image shows the head of the rivet it cut.

In a second phantom, images were taken of a riveted aircraft part where one of the rivets was partially cut. Figure 117 shows the low x-ray energy image of the good rivet on the left and the cut rivet on the right. The construction of this aluminum–steel rivet is shown in figure 118. From the image, one can not tell if there is a cut in the aluminum band or in the steel pin. As there was steel in the image, reconstructions were made using the copper-thin plastic calibration data with the 15 parameter A/B fitting equation as this calibration should be better suited to higher Z imaging. Figure 119 shows the steel subtracted image on the left and the aluminum subtracted image on the right where we see that the aluminum band is intact but the head of the steel pin is cut. Figure 120 shows photographs of the front and back of the phantom.

Reproduced with permission of the copyright owner. Further reproduction prohibited without permission.

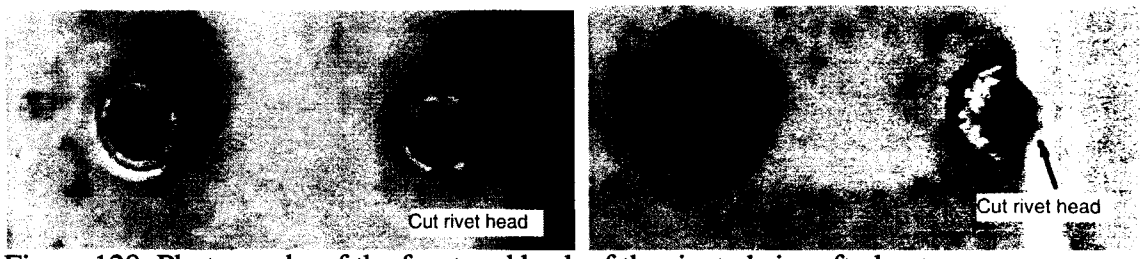

Figure 120: Photographs of the front and back of the riveted aircraft phantom.

In the final phantom, images were taken of 25 μm thick tungsten foils embedded in 1/2" thick Plexiglas sitting on the aluminum plate with holes and simulated cracks used in phantom 1. Again, the copper-thin plastic calibration data with the 15 parameter A/B fitting equation was used as this provided the lowest noise reconstructions. Figure 121 shows the original low energy x-ray image (left), tungsten subtracted image (middle), and aluminum subtracted image (right). One can see the tungsten foils totally disappear in the middle image and the aluminum totally disappears in the right image.

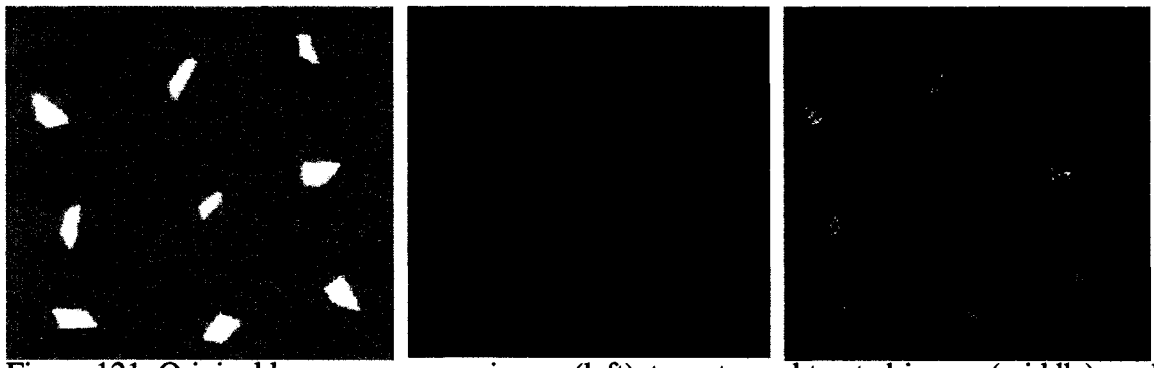
Figure 121: Original low energy x-ray image (left), tungsten subtracted image (middle), and aluminum subtracted image (right) of tungsten foils.

Reproduced with permission of the copyright owner. Further reproduction prohibited without permission.

CHAPTER VI

CONCLUSIONS AND FUTURE DIRECTIONS

These studies show that scanning beam x-radiography has great promise in dual energy imaging, however, there is an issue with noise, low DQE, and scatter. Using special techniques in the construction of the x-ray tube, one can increase the x-ray output up to 35 mA as compared to the 0.5 to 1 mA of the system used in these studies as shown in reference 13. This would significantly raise the DQE for an integrating detector. Another way to improve the DQE of the integrating detector system is to reduce the electronic noise. It is hard to estimate how much of an improvement can be made without replacing the high voltage supply and possibly the entire acquisition system supplied with the x-ray system.

As we saw with the counting measurements, it we stay at a lower rate than the dead time, a counting detector has a very high DQE. The problem is how to handle the high rate of incoming x-rays needed to acquire an image in a reasonable amount of time. There are a few possible options. The first would be an array of mini-PMTs. Attempts were made at achieving this using the Photonis XP1702 64 channel multianode PMT which has about 5% crosstalk between the channels (fig. 122). An 8 x 8 array of 1.5 mm x 1.5 mm x 10 mm YAP pixels were placed into a tungsten frame and attach to the PMT so that the pixels were centered over the 8 x 8 inputs on the face of the PMT (fig. 123). The plan would be to connect each channel from the 8 x 8 output from the PMT to two discriminators with different thresholds – a 128 discriminator system. The discriminator with the lower threshold would count all the x-rays hitting crystal pixel while the discriminator with the higher threshold would count only the higher energy x-rays. The number of low energy x-rays would then be found by subtracting the higher energy x-ray count from the total count. The problem found when the detector was tested with the x-ray system was that the 5%

Reproduced with permission of the copyright owner. Further reproduction prohibited without permission.

cross talk was too high. If one looks at the center crystal, the 5% crosstalk from each of the crystals to the left, right, top and bottom plus the lower crosstalk from corner crystals would make up about 30% of the signal. Since the rate we are trying to achieve is 2 or more counts per μs, the cross talk starts to cause the signals to overlap and destroy the energy information. Tests were made with another version of this PMT which has a fiber optic input face plate which greatly reduces the cross talk. The low light transmission through the fiber optic, however, did not allow one to see x-rays lower than 60 keV. A possible way to overcome this cross talk would be to use small individual PMTs, however, the smallest PMTs have an active area of 1 cm x 1 cm. In order to keep the "point" detector idea, one would have to couple a small array of crystals to fiber optics which would take the light from each crystal to a separate PMT. Unfortunately the light loss in coupling to the fiber has a significant affect on the energy resolution. Figure 124 shows the ^{57}Co energy spectrum from a single 1.5 mm x 1.5 mm x 10 mm YAP crystal coupled to a Photonis XP2262 PMT operated at -1730 V. We see both the full energy peak of 140 keV as well as the escape peak at the lower energy. When the same crystal was coupled through a Mitsubishi Eska[69] 3 mm plastic optical fiber and the PMT was operated at –1950 V, the peaks were totally washed out (fig 125). Figure 124 shows another problem with this method. There will always be the possibility that the full energy of the incoming x-ray will not be captured thus causing an escape peak. This would make a higher energy x-ray appear as a lower energy x-ray thus causing problems in the reconstruction. In theory, the spectrum could be deconvolved to correct for the escaped energy, however, it would have to be done on each image pixel which would greatly complicate the reconstruction. The current version of the dual energy detector does not suffer from this problem as it works on a depth of penetration which is an exponential function of the x-ray energy.

Reproduced with permission of the copyright owner. Further reproduction prohibited without permission.

Figure 122: Photographs of the XP1700 series of multianode PMTs.

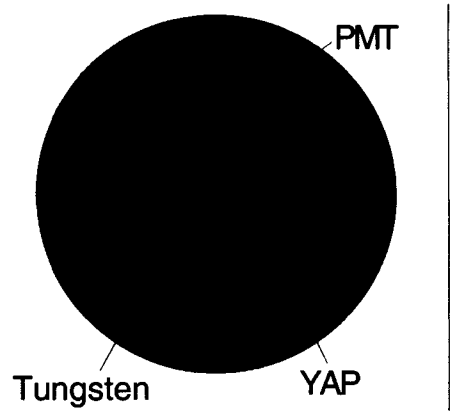

Figure 123: Layout of 8 x 8 YAP crystal array coupled to the XP1702.

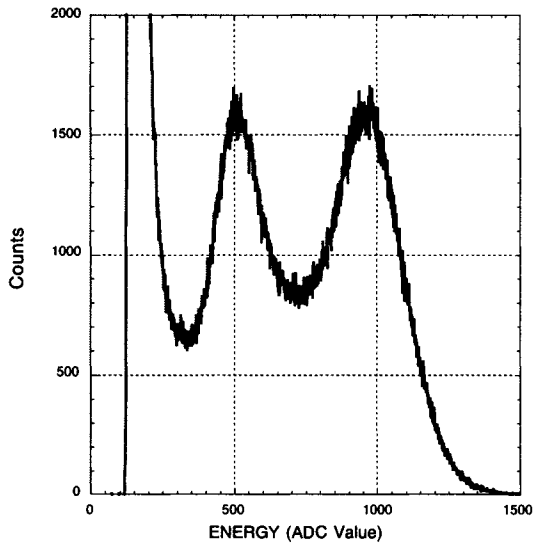

Figure 124: ^{57}Co energy spectrum from a single YAP crystal coupled directly a PMT.

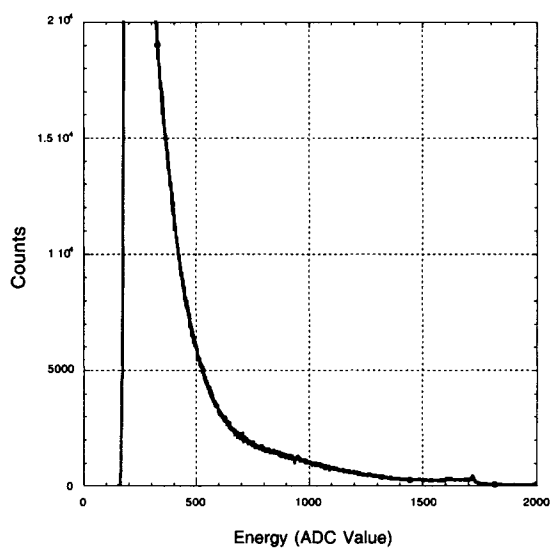

Figure 125: ^{57}Co energy spectrum from a single YAP crystal couple through a 3 mm plastic optical fiber.

The second way to produce a counting detector would be to use a solid state detector such as that developed by David Nygren[49]. This detector is a silicon strip detector where the x-rays enter through the edge of the silicon thus making for a long path length to achieve a high absorption efficiency. The low / high energy detection is given by reading out signals from the front / back of the strip. The down side to solid state detectors is that they are slow however, by making strips on the order of 100 μm, we can fit many individual

Reproduced with permission of the copyright owner. Further reproduction prohibited without permission.

detectors into a small area. The small size of each detector reduces the rate per detector while the large number of detectors produces a reasonable overall rate. With such a detector we do not need real energy resolution, we just count the numbers of x-rays stopped in the front versus the back of the strip. This greatly simplifies the electronics which would be important as we would need to have a couple thousand channels to acquire an image efficiently. This takes us back to a depth of penetration detector but with the advantage of a very high DQE.

Another option would be to use a high pressure xenon gas detector similar to the solid state detector above. There would be front and back collection regions which would give the energy separation. Such a detector built by the University of Siegen has been used quite successfully for noninvasive subtraction coronary angiograph with a synchrotron radiation source at HASYLAB, DESY.[70] They built a detector based on $XeCO_2$ with a (DQE) of at least 58% (for 20,000 photons/pixel) for 33 keV photons. Only at a flux above $2.4x10^{10}$ photons/s pixel did saturation effects become apparent. The down side is that the electronics and mechanics involved with such gas detectors can be much more difficult to deal with.

Reproduced with permission of the copyright owner. Further reproduction prohibited without permission.

APPENDIX A

NORMALIZATION PROGRAM

This program written in C for the Macintosh using Apple's free MPW compiler[71] normalizes the images obtained from the Digiray Reverse Geometry X-ray system using the equation from ref. 64. The output is the Log of the original image.

```
/*************************************************************

This program takes a background file and normalizes the image file according to

"Quantification of Corrosion Damage in Aircraft Skin Using a Novel x-ray
Radiography System", Presented at the 20th Annual Review of Progress in QNDE,
August, 1993

Normalized Image = (image1 - offset1) * (air2 - offset2) / (image2 - offset2) * (air1 -
offset1)
image1 = object image
image2 = background image

for the Digiray NDE system. The output file is also the LOG of the normalized file. This
program handles the new 4 byte/pixel format. The Digiray system runs on a PC while
this
program was written for the Macintosh so the byte order had to be reversed.

Author
    Randy Wojcik  (Jefferson Lab)
    based on original file obtained from Ray Parker(NASA-Langley)

*************************************************************/

#include <stdio.h>
#include <stdlib.h>
#include <string.h>
#include <stddef.h>
#include <math.h>
#include <signal.h>

void main (void);
void exitpgm (char [ ] );
void handler (int);
```

Reproduced with permission of the copyright owner. Further reproduction prohibited without permission.

```
unsigned            *a, *bg;
unsigned short      *result;
long                *c;
FILE                *instream, *instream2, *outstream;
char                filenamelist [2][32][99];
char        fname[32],y,z;
long        X_RAY_IMAGES;

void main(){
  long              filelength, num;
  long              i, j, k,w;
  long              bytes;
  long              jstep;
  unsigned          loop_count=0,num_of_calibrations,parta;
  unsigned short    temp4,temp2,temp3,temp1,temp;
  long              rows, cols;
  long              X1_offset, Y1_offset, X2_offset, Y2_offset;
  long              X1_air, Y1_air, X2_air, Y2_air;
  float             air1, air2, offset1, offset2;
  float             dd, nn,air_area, offset_area,calc;

  X_RAY_IMAGES = 11;                    // set number of files and filenames
  num_of_calibrations = 2;

  strcpy(filenamelist[0][0],"ABLPLHF.RGX");     // [0] file is the background file
  strcpy(filenamelist[0][1],"A10PLHF.RGX");     // High energy images
  strcpy(filenamelist[0][2],"A9PLHF.RGX");
  strcpy(filenamelist[0][3],"A8PLHF.RGX");
  strcpy(filenamelist[0][4],"A7PLHF.RGX");
  strcpy(filenamelist[0][5],"A6PLHF.RGX");
  strcpy(filenamelist[0][6],"A5PLHF.RGX");
  strcpy(filenamelist[0][7],"A4PLHF.RGX");
  strcpy(filenamelist[0][8],"A3PLHF.RGX");
  strcpy(filenamelist[0][9],"A2PLHF.RGX");
  strcpy(filenamelist[0][10],"A1PLHF.RGX");
  strcpy(filenamelist[0][11],"A0PLHF.RGX");

  strcpy(filenamelist[1][0],"ABLPLLF.RGX");     // [0] file is the background file
  strcpy(filenamelist[1][1],"A10PLLF.RGX");     //  Low energy images
  strcpy(filenamelist[1][2],"A9PLLF.RGX");
  strcpy(filenamelist[1][3],"A8PLLF.RGX");
  strcpy(filenamelist[1][4],"A7PLLF.RGX");
  strcpy(filenamelist[1][5],"A6PLLF.RGX");
  strcpy(filenamelist[1][6],"A5PLLF.RGX");
  strcpy(filenamelist[1][7],"A4PLLF.RGX");
  strcpy(filenamelist[1][8],"A3PLLF.RGX");
```

Reproduced with permission of the copyright owner. Further reproduction prohibited without permission.

```
strcpy(filenamelist[1][9],"A2PLLF.RGX");
strcpy(filenamelist[1][10],"A1PLLF.RGX");
strcpy(filenamelist[1][11],"A0PLLF.RGX");


fprintf (stdout," Read file header info...\n");        // get startup information to set up
                                                       //memory allocation
fflush(stdout);
 instream = fopen (filenamelist[0][0], "r");
if (instream == NULL)
  exitpgm ("instream = NULL");

fseek (instream, 54, SEEK_SET);
num = fread ( &temp, sizeof (unsigned short), 1, instream);
temp2 = temp & 255;
temp3 = (unsigned int)(temp / 256);
rows = (temp2 * 256) + temp3;

num = fread ( &temp, sizeof (unsigned short), 1, instream);
temp2 = temp & 255;
temp3 = (unsigned int)(temp / 256);
cols = (temp2 * 256) + temp3;

num = fread ( &temp, sizeof (unsigned short), 1, instream);
temp2 = temp & 255;
temp3 = (unsigned int)(temp / 256);
bytes = (temp2 * 256) + temp3;
if (bytes!=4){
  fprintf (stdout," bytes = %i  temp = %i\n",bytes,temp);
  fflush(stdout);
  exitpgm (" Error in the number of Bytes");}

fclose (instream);

filelength = rows * cols;
fprintf (stdout," rows = %i  cols = %i\n",rows,cols);
fflush(stdout);

fprintf (stdout," Allocate memory...\n");                    // allocate memory
fflush(stdout);

bg = (unsigned *)  malloc (filelength * sizeof (unsigned));
if (bg == 0){
  fprintf(stdout,"\n\rfilelength = %i\n\r",filelength);
  fflush(stdout);
  exitpgm (" Error: malloc (bg) !!!");}
```

Reproduced with permission of the copyright owner. Further reproduction prohibited without permission.

```
a = (unsigned *)  malloc (filelength * sizeof (unsigned));
if (a == 0)
  exitpgm (" Error: malloc (a) !!!");

result = (unsigned short*)  malloc (filelength * sizeof (unsigned short));
if (result == NULL)
  exitpgm (" Error: malloc (result) !!!");

X1_air = 600;                                    //define area to get air from
Y1_air = 230;
X2_air = X1_air + 50;
Y2_air = Y1_air + 50;

air_area = (float)((X2_air - X1_air) * (Y2_air - Y1_air));

X1_offset = 430;                                 // define area to get offset from
Y1_offset = 240;
X2_offset = X1_offset + 50;
Y2_offset = Y1_offset + 50;

offset_area = (float)((X2_offset - X1_offset) * (Y2_offset - Y1_offset));

for (w = 0; w < num_of_calibrations; w++){
  fprintf (stdout," Starting normalization #%i\n",w);
  fflush(stdout);

  instream = fopen (filenamelist[w][0], "rb");          // open background file
  if (instream == NULL) exit (0);
  fseek (instream, 512L, SEEK_SET);

  for (j=0; j< filelength; j++){                        // load back ground file
    num = fread (&parta, 4, 1, instream);
    temp1 = parta / 256;
    temp3 = parta / 65536;
    temp4 = parta / 16777216;
    temp1 = temp1 & 255;
    temp2 = temp2 & 255;
    temp3 = temp3 & 255;          // convert byte order for mac
    temp4 = temp4 & 255;
    bg[j] = ((temp3 * 256) + temp4 + (temp1 * 65536) + (temp2 * 16777216));}
  fclose (instream);

  for (i=1; i<=X_RAY_IMAGES; i++){
    sprintf (fname, "%s normlog2", filenamelist[w][i]);    //create output file
    fprintf (stdout," Create output file %s\n",fname);
```

Reproduced with permission of the copyright owner. Further reproduction prohibited without permission.

```
fflush(stdout);
outstream = fopen (fname, "wb");
if (outstream == NULL) exitpgm (" File open error!!!");

instream = fopen (filenamelist[w][i], "rb");              //Open image file
if (instream == NULL) exitpgm (" Input file error!!!");
fprintf (stdout," Open file: %s\n", filenamelist[w][i]);
fflush(stdout);
fseek (instream, 512L, SEEK_SET);

fprintf (stdout," Reading image file\n");
fflush(stdout);

for (j=0; j< filelength; j++){                            // load image file
  num = fread (&parta, 4, 1, instream);
  temp1 = parta / 256;
  temp3 = parta / 65536;
  temp4 = parta / 16777216;
  temp1 = temp1 & 255;
  temp2 = temp2 & 255;
  temp3 = temp3 & 255;                                    //convert byte order for mac
  temp4 = temp4 & 255;
  a[j] = ((temp3 * 256) + temp4 + (temp1 * 65536) + (temp2 * 16777216));}
fclose (instream);

air1 = air2 = 0;                                          // get average air value
for (k=Y1_air; k<Y2_air; k++){
  for (j=X1_air; j<X2_air; j++){
          jstep = (cols * k) + j;
          air1 += (float) *(a+jstep);
          air2 += (float) *(bg+jstep);}}
air1 /= air_area;
air2 /= air_area;
fprintf (stdout," average air air1 = %f  air2 = %f\n",air1,air2);
fflush(stdout);

offset1 = offset2 = 0;                                    // get average offset value
for (k=Y1_offset; k<Y2_offset; k++){
  for (j=X1_offset; j<X2_offset; j++){
          jstep = (cols * k) + j;
          offset1 += (float) *(a+jstep);
          offset2 += (float) *(bg+jstep);}}
offset1 /= offset_area;
offset2 /= offset_area;
fprintf (stdout," average offset offset1 = %f  offset2 = %f\n",offset1,offset2);
fflush(stdout);
```

Reproduced with permission of the copyright owner. Further reproduction prohibited without permission.

```
    nn = air2 - offset2;
    dd = air1 - offset1;

    fprintf (stdout," doing normalization\n");
    fflush(stdout);

    for (j=0; j<filelength; j++){                    // Perform normalization
      calc = 50000 * ((((float) *(a+j) - offset1) * nn) / (( (float) *(bg+j) - offset2) * dd));
      if (calc < 0) calc = 0;
      if (calc > 65535) calc = 65535;
      *(result+j) = (unsigned short) (calc + .5);}

    air1 = 0;                                        // get new average air value
    for (k=Y1_air; k<Y2_air; k++){
      for (j=X1_air; j<X2_air; j++){
            jstep = (cols * k) + j;
            air1 += (float) *(result+jstep);}}
    air1 /= air_area;
    fprintf (stdout," average air new air1 = %f\n",air1);
    fflush(stdout);

    for (j=0; j<filelength; j++){                    // Take log of image
      calc = (float) (*(result+j));
      calc = -log(calc/air1);
      if (calc < 0) calc = 0;
      calc *= 10000;
      if (calc > 65535) calc = 65535;
      *(result+j) = (unsigned short) (calc + .5);}

    fprintf (stdout," Writing image file\n");        // Write out the results
    fflush(stdout);

    fwrite (result, sizeof (unsigned short), filelength, outstream);
    fclose(outstream);

    fprintf (stdout," NEXT image!!!!\n");
    fflush(stdout);}

  fprintf (stdout,"\n\n NEXT calibration !!!!\n");
  fflush(stdout);}

fprintf (stdout," DONE!!!!\n");
fflush(stdout);
exitpgm ("");}
```

Reproduced with permission of the copyright owner. Further reproduction prohibited without permission.

```
void exitpgm (message)
  char        message[80];{
  fprintf (stderr, " %s\n", message);
  fclose (instream);
  fclose (outstream);
  free (a);free (result);free (c);free (bg);
  exit (0);}


void handler (int sig){
  exitpgm (" Program aborted by  user!!!");}
```

Reproduced with permission of the copyright owner. Further reproduction prohibited without permission.

APPENDIX B

EXAMPLE OF THICKNESS - ENERGY TRANSMISSION DATA

This is an example of the values measured for the thick plastic / aluminum step wedge phantom. The first two columns are the plastic and aluminum thickness. The last two columns are the average values measured from 30 x 80 pixel areas in the normalized high and low energy images.

Plastic Thickness (mm)	Aluminum Thickness (mm)	High Energy Image log(Io/I)	Low Energy Image log(Io/I)
0.0000	0.0000	0.0000	0.0000
0.0000	4.9276	0.24707	0.62001
0.0000	7.9276	0.38557	0.89991
0.0000	10.928	0.52823	1.1610
0.0000	13.928	0.67684	1.4118
0.0000	16.928	0.81992	1.6546
0.0000	19.928	0.94342	1.8750
0.0000	22.928	1.0502	2.0854
0.0000	25.928	1.1683	2.2885
0.0000	28.928	1.3067	2.4825
0.0000	31.928	1.4616	2.6361
5.4356	0.0000	0.059200	0.066289
5.4356	4.9276	0.31836	0.68384
5.4356	7.9276	0.46121	0.96943
5.4356	10.928	0.60912	1.2330
5.4356	13.928	0.76016	1.4917
5.4356	16.928	0.90152	1.7310
5.4356	19.928	1.0269	1.9549
5.4356	22.928	1.1361	2.1646
5.4356	25.928	1.2572	2.3731
5.4356	28.928	1.3990	2.5642
5.4356	31.928	1.5489	2.6746
10.871	0.0000	0.13081	0.14076
10.871	4.9276	0.39537	0.74052
10.871	7.9276	0.54540	1.0363
10.871	10.928	0.69636	1.3048
10.871	13.928	0.84632	1.5574
10.871	16.928	0.98899	1.7934
10.871	19.928	1.1144	2.0098

Reproduced with permission of the copyright owner. Further reproduction prohibited without permission.

10.871	22.928	1.2257	2.2205
10.871	25.928	1.3472	2.4150
10.871	28.928	1.4887	2.5808
10.871	31.928	1.6284	2.6304
16.307	0.0000	0.20819	0.21805
16.307	4.9276	0.47356	0.79503
16.307	7.9276	0.62998	1.0922
16.307	10.928	0.78033	1.3539
16.307	13.928	0.93265	1.6004
16.307	16.928	1.0742	1.8331
16.307	19.928	1.2002	2.0395
16.307	22.928	1.3102	2.2344
16.307	25.928	1.4364	2.4109
16.307	28.928	1.5690	2.5361
16.307	31.928	1.7019	2.5473
21.742	0.0000	0.29351	0.30162
21.742	4.9276	0.55794	0.84719
21.742	7.9276	0.71541	1.1386
21.742	10.928	0.86547	1.3974
21.742	13.928	1.0176	1.6319
21.742	16.928	1.1614	1.8465
21.742	19.928	1.2866	2.0437
21.742	22.928	1.3982	2.2214
21.742	25.928	1.5168	2.3748
27.178	0.0000	0.37937	0.38509
27.178	4.9276	0.63923	0.89740
27.178	7.9276	0.79725	1.1808
27.178	10.928	0.94956	1.4279
27.178	13.928	1.1023	1.6544
27.178	16.928	1.2422	1.8533
27.178	19.928	1.3681	2.0373
27.178	22.928	1.4772	2.1955
27.178	25.928	1.5943	2.3204
32.614	0.0000	0.47023	0.46771
32.614	4.9276	0.72298	0.94307
32.614	7.9276	0.87744	1.2201
32.614	10.928	1.0294	1.4582
32.614	13.928	1.1786	1.6723
32.614	16.928	1.3209	1.8619
32.614	19.928	1.4426	2.0225
32.614	22.928	1.5503	2.1626
32.614	25.928	1.6642	2.2616
38.049	0.0000	0.56176	0.55429
38.049	4.9276	0.80594	0.99789
38.049	7.9276	0.96028	1.2601
38.049	10.928	1.1093	1.4848

Reproduced with permission of the copyright owner. Further reproduction prohibited without permission.

38.049	13.928	1.2586	1.6883
38.049	16.928	1.3960	1.8616
38.049	19.928	1.5206	1.8616
38.049	22.928	1.6262	2.0083
38.049	25.928	1.7290	2.1311
43.485	0.0000	0.64981	0.63218
43.485	4.9276	0.89210	1.0483
43.485	7.9276	1.0410	1.2940
43.485	10.928	1.1921	1.5046
43.485	13.928	1.3395	1.6955
43.485	16.928	1.4738	1.8564
43.485	19.928	1.5954	1.9911
43.485	22.928	1.6976	2.0926
48.920	0.0000	0.74506	0.72028
48.920	4.9276	0.97795	1.1084
48.920	7.9276	1.1269	1.3364
48.920	10.928	1.2755	1.5399
48.920	13.928	1.4204	1.7165
48.920	16.928	1.5562	1.8678
48.920	19.928	1.6720	1.9916
48.920	22.928	1.7725	2.0835
54.356	0.0000	0.85746	0.80463
54.356	4.9276	1.0827	1.1625
54.356	7.9276	1.2315	1.3750
54.356	10.928	1.3771	1.5651
54.356	13.928	1.5184	1.7314
54.356	16.928	1.6516	1.8692
54.356	19.928	1.7672	1.9818
54.356	22.928	1.8623	2.0544

Reproduced with permission of the copyright owner. Further reproduction prohibited without permission.

APPENDIX C

LEAST SQUARES FIT PROGRAM

This program is written in C for the Macintosh using Apple's free MPW compiler and performs a least squares fit to the transmission values such as those measured in appendix B. The output is the Log of the original image. This program also gives the starting values needed by the Levenberg-Marquardt algorithm in Appendix D.

```
/*********************************************************************
 Regular linear least squares fit from Numerical Recipies pg 676 (Ref 66).
This uses equation 21 and 22 from the Alvarez paper. (ref 42)
Written by Randy Wojcik
*********************************************************************/

#include <stdio.h>
#include <stddef.h>
#include <stdlib.h>
#include <math.h>
#include "ranlmfit.h"

#define NR_END 1
#define FREE_ARG char*
#define TOL 1.0e-18
#define PLASTIC 1
#define ALUMINUM 2
#define HIGH 3
#define LOW 4

double      **v,**u,*w,*a,chisq;
DATVEC      x,sal,spl,sh,sl,aluminum,plastic,high,low;
int         ma,ndata,handle,fitting,model;
FILE        *in_file,*out_file;

void nrerror(char error_text[ ]){
  fprintf(stderr,"Numerical Recipes run-time error...\n");
  fprintf(stderr,"%s\n",error_text);
  exit(1);}
```

Reproduced with permission of the copyright owner. Further reproduction prohibited without permission.

```
int *ivector(long nl, long nh){
  int    *v;

  v=(int *)malloc((size_t)((nh-nl+1+NR_END)*sizeof(int)));
  if (!v) nrerror("allocation failure in ivector()");
  return v-nl+NR_END;}

float *vector(long nl, long nh){
  float *v;

  v=(float *)malloc((size_t)((nh-nl+1+NR_END)*sizeof(float)));
  if (!v) nrerror("allocation failure in vector()");
  return v-nl+NR_END;}

double *dvector(long nl, long nh){
  double *v;

  v=(double *)malloc((size_t)((nh-nl+1+NR_END)*sizeof(double)));
  if (!v) nrerror("allocation failure in dvector()");
  return v-nl+NR_END;}

float **matrix(long nrl, long nrh, long ncl, long nch){
  long i,nrow=nrh-nrl+1,ncol=nch-ncl+1;
  float **m;

  m=(float **) malloc((size_t)((nrow+NR_END)*sizeof(float)));
  if (!m) nrerror("allocation failure 1 in matrix()");
  m += NR_END;
  m -= nrl;
  m[nrl]=(float *) malloc((size_t)((nrow*ncol+NR_END)*sizeof(float)));
  if (!m[nrl]) nrerror("allocation failure 2 in matrix()");
  m[nrl] += NR_END;
  m[nrl] -= ncl;
  for(i=nrl+1;i<=nrh;i++) m[i] = m[i-1] + ncol;
  return m;}


int **imatrix(long nrl, long nrh, long ncl, long nch){
  long i,nrow=nrh-nrl+1,ncol=nch-ncl+1;
  int **m;

  m=(int **) malloc((size_t)((nrow+NR_END)*sizeof(int)));
  if (!m) nrerror("allocation failure 1 in imatrix()");
  m += NR_END;
```

Reproduced with permission of the copyright owner. Further reproduction prohibited without permission.

```
  m -= nrl;
  m[nrl]=(int *) malloc((size_t)((nrow*ncol+NR_END)*sizeof(int)));
  if (!m[nrl]) nrerror("allocation failure 2 in matrix()");
  m[nrl] += NR_END;
  m[nrl] -= ncl;
  for(i=nrl+1;i<=nrh;i++) m[i] = m[i-1] + ncol;
  return m;}

double **dmatrix(long nrl, long nrh, long ncl, long nch){
  long i,nrow=nrh-nrl+1,ncol=nch-ncl+1;
  double **m;

  m=(double **) malloc((size_t)((nrow+NR_END)*sizeof(double)));
  if (!m) nrerror("allocation failure 1 in dmatrix()");
  m += NR_END;
  m -= nrl;
  m[nrl]=(double *) malloc((size_t)((nrow*ncol+NR_END)*sizeof(double)));
  if (!m[nrl]) nrerror("allocation failure 2 in matrix()");
  m[nrl] += NR_END;
  m[nrl] -= ncl;
  for(i=nrl+1;i<=nrh;i++) m[i] = m[i-1] + ncol;
  return m;}

void free_ivector(int *v, long nl, long nh){
  free((FREE_ARG)(v+nl-NR_END));
  nl = nh;}

void free_vector(float *v, long nl, long nh){
  free((FREE_ARG)(v+nl-NR_END));
  nl = nh;}

void free_dvector(double *v, long nl, long nh){
  free((FREE_ARG)(v+nl-NR_END));
  nl = nh;}

void free_matrix(float **m, long nrl, long nrh, long ncl, long nch){
  free((FREE_ARG)(m[nrl]+ncl-NR_END));
  free((FREE_ARG)(m+nrl-NR_END));
  nrl = nrh + nch;}


void free_dmatrix(double **m, long nrl, long nrh, long ncl, long nch){
  free((FREE_ARG)(m[nrl]+ncl-NR_END));
  free((FREE_ARG)(m+nrl-NR_END));
  nrl = nrh + nch;}
```

Reproduced with permission of the copyright owner. Further reproduction prohibited without permission.

```
void fill_matrix(double x,double p[], double y){
  int i;

  i = (int)x;
  switch(model){
    case 10:    if (fitting == PLASTIC || fitting == ALUMINUM){ // 8 param A/B
                  p[0] = 1;
                  p[1] = high[i];
                  p[2] = low[i];
                  p[3] = high[i] * high[i];
                  p[4] = high[i] * low[i];
                  p[5] = low[i] * low[i];

                  p[6] = -y * high[i];
                  p[7] = -y * low[i];}
                else{
                  p[0] = 1;
                  p[1] = aluminum[i];
                  p[2] = plastic[i];
                  p[3] = aluminum[i] * aluminum[i];
                  p[4] = aluminum[i] * plastic[i];
                  p[5] = plastic[i] * plastic[i];

                  p[6] = -y * aluminum[i];
                  p[7] = -y * plastic[i];}
                break;
    case 12:    if (fitting == PLASTIC || fitting == ALUMINUM){ // 18 param sqr root
                  p[0] = 1;
                  p[1] = high[i];
                  p[2] = low[i];
                  p[3] = high[i] * high[i];
                  p[4] = high[i] * low[i];
                  p[5] = low[i] * low[i];
                  p[6] = high[i] * high[i] * high[i];
                  p[7] = high[i] * high[i] * low[i];
                  p[8] = high[i] * low[i] * low[i];
                  p[9] = low[i] * low[i] * low[i];

                  p[10] = -y * high[i];
                  p[11] = -y * low[i];
                  p[12] = -y * high[i] * high[i];
                  p[13] = -y * high[i] * low[i];
                  p[14] = -y * low[i] * low[i];
```

Reproduced with permission of the copyright owner. Further reproduction prohibited without permission.

```
            p[15] = -y * y;
            p[16] = -y * y * high[i];
            p[17] = -y * y * low[i];}
          else{
            p[0] = 1;
            p[1] = aluminum[i];
            p[2] = plastic[i];
            p[3] = aluminum[i] * aluminum[i];
            p[4] = aluminum[i] * plastic[i];
            p[5] = plastic[i] * plastic[i];
            p[6] = aluminum[i] * aluminum[i] * aluminum[i];
            p[7] = aluminum[i] * aluminum[i] * plastic[i];
            p[8] = aluminum[i] * plastic[i] * plastic[i];
            p[9] = plastic[i] * plastic[i] * plastic[i];

            p[10] = -y * aluminum[i];
            p[11] = -y * plastic[i];
            p[12] = -y * aluminum[i] * aluminum[i];
            p[13] = -y * aluminum[i] * plastic[i];
            p[14] = -y * plastic[i] * plastic[i];

            p[15] = -y * y;
            p[16] = -y * y * aluminum[i];
            p[17] = -y * y * plastic[i];}
          break;
case 13:    if (fitting == PLASTIC || fitting == ALUMINUM){ // 15 param A/B
            p[0] = 1;
            p[1] = high[i];
            p[2] = low[i];
            p[3] = high[i] * high[i];
            p[4] = high[i] * low[i];
            p[5] = low[i] * low[i];
            p[6] = high[i] * high[i] * high[i];
            p[7] = high[i] * high[i] * low[i];
            p[8] = high[i] * low[i] * low[i];
            p[9] = low[i] * low[i] * low[i];

            p[10] = -y * high[i];
            p[11] = -y * low[i];
            p[12] = -y * high[i] * high[i];
            p[13] = -y * high[i] * low[i];
            p[14] = -y * low[i] * low[i];}
          else{
            p[0] = 1;
            p[1] = aluminum[i];
            p[2] = plastic[i];
```

Reproduced with permission of the copyright owner. Further reproduction prohibited without permission.

```
        p[3] = aluminum[i] * aluminum[i];
        p[4] = aluminum[i] * plastic[i];
        p[5] = plastic[i] * plastic[i];
        p[6] = aluminum[i] * aluminum[i] * aluminum[i];
        p[7] = aluminum[i] * aluminum[i] * plastic[i];
        p[8] = aluminum[i] * plastic[i] * plastic[i];
        p[9] = plastic[i] * plastic[i] * plastic[i];

        p[10] = -y * aluminum[i];
        p[11] = -y * plastic[i];
        p[12] = -y * aluminum[i] * aluminum[i];
        p[13] = -y * aluminum[i] * plastic[i];
        p[14] = -y * plastic[i] * plastic[i];}
      break;
case 14:  if (fitting == PLASTIC || fitting == ALUMINUM){ // 9 param sqr root
        p[0] = 1;
        p[1] = high[i];
        p[2] = low[i];
        p[3] = high[i] * high[i];
        p[4] = high[i] * low[i];
        p[5] = low[i] * low[i];

        p[6] = -y * high[i];
        p[7] = -y * low[i];

        p[8] = -y * y;}
      else{
        p[0] = 1;
        p[1] = aluminum[i];
        p[2] = plastic[i];
        p[3] = aluminum[i] * aluminum[i];
        p[4] = aluminum[i] * plastic[i];
        p[5] = plastic[i] * plastic[i];

        p[6] = -y * aluminum[i];
        p[7] = -y * plastic[i];

        p[8] = -y * y;}
      break;
case 16:  if (fitting == PLASTIC || fitting == ALUMINUM){ // 9 param linear
        p[0] = high[i];
        p[1] = low[i];

        p[2] = high[i] * high[i];
        p[3] = high[i] * low[i];
        p[4] = low[i] * low[i];
```

Reproduced with permission of the copyright owner. Further reproduction prohibited without permission.

```
            p[5] = high[i] * high[i] * high[i];
            p[6] = high[i] * high[i] * low[i];
            p[7] = high[i] * low[i] * low[i];
            p[8] = low[i] * low[i] * low[i];}
          else{
            p[0] = aluminum[i];
            p[1] = plastic[i];

            p[2] = aluminum[i] * aluminum[i];
            p[3] = aluminum[i] * plastic[i];
            p[4] = plastic[i] * plastic[i];

            p[5] = aluminum[i] * aluminum[i] * aluminum[i];
            p[6] = aluminum[i] * aluminum[i] * plastic[i];
            p[7] = aluminum[i] * plastic[i] * plastic[i];
            p[8] = plastic[i] * plastic[i] * plastic[i];}
          break;
case 17:    if (fitting == PLASTIC || fitting == ALUMINUM){ // 14 param linear
            p[0] = high[i];
            p[1] = low[i];

            p[2] = high[i] * high[i];
            p[3] = high[i] * low[i];
            p[4] = low[i] * low[i];

            p[5] = high[i] * high[i] * high[i];
            p[6] = high[i] * high[i] * low[i];
            p[7] = high[i] * low[i] * low[i];
            p[8] = low[i] * low[i] * low[i];

            p[9] = high[i] * high[i] * high[i] * high[i];
            p[10] = high[i] * high[i] * high[i] * low[i];
            p[11] = high[i] * high[i] * low[i] * low[i];
            p[12] = high[i] * low[i] * low[i] * low[i];
            p[13] = low[i] * low[i] * low[i] * low[i];}
          else{
            p[0] = aluminum[i];
            p[1] = plastic[i];

            p[2] = aluminum[i] * aluminum[i];
            p[3] = aluminum[i] * plastic[i];
            p[4] = plastic[i] * plastic[i];

            p[5] = aluminum[i] * aluminum[i] * aluminum[i];
            p[6] = aluminum[i] * aluminum[i] * plastic[i];
```

Reproduced with permission of the copyright owner. Further reproduction prohibited without permission.

```
            p[7] = aluminum[i] * plastic[i] * plastic[i];
            p[8] = plastic[i] * plastic[i] * plastic[i];

            p[9] = aluminum[i] * aluminum[i] * aluminum[i] * aluminum[i];
            p[10] = aluminum[i] * aluminum[i] * aluminum[i] * plastic[i];
            p[11] = aluminum[i] * aluminum[i] * plastic[i] * plastic[i];
            p[12] = aluminum[i] * plastic[i] * plastic[i] * plastic[i];
            p[13] = plastic[i] * plastic[i] * plastic[i] * plastic[i];}
          break;
case 18:    if (fitting == PLASTIC || fitting == ALUMINUM){ // 15 param linear
            p[0] = 1;
            p[1] = high[i];
            p[2] = low[i];

            p[3] = high[i] * high[i];
            p[4] = high[i] * low[i];
            p[5] = low[i] * low[i];

            p[6] = high[i] * high[i] * high[i];
            p[7] = high[i] * high[i] * low[i];
            p[8] = high[i] * low[i] * low[i];
            p[9] = low[i] * low[i] * low[i];

            p[10] = high[i] * high[i] * high[i] * high[i];
            p[11] = high[i] * high[i] * high[i] * low[i];
            p[12] = high[i] * high[i] * low[i] * low[i];
            p[13] = high[i] * low[i] * low[i] * low[i];
            p[14] = low[i] * low[i] * low[i] * low[i];}
          else{
            p[0] = 1;
            p[1] = aluminum[i];
            p[2] = plastic[i];

            p[3] = aluminum[i] * aluminum[i];
            p[4] = aluminum[i] * plastic[i];
            p[5] = plastic[i] * plastic[i];

            p[6] = aluminum[i] * aluminum[i] * aluminum[i];
            p[7] = aluminum[i] * aluminum[i] * plastic[i];
            p[8] = aluminum[i] * plastic[i] * plastic[i];
            p[9] = plastic[i] * plastic[i] * plastic[i];

            p[10] = aluminum[i] * aluminum[i] * aluminum[i] * aluminum[i];
            p[11] = aluminum[i] * aluminum[i] * aluminum[i] * plastic[i];
            p[12] = aluminum[i] * aluminum[i] * plastic[i] * plastic[i];
            p[13] = aluminum[i] * plastic[i] * plastic[i] * plastic[i];
```

Reproduced with permission of the copyright owner. Further reproduction prohibited without permission.

```
            p[14] = plastic[i] * plastic[i] * plastic[i] * plastic[i];}
          break;
    case 19:    if (fitting == PLASTIC || fitting == ALUMINUM){ // 10 param linear
            p[0] = 1;
            p[1] = high[i];
            p[2] = low[i];

            p[3] = high[i] * high[i];
            p[4] = high[i] * low[i];
            p[5] = low[i] * low[i];

            p[6] = high[i] * high[i] * high[i];
            p[7] = high[i] * high[i] * low[i];
            p[8] = high[i] * low[i] * low[i];
            p[9] = low[i] * low[i] * low[i];}
          else{
            p[0] = 1;
            p[1] = aluminum[i];
            p[2] = plastic[i];
            p[3] = aluminum[i] * aluminum[i];
            p[4] = aluminum[i] * plastic[i];
            p[5] = plastic[i] * plastic[i];
            p[6] = aluminum[i] * aluminum[i] * aluminum[i];
            p[7] = aluminum[i] * aluminum[i] * plastic[i];
            p[8] = aluminum[i] * plastic[i] * plastic[i];
            p[9] = plastic[i] * plastic[i] * plastic[i];}
          break;}}


void read_file(int *m){
  float  num;
  int    e;
  char   junk[120];

    for (*m = e = -1; e < 3; e++) fscanf(in_file,"%s",junk);
    while (!feof(in_file)){
      (*m)++;
      if (fscanf(in_file,"%f",&num) == EOF){
        (*m)--;
        return;}
      plastic[*m] = (double)num;
      if (fscanf(in_file,"%f",&num) == EOF){
        nrerror("end of file error");
        (*m)--;
        return;}
      aluminum[*m] = (double)num;
```

Reproduced with permission of the copyright owner. Further reproduction prohibited without permission.

```
      if (fscanf(in_file,"%f",&num) == EOF){
        nrerror("end of file error");
        (*m)--;
        return;}
      high[*m] = (double)num;
      if (fscanf(in_file,"%f",&num) == EOF){
        nrerror("end of file error");
        (*m)--;
        return;}
      low[*m] = (double)num;
      sal[*m] = spl[*m] = 1;//sqrt((1/exp(-high[*m])) + (1/exp(-low[*m])));
      sh[*m] = sl[*m] = 1;//sqrt((1/exp(plastic[*m])) + (1/exp(aluminum[*m])));
      printf("\nplastic = %f  aluminum = %f  high = %f  low = %f  sh = %f  sl = %f
",plastic[*m],aluminum[*m],high[*m],low[*m],sh[*m],sl[*m]);}}

double pythag(double a, double b){
  double absa,absb;

  absa=fabs(a);
  absb=fabs(b);
  if (absa > absb) return absa*sqrt(1.0+SQR(absb/absa));
  else return (absb == 0.0 ? 0.0: absb*sqrt(1.0+SQR(absa/absb)));}

void svdfit(double x[], double y[], double sig[], int ndata, double a[], int ma,
            double **u, double **v, double w[], double *chisq,
            void(*funcs)(double,double [],double)){
  void svbksb(double **u, double w[], double **v, int m, int n, double b[],
              double x[]);
  void svdcmp(double **a, int m, int n, double w[], double **v);
  int j,i,k;
  double wmax,tmp,thresh,sum,*afunc,*b;

  b = dvector(0,ndata);
  afunc=dvector(0,ma);
  for (i=0;i<=ndata;i++){
    (*funcs)(x[i],afunc,y[i]);
    tmp = 1.0/sig[i];
    for (j=0;j<=ma;j++) u[i][j]=afunc[j]*tmp;
    b[i] = y[i]*tmp;}
  svdcmp(u,ndata,ma,w,v);
  wmax=0.0;
  for (j=0;j<=ma;j++) if (w[j] > wmax) wmax = w[j];
  thresh = TOL*wmax;
  for (j=0;j<=ma;j++) if (w[j] < thresh) w[j] = 0.0;
  svbksb(u,w,v,ndata,ma,b,a);
  *chisq=0.0;
```

Reproduced with permission of the copyright owner. Further reproduction prohibited without permission.

```
  k = 0;
  for (i=0;i<=ndata;i++){
    (*funcs)(x[i],afunc,y[i]);   // x is the calibration point, afunc[2] is the high and low
transmission through that point
    for (sum=0.0,j=0;j<=ma;j++) sum += a[j]*afunc[j];  // Sum = a1 * L + a2 * H + a3 *
L*L + a4 * H*H + a5 * L*H
    *chisq = (tmp=(y[i]-sum)/sig[i],tmp*tmp);
    if ((model == 13) && (fitting == ALUMINUM)){
      printf("%f    ",tmp);
      k++;
      if (k > 6){
        printf("\n");
        k = 0;}}}
  free_dvector(afunc,0,ma);
  free_dvector(b,0,ndata);}


void svdcmp(double **a, int m, int n, double w[], double **v){
  double pythag(double a, double b);
  int flag,i,its,j,jj,k,l,nm;
  double anorm,c,f,g,h,s,scale,x,y,z,*rv1;

  rv1=dvector(0,n);
  g=scale=anorm=0.0;
  for (i = 0; i <= n; i++){
    l=i+1;
    rv1[i] = scale * g;
    g=s=scale=0.0;
    if (i <= m){
      for (k=i;k<=m;k++) scale += fabs(a[k][i]);
      if (scale){
        for (k=i;k<=m;k++){
          a[k][i] /= scale;
          s += a[k][i] * a[k][i];}
        f = a[i][i];
        g = -SIGN(sqrt(s),f);
        h = f*g-s;
        a[i][i]=f-g;
        for (j=l;j<=n;j++){
          for (s=0.0,k=i;k<=m;k++) s += a[k][i] * a[k][j];
          f = s/h;
          for (k=i;k<=m;k++) a[k][j] += f*a[k][i];}
        for (k=i;k<=m;k++) a[k][i] *= scale;}}
    w[i] = scale * g;
    g = s = scale = 0.0;
    if (i <= m && i != n){
```

Reproduced with permission of the copyright owner. Further reproduction prohibited without permission.

```
      for (k=l;k<=n;k++) scale += fabs(a[i][k]);
      if (scale){
        for (k=l;k<=n;k++){
          a[i][k] /= scale;
          s += a[i][k] * a[i][k];}
        f = a[i][l];
        g = -SIGN(sqrt(s),f);
        h = f*g-s;
        a[i][l] = f-g;
        for (k=l;k<=n;k++) rv1[k]=a[i][k]/h;
        for (j=l;j<=m;j++){
          for (s=0.0,k=l;k<=n;k++) s += a[j][k] * a[i][k];
          for (k=l;k<=n;k++) a[j][k] += s*rv1[k];}
        for (k=l;k<=n;k++) a[i][k] *= scale;}}
    anorm = FMAX(anorm,(fabs(w[i])+fabs(rv1[i])));}
  for (i=n;i>=0;i--){
    if (i<n){
      if (g){
        for (j=l;j<=n;j++) v[j][i]= (a[i][j]/a[i][l])/g;
        for (j=l;j<=n;j++){
          for (s=0.0,k=l;k<=n;k++) s += a[i][k]*v[k][j];
          for (k=l;k<=n;k++) v[k][j] += s*v[k][i];}}
      for (j=l;j<=n;j++) v[i][j] = v[j][i] = 0.0;}
    v[i][i]=1.0;
    g=rv1[i];
    l=i;}
  for (i=IMIN(m,n);i>=0;i--){
    l=i+1;
    g=w[i];
    for (j=l;j<=n;j++) a[i][j] = 0.0;
    if (g){
      g = 1.0/g;
      for (j=l;j <=n;j++){
        for (s=0.0,k=l;k<=m;k++) s += a[k][i]*a[k][j];
        f = (s/a[i][i])*g;
        for (k=i;k<=m;k++) a[k][j] += f*a[k][i];}
      for (j=i;j<=m;j++) a[j][i] *= g;}
    else for (j = i; j<=m;j++) a[j][i] = 0.0;
    ++a[i][i];}
  for(k=n;k>=0;k--){
    for (its=1;its<=30;its++){
      flag=1;
      for (l=k;l>=0;l--){
        nm=l-1;
        if ((double)(fabs(rv1[l])+anorm) == anorm){
          flag = 0;
```

Reproduced with permission of the copyright owner. Further reproduction prohibited without permission.

```
      break;}
    if ((double)(fabs(w[nm])+anorm) == anorm) break;}
  if (flag){
    c = 0.0;
    s = 1.0;
    for (i=l;i<=k;i++){
      f=s*rv1[i];
      rv1[i] = c*rv1[i];
      if ((double)(fabs(f)+anorm) == anorm) break;
      g = w[i];
      h = pythag(f,g);
      w[i] = h;
      h = 1.0/h;
      c = g*h;
      s = -f*h;
      for (j=0;j<=m;j++){
        y=a[j][nm];
        z=a[j][i];
        a[j][nm]=y*c+z*s;
        a[j][i]=z*c-y*s;}}}
  z = w[k];
  if (l == k){
    if (z < 0.0){
      w[k] = -z;
      for (j = 0; j<=n;j++) v[j][k] = -v[j][k];}
    break;}
  if (its == 30) nrerror("no convergence in 30 svdcmp iterations");
  x=w[l];
  nm=k-1;
  y=w[nm];
  g=rv1[nm];
  h=rv1[k];
  f=((y-z)*(y+z)+(g-h)*(g+h))/(2.0*h*y);
  g=pythag(f,1.0);
  f=((x-z)*(x+z)+h*((y/(f+SIGN(g,f)))-h))/x;
  c=s=1.0;
  for (j=l;j<=nm;j++){
    i=j+1;
    g=rv1[i];
    y=w[i];
    h=s*g;
    g=c*g;
    z=pythag(f,h);
    rv1[j]=z;
    c=f/z;
    s=h/z;
```

Reproduced with permission of the copyright owner. Further reproduction prohibited without permission.

```
            f=x*c+g*s;
            g=g*c-x*s;
            h=y*s;
            y *=c;
            for (jj=0;jj<=n;jj++){
              x=v[jj][j];
              z=v[jj][i];
              v[jj][j]=x*c+z*s;
              v[jj][i]=z*c-x*s;}
            z=pythag(f,h);
            w[j]=z;
            if (z) {
              z=1.0/z;
              c=f*z;
              s=h*z;}
            f=c*g+s*y;
            x=c*y-s*g;
            for (jj=0;jj<=m;jj++){
              y=a[jj][j];
              z=a[jj][i];
              a[jj][j] = y*c+z*s;
              a[jj][i] = z*c-y*s;}}
          rv1[l]=0.0;
          rv1[k]=f;
          w[k]=x;}}
  free_dvector(rv1,0,n);}

void svbksb(double **u, double w[], double **v, int m, int n, double  b[], double x[]){
  int jj,j,i;
  double s,*tmp;

  tmp = dvector(0,n);
  for (j=0;j<=n;j++){
    s = 0.0;
    if (w[j]){
      for (i=0;i<=m;i++) s += u[i][j]*b[i];
      s /= w[j];}
    tmp[j] = s;}
  for (j=0;j<=n;j++){
    s=0.0;
    for (jj=0;jj<=n;jj++) s += v[j][jj] * tmp[jj];
    x[j] = s;}
  free_dvector(tmp,0,n);}

void main(){
// x = linear count 1,2,3,4,...
```

Reproduced with permission of the copyright owner. Further reproduction prohibited without permission.

```
// aluminum = the thickness of the Al
// plastic = the thickness of the Pl
// sal = the standard deviations   sqrt((1/exp(low energy reading)) + (1/exp(high energy
reading)
// spl = the standard deviations   sqrt((1/exp(low energy reading)) + (1/exp(high energy
reading)
// m = number of calibration points Al-Pl combinations
// n = number of fitting coeficients - number of a's
// the_a is a global variable used in fill_matrix, the fitting function y = Sum(n) (a(n) *
fill_matrix(n)(x))
//          the_a contains the low (L) and high energy (H) log transmission readings
//        fill_matrix = a1 H + a2 L + a3 H*H + a4 L*L + a5 L*H
//                              p[1] = the_a[i][1];
//                              p[2] = the_a[i][2];
//                              p[3] = the_a[i][1] * the_a[i][1];
//                              p[4] = the_a[i][2] * the_a[i][2];
//                              p[5] = the_a[i][1] * the_a[i][2];
//        This is the calibration equation from Macovski Med Phys Vol 8, #5, spet oct 1981
equation 21 or 22
//        hence the names read_file21 and read_file22

  int  e,m,n;
  m=500;
  n=20;
  w = dvector(0,n);
  u = dmatrix(0,m,0,n);
  v = dmatrix(0,n,0,n);
  a = dvector(0,n);
  if ((in_file = fopen("thichplnasastepresults.txt","rt")) == NULL){
    printf("Error Opening File\n");
    exit(1);}
  read_file(&m);
  fclose(in_file);
  for (e = 0;e <= m; e++) x[e] = e;  // fill in linear count

  n = 7;
  model = 10;
  fitting = ALUMINUM;
  printf("\n\n8 param A/B case 10**************************************");
  svdfit(x,aluminum,sal,m,a,n,u,v,w,&chisq,fill_matrix);
  printf("\nThe aluminum fitting params are:");  // these are the fitting parameters
  printf("\n\n%f\n%f\n%f\n%f",a[0],a[1],a[2],a[3]);  // these are the fitting parameters
  printf("\n%f\n%f\n%f\n%f",a[4],a[5],a[6],a[7]);
  printf("\nChisq = %f",chisq);
  fitting = PLASTIC;
  svdfit(x,plastic,spl,m,a,n,u,v,w,&chisq,fill_matrix);
```

Reproduced with permission of the copyright owner. Further reproduction prohibited without permission.

```
printf("\n\nThe plastic fitting params are:"); // these are the fitting parameters
printf("\n\n%f\n%f\n%f\n%f",a[0],a[1],a[2],a[3]); // these are the fitting parameters
printf("\n%f\n%f\n%f\n%f",a[4],a[5],a[6],a[7]);
printf("\nChisq = %f",chisq);
fitting = HIGH;
svdfit(x,high,sh,m,a,n,u,v,w,&chisq,fill_matrix);
printf("\n\nThe high fitting params are:"); // these are the fitting parameters
printf("\n\n%f\n%f\n%f\n%f",a[0],a[1],a[2],a[3]); // these are the fitting parameters
printf("\n%f\n%f\n%f\n%f",a[4],a[5],a[6],a[7]);
printf("\nChisq = %f",chisq);
fitting = LOW;
svdfit(x,low,sl,m,a,n,u,v,w,&chisq,fill_matrix);
printf("\n\nThe low fitting params are:"); // these are the fitting parameters
printf("\n\n%f\n%f\n%f\n%f",a[0],a[1],a[2],a[3]); // these are the fitting parameters
printf("\n%f\n%f\n%f\n%f",a[4],a[5],a[6],a[7]);
printf("\nChisq = %f",chisq);

n = 17;
model = 12;
fitting = ALUMINUM;
printf("\n\n18 param sqr root case 12**************************");
svdfit(x,aluminum,sal,m,a,n,u,v,w,&chisq,fill_matrix);
printf("\nThe aluminum fitting params are:"); // these are the fitting parameters
printf("\n\n%f\n%f\n%f\n%f",a[0],a[1],a[2],a[3]); // these are the fitting parameters
printf("\n%f\n%f\n%f\n%f",a[4],a[5],a[6],a[7]);
printf("\n%f\n%f\n%f\n%f",a[8],a[9],a[10],a[11]);
printf("\n%f\n%f\n%f\n%f",a[12],a[13],a[14],a[15]);
printf("\n%f\n%f",a[16],a[17]);
printf("\nChisq = %f",chisq);
fitting = PLASTIC;
svdfit(x,plastic,spl,m,a,n,u,v,w,&chisq,fill_matrix);
printf("\n\nThe plastic fitting params are:"); // these are the fitting parameters
printf("\n\n%f\n%f\n%f\n%f",a[0],a[1],a[2],a[3]); // these are the fitting parameters
printf("\n%f\n%f\n%f\n%f",a[4],a[5],a[6],a[7]);
printf("\n%f\n%f\n%f\n%f",a[8],a[9],a[10],a[11]);
printf("\n%f\n%f\n%f\n%f",a[12],a[13],a[14],a[15]);
printf("\n%f\n%f",a[16],a[17]);
printf("\nChisq = %f",chisq);
fitting = HIGH;
svdfit(x,high,sh,m,a,n,u,v,w,&chisq,fill_matrix);
printf("\n\nThe high fitting params are:"); // these are the fitting parameters
printf("\n\n%f\n%f\n%f\n%f",a[0],a[1],a[2],a[3]); // these are the fitting parameters
printf("\n%f\n%f\n%f\n%f",a[4],a[5],a[6],a[7]);
printf("\n%f\n%f\n%f\n%f",a[8],a[9],a[10],a[11]);
printf("\n%f\n%f\n%f\n%f",a[12],a[13],a[14],a[15]);
printf("\n%f\n%f",a[16],a[17]);
```

Reproduced with permission of the copyright owner. Further reproduction prohibited without permission.

```
printf("\nChisq = %f",chisq);
fitting = LOW;
svdfit(x,low,sl,m,a,n,u,v,w,&chisq,fill_matrix);
printf("\n\nThe low fitting params are:"); // these are the fitting parameters
printf("\n\n%f\n%f\n%f\n%f",a[0],a[1],a[2],a[3]); // these are the fitting parameters
printf("\n%f\n%f\n%f\n%f",a[4],a[5],a[6],a[7]);
printf("\n%f\n%f\n%f\n%f",a[8],a[9],a[10],a[11]);
printf("\n%f\n%f\n%f\n%f",a[12],a[13],a[14],a[15]);
printf("\n%f\n%f",a[16],a[17]);
printf("\nChisq = %f",chisq);

n = 14;
model = 13;
fitting = ALUMINUM;
printf("\n\n15 param A/B case 13**************************************");
svdfit(x,aluminum,sal,m,a,n,u,v,w,&chisq,fill_matrix);
printf("\nThe aluminum fitting params are:"); // these are the fitting parameters
printf("\n\n%f\n%f\n%f\n%f",a[0],a[1],a[2],a[3]); // these are the fitting parameters
printf("\n%f\n%f\n%f\n%f",a[4],a[5],a[6],a[7]);
printf("\n%f\n%f\n%f\n%f",a[8],a[9],a[10],a[11]);
printf("\n%f\n%f\n%f",a[12],a[13],a[14]);
printf("\nChisq = %f",chisq);
fitting = PLASTIC;
svdfit(x,plastic,spl,m,a,n,u,v,w,&chisq,fill_matrix);
printf("\n\nThe plastic fitting params are:"); // these are the fitting parameters
printf("\n\n%f\n%f\n%f\n%f",a[0],a[1],a[2],a[3]); // these are the fitting parameters
printf("\n%f\n%f\n%f\n%f",a[4],a[5],a[6],a[7]);
printf("\n%f\n%f\n%f\n%f",a[8],a[9],a[10],a[11]);
printf("\n%f\n%f\n%f",a[12],a[13],a[14]);
printf("\nChisq = %f",chisq);
fitting = HIGH;
svdfit(x,high,sh,m,a,n,u,v,w,&chisq,fill_matrix);
printf("\n\nThe high fitting params are:"); // these are the fitting parameters
printf("\n\n%f\n%f\n%f\n%f",a[0],a[1],a[2],a[3]); // these are the fitting parameters
printf("\n%f\n%f\n%f\n%f",a[4],a[5],a[6],a[7]);
printf("\n%f\n%f\n%f\n%f",a[8],a[9],a[10],a[11]);
printf("\n%f\n%f\n%f",a[12],a[13],a[14]);
printf("\nChisq = %f",chisq);
fitting = LOW;
svdfit(x,low,sl,m,a,n,u,v,w,&chisq,fill_matrix);
printf("\n\nThe low fitting params are:"); // these are the fitting parameters
printf("\n\n%f\n%f\n%f\n%f",a[0],a[1],a[2],a[3]); // these are the fitting parameters
printf("\n%f\n%f\n%f\n%f",a[4],a[5],a[6],a[7]);
printf("\n%f\n%f\n%f\n%f",a[8],a[9],a[10],a[11]);
printf("\n%f\n%f\n%f",a[12],a[13],a[14]);
printf("\nChisq = %f",chisq);
```

Reproduced with permission of the copyright owner. Further reproduction prohibited without permission.

```
n = 8;
model = 14;
fitting = ALUMINUM;
printf("\n\n9 param sqr rt case 14*******************************");
svdfit(x,aluminum,sal,m,a,n,u,v,w,&chisq,fill_matrix);
printf("\nThe aluminum fitting params are:"); // these are the fitting parameters
printf("\n\n%f\n%f\n%f\n%f",a[0],a[1],a[2],a[3]); // these are the fitting parameters
printf("\n%f\n%f\n%f\n%f\n%f",a[4],a[5],a[6],a[7],a[8]);
printf("\nChisq = %f",chisq);
fitting = PLASTIC;
svdfit(x,plastic,spl,m,a,n,u,v,w,&chisq,fill_matrix);
printf("\n\nThe plastic fitting params are:"); // these are the fitting parameters
printf("\n\n%f\n%f\n%f\n%f",a[0],a[1],a[2],a[3]); // these are the fitting parameters
printf("\n%f\n%f\n%f\n%f\n%f",a[4],a[5],a[6],a[7],a[8]);
printf("\nChisq = %f",chisq);
fitting = HIGH;
svdfit(x,high,sh,m,a,n,u,v,w,&chisq,fill_matrix);
printf("\n\nThe high fitting params are:"); // these are the fitting parameters
printf("\n\n%f\n%f\n%f\n%f",a[0],a[1],a[2],a[3]); // these are the fitting parameters
printf("\n%f\n%f\n%f\n%f\n%f",a[4],a[5],a[6],a[7],a[8]);
printf("\nChisq = %f",chisq);
fitting = LOW;
svdfit(x,low,sl,m,a,n,u,v,w,&chisq,fill_matrix);
printf("\n\nThe low fitting params are:"); // these are the fitting parameters
printf("\n\n%f\n%f\n%f\n%f",a[0],a[1],a[2],a[3]); // these are the fitting parameters
printf("\n%f\n%f\n%f\n%f\n%f",a[4],a[5],a[6],a[7],a[8]);
printf("\nChisq = %f",chisq);

n = 8;
model = 16;
fitting = ALUMINUM;
printf("\n\n9 param linear case 16*********************************");
svdfit(x,aluminum,sal,m,a,n,u,v,w,&chisq,fill_matrix);
printf("\nThe aluminum fitting params are:"); // these are the fitting parameters
printf("\n\n%f\n%f\n%f\n%f",a[0],a[1],a[2],a[3]); // these are the fitting parameters
printf("\n%f\n%f\n%f\n%f\n%f",a[4],a[5],a[6],a[7],a[8]);
printf("\nChisq = %f",chisq);
fitting = PLASTIC;
svdfit(x,plastic,spl,m,a,n,u,v,w,&chisq,fill_matrix);
printf("\n\nThe plastic fitting params are:"); // these are the fitting parameters
printf("\n\n%f\n%f\n%f\n%f",a[0],a[1],a[2],a[3]); // these are the fitting parameters
printf("\n%f\n%f\n%f\n%f\n%f",a[4],a[5],a[6],a[7],a[8]);
printf("\nChisq = %f",chisq);
fitting = HIGH;
svdfit(x,high,sh,m,a,n,u,v,w,&chisq,fill_matrix);
```

Reproduced with permission of the copyright owner. Further reproduction prohibited without permission.

```
printf("\n\nThe high fitting params are:");  // these are the fitting parameters
printf("\n\n%f\n%f\n%f\n%f",a[0],a[1],a[2],a[3]);  // these are the fitting parameters
printf("\n%f\n%f\n%f\n%f\n%f",a[4],a[5],a[6],a[7],a[8]);
printf("\nChisq = %f",chisq);
fitting = LOW;
svdfit(x,low,sl,m,a,n,u,v,w,&chisq,fill_matrix);
printf("\n\nThe low fitting params are:");  // these are the fitting parameters
printf("\n\n%f\n%f\n%f\n%f",a[0],a[1],a[2],a[3]);  // these are the fitting parameters
printf("\n%f\n%f\n%f\n%f\n%f",a[4],a[5],a[6],a[7],a[8]);
printf("\nChisq = %f",chisq);


n = 13;
model = 17;
fitting = ALUMINUM;
printf("\n\n14 param linear case 17**********************************");
svdfit(x,aluminum,sal,m,a,n,u,v,w,&chisq,fill_matrix);
printf("\nThe aluminum fitting params are:");  // these are the fitting parameters
printf("\n\n%f\n%f\n%f\n%f",a[0],a[1],a[2],a[3]);  // these are the fitting parameters
printf("\n%f\n%f\n%f\n%f\n%f",a[4],a[5],a[6],a[7],a[8]);
printf("\n%f\n%f\n%f\n%f\n%f",a[9],a[10],a[11],a[12],a[13]);
printf("\nChisq = %f",chisq);
fitting = PLASTIC;
svdfit(x,plastic,spl,m,a,n,u,v,w,&chisq,fill_matrix);
printf("\n\nThe plastic fitting params are:");  // these are the fitting parameters
printf("\n\n%f\n%f\n%f\n%f",a[0],a[1],a[2],a[3]);  // these are the fitting parameters
printf("\n%f\n%f\n%f\n%f\n%f",a[4],a[5],a[6],a[7],a[8]);
printf("\n%f\n%f\n%f\n%f\n%f",a[9],a[10],a[11],a[12],a[13]);
printf("\nChisq = %f",chisq);
fitting = HIGH;
svdfit(x,high,sh,m,a,n,u,v,w,&chisq,fill_matrix);
printf("\n\nThe high fitting params are:");  // these are the fitting parameters
printf("\n\n%f\n%f\n%f\n%f",a[0],a[1],a[2],a[3]);  // these are the fitting parameters
printf("\n%f\n%f\n%f\n%f\n%f",a[4],a[5],a[6],a[7],a[8]);
printf("\n%f\n%f\n%f\n%f\n%f",a[9],a[10],a[11],a[12],a[13]);
printf("\nChisq = %f",chisq);
fitting = LOW;
svdfit(x,low,sl,m,a,n,u,v,w,&chisq,fill_matrix);
printf("\n\nThe low fitting params are:");  // these are the fitting parameters
printf("\n\n%f\n%f\n%f\n%f",a[0],a[1],a[2],a[3]);  // these are the fitting parameters
printf("\n%f\n%f\n%f\n%f\n%f",a[4],a[5],a[6],a[7],a[8]);
printf("\n%f\n%f\n%f\n%f\n%f",a[9],a[10],a[11],a[12],a[13]);
printf("\nChisq = %f",chisq);

n = 14;
model = 18;
```

Reproduced with permission of the copyright owner. Further reproduction prohibited without permission.

```
  fitting = ALUMINUM;
  printf("\n\n15 param linear case
18*****************************************");
  svdfit(x,aluminum,sal,m,a,n,u,v,w,&chisq,fill_matrix);
  printf("\nThe aluminum fitting params are:"); // these are the fitting parameters
  printf("\n\n%f\n%f\n%f\n%f",a[0],a[1],a[2],a[3]); // these are the fitting parameters
  printf("\n%f\n%f\n%f\n%f",a[4],a[5],a[6],a[7]);
  printf("\n%f\n%f\n%f\n%f",a[8],a[9],a[10],a[11]);
  printf("\n%f\n%f\n%f",a[12],a[13],a[14]);
  printf("\nChisq = %f",chisq);
  fitting = PLASTIC;
  svdfit(x,plastic,spl,m,a,n,u,v,w,&chisq,fill_matrix);
  printf("\n\nThe plastic fitting params are:"); // these are the fitting parameters
  printf("\n\n%f\n%f\n%f\n%f",a[0],a[1],a[2],a[3]); // these are the fitting parameters
  printf("\n%f\n%f\n%f\n%f",a[4],a[5],a[6],a[7]);
  printf("\n%f\n%f\n%f\n%f",a[8],a[9],a[10],a[11]);
  printf("\n%f\n%f\n%f",a[12],a[13],a[14]);
  printf("\nChisq = %f",chisq);
  fitting = HIGH;
  svdfit(x,high,sh,m,a,n,u,v,w,&chisq,fill_matrix);
  printf("\n\nThe high fitting params are:"); // these are the fitting parameters
  printf("\n\n%f\n%f\n%f\n%f",a[0],a[1],a[2],a[3]); // these are the fitting parameters
  printf("\n%f\n%f\n%f\n%f",a[4],a[5],a[6],a[7]);
  printf("\n%f\n%f\n%f\n%f",a[8],a[9],a[10],a[11]);
  printf("\n%f\n%f\n%f",a[12],a[13],a[14]);
  printf("\nChisq = %f",chisq);
  fitting = LOW;
  svdfit(x,low,sl,m,a,n,u,v,w,&chisq,fill_matrix);
  printf("\n\nThe low fitting params are:"); // these are the fitting parameters
  printf("\n\n%f\n%f\n%f\n%f",a[0],a[1],a[2],a[3]); // these are the fitting parameters
  printf("\n%f\n%f\n%f\n%f",a[4],a[5],a[6],a[7]);
  printf("\n%f\n%f\n%f\n%f",a[8],a[9],a[10],a[11]);
  printf("\n%f\n%f\n%f",a[12],a[13],a[14]);
  printf("\nChisq = %f",chisq);

  n = 9;
  model = 19;
  fitting = ALUMINUM;
  printf("\n\n10 param linear case
19*****************************************");
  svdfit(x,aluminum,sal,m,a,n,u,v,w,&chisq,fill_matrix);
  printf("\nThe aluminum fitting params are:"); // these are the fitting parameters
  printf("\n\n%f\n%f\n%f\n%f",a[0],a[1],a[2],a[3]); // these are the fitting parameters
  printf("\n%f\n%f\n%f\n%f",a[4],a[5],a[6],a[7]);
  printf("\n%f\n%f",a[8],a[9]);
  printf("\nChisq = %f",chisq);
```

Reproduced with permission of the copyright owner. Further reproduction prohibited without permission.

```
fitting = PLASTIC;
svdfit(x,plastic,spl,m,a,n,u,v,w,&chisq,fill_matrix);
printf("\n\nThe plastic fitting params are:"); // these are the fitting parameters
printf("\n\n%f\n%f\n%f\n%f",a[0],a[1],a[2],a[3]); // these are the fitting parameters
printf("\n%f\n%f\n%f\n%f",a[4],a[5],a[6],a[7]);
printf("\n%f\n%f",a[8],a[9]);
printf("\nChisq = %f",chisq);
fitting = HIGH;
svdfit(x,high,sh,m,a,n,u,v,w,&chisq,fill_matrix);
printf("\n\nThe high fitting params are:"); // these are the fitting parameters
printf("\n\n%f\n%f\n%f\n%f",a[0],a[1],a[2],a[3]); // these are the fitting parameters
printf("\n%f\n%f\n%f\n%f",a[4],a[5],a[6],a[7]);
printf("\n%f\n%f",a[8],a[9]);
printf("\nChisq = %f",chisq);
fitting = LOW;
svdfit(x,low,sl,m,a,n,u,v,w,&chisq,fill_matrix);
printf("\n\nThe low fitting params are:"); // these are the fitting parameters
printf("\n\n%f\n%f\n%f\n%f",a[0],a[1],a[2],a[3]); // these are the fitting parameters
printf("\n%f\n%f\n%f\n%f",a[4],a[5],a[6],a[7]);
printf("\n%f\n%f",a[8],a[9]);
printf("\nChisq = %f",chisq);

m=300;
n=20;
free_dmatrix(u,0,m,0,n);
free_dmatrix(v,0,n,0,n);
free_dvector(w,0,n);
free_dvector(a,0,n);}



/* Module "ranlmfit.h" (Header with Conventions and Prototypes)    */

#define PARDIM 20  /* maximal number of parameters: up to 20   */
#define DATDIM 500  /* maximal data of data points (up to 500)  */

#define NUL 0.0    /* for convenience                          */
#define ITMAX 10000   /* maximum number of iterations, changeable */
#define TRUE  1    /* to simulate boolean values               */
#define FALSE 0
#define INC 1.0E-5       /* increment in "derivative"          */
#define CRITERION 1.0E-19 /* of a small eigenvalue in "search"  */
#define EPSCONVER 1.0E-19  /* exit criterion in "significant"    */
#define MYMAX 1.0E19      /* maximal damping value in "search"  */

typedef double PARVEC [PARDIM];    /* vector type for parameter */
```

Reproduced with permission of the copyright owner. Further reproduction prohibited without permission.

```
typedef double MAT [PARDIM][PARDIM];/* parameter matrices      */
typedef double DATVEC [DATDIM];    /* vector type for data     */

typedef int BOOL ;              /* simulates boolean type   */

/* now protoypes of all functions used by "main"-"frame"       */

void   frame (void);              /* program frame       */
double predict (int k, PARVEC p);     /* the Model!          */
void   datinput(void);            /* data input          */
void   dumpdata(void);              /* dump all data as read */
void   checkinput(void);            /* check input data     */
void   inspect (void);            /* graphics of input data*/
void   itoutput (void);           /* intermediate output  */
void   finoutput (void);           /* final output        */
void   search (void);             /* fitting strategy     */
double squaresum (PARVEC p);         /* calc. of fit criterion*/
void   derivative (int k);          /* calc. of derivatives  */
void   fill (void);               /* fill inform. matrix   */
void   scale (void);              /* calcul. correl. matrix*/
void   decompose(void);             /* eigenvalue/eigenvector*/
void   explore (void);            /* explore param. point  */
void   find (void);               /* find new param. point */
BOOL   inside (PARVEC p);           /* check admissibility   */
void   accept (void);             /* accept new parameters */
BOOL   significant (PARVEC q1, PARVEC q2, double fq1,double fq2);
                          /* test for convergence  */
void nrerror(char error_text[]);
double *dvector(long nl, long nh);
double **dmatrix(long nrl, long nrh, long ncl, long nch);
void free_dvector(double *v, long nl, long nh);
void free_dmatrix(double **m, long nrl, long nrh, long ncl, long nch);
void fill_matrix(double x,double p[], double y);
double pythag(double a, double b);
void svdfit(double x[ ], double y[ ], double sig[ ], int ndata, double a[ ], int ma,
            double **u, double **v, double w[ ], double *chisq,
            void(*funcs)(double,double [ ],double));
void svdcmp(double **a, int m, int n, double w[], double **v);
void svbksb(double **u, double w[], double **v, int m, int n, double  b[ ], double x[ ]);

static double sqrarg;
#define SQR(a) ((sqrarg=(a)) == 0.0 ? 0.0:sqrarg*sqrarg)

static double maxarg1,maxarg2;
#define FMAX(a,b) (maxarg1=(a), maxarg2=(b), (maxarg1) > (maxarg2) ?\
(maxarg1):(maxarg2))
```

Reproduced with permission of the copyright owner. Further reproduction prohibited without permission.

```
static int iminarg1,iminarg2;
#define IMIN(a,b) (iminarg1=(a),iminarg2=(b),(iminarg1) < (iminarg2) ?\
(iminarg1):(iminarg2))

#define SIGN(a,b) ((b) > 0.0 ? fabs(a) : -fabs(a))

void nrerror(char error_text[ ]);

/*  end of header file ("ranlmfit.h")                    */
```

Reproduced with permission of the copyright owner. Further reproduction prohibited without permission.

APPENDIX D

LEVENBERG-MARQUARDT PROGRAM

This program is written in C for the Macintosh using Apple's free MPW compiler and performs a Levenberg-Marquardt fit to the transmission values such as those measured in appendix B using the starting values needed given by the least squares fitting routine in Appendix C.

```
#include <stdio.h>
#include "cbox1.h"              /* <math.h> here not necessary */
#include <math.h>

/* set of global definitions used by "frame" and by dependents:  */

int model;       /* model selector, useful in "predict"       */
int  m,n;       /* number of data and of parameters, resp.    */
             /* in C-language called from 0 to m-1, n-1 !  */

char  filename[255];

DATVEC x1,x2,response,aluminum,plastic,high,low;

PARVEC pstart,upper,lower;
             /* start vector of parameters, of upper and   */
             /*   lower permissible limits, n-vectors      */

PARVEC popt,sdev,d,eig;
             /* optimal vector of parameters (if found)    */
             /* vector of standard deviations              */
             /* vector -d- of scale factors                */
             /* vector -eig- of eigenvalues                */

double sqsum,my;     /* final value of sum of squares          */

DATVEC fit;       /* predictions of measurements after fitting  */

BOOL fullresp,redundant,conver;              /* diagnostic indices of course of search
*/

int it,i,fitting;          /* number of iterations as performed        */
```

Reproduced with permission of the copyright owner. Further reproduction prohibited without permission.

```
PARVEC dif, p,p1, grad;

MAT info,correl,bas,inv;

     /* matrices required for detailed study of algorithm    */
     /* info: information matrix G (eq. 2.5)                 */
     /* correl: its scaled form, correlation matrix           */
     /* bas: contains the eigenvectors of correl              */
     /* inv: the inverted matrix of J (eq.2.29)              */

#define PLASTIC 1
#define ALUMINUM 2
#define HIGH 3
#define LOW 4

void main(void){
  strcpy(filename,"thickplnasastepcalib2.dat");
  printf("\n\n%s\n",filename);
  datinput();
  fitting = ALUMINUM;
  fitting = PLASTIC;
  switch(fitting){
    case PLASTIC:    for (i = 0; i < m; i++){
                       x2[i] = high[i];
                       x1[i] = low[i];
                       response[i] = plastic[i];}
                     printf("Plastic fit ");
                     break;
    case ALUMINUM:         for (i = 0; i < m; i++){
                       x2[i] = high[i];
                       x1[i] = low[i];
                       response[i] = aluminum[i];}
                     printf("Aluminum fit ");
                     break;
    case HIGH:         for (i = 0; i < m; i++){
                       x1[i] = plastic[i];
                       x2[i] = aluminum[i];
                       response[i] = high[i];}
                     printf("High fit ");
                     break;
    case LOW :         for (i = 0; i < m; i++){
                       x1[i] = plastic[i];
                       x2[i] = aluminum[i];
                       response[i] = low[i];}
                     printf("Low fit ");
```

Reproduced with permission of the copyright owner. Further reproduction prohibited without permission.

```
            break;}
  dumpdata();
  checkinput();
  search();
  if (fullresp==TRUE || it > 1) finoutput();
  else {                /* if not: no sense in calling output! */
    printf("lack of response, check scale vector!");
    for (i=0; i<n; i++){
      printf("%18.6f",d[i]);
      if (i % 3 == 0) printf("\n");}}} /* "d" tells you which parameter is void   */

double predict (int k, PARVEC p){
   /*  this defines the fitting equation for the k-th data     */
   /*  point and parameter vector p.                          */
  /*  Attention! Errors are frequent! See section 3.4         */
   /*  requires global variable DATVEC x                      */
   /*  may require further user-defined globals which have     */
   /*  then to be included                                    */
   /*  in this example int model is included as selector       */

  extern int model;
  extern DATVEC x1;
  double acc,xa1,xa2,xa3,A,B,C,rad;
  int sw;

  sw = model;
  switch(sw){
    case 10:  A = p[0] + p[1] * x2[k] + p[2] * x1[k] + p[3]  * x2[k] * x2[k] + p[4] * x1[k]
* x2[k] + p[5] * x1[k] * x1[k];
          B = 1 + p[6] * x2[k] + p[7] * x1[k];
          C = 0;          // 8 param A/B
          acc = A / B;
          break;
    case 12:  A = p[0] + p[1] * x2[k] + p[2] * x1[k] + p[3]  * x2[k] * x2[k] + p[4] * x1[k]
* x2[k] + p[5] * x1[k] * x1[k] + p[6]  * x2[k] * x2[k] * x2[k] + p[7] * x2[k] * x2[k] *
x1[k] + p[8] * x2[k] * x1[k] * x1[k] + p[9] * x1[k] * x1[k] * x1[k];
          B = 1 + p[10] * x2[k] + p[11] * x1[k] + p[12]  * x2[k] * x2[k] + p[13] * x1[k] *
x2[k] + p[14] * x1[k] * x1[k];
          C = p[15] + p[16] * x2[k] + p[17] * x1[k];          // 18 param sqrt equation
          rad = B * B + 4 * A * C;
          //if (rad < 0) rad = 100000000;  // penalized neg square root
          rad = sqrt(rad);
          acc = (rad - B) / (2*C);
          break;
```

Reproduced with permission of the copyright owner. Further reproduction prohibited without permission.

```
    case 13:  A = p[0] + p[1] * x2[k] + p[2] * x1[k] + p[3]  * x2[k] * x2[k] + p[4] * x1[k]
* x2[k] + p[5] * x1[k] * x1[k] + p[6]  * x2[k] * x2[k] * x2[k] + p[7] * x2[k] * x2[k] *
x1[k] + p[8] * x2[k] * x1[k] * x1[k] + p[9] * x1[k] * x1[k] * x1[k];
            B = 1 + p[10] * x2[k] + p[11] * x1[k] + p[12]  * x2[k] * x2[k] + p[13] * x1[k] *
x2[k] + p[14] * x1[k] * x1[k];
            C = 0;          // 15 param A/B
            acc = A / B;
            break;
    case 14:  A = p[0] + p[1] * x2[k] + p[2] * x1[k] + p[3]  * x2[k] * x2[k] + p[4] * x1[k]
* x2[k] + p[5] * x1[k] * x1[k];
            B = 1 + p[6] * x2[k] + p[7] * x1[k];
            C = p[8];               // 9 param sqrt equation
            rad = B * B + 4 * A * C;
            //if (rad < 0) rad = 100000000;  // penalized neg square root
            rad = sqrt(rad);
            acc = (rad - B) / (2*C);
            break;
    case 16:  acc = p[0] * x2[k] + p[1] * x1[k] + p[2]  * x2[k] * x2[k] + p[3] * x1[k] *
x2[k] + p[4] * x1[k] * x1[k] + p[5]  * x2[k] * x2[k] * x2[k] + p[6] * x2[k] * x2[k] * x1[k]
+ p[7] * x2[k] * x1[k] * x1[k] + p[8] * x1[k] * x1[k] * x1[k];
            // 9 param linear equation
            break;
    case 17:  acc = p[0] * x2[k] + p[1] * x1[k] + p[2]  * x2[k] * x2[k] + p[3] * x1[k] *
x2[k] + p[4] * x1[k] * x1[k] + p[5]  * x2[k] * x2[k] * x2[k] + p[6] * x2[k] * x2[k] * x1[k]
+ p[7] * x2[k] * x1[k] * x1[k] + p[8] * x1[k] * x1[k] * x1[k] + p[9] * x2[k] * x2[k] *
x2[k] * x2[k] + p[10] * x2[k] * x2[k] * x2[k] * x1[k] + p[11] * x2[k] * x2[k] * x1[k] *
x1[k] + p[12] * x2[k] * x1[k] * x1[k] * x1[k] + p[13] * x1[k] * x1[k] * x1[k] * x1[k];
            // 14 param linear equation
            break;
    case 18:  acc = p[0] + p[1]  * x2[k] + p[2] * x1[k] + p[3]  * x2[k] * x2[k] + p[4] *
x1[k] * x2[k] + p[5] * x1[k] * x1[k] + p[6]  * x2[k] * x2[k] * x2[k] + p[7] * x2[k] * x2[k]
* x1[k] + p[8] * x2[k] * x1[k] * x1[k] + p[9] * x1[k] * x1[k] * x1[k] + p[10] * x2[k] *
x2[k] * x2[k] * x2[k] + p[11] * x2[k] * x2[k] * x2[k] * x1[k] + p[12] * x2[k] * x2[k] *
x1[k] * x1[k] + p[13] * x2[k] * x1[k] * x1[k] * x1[k] + p[14] * x1[k] * x1[k] * x1[k] *
x1[k];
            // 15 param linear equation
            break;
    case 19:  acc = p[0] + p[1] * x2[k] + p[2] * x1[k] + p[3]  * x2[k] * x2[k] + p[4] *
x1[k] * x2[k] + p[5] * x1[k] * x1[k] + p[6]  * x2[k] * x2[k] * x2[k] + p[7] * x2[k] * x2[k]
* x1[k] + p[8] * x2[k] * x1[k] * x1[k] + p[9] * x1[k] * x1[k] * x1[k];
            // 10 param linear equation
            break;
}  /* end of the whole switch */

  return (acc);}      /* all switch cases jump to this exit */
```

Reproduced with permission of the copyright owner. Further reproduction prohibited without permission.

```
void datinput (void){
 /* A simple way to transmit input data. Others are possible.   */
 /* A predefined file "indata." is assumed, of the form of the  */
 /* sets in section 3.15 (see there), namely:                   */
 /* int model, m, n, DATVEC x-response-pairs,                   */
 /* PARVEC pstart-upper-lower triples                           */
  extern int model, m, n;
  extern DATVEC x1,x2, response,response2;
  extern PARVEC pstart, upper, lower;
  int i, k;
  FILE *infile;                 /*      a file pointer     */

  infile = fopen (filename,"r");     /*  points now to "indata." */
  fscanf(infile,"%i%i%i",&model,&m,&n);    /* reads data        */
  for (k=0; k<m; k++)
fscanf(infile,"%lf%lf%lf%lf",&plastic[k],&aluminum[k],&high[k],&low[k]);
  for (i=0; i<n; i++){
    fscanf(infile,"%lf",&pstart[i]);
    upper[i] = 10000;
    lower[i] = -10000;}
  fclose(infile);}

void dumpdata (void){
 /* function echoes input data, for detection of format errors  */
 extern int model, m, n;
 extern DATVEC x1,response,fit;
 extern PARVEC pstart, upper, lower;
 int i, k;
 DATVEC dev;
  printf("\nModel selector: %2i", model);
  printf("\nNumber of observations: %3i",m);
  printf("\nNumber of parameters: %3i",n);
  printf("\nIndependent variable:\n");
  for (k=0; k<m; k++){
    printf("%16.6f%16.6f",x1[k],x2[k]);
    if (k % 4 ==3) printf("\n");}
  printf("\nResponse Vector\n");
  for (k=0; k<m; k++){
    printf("%16.6f",response[k]);
    if (k % 4 ==3) printf("\n");}
  printf("\nStart vector, upper and lower limits:\n");
  for (i=0; i<n; i++){
    printf("%16.8f",pstart[i]);
    if (i % 4 ==3) printf("\n");}
  printf("\n");
  for (i=0; i<n; i++){
```

Reproduced with permission of the copyright owner. Further reproduction prohibited without permission.

```
    printf("%16.1f",upper[i]);
    if (i % 4 ==3) printf("\n");}
  printf("\n");
  for (i=0; i<n; i++){
    printf("%16.1f",lower[i]);
    if (i % 4 ==3) printf("\n");}
  printf("\nInitial fit, predict: \n");

  for (k=0; k<m; k++) fit[k]=predict(k,pstart);
  for (k=0; k<m; k++){
    printf("%16.6f   ",fit[k]);
    if (k % 7 ==6) printf("\n");}
  for (k=0; k<m; k++) dev[k]=fit[k]-response[k];          /* residual vector */
  printf("\nResiduals: \n");
  for (k=0; k<m; k++){
    printf("%16.7f   ",dev[k]);
    if (k % 7 ==6) printf("\n");}
  printf("\n");}

  void checkinput (void){
/* Calculation of initial fit criterion                    */
/* Only if this is successful there can start a fitting cycle   */
/* User may add plausibility tests, e.g. limits of start-vector */
/* or others according to knowledge of data structure          */
extern int m;
extern DATVEC response;
extern PARVEC pstart;
int k;
double fst, depot, acc;

  printf("attempt to calculate initial fit criterion\n");
  printf("an interrupt points to bug in model or data structure\n");
  depot = 0.0;
  for (k=0; k<m; k++){
    acc  = predict(k,pstart);
    acc -= response[k];
    depot += acc * acc;}
  fst = depot;
  printf("\n\nsuccessful calculation, root of mean square%18.8f",sqrt(fst/m));
  depot = 0.0;
  for (k=0; k<m; k++) depot += response[k];
  if (depot > 0.0) depot = sqrt(fst/m)/depot*m*100.0;
  printf("\nin percent of average response:%8.1f\n\n",depot);
  if (depot > 50.0) printf("\nHigh value! Better start available?\n\n");}
```

Reproduced with permission of the copyright owner. Further reproduction prohibited without permission.

```
void inspect (void){
 /* so far only a dummy. User may declare externs and use them   */
 /* for graphid output, possibly with a device to improve the    */
 /* start vector                                                 */
 } /* end of inspect and of box 7  */

void itoutput(void){
 /* during each iteration (counter it) the decadic exponent of   */
 /* my and f is displayed in one line. It is a short statement   */
 /* of what is going on during the iteration cycle               */

  extern double my,f;
  extern int it;
  int expmy;

  expmy = (int) (log10(my) + 0.5);  /* rounding the exponent of "my"   */
  if (my < 1) expmy--;    /* correcting in the case of a negative value  */
}


void finoutput(void){
 /* the final output and mathematical analysis of the final fit! */
 /* the formalism is described in section 2.10                   */

 /* particular statistical quantities as calculated:             */
 /* - optimal parameter set with standard error, eq.2.33         */
 /* - final value of fit criterion, eq. 1.3                      */
 /* - eigenvalues of correlation matrix (eq.2.20, matrix L)      */
 /* - optimal prediction versus measured response (eq. 2.36)     */
 /* - run test on residuals (eq. 2.40, 41)                       */
 /* - neighborhood correlation of residuals (eq. 2.43)           */
 /* - test on m/2 positive signs: eq. 2.37                       */
 /* - diagnostic booleans                                        */

 /* the following globals are required for the final fit:        */
  extern int it, m, n;
  extern double sqsum;
  extern PARVEC popt, sdev, eig, d;
  extern DATVEC response, fit;
  extern BOOL fullresp, conver, redundant;
  int i, k, pluses, runs;
  double rho, depot, store, ax1, ax2, ay1, ay2, ak, acc;
  DATVEC dev;

  printf("\nFinal parameter values:\n");
  for (i=0; i<n; i++){
```

Reproduced with permission of the copyright owner. Further reproduction prohibited without permission.

```
  printf("%14.8f  ",popt[i]);
  if (i % 7 ==6) printf("\n");}
printf("\nStandard deviations:\n");
for (i=0; i<n; i++){
  printf("%12f  ",sdev[i]);
  if (i % 7 ==6) printf("\n");}
if (eig[n-1]<CRITERION) printf("\nAt least one redundant direction deleted!\n");
printf("\nScale vector at final point:\n");
for (i=0; i<n; i++){
  printf("%12f  ",d[i]);
  if (i % 7 ==6) printf("\n");}
printf("\nEigenvalues of correlation matrix:\n");
for (i=0; i<n; i++){
  printf("%12f  ",eig[i]);
  if (i % 7 ==6) printf("\n");}
printf("\nFit criterion at final point: %12f\n", sqsum);
depot=0.0;
for (k=0; k<m; k++) depot += response[k];
printf("Root of mean square, percent of average response:");
if (depot > 0.0) depot = sqrt(sqsum/m) / depot*m*100;
printf("%6.1f", depot);
for (k=0; k<m; k++) fit[k]=predict(k,popt);
printf("\nFinal fit, predict: \n");
for (k=0; k<m; k++){
  printf("%16.6f  ",fit[k]);
  if (k % 7 ==6) printf("\n");}
printf("\nVersus response: \n");
for (k=0; k<m; k++){
  printf("%16.6f  ",response[k]);
  if (k % 7 ==6) printf("\n");}
for (k=0; k<m; k++)
dev[k]=fit[k]-response[k];          /* residual vector */
ax1 = ay1 = ak = 0.0;
runs=1;
printf("\nResiduals: \n");
for (k=0; k<m; k++){
  printf("%16.7f  ",dev[k]);
  if (k % 7 ==6) printf("\n");}
if (dev[m-1]>0) pluses=1;
else pluses=0;
for (k=0; k<m-1; k++){
  if (dev[k]>0) pluses++;
  if (dev[k]*dev[k+1] <= 0) runs++;
  ax1 += dev[k];          /* sum of residual vectors */
  ay1 += dev[k+1];}
ax1 /= (m-1);
```

Reproduced with permission of the copyright owner. Further reproduction prohibited without permission.

```
  ay1 /= (m-1);              /* mean of residual vectors */
  ax2 = ay2 = 0.0;
  for (k=0; k<m-1; k++){
    ax2 += (dev[k]-ax1)*(dev[k]-ax1);
     ay2 += (dev[k+1]-ay1)*(dev[k+1]-ay1);
    ak  += (dev[k]-ax1)*(dev[k+1]-ay1);}
  if (ax2*ay2 != 0.0) rho = ak/sqrt(ax2*ay2);
  else rho=0.0;          /* neighborhood correlation coefficient */
  printf("\nCorrelation coefficient of neighbors, deg. of freedom:\n");
  printf(" %7.4f    %4i: ", rho, m-3);
  if (fabs(rho) < 1.7/sqrt(m-1)) printf("not significant!\n");
  else printf("significant! Indicates systematic deviations!\n");
  printf("Number of plus deviations: %3i out of %3i: ", pluses, m);
  if (m >= 6){
    if (fabs(2*pluses-m) < 1.645 * sqrt(m)) printf("not significant!\n");
    else printf("significant! Outliers present?\n");}
  else printf("not enough data for statistics!\n");
  printf("Number of runs: %3i:  ", runs);
  depot=2.0 * pluses *(m-pluses) / m + 1.0;
  if (pluses >= 4 && m-pluses >= 4){
    store=1.645*sqrt((depot-1)*(depot-2)/(m-1));
    if (runs<=depot+0.5+store && runs>=depot-0.5-store)
    printf("not significant!\n");
    else printf("significant! Indicates systematic trends!\n");}
  else printf("Not enough data for statistics!\n");
  printf("Diagnostic indices: ");
  if (conver==FALSE) printf("no ");
  printf("convergence obtained.\n");
  if (fullresp==FALSE) printf("Lack of response at final point!\n");
  if (redundant==TRUE) printf("Parameter redundancy!\n");
  else printf("No parameter redundancy!\n");
  printf("Iterations until exit: %i\n",it);
  depot = 0.0;
  for (k=0; k<m; k++){
    acc  = predict(k,popt);
    acc -= response[k];
    depot += acc * acc;}
  printf("successful calculation, root of mean square%18.8f\n",sqrt(depot/m));
  printf("End of program, follows graphics (if programmed)");
  inspect();} /* end of "finoutput" and of module box 9 */

/* "Search" is the main routine that steers the curve fitting   */
/* explained in detail in chapter 2, in particular section 2.7  */

/*  Presupposes the header files in "cbox1.h"                   */
/*  "Search" is called by "frame", requires globals from there  */
```

Reproduced with permission of the copyright owner. Further reproduction prohibited without permission.

```
/*  "search" has a few own globals and constants. Definitions:  */

double my,f,f1,fold;     /* my: damping factor; the f's are    */
                  /* fit criteria during iteration      */

PARVEC dif,p,p1,pold,grad; /* dif: derivatives; p,p1 contain    */
                  /* parameter values during iteration  */

void search (void){
 /* the following extern variables are defined and explained at  */
 /* the head of "frame" in "cbox1.h"                             */
  extern int m,n;
  extern DATVEC x1, response;
  extern PARVEC pstart, upper, lower;
  extern PARVEC popt, sdev, d, eig;
  extern double sqsum;
  extern DATVEC fit;
  extern BOOL fullresp, redundant, conver;
  extern int it;
  extern MAT info, correl, bas, inv;
  BOOL success;
  int i;
                  /* steps are defined in table 3.1   */
  my=0.01;              /*   this starts step 1          */
  it=0;
  for (i=0; i<n; i++) p[i]=pstart[i];
  f = squaresum (p);     /* initial sum of squares         */
  for (i=0; i<n; i++) pold[i]=p[i];
  fold=f;
  do{                        /* main iteration loop, step 2   */
    success = FALSE;                    /*   step 3   */
    explore();                        /*   step 4   */
    it++;                             /*   step 5   */
    if (fullresp==TRUE)                 /*   step 6   */
      while (my<=MYMAX && success==FALSE){   /*   step 7   */
              /* this starts the my-loop (damping loop) */
        find();                         /*   step 8   */
        if (inside(p1)==TRUE){              /*   step 9   */
          f1=squaresum(p1);       /* test of new parameter vector */
          if (f1<f){                    /*   step 10  */ /* better parameter vector    */
            accept();                   /* steps 11 and 12 */
            success=TRUE;}}                 /*   step 13  */
        my *= 10.0;                     /*   step 14  */
        itoutput();}}                 /* iteration output:cbox9.c */
                        /* the "still progress" condition to continue the do-loop:     */
```

Reproduced with permission of the copyright owner. Further reproduction prohibited without permission.

```
  while (it<ITMAX && success==TRUE && significant(pold,p,fold,f)==TRUE); /*
step 16 */
  if (success==TRUE) explore();                    /* step 17 */
  if (fullresp==FALSE) conver=FALSE ;
  else{
    redundant = FALSE;
    for ( i=0; i<n; i++) if (eig[i]<CRITERION) redundant = TRUE;
    find();
    if (m>n) for ( i=0; i<n; i++) sdev[i]= sqrt(inv[i][i]*f/(m-n));
    conver= significant(p,p1,f,f)==TRUE ? FALSE : TRUE ;}
  for ( i=0; i<n; i++) popt[i]=p[i];
  sqsum=f;              // end of search
  return;}        /* end of "search" and of module box 10 */

double squaresum (PARVEC p){
   /* calculates the sum of squared deviations (fit criterion) */
   /* for the proposed parameter vector p , eq.1.3, without    */
   /* weighting (see chapter 6 for that matter)                */

   /* requires global variables from "cbox1.h"                 */
   /* int m, DATVEC response                                   */
   /* calls function "predict"                                 */
  extern int m;
  extern DATVEC response;
  double depot = 0.0;
  double acc;
  int k;
  for (k=0; k<m; k++){
    acc = predict(k,p) - response[k];
    depot += acc*acc;}
  return (depot);}        /* end of "squaresum" and of module box 11 */

void derivative (int k){
 /* this function calculates, by a difference formula, the     */
 /* contribution of the k-th data point to the derivative with */
 /* respect to each one of the parameters, i.e. it fills the   */
 /* global vector PARVEC dif. See section 2.3, eq. 2.14        */

 /* "derivative" calls function "predict"                      */

 /* requires global variables from "cbox1.h"                   */
 /* int n, PARVEC p, and the constant INC (defined Box 10)     */
  extern int n;
  extern PARVEC p, dif;
  PARVEC incp,decp;  int j;
  double del,ps, finc, fdec;
```

Reproduced with permission of the copyright owner. Further reproduction prohibited without permission.

```
 for (j=0; j<n; j++){
   incp[j] = p[j];
   decp[j] = p[j];}
 for (j=0; j<n; j++){
   ps  = p[j];
   del = INC * ps;    /* "INC" is a global relative increment   */
   if (ps==0.0)       /* defined in "cbox1.h"                   */
     del=INC;
   incp[j] = ps + del;          /* increased parameter value   */
   decp[j] = ps - del;          /* decreased parameter value   */
   finc    = predict(k,incp);    /* function value of incp     */
   fdec    = predict(k,decp);    /* function value of decp     */
   dif[j]  = (finc-fdec)/2.0/del; /* central difference formula  */
   incp[j] = ps;                /* returning to original value */
   decp[j] = ps;}}   /* end of "derivative" and of module box 12 */


void fill (void){
 /* this function fills the information matrix (eq.2.5) and the */
 /* gradient (eq. 2.1) by a difference procedure explained in   */
 /* section 2.3                                                 */

 /*"fill" calls function "derivative" returning PARVEC dif     */
 /*      calls function "predict"                              */

 /* requires global variables from "cbox1.h"                   */
 /* int m, int n, DATVEC response                              */
 /* fills global variables BOOL fullresp, MAT info,            */
 /*                        PARVEC grad, d                      */

 extern int m,n;
 extern DATVEC response;
 extern PARVEC p, grad, d, dif;
 extern MAT info;
 extern BOOL fullresp;

 int i,j,k;

  fullresp=TRUE;
  for (i=0; i<n; i++)
   {
    for (j=i; j<n; j++)
     info[i][j]=0.0;
    grad[i]=0.0;
   }
```

Reproduced with permission of the copyright owner. Further reproduction prohibited without permission.

```
  for (k=0; k<m; k++)
   {
    derivative(k);
    for (i=0; i<n; i++)
     {
      for (j=i; j<n; j++)
       info[i][j] += dif[i] * dif[j];
      grad[i]    += dif[i]*(predict(k,p)-response[k]);
     }
   }
  for (i=0; i<n; i++)
   {
    d[i] =sqrt(info[i][i]);
    if (d[i]==0.0)
     fullresp=FALSE;
    for (j=0; j<i; j++)
     info[i][j]=info[j][i];}}  /* end of "fill" and of module box 13 */


void scale (void){
    /* this function reduces the global "info"-matrix to its   */
    /* scaled form "correl", using the scale vector "d"        */
    /* see section 2.4, eqs. 2.15, 2.16                        */

    /* requires global variables from "cbox1.h"                */
    /* int n, PARVEC d, MAT info                               */
    /* returns  global variable MAT correl                     */
  extern int n;
  extern PARVEC d ;
  extern MAT info, correl;
  int i,j;

  for (i=0; i<n; i++)
    for (j=i; j<n; j++){
      correl[i][j] = info[i][j]/d[i]/d[j];
      correl[j][i] = correl[i][j];}}          /* end of  "scale" and of module box 14 */


void decompose(void){
 /* symmetric n*n "bas", a correlation matrix, is transformed   */
 /* to its eigensystem by an iterative procedure due to         */
 /* H.F. Kaiser (Comp. J. 15 (1972) 271-273)                    */
 /* "bas" is overwritten; result is eigenvector matrix          */
 /* n-vector "eig" receives eigenvalues decreasingly ordered    */
 /* see explanation in section 2.5                              */
```

Reproduced with permission of the copyright owner. Further reproduction prohibited without permission.

```
/* requires global int n                                    */
/* requires and changes global MAT bas                      */
/* fills PARVEC eig                                         */
 extern int n;
 extern MAT bas;
 extern PARVEC eig;
 #define EPSANGLE 1.0E-8
 #define ITBOUND 10
 double scalprod,ww,wij,wih,jlong,hlong;
 int i,j,h,ki,ni,itcount;
 double teta,cteta,steta,flip,ac,le;

 itcount=0;
 ni = n * (n-1)/2;
 ki=ni;
 do{
   ++itcount;
   for (j=0; j<n-1; j++){
     for (h=j+1; h<n; h++){
       scalprod = jlong = hlong = 0.0;
     for (i=0; i<n; i++){
       wij = bas [i][j];
       wih = bas [i][h];
       scalprod += wij*wih;
       jlong    += wij*wij;
       hlong    += wih*wih;}
     le=sqrt(jlong*hlong);
     if (le > 0.0) ac = fabs(scalprod/le);
     else ac = 0.0;
     scalprod += scalprod;
       ww = jlong-hlong;
     if ((ac>EPSANGLE)||(ww<0.0)){
       if((fabs(ww)>=fabs(scalprod))){
         teta =fabs(scalprod/ww);
         cteta=1.0/sqrt(1.0+teta*teta);
         steta=teta*cteta;}
       else{
         teta =fabs(ww/scalprod);
         steta=1.0/sqrt(1.0+teta*teta);
         cteta=steta*teta;}
       cteta =sqrt((1.0+cteta)/2.0);
       steta /= 2.0*cteta;
       if (ww<0.0){
         flip  = cteta;
         cteta = steta;
         steta = flip;}
```

Reproduced with permission of the copyright owner. Further reproduction prohibited without permission.

```
        if (scalprod<0.0) steta = -steta;
        for (i=0; i<n; i++){
          flip = bas[i][j];
          bas[i][j] = bas [i][h]*steta + flip * cteta;
          bas[i][h] = bas [i][h]*cteta - flip * steta;}
        ki = ni;}          /* of if ac>EPSANGLE etc. */
      else
        ki--;}}}        /* of h-loop  */
  while ((ki>0)&&(itcount<ITBOUND)); /* now calculation of eigenvalues */
  for (j=0; j<n; j++){
    eig[j]=0.0;
    for (i=0; i<n; i++) eig[j] += bas[i][j]*bas[i][j];
    eig[j]=sqrt(eig[j]);}/* now calculation of eigenvectors  */
  for (j=0; j<n; j++){
    if (eig[j]!=0.0) for (i=0; i<n; i++) bas[i][j] /= eig[j];}
  return;}  /* end of "decompose" and of module box 15  */


void explore(void){
 /* this function fills gradient (eq.2.1) and information matrix */
 /* (eq.2.5), scales it (eqs. 2.15 and 2.16), and finds the      */
 /* the eigensystem decomposition (eq. 2.20)                     */

 /* module requires global variables from "cbox1.h"             */
 /* int n, BOOL fullresp, MAT correl                            */
 /* returns global variable MAT bas                            */
 /* calls functions "fill" and "decompose"                      */
  extern n;
  extern BOOL fullresp;
  extern MAT correl, bas ;
  int i,j;

  fill ();              /* fills vector grad and matrix info */
                      /* eqs. 2.1 and 2.5 !              */
  if (fullresp==TRUE){
    scale();                              /* eq. 2.16 ! */
            /* scales "info" to "correl", scale vector "d" */
  for (j=0; j<n; j++)
    for (i=0; i<n; i++) bas[i][j] = correl[i][j];
  decompose();}}  /* decomposition of "correl"-matrix (eq.2.20)  */



void find (void){
 /* this module calculates, for a given my-value and for given  */
 /* principal axes and eigenvalues, a new trial parameter       */
```

Reproduced with permission of the copyright owner. Further reproduction prohibited without permission.

```
 /* (eqs. 2.29 and 2.30)                                    */

 /* requires global variables as defined in "cbox1.h"       */
 /* int n, double my, PARVEC eig, d, p, grad, MAT bas       */
 /* fills MAT inv, PARVEC p1                                */
  extern int n;
  extern double my;
  extern PARVEC eig, d, p, grad, p1;
  extern MAT bas, inv;
  int h,i,j;
  double depot;
  for (i=0; i<n; i++)
    for (j=0; j<n; j++){
      depot=0.0;              /*  for accumulation of inverse  */
      for (h=0; h<n; h++)
      if (my>0.0 || my==0.0 && eig[h]>1.0e-6)
      depot += bas[i][h] * bas[j][h] / d[i] / d[j] / (eig[h]+my);
      inv[i][j]= inv[j][i] = depot;}      /* see eq. 2.39 !  */
    for (i=0; i<n; i++){
      depot=0.0;                  /* for accumulation of step  */
      for (j=0; j<n; j++)
      depot -= inv[i][j] * grad[j];       /* see eq. 2.30 !   */
      p1[i] = p[i] + depot;}}      /* end of "find" and of module box 17 */


BOOL inside (PARVEC p){
  /*  this module has the only task to prevent too large a step */
  /*  further attempts with higher damping factor will follow   */
  /*  inside == TRUE means that the step remains within limits  */

  /*  requires global variables from "cbox1.h"                */
  /*  int n, PARVEC p, upper, lower                           */
  extern int n;
  extern PARVEC upper, lower;
  int i;
  BOOL outside;

  outside = FALSE;
  for (i=0; i<n; i++) if (p[i]>=upper[i] || p[i]<=lower[i] ) outside = TRUE;
  return (outside==TRUE ?  FALSE : TRUE );}        /* end of "inside" and of module
box 18 */
```

Reproduced with permission of the copyright owner. Further reproduction prohibited without permission.

```
void accept (void){
  /* this function performs restoring of old and current para- */
  /* ter vectors and of pertinent fit criteria after accepting */

  /* requires global variables from "cbox1.h"              */
  /* int n, double f1, PARVEC p1                    */
  /* requires and changes PARVEC p, double f          */
  /* fills new PARVEC pold, double fold, my           */
  extern int n;
  extern double f, f1, fold, my;
  extern PARVEC p, p1, pold;
  int i;
  for (i=0; i<n; i++){
    pold[i] = p[i];
    p[i] = p1[i];}
  fold = f ;
  f = f1;
  my /= 100.0;}        /* end of "accept" and of module box 19 */


BOOL significant (PARVEC q1, PARVEC q2, double fq1, double fq2){
 /* "significant" becomes true when the step between parameter  */
 /* vectors q1 and q2 is either long enough or improves the fit */
 /* criterion fq2 over fq1 significantly.                */

 /* requires global variable from "cbox1.h"              */
 /* int n,  constant EPSCONVER (defined Box 10)          */

  extern int n;
  BOOL ac;
  int i;

  ac = FALSE;
  for (i=0; i<n; i++)
    if (fabs(1.0 - q2[i]/q1[i]) > EPSCONVER ) ac = TRUE;
  if (fabs(1.0-fq2/fq1) > EPSCONVER) ac = TRUE;
  return(ac);} /* end of "signficant" and of module box 20 */
```

Reproduced with permission of the copyright owner. Further reproduction prohibited without permission.

```
/* Module "cbox1.h" (Header with Conventions and Prototypes)    */

/* to be placed before box 2 ("main" and "frame")              */

/* the following constants are for later activation of debugging */
/* output. DEBUG 1 means that in cbox12.C and cbox15.C the test  */
/* output will be compiled. DBUG 1 means the same for cbox10.C . */
/* After debugging the whole program should be recompiled with   */
/* both constants being defined 0.This suppresses that output    */

#define DEBUG 0    /* selector for debugging cboxes 12 and 15   */
#define DBUG  0    /* the same for cbox 10                      */

/* now follow constants for the program, and data types.        */

#define PARDIM 20  /* maximal number of parameters: up to 20    */
#define DATDIM 500 /* maximal data of data points (up to 500)   */

#define NUL 0.0    /* for convenience                           */
#define ITMAX 10000   /* maximum number of iterations, changeable  */
#define TRUE  1    /* to simulate boolean values                */
#define FALSE 0
#define INC 1.0E-5       /* increment in "derivative"           */
#define CRITERION 1.0E-9 /* of a small eigenvalue in "search"   */
#define EPSCONVER 1.0E-9  /* exit criterion in "significant"    */
#define MYMAX 1.0E9      /* maximal damping value in "search"   */

typedef double PARVEC [PARDIM];    /* vector type for parameter */
typedef double MAT [PARDIM][PARDIM];/* parameter matrices       */
typedef double DATVEC [DATDIM];    /* vector type for data      */

typedef int BOOL ;              /* simulates boolean type      */

/* now protoypes of all functions used by "main"-"frame"        */

void   frame (void);              /* program frame             */
double predict (int k, PARVEC p);     /* the Model!            */
void   datinput(void);            /* data input                */
void   dumpdata(void);              /* dump all data as read */
void   checkinput(void);            /* check input data        */
void   inspect (void);            /* graphics of input data*/
void   itoutput (void);           /* intermediate output       */
void   finoutput (void);          /* final output              */
void   search (void);             /* fitting strategy          */
double squaresum (PARVEC p);          /* calc. of fit criterion*/
void   derivative (int k);        /* calc. of derivatives      */
```

Reproduced with permission of the copyright owner. Further reproduction prohibited without permission.

```
void   fill (void);                  /* fill inform. matrix   */
void   scale (void);                  /* calcul. correl. matrix*/
void   decompose(void);                   /* eigenvalue/eigenvector*/
void   explore (void);                /* explore param. point  */
void   find (void);                  /* find new param. point */
BOOL   inside (PARVEC p);                 /* check admissibility   */
void   accept (void);                 /* accept new parameters */
BOOL   significant (PARVEC q1, PARVEC q2, double fq1,double fq2);
                              /* test for convergence  */

/*  end of header file ("cbox1.h")                          */
```

Reproduced with permission of the copyright owner. Further reproduction prohibited without permission.

APPENDIX E

DUAL ENERGY SCANNING BEAM X-RAYDIOGRAPHY PATENT #5,742,660

US005742660A

United States Patent [19]

Majewski et al.

[11] **Patent Number: 5,742,660**

[45] **Date of Patent: Apr. 21, 1998**

[54] **DUAL ENERGY SCANNING BEAM LAMINOGRAPHIC X-RADIOGRAPHY**

[75] Inventors: **Stanislaw Majewski**, Grafton; **Randolph F. Wojcik**, Yorktown, both of Va.

[73] Assignee: **Southeastern Universities Research Association, Inc.**, Newport News, Va.

[21] Appl. No.: **781,722**

[22] Filed: **Jan. 10, 1997**

[51] **Int. Cl.**[6] **H05G 1/64**

[52] **U.S. Cl.** **378/98.9**; 378/146

[58] **Field of Search** 378/98.9, 98.8, 378/46, 51, 19, 156, 185, 175, 146

[56] **References Cited**

U.S. PATENT DOCUMENTS

4,972,900 11/1990 Sones et al. 378/98.9
4,979,201 12/1990 Kruger 378/175

Primary Examiner—Don Wong

[57] **ABSTRACT**

A multiple x-ray energy level imaging system includes a scanning x-ray beam and two detector design having a first low x-ray energy sensitive detector and a second high x-ray energy sensitive detector. The low x-ray energy detector is placed next to or in front of the high x-ray energy detector. The low energy sensitive detector has small stopping power for x-rays. The lower energy x-rays are absorbed and converted into electrical signals while the majority of the higher energy x-rays pass through undetected. The high energy sensitive detector has a large stopping power for x-rays as well as it having a filter placed between it and the object to absorb the lower energy x-rays. In a second embodiment; a single energy sensitive detector is provided which provides an output signal proportional to the amount of energy in each individual x-ray it absorbed. It can then have an electronic threshold or thresholds set to select two or more energy ranges for the images. By having multiple detectors located at different positions, a dual energy laminography system is possible.

20 Claims, 2 Drawing Sheets

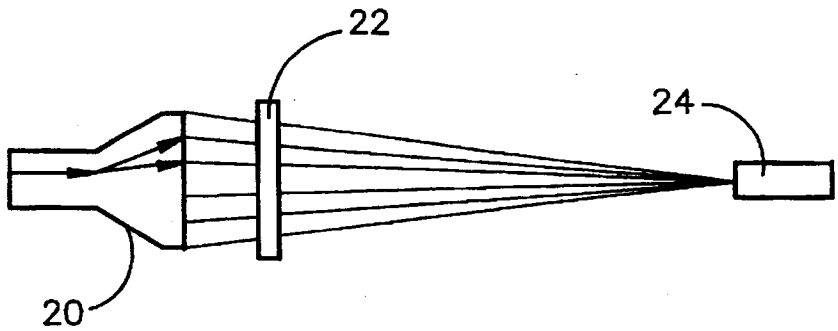

Reproduced with permission of the copyright owner. Further reproduction prohibited without permission.

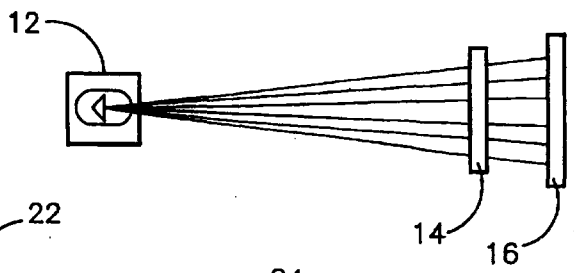

FIG. 1

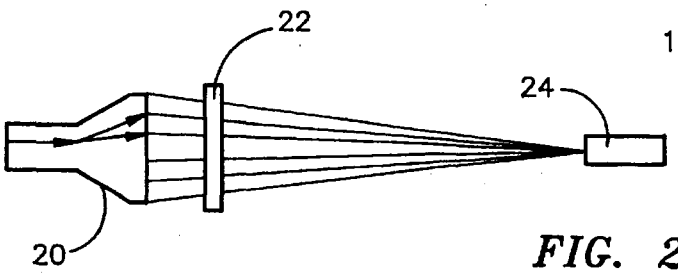

FIG. 2

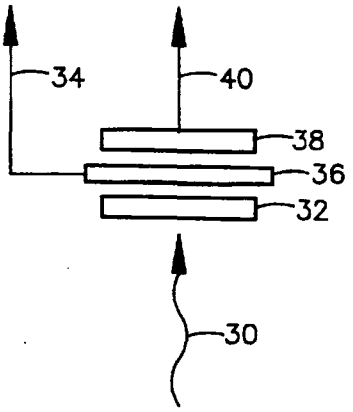

FIG. 3

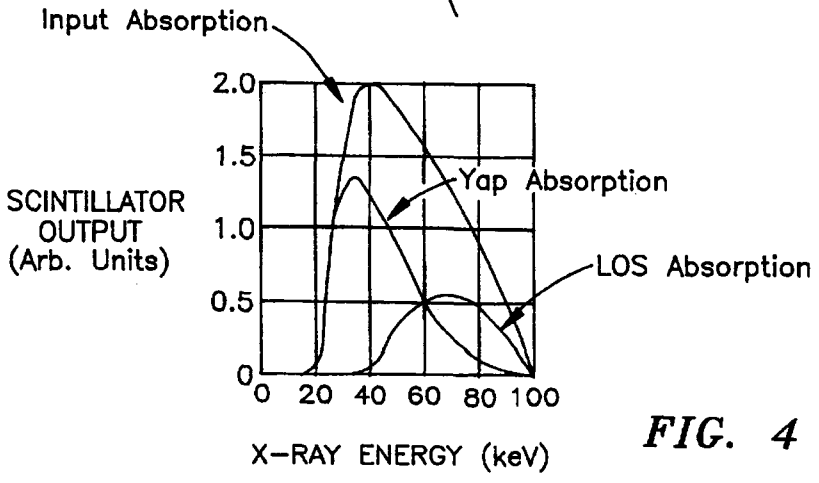

FIG. 4

Reproduced with permission of the copyright owner. Further reproduction prohibited without permission.

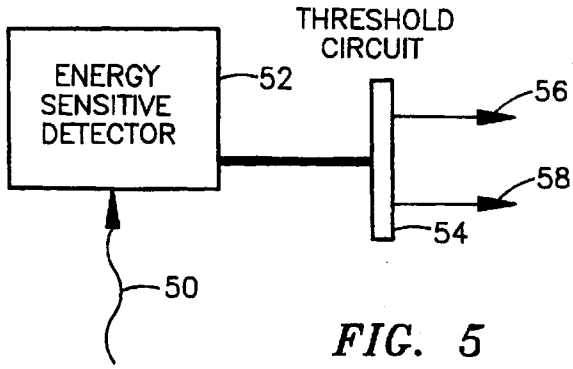

FIG. 5

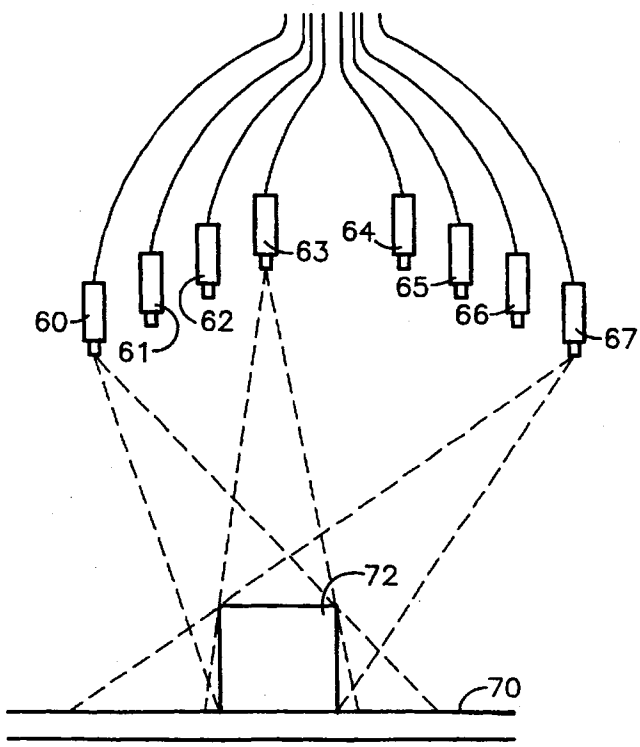

FIG. 6

Reproduced with permission of the copyright owner. Further reproduction prohibited without permission.

DUAL ENERGY SCANNING BEAM LAMINOGRAPHIC X-RADIOGRAPHY

GOVERNMENT RIGHTS

The United States may have certain rights to this invention under management and operating Contract DE-AC05-84 ER 40150 from the United States Department of Energy.

BACKGROUND OF THE INVENTION

1. Field of the Invention

The present invention pertains to x-radiology systems and more particularly to dual energy x-radiography in which images having multiple densities present can be distinguished.

2. Related Prior Art

Most x-radiography systems in use today measure the bulk x-ray transmission of an object in order to produce an image. In this approach, an object is situated in front of a photographic medium. X-radiation is generated and directed toward the object. A portion of the incident x-rays are absorbed by the object. The remainder of the x-rays pass through the object and expose the photographic medium. The problem with this approach is that a low density thick object looks the same as a high density thin object in the image. Thus, in an image with both types of objects, the images can not be distinguished to identify the specific features present. Also, if the features of a low-Z material in the presence of an overlying high-Z material are to be determined, the high-Z material can partially hide these features. A method used to overcome these problems is computed tomography (CT) which takes images from many hundreds of different angles. This technique, however, suffers from "beam hardening" which means that the lower energy x-rays are absorbed easier than the higher energy x-rays, which causes artifacts in the image. Again, this problem is due to the fact that only the bulk x-ray transmission is measured. X-rays with an energy less than two hundred keV interact with matter primarily only through photoelectric and Compton interactions. A photoelectric type of interactions are dominated by the Z of the material while Compton type of interactions are dominated by the electron density of the material. By separately measuring high energy x-rays vs. low energy x-rays, the photoelectric vs. Compton interactions can be reconstructively measured, which are dependent on the type of material and not its thickness. The image can be reconstructed as if it had been taken with mono-energetic x-rays.

In the past, dual energy x-radiography has been attempted in many ways. In one method, two images of an object are taken, one at a low keV setting on the x-ray tube and one at a high keV setting on the x-ray tube. In this method a bulk x-ray imaging system is used. Movement of the object between images can cause problems in the reconstruction. Also, the high keV setting produces a significant number of low energy x-rays thus reducing the ability of effectively separating the types of interactions.

A second method uses two detectors, one detector sensitive to low energy x-rays in front of another detector that is sensitive to high energy x-rays. The high-low x-ray energy sensitivity is mechanically built into the detector and can not be changed without mechanical modifications. This detector, or array of such detectors, is mechanically scanned over the object. Mechanical scanning is a relatively slow process and can take many seconds to minutes even for a low resolution image. The larger the array, the faster the image acquisition, however, the amount of readout electronics increases rapidly as does the cost of the system. Also, very high resolutions require the size of the detectors to be on the order of a few hundred microns which require expensive microelectronics technology.

A third method which has been attempted is to use energy sensitive detectors which actually measure the energy of the incoming x-ray. The problem with such detectors is that they can not handle very high rates and thus, it takes longer to acquire an image. To increase the speed of acquisition, an array of detectors as large as the object is needed with many thousands of electronic channels. The advantage of such a system is that the detectors can be electronically tuned to select the cutoff between the high versus low energy x-ray detection.

Scanning x-ray beam radiography has also been developed, most notably the Reverse Geometry X-radiography system. In this system, the x-ray beam is rastered across an object and one or more detectors are used to obtain an image. These detectors, however, only measure the bulk x-ray transmission of the object. Consequently, this system suffers from the same problems noted in the methods noted above. Using several of these detectors a Laminography system can be obtained. This Laminography system is basically a low resolution CT or computed tomography system.

Dual energy has also been used in computed tomography systems, however, to obtain a high resolution system, detectors of a few microns and a great deal of readout electronics to handle the detector output are required. These systems also require a significant amount of time totaling several minutes to acquire an image. This occurs since the detector must be rotated around the object as well as moved up and down the object for a three dimensional image.

Examples of related art methods and apparatus that are used in obtaining sophisticated x-ray images are illustrated in the following United States patents.

U.S. Pat. No. 4,864,594, titled "Bone Mineral Density Measurement", issued to Dan Inbar et al., relates to an in-vivo bone measuring system using a modified emission computed tomographic gamma camera arrangement. This arrangement is used for detecting radiation from two separate sources located outside of the body of the patient. The two separate sources are oppositely disposed to the gamma camera during rotation of the gamma camera and the radiation sources about the patient for obtaining tomographic data. The two separate sources emit at least two different energy levels. The system includes a processing system for processing the detected radiation to provide a bone mineral density map.

U.S. Pat. No. 5,020,085, titled "X-ray Image Processing Device", issued to Toshiyuki Kawara et al., relates to an x-ray image processing device that uses a dual energy projection radiography method. In this method the low energy image and the high energy image are subjected to a subtraction process to provide a first image such as a conventional bone x-ray image. The first image, similar to a conventional bone x-ray, and the low energy image are subjected to a second subtraction process to produce a second image. The second image is similar to a soft tissue x-ray image. This two step process is alleged to be capable of its image production without deterioration of the x-ray image.

U.S. Pat. No. 5,402,460, titled "Three-Dimensional Microtomographic Analysis System", issued to Roger H. Johnson et al., relates to a microtomographic system that is

Reproduced with permission of the copyright owner. Further reproduction prohibited without permission.

used to generate a three dimensional image of a specimen. The microtomographic system includes an x-ray generator that produces an x-ray beam, a specimen holder that holds the specimen in the beam and an x-ray detector that measures the attenuation of the beam through the specimen. Two projections of each view of the specimen are made. Each projection is made with a different intensity x-ray beam. After a set of projections of one view of the specimen is made, the specimen is rotated on the specimen holder and another set of projections is made. The projections of each view of the specimen are analyzed together to provide a quantitative indication of the phase fraction of the material comprising the specimen. The projections of the different views are combined to provide a three dimensional image of the specimen.

SUMMARY OF THE INVENTION

The present invention provides a method of operation in which an x-ray image is obtained by raster scanning an x-ray beam over an object. An energy discriminating detector is situated so that it absorbs the x-rays that have passed through the object. The energy discriminating detector of the present invention can be of two types. The first embodiment of the energy discriminating detector of present invention is a two detector design made up of a low x-ray energy sensitive detector placed next to or in front of a high x-ray energy sensitive detector. The low x-ray energy sensitive detector is made so by virtue of its small stopping power for x-rays. The lower energy x-rays are absorbed and converted into electrical signals while the majority of the higher energy x-rays pass through undetected. The high energy sensitive detector is made so by virtue of it having a large stopping power for x-rays as well as it having a filter placed between it and the object to absorb the lower energy x-rays.

In the second embodiment of the energy discriminating detector of the present invention, a single energy sensitive detector is used which provides an output signal proportional to the amount of energy in each individual x-ray it absorbed. It can then have an electronic threshold or thresholds set to select two or more energy ranges for the images.

By having a few tens of these detectors located at different positions, a dual energy laminography system can be achieved. With multiple detectors located at different positions, an accurate three dimensional image of an object having multiple densities can be obtained.

BRIEF DESCRIPTION OF THE DRAWINGS

FIG. 1 is a partial block diagram of a co x-radiography imaging system.

FIG. 2 is a partial block diagram of an x-radiography imaging system in which the present invention may be utilized.

FIG. 3 is a partial block diagram of a first embodiment of a dual energy x-radiography imaging system.

FIG. 4 of a graph illustrating the x-ray absorptions of the dual energy detector of FIG. 3.

FIG. 5 is a partial block diagram of a second embodiment of a dual energy x-radiography imaging system.

FIG. 6 is a partial block diagram of a laminographic multiple energy sensitive detector system.

DESCRIPTION OF THE PREFERRED EMBODIMENT

In standard x-radiography, only a two dimensional shadow outline of an object is obtained. Differentiation between a thick low stopping power object and a thin high stopping power object can not be obtained. A partial block diagram of a conventional x-radiography imaging system is illustrated in FIG. 1. In a conventional x-radiography system, an x-ray point source 12 is used to generate x-rays to be incident upon an object 14. A photographic film 16 is placed behind object 14. Film 16 acts as a detector, being exposed by x-rays that are not absorbed by object 14. As indicated previously, the Z of the object cannot be differentiated and the photographic image is the same whether the object is thick object having a low stopping power or low absorption ability for x-rays, or a thin object having a high stopping power or high absorption ability for x-rays.

FIG. 2 illustrates a x-radiography system of the type for use with the present invention. A raster scanning x-ray tube 20 is used instead of a point source. An object 22 is placed next to or in juxtaposition with scanning x-ray 20 so that the x-rays generated by tube 20 are incident upon object 22. Some x-rays are absorbed by object 22 and others travel to and are focused on point detector 24. In this system; an advantage is obtained by using a point detector. Scattered x-rays and other non-focused x-rays that may blur or cloud the image of object 22 are not detected. Only focused x-rays are detected and contribute to the image produced by detector. Detector 24 may be as simple as being composed of a scintillator and a photomultiplier tube (PMT), which measures the intensity of the transmitted x-ray flux. The signal produced by the detector is digitized by a sampling twelve bit analog to digital convertor and correlated to the location of the x-ray spot to build up a two dimensional image. By using this system, it is possible to shrink the raster pattern and achieve linear magnification of up to twenty-five times. The raster pattern can also be electronically panned over the face of the tube to look at different areas. Due to its high scanning rate and its ability to read two point detectors at the same time, stereoscopic x-ray images can be obtained.

Referring now to FIG. 3, a block diagram of a first embodiment of the present invention is illustrated. Incoming x-rays 30 are incident upon low x-ray energy sensitive detector 32. The signal produced through x-ray energy absorption by low x-ray energy detector 32 is transmitted to a display (not shown) via low energy image connection 34. High energy x-rays pass through detector 32 and are incident upon energy separation filter 36 if required. Filter 36 is required only if detector 32 is incapable of absorbing most of the low energy x-rays. Behind filter 36 is located a high x-ray energy sensitive detector 38 which receives all x-radiation that has not been absorbed by either low x-ray energy sensitive detector 32 or filter 36. Low x-ray energy sensitive detector 38 provides signals relating to a high energy image via high energy image connection 40. The signals provided by low x-ray energy sensitive detector 32 and high x-ray energy sensitive detector 38 may be provided to any current display in use in the arts such as a cathode ray tube, etc.

In the preferred embodiments low x-ray energy sensitive detector 32 is preferably made of a three hundred micrometer thick piece of Yttrium aluminum perovskite (YAP). However, any suitable material known in the art for absorbing low energy x-rays may be used. Filter 36 is preferably a 0.38 mm copper filter to enhance the low vs. high energy separation. Any type of filter may be used as long as it is capable of effecting the low vs. high energy separation. High x-ray energy sensitive detector 38 is preferably a one centimeter thick piece of lutetium oxyorthosilicate (LSO), although, as with the low energy x-ray detector, any suitable type of detector for absorbing high energy x-rays Currently available in the art may be used.

Reproduced with permission of the copyright owner. Further reproduction prohibited without permission.

FIG. 4 of a graph illustrating the x-ray absorption characteristics of the crystalline materials used in the dual energy detector of FIG. 3. In order to determine the required thicknesses of the absorption crystals used as low x-ray energy sensitive detector **32**, Yttrium aluminum perovskite, and high x-ray energy sensitive detector **38**, lutetium oxyorthosilicate, a simulation was made using Photocoef. This simulation was performed to analyze the various x-ray absorption of the substances used in the preferred embodiment. A simple bremsstrahlung spectrum filtered by two millimeter aluminum was assumed as an input spectrum and is shown as curve A. This assumption was made without taking tungsten's characteristic lines into account. In the preferred embodiment, the scanning x-ray plate emits x-rays produced by a microfocused beam of up to one hundred keV electrons striking a tungsten target or window anode. In this type of system the input spectrum will have characteristic wavelength bands from tungsten in the input spectrum, but for this application, the bands will not significantly affect the outcome. The yttrium aluminum perovskite (YAP) absorption peaks around thirty-five keV as shown by curve B. The lutetium oxyorthosilicate (LSO), with copper filter **36**, peaks around seventy keV as shown by curve C. In a dual energy imaging system, the main factors affecting image quality are the energy separation and the detected photon fluences. A separation of thirty-five keV is quite good.

In FIG. **5** a partial block diagram of a second embodiment of a dual energy x-radiography imaging system is illustrated as having incoming x-rays **50** incident upon an x-ray energy sensitive detector **52**. X-ray energy sensitive detector **52** is connected to a threshold circuit **54**. Threshold circuit **54** provides two outputs, one relating to a low energy image at output **56** and one relating to a high energy image at output **58**.

In this embodiment, a single dual sensitive detector is used that is capable of detecting two or more x-ray energy levels at the same time. It produces one signal in response to the absorption of low energy x-rays and a second signal in response to absorption of high energy x-rays. These two images are formed separately and combined to produce a single image. Combining the two images is possible since the images are obtained simultaneously.

Referring now to FIG. **6** a partial block diagram of a laminographic multiple energy sensitive detector system is illustrated. Multiple detectors **60–67** are spaced apart along an area **68**, each detector having a different view of the object of which an image is to be taken. Scanning x-ray plate **70** emits x-rays produced by a microfocused beam of up to one hundred keV electrons striking a tungsten target or window anode. Magnetic deflection coils are used to sweep the electron beam in a raster pattern across the broad anode plate producing a moving point x-ray source. The x-rays are emitted in a range under two hundred keV. The x-rays pass through object **72** and are incident upon detectors **60–67**. By determining the amount of x-rays absorbed, an image of the object and its density or densities can be determined as previously explained. Because of the positioning of detectors **60–67** a three dimensional image may be obtained. Detector **60** views object **72** from a totally different view than detector **67**. The image received by detector **61** provides a slightly different view than that obtained by detector **60**. In a similar manner, the image received by detector **62** is slightly different than that received by detector **61**. Each of the detectors **60–67** receives a slightly different image, at a slightly different angle and containing more of one side or the other side, than each of the other detectors. In this manner, a three dimensional image can be created from the individual images provided by each of detectors **60–67**. With the dual energy capability of the detectors, a three dimensional, density identified image can be made which accurately approximates the appearance of the object under analysis.

Combining a scanning x-ray beam with either of the two embodiments of the present invention produces an inexpensive, simple and fast dual energy x-ray imaging system. Since the speed of acquisition is defined by how fast the x-rays can be tastered over the object, which is much faster than any mechanical scanning, speed is greatly improved. Also, since the resolution is defined by how the x-ray source is rastered, the size of the detectors has little impact on the resolution and no impact on the speed. Using an array of a few hundred small energy sensitive detectors (as compared to a few thousand above) an image can be acquired at about the same speed as before but with a factor of ten decrease in complexity and cost. When used with multiple detectors at various positions, a three dimensional image can be obtained without image artifacts again with reduced complexity and cost over a standard CT system.

The apparatus and method of the present invention includes the ability to use relatively large size inexpensive energy sensitive detectors to produce high resolution dual energy laminographic images. The scanning x-ray beam technique allows one to obtain dual energy images much faster than with mechanical scanning used in conventional dual energy radiography. The simplicity of the dual energy detector system of the apparatus of the present invention allows reduced complexity and cost as compared to conventional dual energy x-radiography or CT.

While there has been illustrated and described particular embodiments of the present invention, it will be appreciated that numerous changes and modifications will occur to those skilled in the art, and it is intended in the appended claims to cover all those changes and modifications which fall within the true spirit and scope of the present invention.

We claim:

1. A multiple x-ray energy level imaging system comprising:

apparatus for providing a raster pattern scanning x-ray tube beam; and a single point detector apparatus for detecting at least two different energy level x-rays as said raster pattern is scanned.

2. The multiple x-ray energy level imaging system according to claim 1 wherein said single point detector apparatus for detecting includes:

a first low x-ray energy sensitive single point detector; and

a second high x-ray energy sensitive single point detector placed near said low x-ray energy single point detector.

3. The multiple x-ray energy level imaging system according to claim 2 wherein said first low energy sensitive single point detector has small stopping power for x-rays.

4. The multiple x-ray energy level imaging system according to claim 3 wherein said first low energy sensitive single point detector absorbs and converts the lower energy x-rays into electrical signals while the majority of the higher energy x-rays pass through undetected.

5. The multiple x-ray energy level imaging system according to claim 2 wherein said second high energy sensitive single point detector has a large stopping power for x-rays.

6. The multiple x-ray energy level imaging system according to claim 5 wherein said second high energy sensitive single point absorbs and converts the high energy x-rays into electrical signals.

Reproduced with permission of the copyright owner. Further reproduction prohibited without permission.

7. The multiple x-ray energy level imaging system according to claim 2 also including a filter placed between said first low x-ray energy sensitive single point detector said second high x-ray energy sensitive single point detector to absorb the lower energy x-rays.

8. The multiple x-ray energy level imaging system according to claim 1 wherein said single point detector apparatus for detecting includes:

an energy sensitive single point detector which provides an output signal proportional to the amount of energy in each individual x-ray detected.

9. A method for imaging multiple x-ray energy levels comprising:

raster pattern scanning an object with an x-ray beam emanating from a raster scanned source of x-rays and detecting using a single point detector apparatus at least two different energy level x-rays as said raster pattern is scanned.

10. The method for imaging multiple x-ray energy levels according to claim 9 wherein said detecting includes:

distinguishing a first low x-ray energy level with a low x-ray energy single point detector; and

distinguishing a second high x-ray energy level with a high x-ray energy single point detector placed near said low x-ray energy single point detector.

11. The method for imaging multiple x-ray energy levels according to claim 10 wherein distinguishing a first low energy level includes stopping low energy x-rays.

12. The method for imaging multiple x-ray energy levels according to claim 11 wherein said stopping low energy x-rays includes:

absorbing lower energy x-rays;

converting lower energy x-rays into electrical signals; and

passing higher energy x-rays.

13. The method for imaging multiple x-ray energy levels according to claim 10 wherein said distinguishing a second high x-ray energy level includes stopping high energy x-rays.

14. The method for imaging multiple x-ray energy levels according to claim 10 also includes:

providing a filter between said low x-ray energy single point detector and said high x-ray energy single point detector; and

absorbing lower energy x-rays in said filter.

15. The method for imaging multiple x-ray energy levels according to claim 14 wherein said stopping high energy x-rays includes:

absorbing high energy x-rays; and

converting high energy x-rays into electrical signals.

16. The method for imaging multiple x-ray energy levels according to claim 9 wherein said detecting includes:

providing an output signal proportional to the amount of energy in each individual x-ray detected.

17. A multiple x-ray energy level imaging system for providing an image of an object having a plurality of densities comprising:

apparatus for providing a raster pattern scanning x-ray beam having multiple energy levels; and

a single point detector apparatus for detecting at least two different energy level x-rays and absorbing said different energy level x-rays and converting each of said absorbed different energy level x-rays into electrical signals representative of the intensity of said different energy level x-rays.

18. The multiple x-ray energy level imaging system according to claim 17 wherein said single point detector apparatus for detecting includes a plurality of spaced apart single point detector apparatus, each having:

a first low x-ray energy sensitive single point detector; and

a second high x-ray energy sensitive single point detector placed near said low x-ray energy detector.

19. The multiple x-ray energy level imaging system according to claim 18 also including a filter placed between each said first low x-ray energy sensitive single point detector and said second high x-ray energy sensitive single point detector to absorb lower energy x-rays.

20. The multiple x-ray energy level imaging system according to claim 17 wherein said single point detector apparatus for detecting includes:

a plurality of energy sensitive single point detectors spaced apart in an area near an object which provide output signals proportional to the amount of energy of each individual x-ray detected passing through said object.

* * * * *

Reproduced with permission of the copyright owner. Further reproduction prohibited without permission.

REFERENCES

1. From the World Wide Web page *http://www.resonancepub.com/wroentgen.htm* maintained by Resonance Publications, Inc.
2. J. A. Del Regato, Radiological Physicists, Springer Verlag, New York, NY, 1985.
3. From the World Wide Web page *http://www.xray.hmc.psu.edu/rci/ss1/ss1_2.html* maintained by Radiology Centennial, Inc., Reston, Virginia.
4. From the World Wide Web page *http://www.orau.org/ptp/collection/xraytubescoolidge xraytubescoolidge.htm* maintained by the Oak Ridge Associated Universities, Oak Ridge, Tennessee.
5. A. Chilton, J. Shultis, and R. Faw, Principles of Radiation Shielding, Prentice-Hall, Inc., Englewood Cliffs, NJ, 1984, page 110.
6. From the World Wide Web page *http://learntech.uwe.ac.uk /radiography/Rscience /diag_xray_tube/rotating_xray_tube.htm* maintained by the University of the West of England, Coldharbour Lane, Bristol, England.
7. S. Flugge (ed.), Handbuch der Physik, Vol. 30, Springer-Verlag, Berlin, 1957.
8. A. Chilton, J. Shultis, and R. Faw, Principles of Radiation Shielding, Prentice-Hall, Inc., Englewood Cliffs, NJ, 1984, page 114.
9. A. Chilton, J. Shultis, and R. Faw, Principles of Radiation Shielding, Prentice-Hall, Inc., Englewood Cliffs, NJ, 1984, page 110.
10. N. Dyson, X-rays in atomic and nuclear physics, Cambridge University Press, New York, 1973, pp 11-24.
11. R. Evans, The Atomic Nucleus, McGraw-Hill Book Company, Inc, New York, 1955, pg 672.
12. A. Chilton, J. Shultis, and R. Faw, Principles of Radiation Shielding, Prentice-Hall, Inc., Englewood Cliffs, NJ, 1984, page 43.
13. Calculated using "PHOTCOEF" software, AIC Software, Grafton, MA.

Reproduced with permission of the copyright owner. Further reproduction prohibited without permission.

14. R. Evans, The Atomic Nucleus, McGraw-Hill Book Company, Inc, New York, 1955, pg 684.
15. R. Lapp and H. Andrews, Nuclear Radiation Physics, Printice-Hall, Inc, Englewood Cliffs, NJ, 1972, pg 240.
16. N. Dyson, X-rays in atomic and nuclear physics, Cambridge University Press, New York, 1973, pp 222.
17. N. Dyson, X-rays in atomic and nuclear physics, Cambridge University Press, New York, 1973, pp 222.
18. R. Evans, The Atomic Nucleus, McGraw-Hill Book Company, Inc, New York, 1955, pg 711.
19. N. Dyson, X-rays in atomic and nuclear physics, Cambridge University Press, New York, 1973, pp 200.
20. See for example the SENOSCAN Digital Mammography System produced by the Fischer Imaging Corporation, Denver, CO.
21. Trademark of Digiray Corporation, San Ramon, CA.
22. Image courtesy of Digiray Corporation, San Ramon, CA.
23. E. Solomon, et. al, "Low-exposure scanning-beam x-ray fluoroscopy system," Proceedings of SPIE, Vol. 2707, 140-149, 1996.
24. 1. Z. des Plantes, Eine neue Methode zur Differenzierung in der Röntgenographie, Acta Radio, vol. 13 (1932) 182.
25. Images acquired and reconstructed by Bill Winfree, NASA-Langley, Hampton, VA.
26. Hamamatsu Corporation, 360 Foothill Rd, Bridgewater, NJ.
27. Scionix, LA Bunnik, The Netherlands.
28. M. Moszynski, et. al, "Timing properties of GSO, LSO, and other Ce doped scintillators," Nuclear Instruments and Methods in Physics Research, A372 (1996) 51-58.

Reproduced with permission of the copyright owner. Further reproduction prohibited without permission.

29. Hitachi Chemical Co., Ltd. represented by Marubeni Specialty Chemical Co., White Plains, NY.

30. Chuck Melcher of Schlumberger-Doll Research, Ridgefield CT.

31. Carl Zorn, Jefferson Lab, 12000 Jefferson Ave., Newport News, VA 23606, private communication.

32. Photomultiplier tubes principles & applications, Philips Photonics, 100 Providence Pike, Slaterville, RI 02876, 1994.

33. Electron Tubes Limited, 100 Forge Way, Rockaway, NJ.

34. Photonis, Avenue Roger Roncier Z.I. Beauregard B.P. 520 19106 BRIVE Cedex, France.

35. Photomultiplier tubes principles & applications, Philips Photonics, 100 Providence Pike, Slaterville, RI 02876, 1994.

36. Lumatec, Linienstrasse 9-13, Deisenhofen, Germany 82041.

37. See for example G.T. Barnes, "Detector for Dual-Energy Digital Radiography," Radiology Vol 156, 1985, pp 537-540.

38. A.C. Kak, "Computerized tomography with x-ray emission and ultrasound sources," Proc. IEEE, Vol 67, pp. 1245-1272, 1979.

39. L. Lehmann, et. al, "Generalized image combinations in dual KVP digital radiography," Med. Phys., 8(5),Sept./Oct. 1981.

40. W. Press et. al, "Numerical Recipes in C, the Art of Scientific Computing, 2nd ed., Cambridge University Press, 1992.

41. H. Cardinal and A. Fenster, "An accurate method for direct dual-energy calibration and decomposition," Med. Phys., 17(3),May/Jun. 1990.

42. R.E. Alverez and A. Macovski, "Energy-selective reconstructions in x-ray computerized tomography," Phys. Med. Biol., 21,733(1976).

Reproduced with permission of the copyright owner. Further reproduction prohibited without permission.

43. W.R. Brody, G. Butt, A. Hall, and A. Macovski, "A method for selective tissue and bone visualization using dual energy scanned projection radiography," Med Phys, Vol. 8 (1981), pp. 353-357.

44. See, for example, Varian Medical Systems' PaxScan 4030, Palo Alto, CA, http://www.varian.com/prd/prd403.html.

45. R.A. Brooks and G Di Chiro, "Split-Detector Computed Tomography: A Preliminary Report," Radiology, Vol. 126 (1978) pp. 255-257.

46. D.L. Ergun et al., "Single-exposure dual-energy computed radiography: Improved detection and Processing," Radiology Vol 174, (1990) pp.243-249.

47. M.M. Tesic, R.A. Mattson, G.T. Barnes, R.A. Sones, and J.B. Stickney, "Digital radiography of the chest: design features and considerations for a prototype unit," Radiology Vol 148 (1983) pp. 259-264.

48. D.R. Morgan, R.A. Sones, and G.T. Barnes, "Performance characteristics of a dual-energy detector for digital scan projection radiography," Med Phys, Vol. 14, No. 5 (1987) pp. 728-735.

49. E. Beuville, et al, "High Resolution x-ray Imaging Using Silicon Strip Detector," IEEE Trans Nucl Sci, Vol 45 (1998) pp. 3059-3063.

50. R.M. Harrison, "Digital radiography – a review of detector design," Nuclear Instruments and Methods, Vol. A310 (1991) pp. 24-34.

51. See, for example, Lumar Corporation, Madison, Wisconsin, http://www.lunarcorp.com.

52. See, for example, Analogic Corporation, 8 Centennial Drive, Peabody, MA, http://www.analogic.com/.

53. C.L. Melcher and J.S. Schweitzer, "Cerium-doped Lutetium Oxyorthosilicate: A Fast, Efficient New Scintillator," IEEE Trans Nucl Sci, Vol 39, No. 4 (1992) pp. 502-505.

54. R. Wojcik, et. al, "Embedded Waveshifting Fiber Readout of Long Scintillators," IEEE Nuclear Science Symposium Conference Record, Oct 25-31, 1992.

Reproduced with permission of the copyright owner. Further reproduction prohibited without permission.

55. Information from the Scionix USA website, Orlando, Florida http://www.scionixusa.com/crystals.html.

56. M.V. Korzhik, O.V. Misevich, and A.A. Fyodorov, "$YAlO_3$:Ce Scinitillators: application for X- and soft γ-ray detection," Nucl Inst Meth, B72 (1992) pp. 499-501.

57. S. Baccaro et al., "Scintillation properties of YAP:Ce," Nucl Inst Meth A361 (1995) pp. 209-215.

58. M. Moszynski et al., "Timing properties of GSO, LSO, and other Ce doped scintillators," Nucl Inst Meth A372 (1996) pp. 51-58.

59. Bicron Newbury, Newbury, Ohio 44065.

60. Sample kindly provided by Bicron Newbury.

61. Wavetek, San Diego, CA 92123.

62. Viscasil 60,000 M, GE Silicones, Waterford, NY 12188.

63. G.F. Knoll, Radiation Detection and Measurement, 2nd edition, John Wiley & Sons, New York, NY, pp 120-128.

64. E.A. Birt, F.R. Parker, and W.P. Winfree, "Quantification of Corrosion Damage in Aircraft Skin Using a Novel X-ray Radiography System," Presented at the 20th Annual review of Progress in QNDE held in Brunswick, ME, August 1993.

65. Soyee Product Inc, Danielson, CT.

66. W.H. Press et al., Numerical Recipes in C, The Art of Scientific Computing, Second edition. Cambridge University Press, New York, 1992.

67. J.G. Reich, C Curve Fitting and Modeling for Scientists and Engineers, McGraw-Hill, Inc., New York, 1991.

68. Imagej, Research Services Branch, National Institute of Mental Health, Bethesda, Maryland, USA, http://rsb.info.nih.gov/ij/.

69. Mitsubishi Rayon Co., Optical Fiber Department, Tokyo, Japan.

Reproduced with permission of the copyright owner. Further reproduction prohibited without permission.

70. Hans-Juergen Besch et al., "Imaging ionization chamber for medical application with synchrotron radiation" Proceedings of SPIE -- Volume 2278 X-Ray and UV Detectors, Richard B. Hoover, Mark W. Tate, Editors, July 1994, pp. 30-38.

71. Apple Computer, Inc., Cupertino, CA 95014

Reproduced with permission of the copyright owner. Further reproduction prohibited without permission.

VITA

Randolph Frank Wojcik

Randolph Frank Wojcik was born in Fort Churchill, Manitoba, Canada on June 30, 1963. After living in Africa, Florida, Taiwan, Virginia, and Pennsylvania, he graduated from Phoenixville High School in Phoenixville, PA in June 1981. In July 1981, he entered the United States Air Force and was trained in radio maintenance. After two years, he was awarded a full ROTC scholarship and entered the University of Florida in June, 1983 to study physics. After graduating in May 1987, he spent a year as a student assistant working for Stan Majewski before attending the Weitzmann Institute in Rehovot, Israel for a year of graduate school in 1989. In January, 1990 he was offered a position at the Continuous Electron Beam Accelerator Facility (now known as Jefferson Lab) in Newport News, Virginia. In August, 1990, he started graduate school in Applied Science at The College of William and Mary as a part time student. In 1992 he designed and built his house. In 1994, Randy started his first company called Vorg Electronics which is an electronics assembly company. In 1995 he started his second company, Ray Visions Inc., to produce liquid core light guides and radiation imaging equipment. Both companies were ran from his garage and spare bedrooms in his house. With all these additional commitments, work on his dissertation was slowed down and he finally defended in November, 2004. He is currently still working at Jefferson Lab as well as continuing to grow his companies.

Reproduced with permission of the copyright owner. Further reproduction prohibited without permission.